The role of ice shelves in Antarctic ice dynamics

Tom Mitcham

A dissertation submitted to the University of Bristol in accordance with the requirements for award of the degree of Doctor of Philosophy in the Faculty of Science

School of Geographical Sciences

March 2022

Word count: 46,200

Abstract

Ice shelves can control ice discharge from the Antarctic Ice Sheet (AIS) by providing resistive forces to their tributary glaciers – a process known as ice-shelf buttressing. The loss of buttressing through ice-shelf thinning or collapse is driving the present, observed mass loss from the AIS and its associated contribution to global sea level rise. The aim of this thesis is to better understand the buttressing capacity of ice shelves, and where within ice shelves that buttressing is generated. The Larsen C Ice Shelf (LCIS) is a particular focus as its future viability has been called into question following the collapse of its neighbouring ice shelves.

The first research chapter uses an ice flow model to calculate the total buttressing provided by the LCIS. It is found that the majority of the buttressing is generated in the first few kilometres of the ice shelf downstream of the grounding line. In the second research chapter, transient model experiments demonstrate that LCIS grounding line dynamics and mass loss are most sensitive to the calving of ice close to the grounding line, and that the loss of the Bawden and Gipps Ice Rises would have a very limited, direct impact on the grounded tributary glaciers.

The third research chapter uses Antarctic-wide modelling experiments to reveal that the total buttressing capacity of Antarctic ice shelves varies by two orders of magnitude. It is also found that the distribution of the buttressing within an ice shelf is controlled by the ice-shelf geometry, and that a greater area of Antarctica's ice shelves could be considered 'passive' than previously thought.

In the final research chapter, it is shown that the 'stress-flow angle' – a metric proposed to describe the structural integrity of ice shelves – is not frame-indifferent, which raises problems for its use as a metric of ice-shelf stability. Overall, this thesis develops a novel approach to quantifying the total buttressing capacity of ice shelves, and by doing so provides new insights into which regions of Antarctica's ice shelves are most important for buttressing the grounded ice sheet.

Acknowledgements

Firstly, I would like to thank my supervisors, Professor Jonathan Bamber and Professor Hilmar Gudmundsson. Jonathan, for your guidance throughout this research, and your eye for the most interesting questions to pursue. Hilmar, for introducing me to ice-sheet modelling and for the many discussions which have developed my thinking about science and glaciology. I would also like to thank Professor Dan Lunt for his advice which kept me going in moments of doubt.

Thanks to those in the Bristol Glaciology Centre who have helped me over the last four years with conversations about my work and regular coffee breaks – both real and virtual. Particular thanks go to Jenny for her support during the final few months writing this thesis. To my fellow PGR students in 'Browns', of whom there are too many to name, thank you; I really missed working alongside you every day over the last two years.

The researchers in the glaciology group at Northumbria University have been an immense source of knowledge and help; our discussions of recent research were always illuminating. I thoroughly enjoyed my trips to Newcastle in the early years of this PhD, and being able to join the virtual seminars has been a real bonus of the remote working life.

To my friends in Bristol and beyond who have been there throughout, thank you for all the support you have given, and I'm sure you'll all be as glad as I am that this thesis is submitted! In particular, to Aoife, Aimée, Izzy and Anna, I couldn't have asked for more fun and caring friends to live with over the last few years, thank you all so much.

Finally, to my family – and to Mum, Dad and Catherine in particular – I couldn't have done this without you. Your love and belief is what led me to undertake this PhD and got me through to this point. Thank you for everything.

This thesis was supported with funding from the NERC GW4+ DTP (NE/L002434/1).

Author's Declaration

I declare that the work in this dissertation was carried out in accordance with the requirements of the University's *Regulations and Code of Practice for Research Degree Programmes* and that it has not been submitted for any other academic award. Except where indicated by specific reference in the text, the work is the candidate's own work. Work done in collaboration with, or with the assistance of, others, is indicated as such. Any views expressed in the dissertation are those of the author.

SIGNED: ..... DATE:.....

Contents

List of Figures

List of Tables

Chapter 1

Introduction

1.1 Research context and thesis aims

The Antarctic Ice Sheet (AIS) contains enough ice to raise global mean sea level (GMSL) by around 58 m if it were to melt entirely (Morlighem et al., 2020). Over the last three decades the ice sheet has been losing mass, with the cumulative ice loss over that period raising GMSL by 7.6 ± 3.9 mm (Shepherd et al., 2018, Bamber et al., 2018). The contribution of the AIS to changes in GMSL under anthropogenic climate change is a source of deep uncertainty in future climate projections (Oppenheimer et al., 2019), due largely to the possibility of ice-sheet instabilities being triggered (e.g. Schoof, 2007, DeConto and Pollard, 2016).

The AIS is fringed by floating ice shelves, and over 80% of the fast-flowing ice streams and glaciers that control the dynamics of the ice sheet terminate in these ice shelves (Pritchard et al., 2012). Due to their confinement in embayments, or from where they locally ground at pinning points, ice shelves generate resistive forces which act to reduce the ice flux across the grounding line – a process known as ice-shelf buttressing (e.g. Thomas, 1979b, Gudmundsson, 2013). They can therefore control the rate at which mass is lost from the ice sheet. The increased mass loss from the AIS has been attributed to a reduction in the buttressing forces provided by its ice shelves, as they have thinned due to increased ocean melting (e.g. Paolo et al., 2015, Adusumilli et al., 2020) or collapsed entirely (e.g. Rott et al., 1996, Scambos et al., 2004). This reduction in buttressing leads to an increase in the ice speed of the grounded tributary glaciers and consequently an increase in

ice discharge (e.g. Gardner et al., 2018, Rignot et al., 2019).

The Antarctic Peninsula (AP), the most northerly region of the AIS, experienced atmospheric warming at more than five times the global average during the twentieth century (Vaughan et al., 2003, Khazendar et al., 2011). In 1995, the Larsen A Ice Shelf (LAIS) calving front retreated rapidly (Rott et al., 1996), and then in 2002 the Larsen B Ice Shelf (LBIS) collapsed in the space of 6 weeks (Scambos et al., 2004), thought to be caused by increased surface melting and hydrofracture (van den Broeke, 2005, Banwell et al., 2013). Following these ice-shelf collapses – and the sudden reduction in buttressing – tributary glaciers accelerated, with some increasing in speed by more than 800% (Rignot et al., 2004), and ice velocities in the region remain elevated to the present day (Berthier et al., 2012, Rott et al., 2018). The rapid collapse of these two ice shelves has raised questions about the future viability of the Larsen C Ice Shelf (LCIS) (Holland et al., 2015, Jansen et al., 2015), the fourth-largest ice shelf in Antarctica and southerly neighbour of the LBIS. In July 2017 the LCIS calved the A68 iceberg, reducing the areal extent of the LCIS by $\sim 10\%$ (Hogg and Gudmundsson, 2017).

Existing work has sought to characterise the buttressing provided by ice shelves through different methods, including: modelling the changes in stress state at the grounding line due to the presence of an ice shelf (e.g. Gudmundsson, 2013, De Rydt et al., 2015, Royston and Gudmundsson, 2016); calculating local 'buttressing numbers' within an ice shelf (e.g. Borstad et al., 2013, Fürst et al., 2016); determining the sensitivity of the grounding line flux to small perturbations in ice-shelf thickness (e.g. Reese et al., 2018b, Zhang et al., 2020); or simulating the transient evolution of the grounded ice sheet to the complete removal of ice shelves (e.g. Schannwell et al., 2018, Martin et al., 2019, Sun et al., 2020).

However, to date, the total buttressing capacity of the LCIS – and other Antarctic ice shelves – has not been determined. Quantifying this would allow for the contribution of different regions of the ice shelves (and features within the ice shelves, such as ice rises) to the total buttressing capacity to be assessed. This would provide further insight into the regions of Antarctica's ice shelves that generate the majority of the total buttressing provided to the ice sheet, and give an alternative and complementary view of ice-shelf buttressing to that obtained in existing studies (e.g. Fürst et al., 2016, Reese et al., 2018b).

On this basis, the research presented in this thesis has three primary aims. The first is to quantify the total buttressing capacity of the LCIS, and to determine where within the ice shelf the majority of that buttressing is generated. Through this approach, the importance of two ice rises at the front of the shelf (the Bawden and Gipps Ice Rises) to the total buttressing provided by the LCIS can also be assessed. The second research aim is to determine the relationship between a reduction in ice-shelf buttressing on the LCIS and the subsequent, transient evolution of its tributary glaciers and grounding line, and the consequences for mass loss from the region. The third research aim is to extend this analysis and determine the total buttressing capacity of other ice shelves around Antarctica. This can provide an assessment of how the total buttressing capacity of ice shelves varies around the continent, and additionally allows for the drivers of the variation in that buttressing to be explored.

1.2 Thesis structure

To address these research aims, the thesis is structured as follows.

In Chapter 2, the necessary scientific background is outlined and some of the most relevant literature is discussed. This includes sections on the AIS, Antarctic ice shelves, observed trends in the mass balance of both, and the evidence that has been generated for ice-shelf buttressing. Some aspects of ice-sheet modelling are then briefly discussed, together with an outline of the potential instabilities in AIS dynamics. In the final section, the key literature on ice-shelf buttressing – to which this thesis most directly relates – is discussed and the knowledge gaps this thesis seeks to fill are highlighted.

In Chapter 3, the ice flow model Úa, which is used throughout this thesis, is introduced and the governing equations and numerical methods are outlined.

Chapter 4 is the first research chapter, and it uses Úa in a diagnostic mode to explore the buttressing capacity of the LCIS. The instantaneous response of the ice-shelf and its tributary glaciers to the calving of the A68 iceberg is modelled and compared to observations. Through a series of idealised calving, thinning and ice-rise ungrounding experiments, the total buttressing capacity of the LCIS is characterised, and it is determined where within the ice shelf (and from what features) that buttressing is generated.

In Chapter 5 the transient, or prognostic, capabilities of Úa are used to explore the mass redistribution of the LCIS and its tributary glaciers in response to changes in ice-shelf buttressing driven by the idealised calving and ungrounding experiments from Chapter 4. The impact of the loss of basal contact at the Bawden and Gipps Ice Rises on the transient evolution of the LCIS is examined, and the relationship between changes in ice-shelf buttressing and the subsequent mass loss from the tributary glaciers is characterised.

Chapter 6 uses Úa in a diagnostic mode again, this time to model the entire AIS. The total buttressing capacity of eight major Antarctic ice shelves – in addition to the LCIS – is quantified. This analysis produces the first assessment of the total buttressing capacity of these ice shelves, and allows for both an examination of how buttressing varies around the ice sheet and an exploration of where within these ice shelves the majority of that buttressing is generated. The results are compared with existing maps of ice-shelf buttressing and grounding line flux sensitivity for the AIS.

Chapter 7, the final research chapter, consists of an analysis of a metric that has been used to examine ice-shelf structural integrity and calving-front stability. It is shown that the 'stress-flow angle' – first proposed by Kulessa et al. (2014) and used to analyse the LBIS and LCIS – is not frame-indifferent, which raises problems for its use as a metric for determining the structural integrity or stability of an ice shelf.

Finally, in Chapter 8, the key findings drawn from each research chapter are highlighted and discussed in terms of the original research aims. The thesis concludes with a discussion of the limitations of the work conducted and suggestions for future research.

1.2.1 Published work

The research presented in Chapter 4 has been published in *The Cryosphere* (Mitcham et al., 2022) with the following citation: "**Mitcham, T.**, Gudmundsson, G. H., and Bamber, J. L.: The instantaneous impact of calving and thinning on the Larsen C Ice Shelf, The Cryosphere, 16, 883–901, https://doi.org/10.5194/tc-16-883-2022, 2022."

Much of the 'Ice flow model' subsection of the published manuscript has been moved to the model description in Chapter 3 of this thesis; some of the sections covered in the 'Introduction' of the published manuscript are discussed in the scientific background in Chapter 2 of this thesis.

The research presented in Chapter 7 has been accepted for publication in the *Journal of Glaciology* in a shortened format (to comply with the journal's requirements) under the following citation: "**Mitcham, T.**, Gudmundsson, G. H. (in press): On the validity of the stress-flow angle metric for ice-shelf stability, Journal of Glaciology."

Specific author contributions are highlighted in the Prefaces of Chapters 4 and 7, but in both cases I was responsible for preparing the data, conducting the modelling experiments, performing the analysis and writing the manuscripts. Co-authors discussed the analysis and provided comments on draft manuscripts.

Chapter 2

Background

This chapter outlines the scientific background and context to the research conducted in this thesis. In addition to this, the literature most pertinent to each research chapter is also discussed in the 'Introduction' sections of Chapters 4-7.

Here, the characteristic features of the Antarctic Ice Sheet (AIS) will be presented, and evidence of its present-day mass balance outlined. Our understanding of the role of ice shelves in driving the present-day trends in AIS mass balance will be discussed, with a focus on the collapse of ice shelves in the Antarctic Peninsula and the response of their tributary glaciers. This will lead to a discussion of the Larsen C Ice Shelf, and the reasons that it was chosen as a focus of the research in this thesis.

The use of ice sheet models to aid our understanding of ice dynamics will then be briefly explored, together with a discussion of the ice-dynamic instabilities present in Antarctica. In the final section, the focus turns to the studies of ice-shelf buttressing that have most directly influenced the research conducted in this thesis. This includes work which has mapped ice-shelf buttressing across Antarctica's ice shelves, and more specifically examined the buttressing of the LCIS.

I end by summarising the current gaps in our knowledge of ice-shelf buttressing, and the way that the research in this thesis, through the three primary research aims outlined in Chapter 1, seeks to fill them.

2.1 The Antarctic Ice Sheet

The AIS is the largest ice mass on Earth, presently covering an area of around 13.5 million km^2 (Benn and Evans, 2014; p. 209) and containing approximately 26 million km^3 of ice (Morlighem et al., 2020). Over 60% of Earth's freshwater is stored in the AIS, and it contains enough ice volume above flotation (VAF) to raise global mean sea level (GMSL) by $\sim$ 58 m (Morlighem et al., 2020). Understanding the future behaviour of the AIS, and the consequences of any changes for global sea level rise (SLR), is therefore one of the of the most pressing questions in determining the societal impacts of anthropogenic climate change. However, the future, dynamic behaviour of the AIS – particularly beyond the twenty-first century – is deeply uncertain (Oppenheimer et al., 2019), and the component with the largest uncertainty in future SLR projections is the contribution of the AIS (Bamber et al., 2019).

The AIS is typically considered to comprise of three distinct, connected ice sheets characterised by their topographic settings and dynamic behaviour (Cuffey and Paterson, 2010; p. 134): the East Antarctic Ice Sheet (EAIS), West Antarctic Ice Sheet (WAIS) and the Antarctic Peninsula (AP).

The EAIS is by far the largest, and oldest, of the three regions that make up the AIS (Bell and Seroussi, 2020). It contains enough ice to raise GMSL by $\sim$ 52 m SLE (Morlighem et al., 2020), which accounts for over 90% of the total SLR potential of the AIS. The EAIS rests largely on bedrock that is above sea level, and for that reason is generally thought to be more stable to climatic perturbations than the WAIS and AP (Benn and Evans, 2014; p. 209). There are, however, regions within the EAIS in which the bedrock is significantly below sea level (e.g. in the Wilkes subglacial basin) which may have seen ice-sheet retreat in past climatic warm periods (Cook et al., 2013, DeConto and Pollard, 2016).

The WAIS is an order of magnitude smaller than the EAIS in both areal extent and ice volume, and it is also a younger ice sheet, with evidence that it may have collapsed entirely in previous climatic warm periods (Bell and Seroussi, 2020). It is separated from the EAIS by the Transantarctic Mountains, and its characteristic feature is that, unlike the EAIS, large regions of it rests on bedrock that is below sea level, with the bed reaching depths of up to 2,800 m below sea level (Fretwell et al., 2013) at its deepest. This makes the WAIS a marine ice sheet and, as will be outlined in Sect. 2.3, it is therefore vulnerable to ice-dynamic instabilities that could lead to rapid mass loss and associated

SLR. Mercer (1978) first proposed that a warming climate, driven by the emission of greenhouse gases, could cause rapid SLR from the collapse of the WAIS, and the WAIS has enough ice resting on bedrock below sea level to raise GMSL by ~ 3.3 m (Bamber et al., 2009).

The AP is by far the smallest of the three regions of the AIS. It contains enough ice to raise GMSL by 0.27 m (Morlighem et al., 2020), an order of magnitude less than the WAIS. Its topography is characterised by a mountain range that runs down the spine of the AP, which is an extension of the Andes mountain range in South America. In these mountains glaciers are formed, fed by some of the largest rates of surface accumulation on the AIS (van Wessem et al., 2016). The AP forms a significant focus of this thesis, as it has experienced rapid changes in its climate (Scambos et al., 2014) and the areal extent of its ice shelves (Cook and Vaughan, 2010), and contains the continent's fourth-largest ice shelf – the Larsen C Ice Shelf (LCIS) – the future viability of which has recently been called into question and is the focus of much of this thesis. Whilst its potential contribution to GMSL is limited in comparison with the other regions of the AIS, the AP can be seen as a 'natural laboratory' for examining and understanding the response of the ice sheet to changes in external forcing which could occur in other regions of Antarctica in the future, and which would have far larger consequences for changes in GMSL.

In addition to being described by three geographical regions, the AIS can also be split into three component parts based on the type of ice flow exhibited: ice divides (or inland flow regions); ice streams; and ice shelves (Cuffey and Paterson, 2010; p. 356). In regions of inland flow the driving stresses are small, and there is typically no motion at the ice-bed interface. The little ice flow that does occur is due to the viscous, creep deformation of the ice column. Ice streams are regions of enhanced ice flow, in which the majority of the motion of the ice occurs at the ice-bed interface, and the entire ice column moves via basal sliding. There are many different mechanisms that can account for the relative motion at the ice-bed interface (subsumed into the term 'basal sliding'), but these fall into two main categories: 'deformable-bed' or 'soft-bed' sliding, in which the upper layer of the bed itself deforms due to the basal shear stress if it consists of subglacial till or sediments saturated with water; and 'rigid-bed' or 'hard-bed' sliding in which a thin layer of water forms where the ice base is at the melting point, lubricating the ice-bed interface and allowing the ice column to slide over the bedrock. These fast-flowing regions account for 90% of the drainage of ice from the

AIS (Bamber et al., 2000). Finally, ice shelves form at the margins of the ice sheet, where the ice thins enough to lose contact with the bedrock beneath it and starts to float on the ocean surface. The ice shelves surrounding the Antarctic continent are discussed more extensively in Sect. 2.2.

Due to the presence of these three different regimes of ice flow, ice velocities vary by over three orders of magnitude across the AIS. Figure 2.1 shows the ice velocity over the entire AIS (Rignot et al., 2011) and the regions of slow flow (predominantly across the interior of the EAIS) and channelised regions of fast ice-stream and ice-shelf flow are revealed. A histogram of this velocity field has peaks at 5 ma^{-1} – corresponding to regions of slow, inland flow – and a second peak at ~ 250 ma^{-1} corresponding to the flow of ice streams and ice shelves (Rignot et al., 2011).

2.1.1 Antarctic Ice Sheet mass balance

Whether the AIS gains or loses mass depends primarily on the balance between the surface mass balance (SMB) – which for Antarctica is positive and dominated by snowfall, as surface melting is negligible – and ice discharge across the grounding line at the ice sheet's margins. The contribution of basal melting underneath the grounded ice sheet is typically two orders of magnitude smaller than SMB and ice discharge in Antarctica (Benn and Evans, 2014; p. 212).

2.1.2 Present-day mass balance trends

The arrival of satellite remote sensing methods in the early 1990s transformed the capability for measurements of the mass balance of the AIS to be made (e.g. Wingham et al., 2006, Bamber et al., 2018). Methods used to calculate the mass balance of ice sheets include gravimetry, satellite altimetry, and the input-output or mass-budget method (e.g. McMillan et al., 2014, Helm et al., 2014, Gardner et al., 2018, Rignot et al., 2019, Smith et al., 2020). Each method has its strengths and limitations, related to the resolution of the data provided by the sensors, and to the uncertainties arising from a reliance on outputs from forward models (e.g. for glacial-isostatic adjustment (GIA), SMB, or firn-compaction rates) (e.g. Martín-Español et al., 2017, Bamber et al., 2018).

Recent efforts have focused on synthesising and reconciling the estimates of the mass balance of the AIS generated by this range of methodological approaches (Shepherd et al., 2012, Bamber et al., 2018, Shepherd et al., 2018). Overall, the AIS is found to be losing mass at an increasing

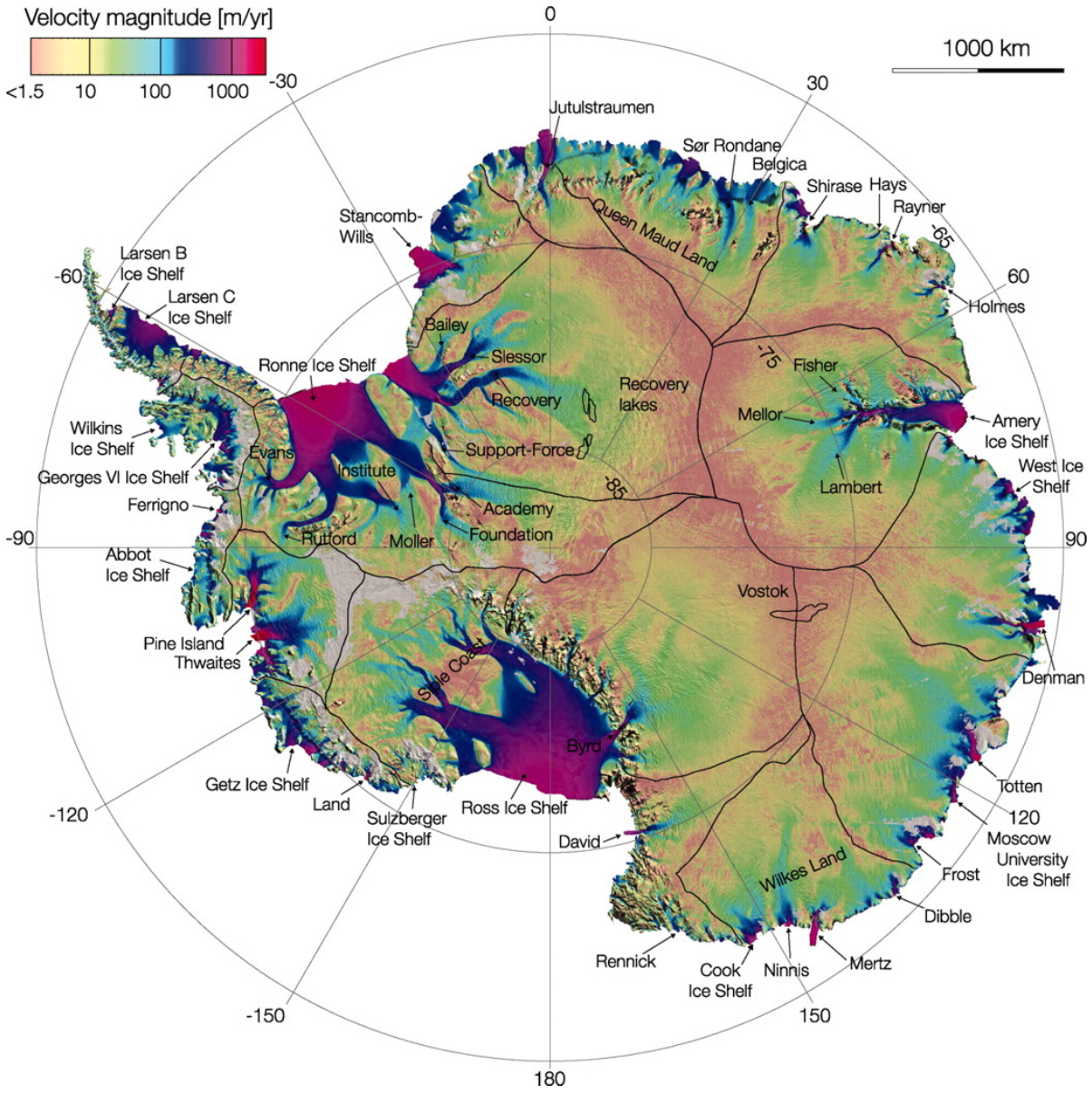

Figure 2.1: The ice velocity of the Antarctic Ice Sheet, with major outlet glaciers and ice shelves labelled and ice drainage basins outlined in black. Figure reprinted from Rignot et al. (2011).

rate. Between 1992 and 1997, the mass balance of the AIS was -49 ± 64 Gt a^{-1}, but for the five years from 2012-2017 the mass balance was -219 ± 43 Gt a^{-1} (Shepherd et al., 2018). Over the period of 1992-2017, the contribution to GMSL from the AIS was 7.6 ± 3.9 mm (ibid.). However, the mass balance of the AIS is highly spatially variable and the present day changes in each region, together with their drivers, are explored below.

The EAIS appears to be close to balance at the present moment, with some approaches measuring

slight mass gains, and others mass losses (Hanna et al., 2020, Bamber et al., 2018, Martín-Español et al., 2017). However, due to its vast size, uncertainties in this region are significant, with small differences in the SMB or biases in the measurement of elevation change corresponding to large changes in the integrated mass balance estimate (Bamber et al., 2018). Gardner et al. (2018) found that the ice discharge of the EAIS has been "remarkably stable" in the period from 2008 to 2015.

By contrast, the WAIS is losing mass at an increasing rate due to the increased discharge from – and associated thinning of – the glaciers in the Amundesn Sea Embayment (ASE) including Pine Island Glacier (PIG) and Thwaites Glacier (TWG) (e.g. Gardner et al., 2018, Rignot et al., 2019). The driver of this imbalance is thought to be the thinning of the ice shelves in the ASE, and the subsequent reduction in ice-shelf buttressing, discussed in more detail in Sect. 2.2.1, demonstrating the crucial role that ice shelves can play in controlling Antarctic ice dynamics. Overall, ocean-driven melting caused the WAIS ice mass loss to increase from 53 ± 29 Gt a^{-1} in 1992-1997, to 159 ± 26 Gt a^{-1} in 2012-2017 (Shepherd et al., 2018). The acceleration and thinning of the tributary glaciers has not only led to increased rates of mass loss, but also to grounding line retreat across the ASE (Konrad et al., 2018).

The AP has also experienced ice-dynamic mass loss over the last 3 decades, directly linked to the loss of buttressing from the ice shelves that collapsed along its eastern edge (e.g. Shuman et al., 2011, Berthier et al., 2012, Wuite et al., 2015). The processes behind the collapse of these northerly AP ice shelves are explored in more detail in Sect. 2.2.1.1. Due to the smaller size of the AP, and its limited potential for significant mass loss, the absolute values of its mass imbalance are smaller. However, despite only accounting for 4% of the total surface area of the AIS, it generated up to 25% of the mass loss from the ice sheet between 1992 and 2011 (Shepherd et al., 2012). Ice mass loss from the AP has increased from 7 ± 13 Gt a^{-1} in 1992-1997, to 33 ± 16 Gt a^{-1} in 2012-2017 (Shepherd et al., 2018).

The mass balance trends over Antarctica's three geographical regions are summarised in Fig. 2.2, which also shows both the temporal variability and the spread in estimates from the three different measurement techniques outlined: gravimetry, altimetry and the input-output method (ibid.).

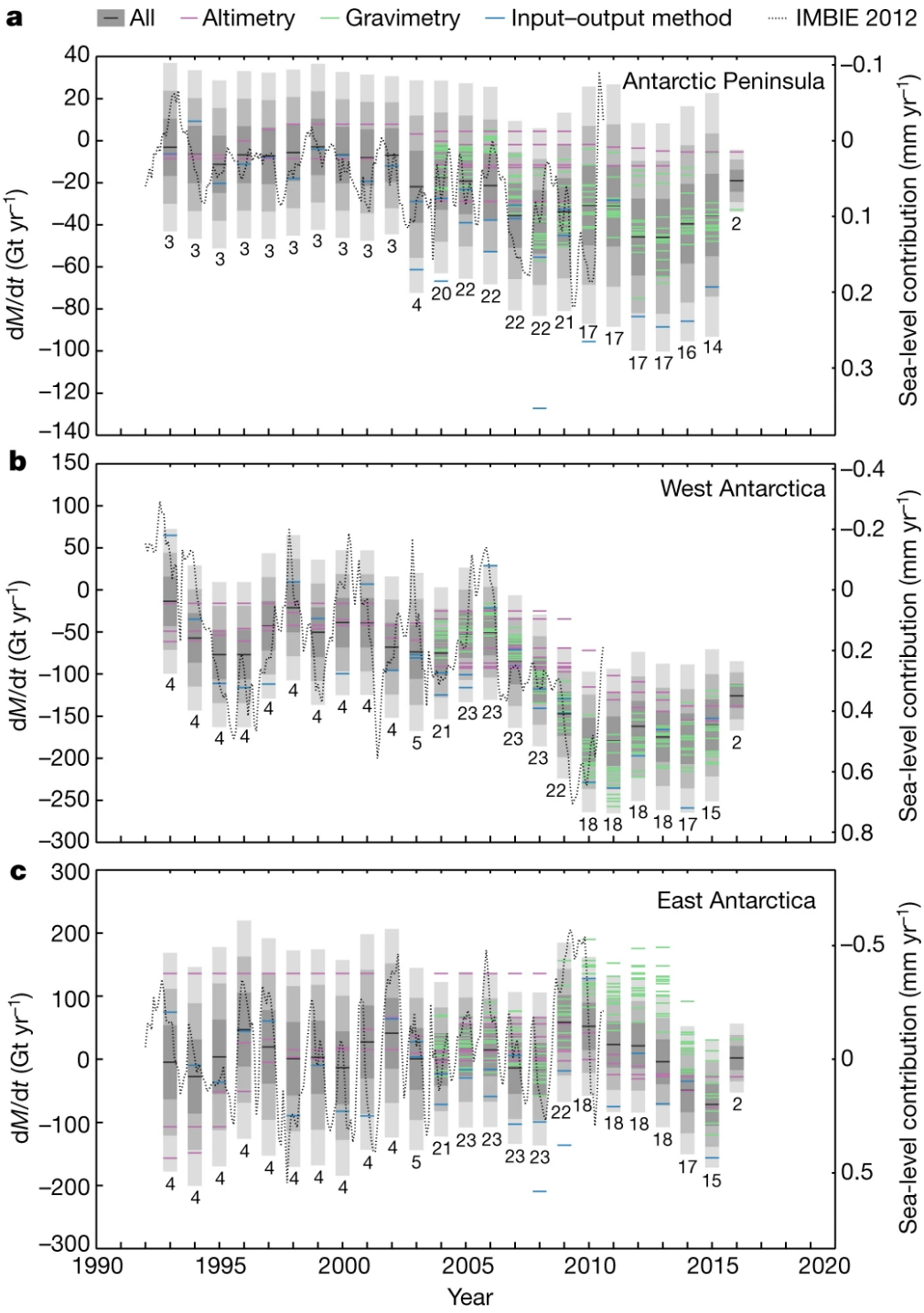

Figure 2.2: Rates of change of ice mass estimates for the years 1992-2017 for the three geographical regions of Antarctica. Individual estimates come from the three different measurement techniques discussed in the main text. In black is the average rate of change of ice mass from the different techniques with the grey shading corresponding to 1σ, 2σ and 3σ uncertainties. Figure reprinted from Shepherd et al. (2018)

2.2 Antarctic ice shelves

This section provides an introduction to Antarctic ice shelves and their importance to the dynamics of the AIS. It then discusses changes that have been observed in the extent and thickness of Antarctic ice shelves over the last three decades and the drivers of that change. In particular, the motivation for studying the LCIS is presented.

Ice shelves are formed at the margins of the AIS where the ice thins and loses contact with the bedrock beneath it. The boundary between the grounded ice and the floating ice shelves is the grounding line, but this boundary should more strictly be thought of as a 'grounding zone' across which the ice sheet adjusts from its grounded state to being in hydrostatic equilibrium with the ocean (Brunt et al., 2010). When ice flows across the grounding line and begins to float it makes its contribution to GMSL. Around 74% of the Antarctic coastline is fringed with floating ice shelves (Bindschadler et al., 2011), and over 80% of the ice discharge from the ice sheet is drained into ice shelves (Pritchard et al., 2012). Ice shelves can be vast in size, with the Ross and Filchner-Ronne Ice Shelves covering $\sim 500,000$ km^2 and $\sim 450,000$ km^2, respectively, and both being approximately twice the areal size of the United Kingdom.

Ice shelves tend to form in embayments, and "smooth the outline" of the AIS (Thomas, 1979a). Unconfined ice shelves around Antarctica are rare, and only seem to exist where they are supported by abutting sea ice (Wearing et al., 2020) (e.g. the Thwaites, Mertz and Drygalski Ice Tongues). When confined in an embayment, or where they locally ground at an ice rise or rumple, ice shelves can generate resistance which is transferred upstream to the grounding line – in a process known as ice-shelf buttressing (e.g. Dupont and Alley, 2005, Gudmundsson, 2013). The buttressing role of ice shelves is central to the research in this thesis, and as such the literature on ice-shelf buttressing is explored in more detail in Sect. 2.4.

2.2.1 Ice-shelf extent and thickness change

Ice shelves gain mass through: ice flux across their grounding lines from the grounded ice sheet; surface accumulation via snowfall; and through the accretion of ice onto the base of the shelf from the freezing of ocean water (Benn and Evans, 2014; p. 181). Ice shelves lose mass primarily through melting at their base by ocean waters above the local melting point, and through the calving of

icebergs (Rignot et al., 2013). They can also lose mass through surface melting, and whilst this process is not widespread around the whole ice sheet, the presence of meltwater on the surface of an ice shelf can have implications for its future viability due to hydrofracture processes, which are thought to have played a significant role in the changes in ice-shelf extent on the AP (e.g. Scambos et al., 2000, van den Broeke, 2005, Banwell et al., 2013).

It was previously thought that ice shelves lost over 90% of their mass through the calving of icebergs (Cuffey and Paterson, 2010; p. 121). However, more recent work has shown that over the whole of Antarctica, the balance between mass loss through calving and basal melting is approximately equal (Depoorter et al., 2013, Rignot et al., 2013). The balance can vary significantly around the continent – as shown in Figure 2.3 – largely driven by the properties of the water masses that flow underneath the different ice shelves. Basal melting accounts for approximately two thirds of the mass loss from the ice shelves of the ASE (Depoorter et al., 2013), where warm Circumpolar Deep Water (CDW) flows up onto the continental shelf and under the ice shelves. In contrast, the Filchner-Ronne and Ross Ice Shelves – which have cold-water ocean cavities beneath them – lose 83% and 81% of their mass through the calving of icebergs, respectively (Depoorter et al., 2013).

Pritchard et al. (2012) found that, between 2003 and 2008, 20 of the 54 Antarctic ice shelves that they analysed were thinning and losing mass. They deduced that this thinning must be driven by increased basal melting after excluding other possible mechanisms, including: a reduction in surface mass balance; firn compaction; or a reduced influx of ice from grounded, tributary glaciers (ibid.). The largest thinning rates were found to be occurring in the ASE, where basal melt rates of up to 6.7 ma^{-1} were calculated (ibid.). From their analysis of a time-series of radar altimetry data sets, Adusumilli et al. (2020) produced estimates of basal melt rates around the AIS for the period 1994-2018. Overall, they found that the net ice mass loss from Antarctic ice shelves was $3,960 \pm 1,100$ Gt during those 24 years, but that this mass loss varied significantly around the ice sheet as well as temporally throughout the observational period.

The map of basal melt rates produced by Adusumilli et al. (2020), reprinted here in Figure 2.4, shows a clear correlation between ice-shelf basal melt rates and the potential temperature of the water mass at the calving front of the ice shelf. The increased access of CDW onto the continental shelf and underneath the ice shelves of the WAIS, which is responsible for the enhanced rates of

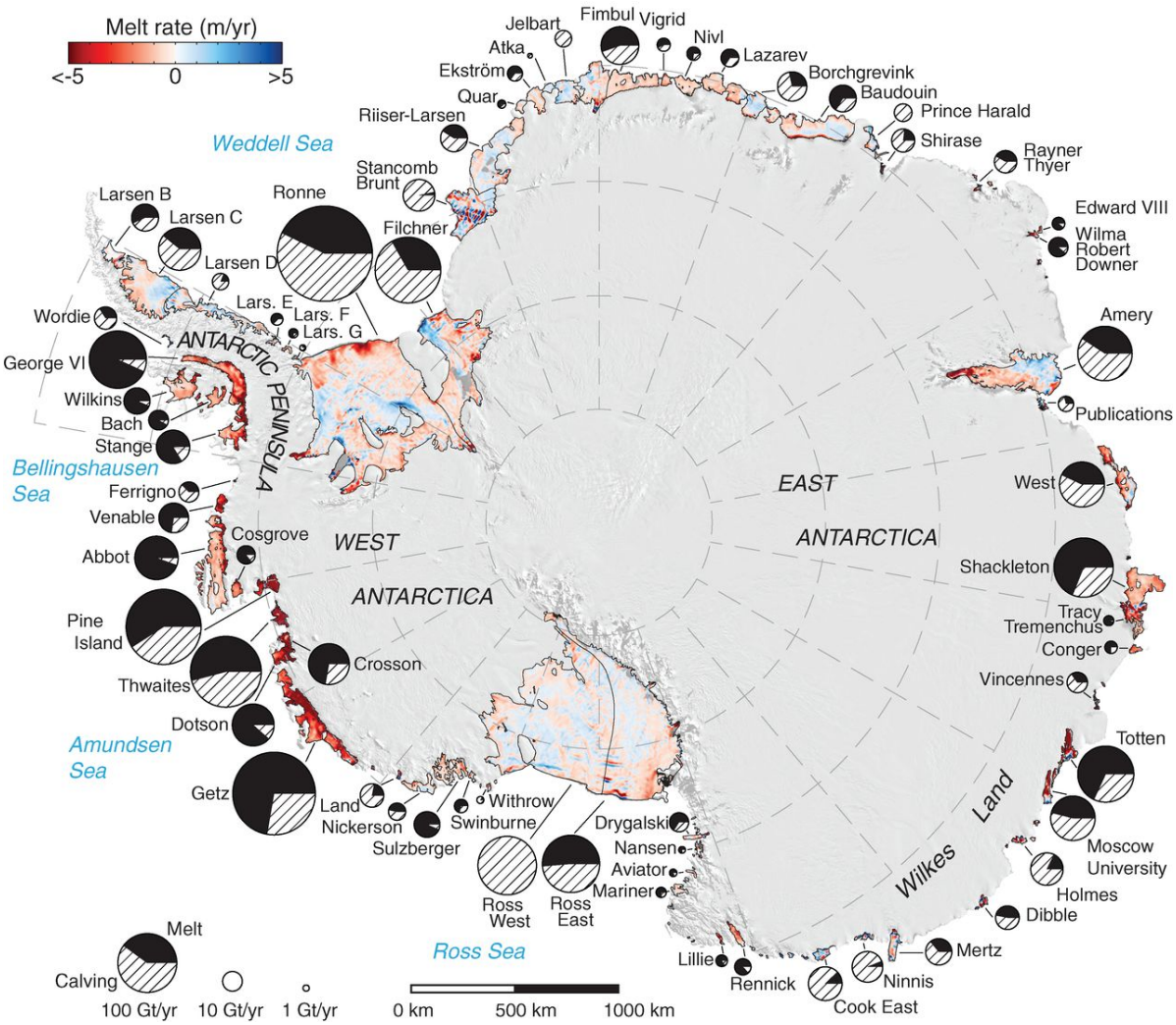

Figure 2.3: Map showing the balance of mass loss between iceberg calving and basal melting for Antarctica's ice shelves. Figure reprinted from Rignot et al. (2013)

basal melting and ice-shelf mass imbalance, is thought to be largely driven by internal climate variability and associated changes in the wind forcing at the ocean surface (e.g. Dutrieux et al., 2014, Jenkins et al., 2018). However, there is now evidence that some of the changes in CDW access underneath ASE ice shelves can be attributed to anthropogenic forcing as well (Holland et al., 2019). It is important to note that basal melt rates are typically elevated close to the grounding line (e.g. Dutrieux et al., 2013, Lazeroms et al., 2018), which are precisely the regions where the flux across the grounding line is found to be most sensitive to perturbations in ice-shelf geometry (Reese et al., 2018b, Goldberg et al., 2019), as explored further in Sect. 2.4 and in the research conducted in this thesis.

Not only are Antarctic ice shelves losing mass, but over the last three decades that mass loss has been accelerating (Paolo et al., 2015). As with the overall patterns of mass loss from the ice sheet, this acceleration in ice-shelf mass loss is spatially and temporally variable, and is thought to be linked with changes in ocean circulation and large-scale climate variability, such as the El Niño–Southern Oscillation (ENSO) (Paolo et al., 2018, Jenkins et al., 2018, Holland et al., 2019). Present rates of ice-shelf thinning vary around the ice sheet, but of particular note is the clear ice-shelf thinning signal observed across the ASE on the WAIS (Pritchard et al., 2012, Paolo et al., 2015, Adusumilli et al., 2020). The reduction in ice-shelf thickness is thought to be the driving cause of the acceleration of tributary glaciers in the ASE and the associated increase in mass loss from this region (Joughin and Alley, 2011, Jenkins et al., 2018).

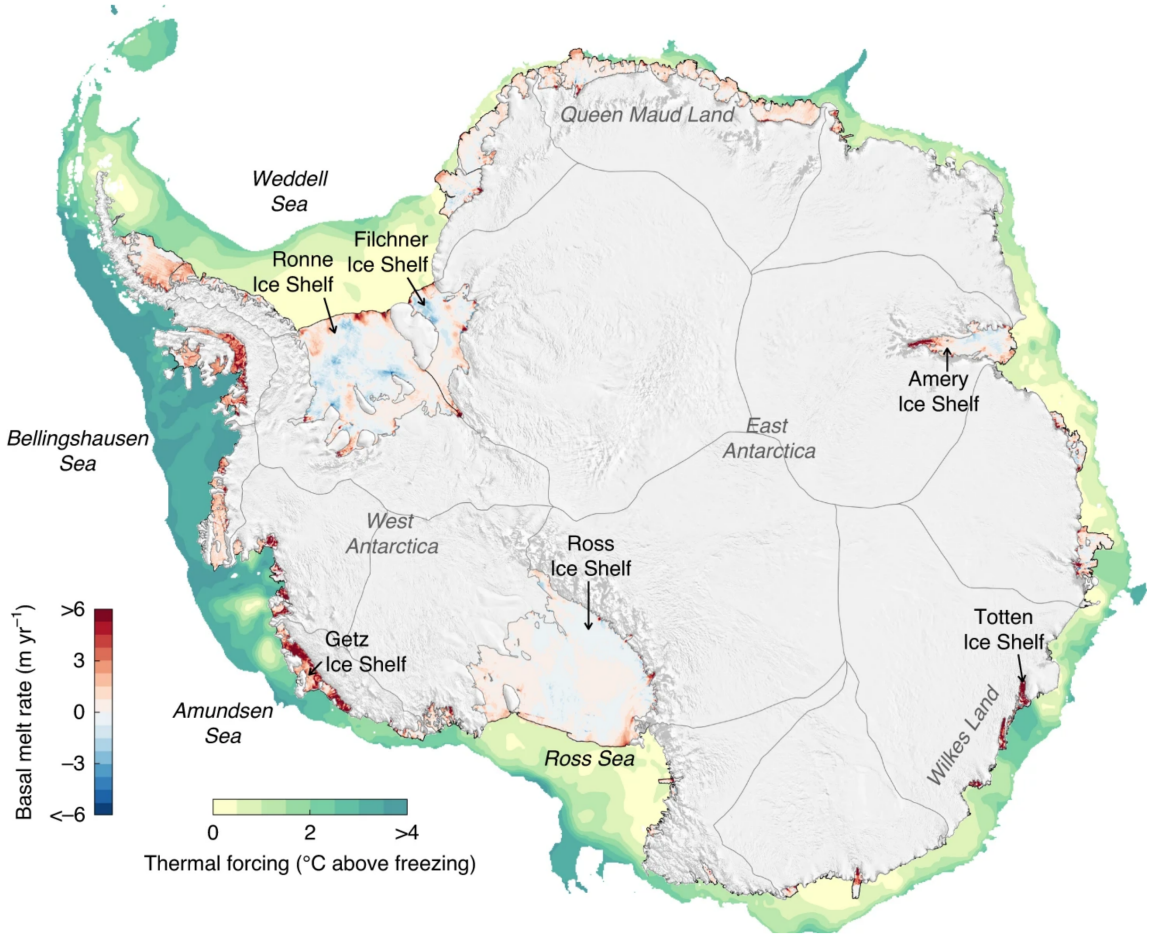

Figure 2.4: Map of ice shelf basal melt rates and ocean thermal forcing around Antarctica. Figure reprinted from Adusumilli et al. (2020)

2.2.1.1 Ice shelves of the Antarctic Peninsula

Outside of the ASE, the other region of the AIS that has seen significant changes in the extent of its ice shelves is the AP (Cook and Vaughan, 2010). In his prescient paper warning of the potential collapse of the WAIS due to the emission of greenhouse gases, Mercer (1978) stated that "one warning sign that a dangerous warming is beginning in Antarctica will be the breakup of ice shelves in the Antarctic Peninsula". Over the course of the twentieth century the AP warmed by over five times the global average, with an increase of 3.7 $\pm$ 1.6 °C (Vaughan et al., 2003, Khazendar et al., 2011). Although this trend did not persist into the twentieth century (Turner et al., 2016), the 2019/20 austral summer saw one of the highest ever recorded melt seasons on the LCIS (Bevan et al., 2020, Banwell et al., 2020).

In response to this climatic warming, over the last two decades of the twentieth century, the ice shelves of the AP have progressively retreated (Vaughan and Doake, 1996, Scambos et al., 2000). In 1995 the Larsen A Ice Shelf calving front retreated rapidly (Rott et al., 1996), and seven years later the larger Larsen B Ice Shelf (LBIS) disintegrated in a matter of 6 weeks from January to March 2002 (Scambos et al., 2004). Analysis of marine sediments from beneath the former LBIS showed that there had been an ice shelf present in that embayment for at least twelve thousand years (Domack et al., 2005).

A number of mechanisms have been proposed as the cause of the demise of the LBIS, including: a weakening of the shear margins within the shelf and accelerated flow speeds (Vieli et al., 2007, Khazendar et al., 2007); the failure of bands of 'marine ice' within the shelf to prevent fracture growth (Holland et al., 2009); increased basal melting inducing ice-shelf thinning and weakening (Shepherd et al., 2003); the loss of a sea ice buffer at the calving front (Massom et al., 2018); and the retreat of the calving front into a less 'stable' configuration (Doake et al., 1998, Kulessa et al., 2014). It is possible that one or more of these processes may have contributed to the priming of the LBIS for collapse, but the process which has gained most acceptance is that of surface-meltwater driven hydrofracture (e.g. van den Broeke, 2005, Banwell et al., 2013), whereby increased surface melting and ponding led to the rapid fracture and breakup of the ice shelf. The speed at which the LBIS disintegrated is thought to be atypical, and due to a rapid increase in the surface meltwater generated on the shelf in the weeks before the collapse (Robel and Banwell, 2019).

In response to the collapse of these ice shelves – and the removal of the buttressing they provided – the tributary glaciers flowing into the shelves were observed to increase in speed rapidly, with one tributary glacier of the former LBIS accelerating by more than 800% between 2000 and 2003, before slowing slightly later in 2003 (Rignot et al., 2004). However, the response was also spatially variable, with some tributaries accelerating significantly whilst others showed a much more modest response to the collapse of the LBIS (Hulbe et al., 2008). Observations confirm that there are still ongoing changes in the flow of the remnant, confined part of the LBIS that did not collapse – the SCAR inlet – up to the present day (Khazendar et al., 2015). Indeed, it was the fact that the SCAR inlet remained intact that allowed mechanisms other than the sudden loss of buttressing to be excluded as explanations for the acceleration of tributary glaciers, making this event a 'natural experiment' for studying the process of ice-shelf buttressing. The changes in the flow of the tributary glaciers of the LAIS and LBIS have been sustained for over a decade following the collapse of the two shelves (e.g. Shuman et al., 2011, Berthier et al., 2012, Rott et al., 2018). The observed response to the collapse of the LAIS and LBIS provided the first incontrovertible evidence for the mechanical role that ice shelves play in controlling grounded ice dynamics through ice-shelf buttressing.

Based on the collapse of these northern AP ice shelves, it has been suggested that the northerly limit for ice-shelf viability in Antarctica is the -9 °C annual isotherm, which at the beginning of the twentieth century cut across the northern part of the LCIS (Morris and Vaughan, 2003). Therefore, recent research has turned to the future viability and dynamic behaviour of the LCIS, and this is one of the reasons that it was chosen as an area of focus for the research conducted in this thesis.

2.2.2 The Larsen C Ice Shelf

The LCIS is the fourth-largest ice shelf in Antarctica, covering an area of approximately 44,000 km^2 on the eastern side of the AP. Its geographic setting, together with the locations of its former, neighbouring ice shelves can be seen in Figure 2.5. The ice shelf is formed of 12 major flow units which emanate from fast-flowing tributary glaciers, as determined from the crevasse patterns that form as the ice flows from the grounded ice sheet into the shelf (Glasser et al., 2009). Glasser et al. (2009) found that there was no evidence to suggest that the LCIS had recently experienced any significant changes to its dynamic state, and assessed that it had been in its present configuration

for at least 560 years, but more likely for at least as long as its neighbouring (now collapsed) LBIS – which Domack et al. (2005) estimated to have been present for at least 12,000 years. Jansen et al. (2010) also suggested that the LCIS was in a stable configuration from an analysis of the modelled stress field following the assimilation of ice velocity data captured 2008/9.

However, observations have shown that, overall, the surface of the LCIS has lowered over the last three decades (e.g. Holland et al., 2015, Adusumilli et al., 2018). Pritchard et al. (2012) argued that surface processes (such as the compaction of the firn layer) could account for the observed surface lowering, and that basal melt rates were likely to be close to those required to maintain ice-shelf mass balance. Shepherd et al. (2003), in contrast, attributed the lowering to increased basal melting, whilst Holland et al. (2015) concluded that ice loss from basal melting and ice divergence, and air loss from the compaction of the firn layer had contributed equally to the observed surface lowering. In a more recent analysis, Adusumilli et al. (2018) suggested that the surface lowering of 1.0 ± 0.3 m between 1994 and 2009 was driven by surface processes and changes in firn air content, but also showed that there had been a sustained increase in surface height across the northern part of the LCIS since 2009 of 0.5 ± 0.3 m. However, they found that over the 23 year observational period the LCIS has lost mass, with 0.4 ma^{-1} of basal melting in excess of that required to maintain the mass balance of the shelf (ibid.).

In-situ observations of the ocean conditions below the LCIS show that the ice-shelf cavity is largely filled with High Salinity Shelf Water – a relatively cold water mass generated during the formation of sea ice in the adjacent Weddell Sea (Nicholls et al., 2012). As a consequence, there is a significant amount of localised refreezing onto the bottom of the LCIS, which forms marine ice bands within the shelf that have different mechanical properties to the meteoric ice which flows into the shelf from the grounded tributary glaciers (e.g. Glasser et al., 2009, Holland et al., 2009, Jansen et al., 2010, McGrath et al., 2014). These marine ice 'suture zones' are thought to suppress the growth of fractures in the ice shelf as the ice there is softer, requiring greater tensile stresses to be reached before fractures can propagate through the suture zones (McGrath et al., 2014). However, from 2014-2017, a crack emanating from the region of the LCIS upstream of the Gipps Ice Rise (GIR) did propagate through the suture zone emanating from the Joerg Peninsula (Borstad et al., 2017, Jansen et al., 2015), and in July 2017 the rift connected to the calving front, leading to the

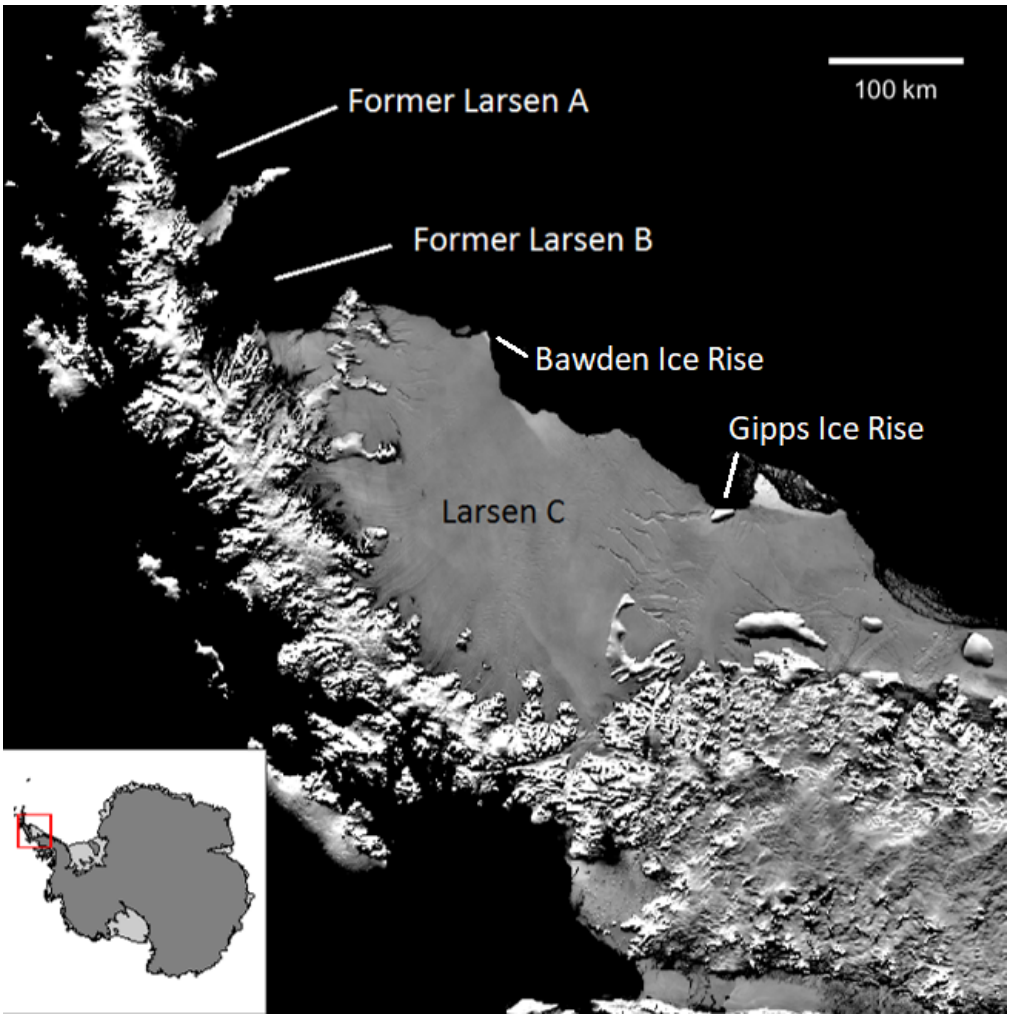

Figure 2.5: MODIS Mosaic of Antarctica image of the Larsen C Ice Shelf (Scambos et al., 2007) prior to the calving of the A68 iceberg. The ocean is in black, and the embayments that formerly contained the Larsen A and B Ice Shelves are highlighted. The two key ice rises (Bawden and Gipps) at the calving front of the shelf are also labelled.

calving of the A68 iceberg (Hogg and Gudmundsson, 2017). This calving event reduced the area of the LCIS by over 10% (ibid.). The replication of this calving event within an ice flow model – and the comparison of this modelling with observations made since the calving event – is undertaken in Chapter 4 of this thesis.

The LCIS contains two prominent ice rises at its calving front, the GIR and the Bawden Ice Rise (BIR), both shown in Figure 2.5. The importance of these ice rises to the dynamics of the ice shelf has been pursued in a number of existing studies (e.g. Jansen et al., 2010, Borstad et al., 2013, Kulessa et al., 2014, Holland et al., 2015, Borstad et al., 2017) and contributing to this ongoing

discussion forms an important part of the research of this thesis. In particular, it has been suggested that the loss of basal contact at the BIR could cause the LCIS stress regime to transition into an unstable configuration (Kulessa et al., 2014, Jansen et al., 2015). Holland et al. (2015) suggested that, given observed melt rates around the BIR, a conservative estimate would expect the ice shelf to lose contact with the BIR within 130 years.

The changes in the thickness of the LCIS, the calving of the A68 iceberg via a rift penetrating through a suture zone, the potential loss of basal contact at the BIR, and the collapse of its neighbouring ice shelves have all led to questions about its future viability (e.g. Kulessa et al., 2014, Jansen et al., 2015, Holland et al., 2015), as well as the consequences of any changes in its structural integrity or extent (Schannwell et al., 2018). Further discussion of the existing work on the buttressing provided by the LCIS is presented in Sect. 2.4.3

2.3 Ice-sheet dynamics and modelling

To understand the ice dynamics of the AIS, and to make predictions about its future behaviour, models of ice flow are required. As has been demonstrated thus far in this chapter, the mass imbalance of the AIS in the present day is driven by ice-dynamic changes, largely thought to be in response to the thinning and retreat of ice shelves. Therefore, a comprehensive understanding of Antarctic ice dynamics, and appropriate models for simulating its potential future behaviour, are of great societal importance for predicting future changes in GMSL.

Ice flow can be modelled as the flow of a viscous fluid via creep deformation under the force of gravity (e.g. Schoof and Hewitt, 2013). The equations that describe this understanding of ice flow are called the full Stokes equations, and they can be prohibitively computationally expensive to solve, particularly when modelling is done on a Antarctic-wide scale. Therefore, approximations are made to the full Stokes equations which require fewer computational resources to solve, and which capture the key aspects of ice flow behaviour described by the full Stokes equations under a specific set of assumptions and in certain limits.

The earliest continental-scale models, developed in the 1990s, used the shallow ice approximation (SIA), which is applicable to ice sheets deforming slowly, and for understating the behaviour of ice sheets over timescales of millennia (Pattyn, 2018). However, the dynamics of the AIS is dominated

by relatively fast ice flow, channelised into ice streams which slide over their bed and are connected to floating ice shelves. The SIA is not applicable to these regions. Uncertainty around the appropriate approximation to use for studying Antarctic ice dynamics led to a disagreement in the field about whether or not ice shelves are mechanically coupled to the flow of the grounded ice sheet, and therefore what their impact was on grounding line stability (Hindmarsh and Le Meur, 2001). Subsequent studies (e.g. Gagliardini et al., 2010, Gudmundsson et al., 2012) and model intercomparison projects (Pattyn et al., 2012; 2013) demonstrated that ice shelves are mechanically coupled to the grounded ice sheet and can control its dynamics through the process of ice-shelf buttressing, explored further in Sect. 2.4, and this argument was finally resolved with the observational evidence obtained following the collapse of the LBIS, as discussed above.

Other approximations, which retain more terms of the full Stokes equations, have been developed, including the shallow-shelf approximation (SSA) (e.g. MacAyeal, 1989, Pegler and Worster, 2012) and so-called 'higher-order models' (e.g. Schoof and Hindmarsh, 2010, Cornford et al., 2013, Pattyn et al., 2017). The model used in this thesis, Úa – which is described in detail in Chapter 3 – uses the shallow-shelf (also known as the shelfy-stream) approximation to the full Stokes equations, valid in regions in which the ice motion is dominated by sliding at the bed over grounded ice and over ice shelves, where vertical shear stresses contribute a negligible amount to the force balance. These are the key regions of focus in this thesis. The conditions under which this approximation is valid are further discussed further in Chapter 3.

In addition to the choice of which approximation to make to the governing equations, the numerical implementation of those equations can also influence the modelled behaviour of an ice sheet. In particular, the dynamic behaviour of a model has been shown to be very sensitive to the resolution of the discretisation scheme used across the grounding line (e.g. Vieli and Payne, 2005, Durand et al., 2009, Pattyn et al., 2012). Because the stress balance in the ice sheet undergoes a transition across this internal boundary, it is crucial to use a high resolution (on the order of one ice thickness) such that the gradients of the stresses are adequately resolved (Cornford et al., 2013). Models which do not resolve the grounding line at the required resolution, due to computational limitations, typically use a parameterisation of the flux across the grounding line based on the theoretical work of Schoof (2007) (e.g. Pollard and DeConto, 2012, Pattyn, 2017). However, the use

of such a parameterisation has recently been questioned, as Reese et al. (2018c) demonstrated that this flux parameterisation breaks down around much of Antarctica's present-day, highly buttressed grounding line.

Further modelling choices must be made regarding the appropriate boundary conditions to apply at the ice sheet's interfaces with the bedrock, the ocean and the atmosphere. For example, the choice of basal sliding law – i.e. the form of the boundary condition at the ice-bed interface – has been shown to have a significant impact on the dynamic behaviour of the model (e.g. Ritz et al., 2015, Brondex et al., 2017, Tsai et al., 2015), and remains a large source of uncertainty in projections of the future behaviour of the AIS (e.g. Sun et al., 2020). It is typically found that more plastic sliding laws result in a greater sensitivity of the grounded ice sheet to perturbations in external forcings (e.g. Ritz et al., 2015, Yu et al., 2018, Cornford et al., 2020). Recent work has indicated the potential for a universal sliding law, which could be equally be applied to regions of hard bedrock and deformable subglacial till (Minchew and Joughin, 2020, Zoet and Iverson, 2020).

At the ice-ocean interface, basal melt rates must be specified beneath the floating ice shelves. Most state-of-the-art ice sheet models employ a parameterisation of the basal melt rate, which takes ocean properties such as temperature and salinity at the ice-shelf front – typically from ocean circulation model output, or from observations – and converts them into a basal melt rate that can vary spatially across the ice shelves within the ice sheet model domain (e.g. Lazeroms et al., 2018, Reese et al., 2018a, Seroussi et al., 2020). The next step to improving the representation of basal melting in ice sheet models is through the development of coupled ice sheet–ocean circulation models, and this is an active area of research (e.g. De Rydt and Gudmundsson, 2016, Naughten et al., 2021). They have been used to test the capabilities of simpler basal melt parameterisations (Favier et al., 2019), but can be prohibitively computationally expensive to run.

Finally, at the ice-atmosphere interface of the ice sheet's surface, a mass balance term must be prescribed, and additionally a surface temperature field if the ice sheet model contains a thermodynamic component. This surface mass balance (SMB) field is typically derived from output from regional climate models – such as RACMO (van Wessem et al., 2018) – but for the recent ISMIP6 projections for Antarctica it was taken directly from output from global climate models (Nowicki et al., 2020). In a warming climate, the SMB over the AIS is predicted to increase by 6-16% by

2100 under different emissions scenarios (Ligtenberg et al., 2013), due to a warmer atmosphere being able to hold more moisture, and therefore increased levels of snowfall. As revealed by the results of the recent Ice Sheet Model Intercomparison Project for CMIP6 (ISMIP6), accurately modelling the balance between the competing processes of increased ice discharge – due to higher basal melt rates and a reduction in ice-shelf buttressing – and increased SMB in a warming climate, is crucial to producing accurate projections of the AIS contribution to GMSL and reducing uncertainty in those projections (e.g. Seroussi et al., 2020, Edwards et al., 2021, Payne et al., 2021).

2.3.1 Ice-sheet instabilities

The key to understanding any rapid transition in the state of the AIS are its ice-dynamic instabilities, particularly those relating to the stability of the grounding line. These instabilities can induce tipping points, which if crossed can rapidly (on glaciological timescales) alter the state of a region of the ice sheet (e.g. Favier et al., 2014, Rosier et al., 2021). The presence of instabilities also leads to the hysteresis behaviour of the AIS, whereby once the ice sheet has crossed a tipping point due to a change in external forcing – e.g. a change in global atmospheric temperatures – a return to the previous external conditions does not cause the ice sheet to return to its previous state (Garbe et al., 2020).

The marine ice sheet instability (MISI) was first proposed in the 1970s (Weertman, 1974, Mercer, 1978) and then confirmed analytically by Schoof (2007) and numerically in the marine ice sheet model intercomparison project (MISMIP and MISMIP3d) experiments (Pattyn et al., 2012; 2013). When a marine ice sheet sits on retrograde bedrock (i.e. topography that slopes downwards inland) an initial perturbation which causes an increase in the grounding line flux (GLF) (e.g. from a reduction in ice-shelf buttressing) will lead to thinning and a retreat of the grounding line. But this retreat takes the grounding line into a deeper region of bedrock, with thicker ice, causing the grounding line flux to increase further, inducing further thinning and further retreat until the region of retrograde bedrock topography ceases. A schematic of this process is shown in Figure. 2.6a. Much of the WAIS rests on bedrock that has such a retrograde formation, in particular the two large glaciers flowing into the ASE, Pine Island and Thwaites, both have large regions of retrograde bed topography and recent studies have suggested that they maybe already be experiencing irreversible

grounding line retreat (Joughin et al., 2014, Rignot et al., 2014, Favier et al., 2014). The possibility of MISI has now been verified in both analytical and numerical studies, however it only strictly applies in the limiting case where there is no buttressing and where the bedrock topography gradients are small (Schoof, 2007). Gudmundsson et al. (2012) demonstrated that the presence of an ice shelf providing buttressing to the grounding line can prevent the initiation of MISI, and lead to stable grounding line positions even on retrograde bedrock slopes. This stabilising feature of ice-shelf buttressing is discussed further in Sect. 2.4. In addition to this, the scale on which the bedrock topography varies can also influence the initiation of MISI, with rougher topographies being found to produce stable grounding lines on retrograde slopes, and even locally unstable grounding lines on prograde bedrock slopes (Sergienko and Wingham, 2022).

In addition to MISI, a further ice-dynamic instability has recently been proposed which is known as the marine ice cliff instability (MICI) (Pollard et al., 2015, DeConto and Pollard, 2016) and a schematic of this process is shown in Figure 2.6b. By this process, the rapid collapse of an ice shelf could expose an ice cliff which would experience tensile stresses that exceed the yield strength of ice – and therefore result in shear failure – if the freeboard is more than 90 m above sea level (Bassis and Walker, 2012). As long as the ice thickness increases upstream of the calving front (on either a retrograde or prograde bed topography) the failure of the cliff would expose an even larger ice cliff, which would itself fail under the same mechanism, leading to runaway retreat of the calving front and the grounding line.

The conception of this mechanism was motivated by paeleo observations of changes in GMSL which DeConto and Pollard (2016) suggested could not be explained by the initiation of MISI alone. However, Edwards et al. (2019) demonstrated that it is possible to recreate past, observed sea level changes within their uncertainty bounds using ice sheet models that do not incorporate MICI. There are currently no ice cliffs in existence which meet the requirements for MICI to be initiated and, therefore, there is no observational evidence from the present day to support the theory, which remains controversial within the ice sheet modelling community (Pattyn and Morlighem, 2020). More recent studies have shown that fully resolving the processes of ice-shelf collapse – and the subsequent viscous flow of the ice – can remove the potential for such high cliffs to form in the first place (Clerc et al., 2019, Robel and Banwell, 2019). Bassis et al. (2021) also showed that factors

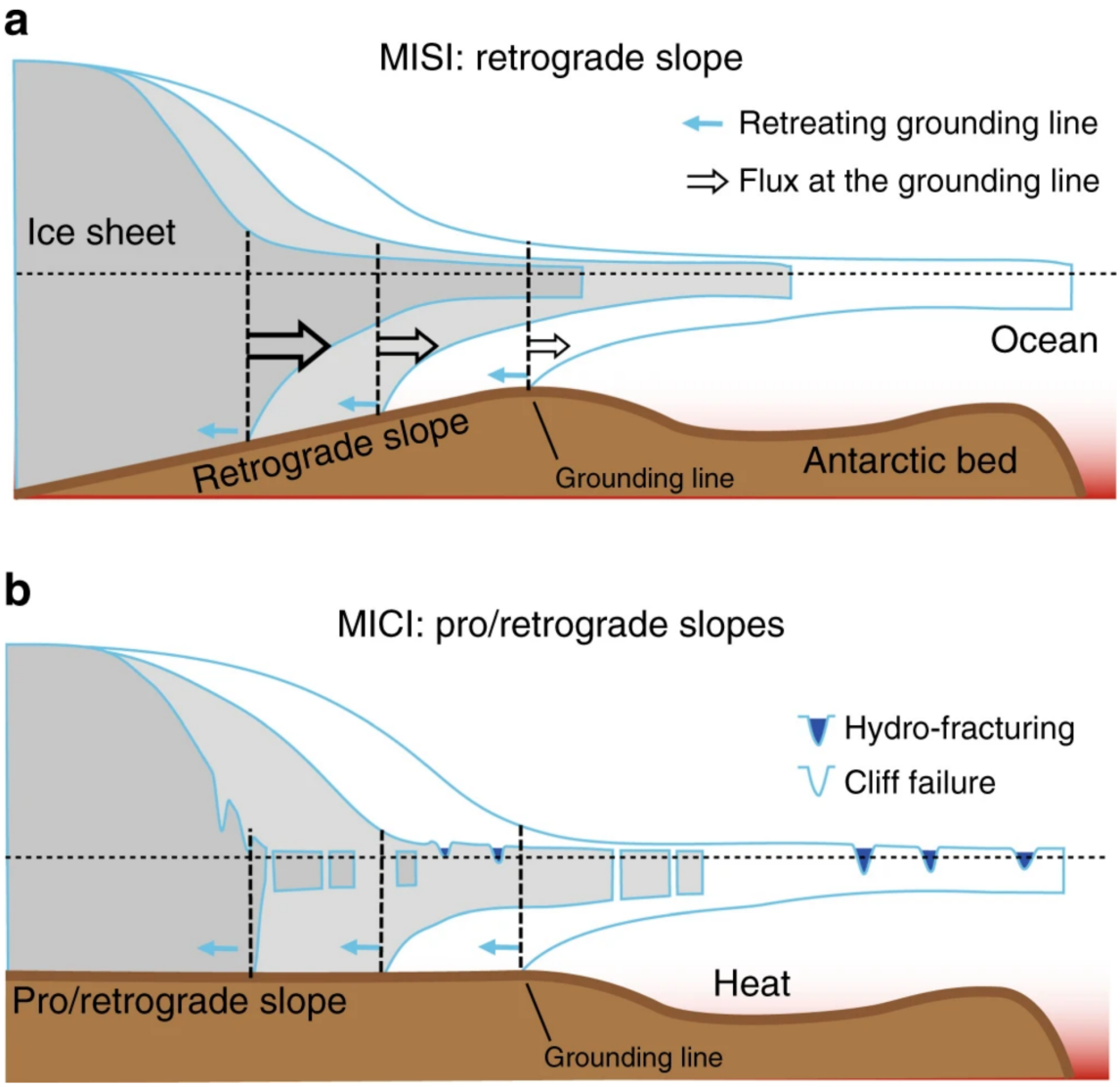

Figure 2.6: Schematic diagram outlining the processes behind **(a)** the marine ice sheet instability (MISI) and **(b)** the marine ice cliff instability (MICI). Figure reprinted from Pattyn (2018)

such as ice rheology and ice-thickness gradients can control the promotion or suppression of MICI.

2.4 Ice-shelf buttressing

Ice-shelf buttressing refers to the phenomena by which resistive stresses generated within an ice shelf are transmitted upstream and alter the stress balance at the grounding line (Thomas, 1979b). It was the loss of this buttressing force that Mercer (1978) hypothesised could lead to the rapid collapse the WAIS, and as outlined thus far in this chapter, reductions in buttressing through ice-

shelf thinning and collapse are thought to be the primary cause of the current, increasing mass loss of the WAIS and the AP.

Lateral shear stresses are generated within an ice shelf when it is confined in an embayment, and additional resistive stresses, due to compression and basal drag, are generated when an ice shelf runs aground at an ice rise or pinning point (Dupont and Alley, 2005, Matsuoka et al., 2015). There is the theoretical possibility of ice-shelf buttressing being generated by hoop stresses – which arise in a diverging flow field due to the resistance to lateral spreading perpendicular to the direction of flow – but this is thought to be insignificant for Antarctic ice shelves (Wearing et al., 2020). As ice shelves are floating on the ocean there is negligible basal resistance to flow, and a perturbation in the stress state at one point within an ice shelf can impact the stress balance at distant points across the shelf, a phenomena termed 'tele-buttressing' by Reese et al. (2018b).

Because stress perturbations are transmitted at the speed of sound through ice, and because the momentum balance equations of ice flow are time-independent, a stress perturbation caused by a change in ice-shelf geometry will impact the stress balance at the grounding line instantaneously (e.g. Dupont and Alley, 2005, Gudmundsson et al., 2019). In that sense ice-shelf buttressing – as defined and used throughout the work in this thesis – refers to the impact of the ice shelf on the stress state at the grounding line. It is important to note here that ice-shelf buttressing is a separate, but linked, process to the subsequent transient redistribution of mass in the ice shelf and its tributary glaciers in response to a loss of ice-shelf buttressing.

In flowline ice sheet models there is no lateral variation in shear stresses, and therefore the terms in the governing equations which are required to replicate ice-shelf buttressing due to lateral shear at the ice shelf margins are not retained. This means that in flowline models the ice shelf is uncoupled from the grounded ice sheet – provided that the ice shelf is not grounded at an ice rise. It was this model that Schoof (2007) used to analyse the stability of marine ice sheets.

However, flowline models have been adapted to incorporate the effect of ice-shelf buttressing by introducing a parameterised form of the lateral shear stresses generated within a confined ice shelf as an additional term into the stress balance equations (e.g. Dupont and Alley, 2005, Gagliardini et al., 2010). By using flow approximations that allowed for the coupling of ice-shelf stresses to the grounded ice sheet, these models demonstrated that a reduction in the buttressing (simulated

by reducing the parameterised lateral shear stresses) could cause an acceleration in the flow of the grounded ice, which in turn could induce a thinning of the grounded ice and a retreat of the grounding line (Dupont and Alley, 2005, Gagliardini et al., 2010).

These flowline models of marine ice sheets – with parameterised lateral drag to represent the buttressing of ice shelves – have been used in recent analytical work exploring the role of ice shelves in controlling grounding line dynamics. Pegler (2018a) used an analysis of this model to show that even small amounts of ice-shelf buttressing could completely control the location of grounding lines in a steady-state, idealised marine ice sheet. With the same set of analytical tools – a flowline model with parameterised ice-shelf buttressing – Haseloff and Sergienko (2018) derived an analytical solution for the grounding line flux (GLF) in the limit of 'strong buttressing'. In this case the GLF is independent of the properties of the ice sheet itself, and is controlled by the geometric properties of the ice shelf used to parameterise the buttressing, in particular the width and length of the shelf. This work also highlights the very different behaviour of steady state grounding lines for buttressed and unbuttressed ice sheets, again showing the importance that ice shelves have in controlling ice-sheet dynamics.

To move beyond parameterising the effect of ice-shelf buttressing – which may be appropriate for idealised settings, but not for the complex geometries of the AIS (Reese et al., 2018c) – it is essential to model ice sheets in two-horizontal dimensions or in 'plan-view', thereby directly capturing gradients in lateral shear stresses. Using a 'plan-view' model, with a highly resolved grounding line, Gudmundsson et al. (2012) demonstrated that the presence of an ice shelf generating sufficient buttressing could produce stable steady-state grounding line positions on the retrograde bedrock region of a marine ice sheet. This result showed that the initiation of MISI is not only a function of the local bedrock topography, but that by altering the stress balance at the grounding line, an ice shelf could prevent MISI from occurring. Once again, this highlights the crucial role that ice-shelf buttressing plays in the dynamics of the AIS. In an accompanying study Gudmundsson (2013) proposed that the impact that an ice shelf has on the stress state at the grounding line could be measured by a 'normal buttressing number', given by

$$K_N = \frac{N - N_0}{N_0}, \tag{2.1}$$

where

$$N_0 = \frac{1}{2}\rho_i \left(1 - \frac{\rho_i}{\rho_w}\right) gh \tag{2.2}$$

is the normal stress at the grounding line – i.e. the component of the stress tensor in the direction perpendicular to the grounding line – in the absence of an ice shelf, ρ_i is the ice density, ρ_w is the ocean density, h is the ice thickness, g the acceleration due to gravity, and N is the normal stress at the grounding line with the ice shelf present.

Numerical models have been used to assess the response of the tributary glaciers feeding both the LAIS and the LBIS to the observed collapse of the ice shelves. In a sense, the sudden removal of these ice shelves provided one of the few avenues for testing the capacity of ice flow models to accurately reproduce the effects of ice-shelf buttressing. Royston and Gudmundsson (2016) assimilated observational data collected prior to the collapse of the LAIS into an ice flow model and then simulated the removal of the shelf using a diagnostic, time-independent experiment. They found that they were able to reproduce the observed ice velocity increase of Drygalski Glacier close to the grounding line, but suggested that further increases in ice velocity upstream were due to transient mass redistribution – which through time changes the surface slope and the stress balance in the tributary glaciers – and could not be replicated with their modelling approach.

De Rydt et al. (2015), simulated the collapse of the LBIS with the same, diagnostic modelling approach. They found that they were able to correctly reproduce the heterogeneous patterns of the initial tributary glacier response, but emphasised that for the full replication of the complex, time-evolving response to the collapse that transient simulations would be required.

In addition to the evidence arising from the AP, the acceleration and mass loss from the ASE has also allowed for the development of combined observation–modelling studies of ice-shelf buttressing. De Rydt et al. (2021) assimilated data captured between 1996 and 2016 into an ice flow model, and determined that for Pine Island Glacier (PIG), ice-shelf calving and basal melting have contributed approximately equally to the loss of buttressing that has caused its significant acceleration in the last two decades. This is complementary to the work of Joughin et al. (2021), who showed that the acceleration of PIG and the increase in GLF between 2017 and 2020 was directly linked to the retreat of the calving front in that time, and the corresponding reduction in ice-shelf buttressing.

2.4.1 Antarctic-wide ice-shelf buttressing studies

Time-independent, or diagnostic, model studies have been used to assess ice-shelf buttressing around Antarctica. Gudmundsson et al. (2019) took observations of ice shelf thinning rates from 1994-2017 (Paolo et al., 2015, Adusumilli et al., 2018, Paolo et al., 2018), and applied them in an ice sheet model as instantaneous changes in ice-shelf thickness. From this, the instantaneous change in ice velocity was mapped, providing what they termed a 'fingerprint' of the impact that the basal-melt driven reduction in buttressing has had on the dynamics of the AIS. As expected, the ice velocities across the grounding line increased in regions in which a significant ice-shelf thinning has been observed, revealing that a loss of ice-shelf buttressing is indeed behind much of the observed mass loss of the AIS (Gudmundsson et al., 2019).

In addition to this work using observed thinning rates, there are two primary studies which have use idealised, diagnostic experiments to assess the buttressing of Antarctic ice shelves (Fürst et al., 2016, Reese et al., 2018b). These two studies have greatly influenced the work in this thesis, and as such they are both discussed in detail below.

2.4.1.1 Passive shelf ice

The first of these two studies is that of Fürst et al. (2016). In this work, a SSA ice flow model was initialised with present-day ice velocity and ice geometry data over the whole AIS, using a mesh with high resolution ($\sim$ 1 km) over the ice shelves and around the grounding line. Using the modelled stress field in the ice, a maximum buttressing number was calculated across all ice shelves of the AIS.

This maximum buttressing number differs to that calculated by other authors (e.g. Borstad et al., 2013, Gudmundsson, 2013) (see Eq. 2.1), who focus on the difference in stresses with and without an ice shelf present in the direction of ice flow or normal to the grounding line. Here, the maximum buttressing number is calculated as the difference between the modelled ice stress in the second principal stress direction and the ocean back-pressure at each point within the ice shelves. This choice has been critiqued by Wearing et al. (2020), who questioned whether it provides information about the resistance to flow locally within an ice shelf. The result is that the values of maximum buttressing number are larger than the equivalent buttressing numbers calculated in the

direction of flow.

From this map of maximum buttressing numbers, isolines of the field are determined and then eleven calving experiments are performed across the whole AIS, along increasing values of maximum buttressing number from 0.1 to 1, followed by the full removal of all ice shelves. The exact location at which these calving fronts were positioned in each calving experiment is, however, unclear from the figures presented in Fürst et al. (2016). The resulting map of maximum buttressing numbers is shown in Figure 2.7.

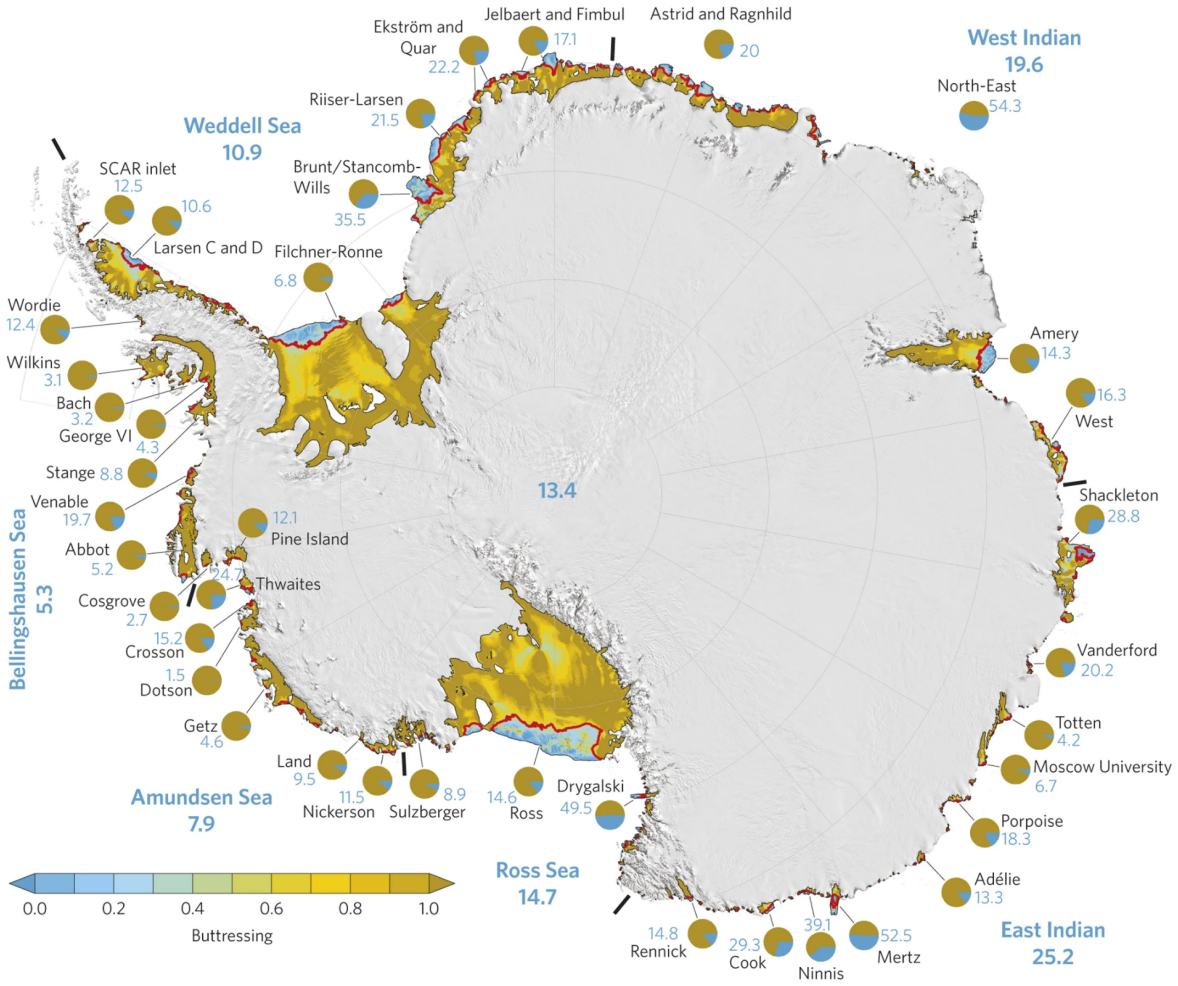

Figure 2.7: Map of the 'maximum buttressing number' for Antarctic ice shelves. The red contours outline regions described as 'passive shelf ice'. Figure reprinted from Fürst et al. (2016).

After each calving experiment, the change in ice flux *across the new calving front* is determined for each ice shelf, and regions which have been removed from the shelf that cause an increase in ice

flux of less than 10% across the new calving front are determined to be 'passive shelf ice'. These are the regions outlined with a red contour in Figure 2.7, and typically contain ice with maximum buttressing numbers < 0.5. Both by calculating locally defined buttressing numbers based on the second principal stress direction, and by quantifying the response in ice shelf velocities to calving perturbations, the focus of the study moves the idea of ice-shelf buttressing from something that originally referred to the integrated impact of ice shelves on the stress state at the grounding line (e.g. Thomas, 1979b, Gudmundsson, 2013), to something that is determined locally at each point within an ice shelf.

Over the whole continent, Fürst et al. (2016) found from this method that 13.4% of Antarctic ice shelves could be considered to be passive shelf ice, however there is significant spatial variation across the continent, as shown in Fig. 2.7. This work has been influential in thinking about the buttressing of Antarctic ice shelves, with, for example, Lai et al. (2020) using the map of passive shelf ice to determine that 60% of Antarctica's ice shelves both provide buttressing to the grounded ice sheet and are potentially vulnerable to collapse through ice-shelf hydrofracture in a hypothetical scenario in which all of Antarctica's ice shelves experience significant surface melting.

2.4.1.2 Buttressing flux response number

An alternative approach to mapping ice-shelf buttressing across Antarctic ice shelves was taken by Reese et al. (2018b). They also assimilated present-day ice velocity, ice thickness and bedrock topography data for the whole of Antarctica into an SSA flow model with a highly resolved grounding line. In their experiments, the ice-shelf thickness was systematically reduced by 1 m within 20 x 20km grid squares defined to cover all Antarctic ice shelves. This resulted in thousands of individual, diagnostic experiments – one for each perturbation cell – and for each experiment the instantaneous change in GLF was computed. This change in grounding line flux was used to calculate a buttressing flux response number (BFRN), given by

$$\theta_B = \frac{R}{P} \tag{2.3}$$

where R is the change in mass flux across all grounding lines over one year in response to the perturbation, P, in ice-shelf mass. A θ_B value of 100% implies that the increase in mass flux across

the grounding line over one year is equal to the reduction in ice-shelf mass due to the thinning perturbation. The map of the BFRN that Reese et al. (2018b) produced from these experiments is shown in Figure 2.8 (note the logarithmic colour scale used, and significant variation in BFRN found across the ice shelves).

The map of BFRN shares similarities with that of the passive ice regions and maximum buttressing numbers of Fürst et al. (2016). In both cases, regions close to the calving fronts of ice shelves are found to be insignificant in the control of both ice shelf and grounding line fluxes. Both studies also find elevated numbers around the ice rises across the major ice shelves, supporting other existing work which has shown that ice rises can play a significant role in the dynamics and stability of grounding lines (Favier and Pattyn, 2015, Favier et al., 2016, Matsuoka et al., 2015).

There are, however, significant differences between the two maps. In particular, there are large regions in the centre of the major ice shelves (see e.g. the BFRN for the Ross and Filchner-Ronne Ice Shelves) in which the GLF is found to be insensitive to perturbations in ice-shelf thickness, but that have large maximum buttressing numbers, and are not classed as passive shelf ice areas. The focus on the impact of ice-shelf perturbations on changes in the flux across the grounding line adopted by Reese et al. (2018b) returns to the original conception of buttressing as being related to the impact that an ice shelf has on the stress state at the grounding line. In addition to this, by not using a metric which is saturated at a value of 1 as the maximum buttressing number of Fürst et al. (2016) was, the much greater sensitivity of the GLF to perturbations close to the grounding line can been revealed.

2.4.2 Transient response to ice-shelf collapse

The two studies outlined in the previous section used diagnostic model experiments to elucidate the buttressing provided by Antarctica's ice shelves. However, of primary societal importance for determining the future contribution of the AIS to GMSL is the transient evolution of the grounded ice sheet to a loss of ice-shelf buttressing.

The Antarctic BUttressing Model Intercomparison Project (ABUMIP) (Sun et al., 2020), involved 15 different ice sheet models running experiments in which the total buttressing capacity of Antarctic ice shelves was removed instantaneously (through either calving or thinning) and the ice

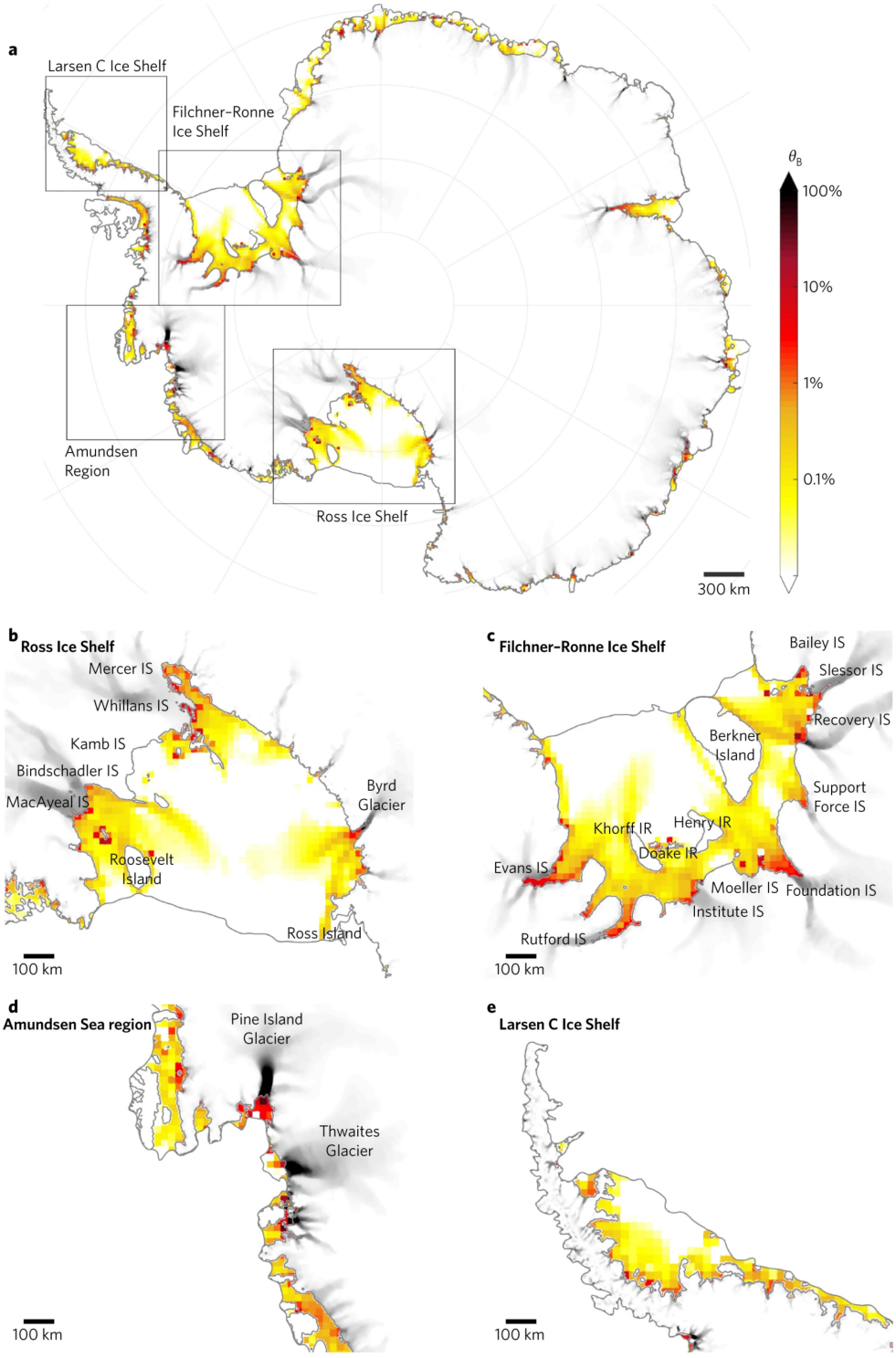

Figure 2.8: Maps of the buttressing flux response number (BFRN) for Antarctic ice shelves, calculated as described in the text (see Eq. 2.3). Figure reprinted from Reese et al. (2018b).

sheet was evolved for 500 years. In response to the complete loss of buttressing there was widespread mass loss around the ice sheet, with the WAIS contributing between 1.91 and 5.08 m of SLE after 500 years, demonstrating unequivocally the central role that ice shelves play in maintaining the present-day state of the AIS. However, within the ensemble of model results there was significant variation, driven largely by the choice of the basal sliding law, with more plastic Coulomb and Weertman sliding laws resulting in an increased sensitivity to the loss of ice-shelf buttressing and greater mass loss (ibid.).

In addition to this model intercomparison study, Martin et al. (2019) used the BISICLES ice sheet model to explore the transient impact of the loss of buttressing from Antarctic ice shelves over a 1,000 year simulation period. Overall, they find that the loss of ice-shelf buttressing is enough to destabilise the grounding lines around the whole of the WAIS, and that when all ice-shelf buttressing is removed simultaneously, this leads to a contribution to GMSL of 4.6 m after 1,000 years. The EAIS, by comparison, is found to be relatively insensitive to a complete loss of ice-shelf buttressing in their experiments. For example, Totten Glacier is found to thin and retreat rapidly at the beginning of the simulation, but this does not result in significant mass loss after 1,000 years. They also find that regional models are sufficient to model the response of individual drainage basins for 400-500 years after ice-shelf collapse, but that whole AIS models may be required for longer timescales as drainage basins begin to interact with each another (ibid.).

2.4.3 Larsen C Ice Shelf buttressing

The first study to calculate a buttressing number for the LCIS was that of Borstad et al. (2013). In that work an ice flow model was used to assimilate ice velocity data and from the modelled stress field a 'flow buttressing' number was calculated. They found that the buttressing number was elevated upstream of the BIR and GIR, and also found larger buttressing numbers in the embayments close to the grounding line, with a similar distribution to that found in the Antarctic-wide study of Reese et al. (2018b). As this modelling study only included the floating ice, and did not specifically model the grounding line or tributary glaciers, the focus was on a locally determined buttressing quantity, rather than an assessment of how the buttressing affects the stress state at the grounding line. Borstad et al. (2013) also used diagnostic experiments to examine the impact

of a loss of basal contact the BIR and GIR. As they did not explicitly model the ice rises within the shelf, in their approach they adjusted the ice viscosity to reproduce the effect of the loss of basal contact. From these experiments they found that the ice velocity of the shelf increased significantly, particularly directly upstream of the ice rises, but that the impact on ice velocities did not extend all the way to the grounding line.

In their supplementary material, Fürst et al. (2016) also focussed in more detail on the buttressing of the LCIS. They presented a calculation of the 'flow buttressing number' for the LCIS, rather than the 'maximum buttressing number' as used throughout the rest of their study, and produced a field very similar to that of Borstad et al. (2013). They also performed an experiment in which the basal contact at the BIR was removed, achieving this by setting the basal friction coefficient to zero over the ice rise. The model produced a very similar ice-shelf velocity response to that of Borstad et al. (2013), with an increase in ice-shelf velocities upstream of the ice rise, but that did not extend to the grounding line.

In a more recent modelling study of the LCIS, Borstad et al. (2017) simulated the stress state in the LCIS prior to the calving of the A68 iceberg, and proposed four possible trajectories along which the rift that would eventually form that iceberg could propagate. In each of the four cases, they modelled the instantaneous change in ice velocity in response to the calving of the iceberg, and found that the ice-shelf velocity increased across 70% of the ice shelf area, and that this increase extended all the way back to the main grounding line of the shelf.

Zhang et al. (2020) examined the links between buttressing numbers that are determined locally in an ice shelf – e.g. as calculated in Borstad et al. (2013) and Fürst et al. (2016) – and the impact on GLF from perturbations in thickness at those same points in the shelf (similar to the approach of Reese et al. (2018b)). They found that for the LCIS there was no meaningful relationship between any of the locally derived buttressing numbers which they calculated and the GLF sensitivity. They therefore concluded that locally derived buttressing numbers do not predict the impact on GLF from perturbations in ice-shelf thickness. Instead they suggest that experiments which directly assess the sensitivity of the GLF to perturbations in the ice shelf are required, as performed in Reese et al. (2018b), Gudmundsson et al. (2019) and throughout the research in this thesis. A key advance that came from the Zhang et al. (2020) paper was the development of an adjoint approach

to calculating the sensitivity of the GLF to small perturbations in the ice shelf. This removes the need for the thousands of diagnostic experiments that Reese et al. (2018b) required to build up their map of BFRN across Antarctica.

There is only one existing study that has specifically examined the transient mass redistribution of the LCIS in response to ice-shelf perturbations using models incorporating the necessary membrane stresses in the momentum equations (Schannwell et al., 2018). In that study, the transient response of the ice shelf and its tributary glaciers to both ice-shelf calving and complete ice-shelf collapse was explored using three different ice sheet models of varying complexity, forced by global climate model output under different greenhouse gas emissions scenarios. In their experiments examining the complete collapse of the LCIS, Schannwell et al. (2018) found that the total ice mass loss, expressed as a contribution to GMSL, was between 0.5 and 1.5 mm SLE after 100 years, and after 300 years was between 0.6 and 4.2 mm SLE. The variation in the mass loss was due to: using models with different flow approximations and representations of ice-shelf buttressing, and therefore of differing applicability to the problem of modelling the response to ice-shelf collapse; different basal sliding laws; and different bedrock topography and ice thickness data sets. As a result of this limited mass loss following the complete collapse of the LCIS, Schannwell et al. (2018) argue that this means that the LCIS does not provide significant buttressing to its tributary glaciers, an argument which is challenged by the research in this thesis and the idea that the buttressing provided by an ice shelf is a separate, but linked process to the transient mass redistribution in response to the loss of that buttressing.

2.5 Knowledge gaps and research questions

As outlined in this chapter, the LCIS has become a focus of recent research due to the collapse of its northerly, neighbouring ice shelves and the calving of the A68 iceberg in 2017, both of which have led to questions about its structural integrity, future viability and what the consequences of its loss might be. Whilst existing work has calculated a range of local buttressing metrics for the LCIS, no study has yet quantified the total buttressing capacity of the ice shelf. This leads directly to the first research aim of this thesis, which sets out to quantify the total amount of buttressing that the LCIS provides to its grounded tributary glaciers.

In addition to this, existing work has examined the instantaneous impact of a loss of basal contact at the BIR and GIR on ice-shelf flow, but the contribution that these ice rises make to the total buttressing capacity of the LCIS has not been previously assessed. Performing modelling experiments to illuminate these two features of the buttressing capacity of the LCIS would further our understanding of how the LCIS buttresses its grounded tributary glaciers, and how any future changes in its extent might reduce that buttressing capacity.

Since the calving of the A68 iceberg, no study has attempted to simulate the response to this exact calving event by prescribing it in an ice flow model and then testing that model prediction against observations. Now that there is sufficient observational data available to perform this comparison, the ability of an ice flow model to replicate the observed behaviour is another key knowledge gap that this thesis seeks to fill. These research questions are explored through a series of diagnostic ice-shelf perturbation experiments on the LCIS in Chapter 4 of this thesis.

Only one existing study has examined in detail the transient response of the LCIS to a complete collapse of the ice shelf (Schannwell et al., 2018). Therefore a further gap in knowledge is what the relationship is for the LCIS between systematic changes in ice-shelf buttressing and the transient mass redistribution in response to the loss of that buttressing. Again, pursuing this question will further our understanding of the consequences that any future reduction in buttressing on the LCIS will have on its grounded tributary glaciers.

Further to this, and despite the significant focus on their role in the ice dynamics of the LCIS, there has been no published study exploring the transient evolution of the LCIS and its tributary glaciers to the loss of basal contact at the BIR and GIR. The results of these experiments would further reveal the importance of the BIR and GIR for the dynamics of the shelf and grounding line, and this is another gap in knowledge of the potential future behaviour of the LCIS that the research in this thesis seeks to fill. The research questions related to the transient evolution of the LCIS in response to perturbations in ice-shelf buttressing are pursued in Chapter 5 of this thesis.

On an Antarctic-wide scale, the buttressing provided by the ice shelves has previously been assessed via the sensitivity of GLF to ice-shelf thickness perturbations (Reese et al., 2018b), and via changes in the flux across new calving fronts in the ice shelves following prescribed, idealised calving events (Fürst et al., 2016). However, as for the LCIS, the total buttressing capacity of Antarctic ice

shelves has not yet been calculated. Filling this knowledge gap is the key research question pursued in Chapter 6 of this thesis. In addition to assessing the total buttressing capacity of other Antarctic ice shelves, tackling this knowledge gap will allow for an understanding of where within Antarctic ice shelves the majority of the buttressing is generated, how that varies around the continent, and what features of ice shelves cause that variation. All of this will add to our understanding of how the AIS is buttressed, and how future changes in the extent of Antarctica's ice shelves might affect the ice sheet's contribution to GMSL in the decades and centuries ahead.

Finally, a criteria proposed for assessing the stability of an ice-shelf – the stress-flow angle – is analysed from the perspective of the principle of *frame-indifference*, which is central to continuum mechanics. The consequences of this metric not being frame-indifferent are discussed, and it is proposed that this fundamental principle must be taken into consideration in the development of future metrics for ice-shelf structural integrity or calving-front stability.

Chapter 3

The Úa ice flow model

3.1 Introduction

A range of different ice sheet models are currently used to study the behaviour of the AIS, many of which have been compared in recent model intercomparison projects (e.g. Cornford et al., 2020, Seroussi et al., 2020). Each of these models takes a different approach to the representation of the underlying physics (e.g. solving the full Stokes equations or an approximation to them); use different numerical methods to solve those equations (e.g. finite-difference or finite-element methods); and derive the initial model state in different ways (e.g. using data assimilation or a 'spin-up' approach). To model the impact of changes in ice-shelf buttressing on the GLF and the flow of the grounded ice sheet, it was essential to use a model that retains the necessary lateral shear and longitudinal stress terms in the full Stokes equations, but which is computationally efficient enough to run century-scale simulations with a high spatial resolution. For this reason, I decided that a model which used the shallow-shelf approximation was most appropriate, although other higher-order models could have been chosen, and comparing the results in this thesis with those from a different model would be a valuable extension to this study. Additionally, to accurately model changes in the stress balance across the grounding line, a model in which the spatial resolution could be increased around the grounding line was required, which excluded models in which a uniform resolution is enforced across the computational domain. Finally, a model in which the present day state of the AIS could be replicated was required, as my experiments aimed to determine the buttressing capacity of Antarctic

ice shelves in their current formation. This meant choosing a model which has the capability to optimise its parameters by assimilating present-day observations of ice velocity and thickness, rather than a model in which the parameters are fixed and the model is 'spun-up' to a steady-state which is different to the present, observed state of the ice sheet.

The ice flow model that satisfied these requirements, and which was used throughout this thesis is called Úa (Gudmundsson, 2013; 2020). It is a finite element ice flow model which can solve either the shallow-ice approximation (SIA) or the shallow-shelf approximation (SSA) to the full Stokes equations used to describe ice flow. In this thesis, only the SSA implementation is used, and the corresponding equations are the ones described in this chapter. The model is written in Matlab and is open-source, with the code freely available to download (Gudmundsson, 2020). It is a vertically-integrated, two-horizontal dimensional 'plan-view' model, and as such retains the necessary horizontal gradients in deviatoric stresses in the momentum balance (Eq. 3.3) to explicitly capture the effects of ice-shelf buttressing. Additionally, the code uses an adaptive finite-element mesh, which allows for the grounding line to be modelled in high resolution, which has been shown to be essential for capturing the mechanical impact of ice shelves on the dynamics of the grounding line (e.g. Durand et al., 2009, Pattyn et al., 2013).

Úa has been used in a range of numerical studies of ice dynamics, including in: idealised settings to study grounding line dynamics (Gudmundsson et al., 2012, Gudmundsson, 2013); model inter-comparison projects with idealised geometries (Pattyn et al., 2012; 2013, Cornford et al., 2020) and Antarctic-wide set-ups (Levermann et al., 2020); diagnostic (time-independent) studies of ice-shelf buttressing in Antarctica and Greenland (e.g. De Rydt et al., 2015, Royston and Gudmundsson, 2016, Minchew et al., 2018, Reese et al., 2018b, Hill et al., 2018, Gudmundsson et al., 2019); full prognostic (time-dependent) simulations of regions of the AIS (e.g. Favier et al., 2014, Hill et al., 2021, Rosier et al., 2021); and recently in a coupled ice-ocean model set-up with the MITgcm ocean model (De Rydt and Gudmundsson, 2016, Naughten et al., 2021).

In the rest of this chapter, I present the equations solved within Úa, briefly discuss key features of the numerical implementation, and outline the approach taken to model initialisation (through data assimilation) used throughout this thesis. A more detailed description of the derivation – and numerical implementation – of these equations within Úa can be found in the accompanying docu-

mentation within the source code of the model (particularly in the Úa Compendium) (Gudmundsson, 2020). The notation used in this chapter follows closely that used in the model documentation.

3.2 Model equations

The fundamental equations solved within Úa are derived from the conservation of linear momentum, the conservation of mass, the constitutive equation for ice and a set of boundary conditions, including a basal sliding law for grounded ice.

3.2.1 Stress balance

When modelling ice sheets, which have extremely small Reynolds numbers, the flow of ice is typically modelled as a viscous creep deformation (e.g. Schoof and Hewitt, 2013), and the equations for the conservation of linear momentum can be simplified – by neglecting inertial terms – to the Stokes equations under gravity, with the form

$$\boldsymbol{\nabla} \cdot \boldsymbol{\sigma} + \rho \boldsymbol{g} = \boldsymbol{0}, \tag{3.1}$$

where $\boldsymbol{\sigma}$ is the Cauchy stress tensor, ρ is the ice density, and $\boldsymbol{g}$ the acceleration due to gravity. Stresses in Úa are expressed as deviatoric stresses, which are linked to the Cauchy stresses through

$$\boldsymbol{\tau} = \boldsymbol{\sigma} + p\boldsymbol{I}, \tag{3.2}$$

where $\boldsymbol{\tau}$ is the deviatoric stress tensor, $\boldsymbol{I}$ is the identity matrix and the pressure, $p = -\frac{1}{3} tr \boldsymbol{\sigma}$.

The shallow-shelf approximation (SSA) to the full Stokes equations can be made – using scaling arguments – by neglecting some terms in the component based expansion of Equation 3.1. For the SSA, these scaling arguments are that the horizontal extent of an ice sheet is typically much greater than its thickness (the thin-film approximation) and that vertical shear stresses in the ice ($\tau_{xz},\ \tau_{yz}$) are negligible when compared with the lateral shear (τ_{xy}) and longitudinal (τ_{xx}, τ_{yy}) stresses. A full derivation of the SSA has been performed in a number of previous studies and can, for example, be found in MacAyeal (1989) or Pegler and Worster (2012), and is also shown in the Úa Compendium (Gudmundsson, 2020). The diagnostic SSA system – when formulated in terms of ice velocities,

rather than stresses as in Eq. 3.3 – is a set of elliptic partial differential equations in two horizontal dimensions (although including the time-dependent prognostic equation, outlined in Sect. 3.2.4, makes it a mixed elliptic/parabolic system). This greatly simplifies the problem when compared with the full Stokes equations, significantly reducing the computational time required to find a solution. The key features of the SSA are: that the driving stress is balanced by resistive stresses generated by basal drag – through the sliding law (Eq. 3.11) – and by horizontal gradients in the lateral shear and longitudinal stresses (together the 'membrane' stresses); that the system is non-local, such that changes in the stress balance in one region of the ice can affect the stress balance elsewhere; and that ice velocities are independent of depth (i.e. a plug-flow), and can be described by two horizontal components. These approximations are found to be valid over ice shelves and fast-flowing ice streams and glaciers where the vast majority of the motion occurs at the bed, and as such the SSA is also sometimes known as the 'shelfy-stream approximation'.

The equation for the vertically-integrated SSA momentum balance can be written as

$$\boldsymbol{\nabla}_{xy} \cdot (h\boldsymbol{R}) - \boldsymbol{t_{bh}} = \rho g h \boldsymbol{\nabla}_{xy} s + \frac{1}{2} g h^2 \boldsymbol{\nabla}_{xy} \rho, \tag{3.3}$$

where

$$\boldsymbol{R} = \begin{pmatrix} 2\tau_{xx} + \tau_{yy} & \tau_{xy} \\ \tau_{xy} & 2\tau_{yy} + \tau_{xx} \end{pmatrix}, \tag{3.4}$$

is the resistive stress tensor, τ_{ij} are the components of the deviatoric stress tensor, $\boldsymbol{\nabla}_{xy} = (\partial_x, \partial_y)^T$, $\boldsymbol{t_{bh}}$ is the horizontal component of the basal traction, h is the ice thickness, s is the ice surface elevation, ρ is the vertically-integrated ice density, and g is the acceleration due to gravity.

Importantly, within Úa the ice density, ρ, can vary in space (but not in time) which leads to the second term on the RHS of Equation 3.3, which is not present in other SSA models which use a spatially-constant ice density. The impact of using a variable ice density, as opposed to a constant ice density of 917 $\mathrm{kg\,m^{-3}}$ is tested in Chapter 4.

3.2.2 Constitutive relation

The most commonly used constitutive relation in ice sheet modelling is Glen's flow law (Glen, 1955), which links the deviatoric stress field in the ice to the rate of deformation, and is given by

$$\dot{\epsilon}_{ij} = A\tau_e^{n-1}\tau_{ij}, \tag{3.5}$$

where $\dot{\epsilon}_{ij}$ are the components of the strain-rate tensor, τ_e is the second invariant of the deviatoric stress tensor, also known as the effective deviatoric stress, and given by

$$\tau_e = \sqrt{\tau_{ij}\tau_{ij}/2}, \tag{3.6}$$

and the rate factor, A – which depends on ice properties including temperature, crystal fabric and damage – is determined through the use of inverse methods (see Sect. 3.4). The creep exponent is set to $n = 3$ throughout the thesis, as is standard in ice flow modelling.

The ice velocity, which is typically the key variable to be solved for in ice flow modelling, enters the system through the strain-rate tensor. The components of the strain-rate tensor are defined as

$$\dot{\epsilon}_{ij} = \frac{1}{2}\left[\frac{\partial u_i}{\partial x_j} + \frac{\partial u_j}{\partial x_i}\right], \tag{3.7}$$

where $u_i = (u, v)^T$ is the two-horizontal dimensional ice-velocity vector in the SSA formulation, and $x_i = (x, y)^T$.

3.2.3 Boundary conditions

Along the calving front the necessary stress boundary condition is given by

$$\boldsymbol{\sigma} \cdot \hat{\boldsymbol{n}} = -p_o\hat{\boldsymbol{n}} \tag{3.8}$$

where $\hat{\boldsymbol{n}}$ is the unit, horizontal normal to the calving front pointing out of the ice front and p_o is the ocean pressure. Within Úa the momentum equation (Eq. 3.3) is written in such a way that this

is the natural boundary condition at the ice margin, and Eq. 3.8 can be reformulated as

$$\boldsymbol{R} \cdot \hat{\boldsymbol{n}} = \frac{g}{2h}(\rho h^2 - \rho_o d^2)\hat{\boldsymbol{n}} \tag{3.9}$$

where $\rho_o = 1027\ \mathrm{kg\,m^{-3}}$ is the ocean density used throughout this thesis, and

$$d = \begin{cases} S - b, & \text{for} \quad S > b \\ 0, & \text{for} \quad S \leq b \end{cases} \tag{3.10}$$

is the ice draft, S is the ocean surface (set to zero throughout this thesis), and b is the ice base elevation. Formulated in this way, the boundary condition can equally be applied to floating or grounded calving fronts and thus can be applied as a natural boundary condition around the entire Antarctic Ice Sheet, as utilised in Chapter 6.

Along the upper surface of the ice, a stress-free boundary condition is applied, given by $\boldsymbol{\sigma} \cdot \boldsymbol{n_s} = \mathbf{0}$, with $\boldsymbol{n_s}$ a unit normal defined pointing out of the ice surface. At the basal boundary of the ice, a 'no-penetration' boundary condition is applied, which is given by $\boldsymbol{u} \cdot \boldsymbol{n_b} = 0$, where $\boldsymbol{n_b}$ is a unit normal pointing out of the ice base, and $\boldsymbol{u}$ is the horizontal ice-velocity vector.

3.2.3.1 Basal sliding law

Additionally, along the interface between the ice and the bedrock in grounded regions of the model domain, a basal sliding law is required, which links the basal ice velocity to the basal shear traction. Throughout this thesis a non-linear Weertman-type sliding law is used (Weertman, 1957), which can be expressed as

$$\boldsymbol{t_{bh}} = C^{-1/m} ||\boldsymbol{u_b}||^{(1-m)/m} \boldsymbol{u_b} \tag{3.11}$$

where $\boldsymbol{t_{bh}}$ is the horizontal component of the the bed-tangential basal traction and $\boldsymbol{u_b}$ the horizontal component of the bed-tangential ice velocity. The basal slipperiness parameter, C, is inferred using inverse methods outlined in the Sect. 3.4, and the stress exponent is typically set to $m = 3$. Within Chapter 4, the sensitivity of the model results to the value of the stress exponent used in the sliding law are examined.

The basal traction described in Equation 3.11 is only applied to nodes in the mesh that are

grounded. Whether or not a node is grounded or floating is determined according to a flotation condition, whereby the node is grounded if $h > h_f$ and floating if $h < h_f$, where h_f, the flotation thickness, is given by

$$h_f = \frac{\rho_o}{\rho}(S - B), \tag{3.12}$$

where B is the bedrock elevation. This process generates a grounded-floating mask which is defined on the nodes of the mesh, such that the grounding line passes through mesh elements, and its precise position within the mesh element is determined by interpolation of the grounded-floating mask across the element.

3.2.4 Mass conservation

The system of equations described thus far can be solved to find the stress balance, and to determine the ice velocities from a given geometry, rate factor field and basal slipperiness field. This system is independent of time, and within glaciology is often referred to as a diagnostic model. To study the impact of ice-shelf perturbations on the state of stress, and hence determine the impact of those perturbations on the ice-shelf buttressing provided by the shelf, these are the only equations that need to be solved (e.g. Fürst et al., 2016, Reese et al., 2018b, Gudmundsson et al., 2019). It is these equations that are solved in Chapters 4 and 6.

To model the time-dependent evolution of the ice geometry and the ice velocities (also known as transient or prognostic model runs), the vertically-integrated form of the conservation of mass must be solved in addition to the equations outlined above. The equation for the local conservation of mass of an incompressible fluid (and accounting for a spatially variable ice density) is given by

$$\boldsymbol{\nabla} \cdot (\rho \boldsymbol{u}) = 0, \tag{3.13}$$

where $\boldsymbol{u}$ is the full, three-dimensional ice velocity. Two additional, kinematic boundary conditions are defined which relate to the evolution of the upper and lower material ice surfaces, and are given

by

$$\partial_t s + u_s \partial_x s + v_s \partial_y s - w_s = a_s \tag{3.14}$$

$$\partial_t b + u_b \partial_x b + v_b \partial_y b - w_b = -a_b, \tag{3.15}$$

where s is the upper ice surface elevation, b ice base elevation, u_s, v_s, and w_s the x, y and z components of the ice velocity at the surface, and u_b, v_b, and w_b, the components of the ice velocity at the ice base. a_s is the surface mass balance, and a_b is the basal mass balance, both measured in ma^{-1}. Ice entering the system is always defined as positive, so basal melting is represented by negative values for a_b.

From these three equations, the vertically-integrated formulation of the mass conservation equation can be derived – also known as the prognostic equation – which has the following form within Úa

$$\rho \partial_t h + \boldsymbol{\nabla}_{xy} \cdot \boldsymbol{q} = \rho a, \tag{3.16}$$

where $\boldsymbol{q} = \rho h \boldsymbol{u}$ is the ice flux, $\boldsymbol{u} = (u, v)^T$ is now the horizontal ice velocity vector, and $a = a_s + a_b$. In the derivation of this formulation of the mass conservation equation, it is assumed that the vertically integrated, spatially-variable density is fixed in time, and is not advected with the ice flow.

In all of the experiments conducted in this thesis, there is no transient evolution of the lateral boundaries of the computational domain. At any ice divides, or 'artificial' boundaries of the domain, this means that a zero ice velocity boundary condition is applied, although the ice thickness is able to change due to the applied mass balance field. For the calving front position to remain fixed in space, this implies that a 'calving rate' is applied along the boundary which is exactly equal to the ice velocity at the calving front, but acting in the opposite direction. The ice flux that leaves the computational domain through the calving front can freely vary in time as both the ice velocity and thickness at the calving front are unconstrained.

There is no thermodynamic component or evolution equation within Úa. The impact that ice temperature has on the flow is implicitly incorporated into the model through the data assimilation methods used to determine the rate factor, A, in Equation 3.5, as outlined in Sect. 3.4. However,

thermodynamic effects are assumed to have a negligible impact on ice dynamics over the timescale (decades) explored in Chapter 5 of this thesis.

3.3 Numerical methods

One of the key features of Úa is its use of an unstructured, finite element mesh, which allows for mesh refinement and a high spatial resolution in regions where the solution may vary rapidly in space, including at the grounding line.

To generate the finite element meshes in this thesis, the following procedure is used. First, an initial mesh is defined over the model domain. Next, a series of 'global' mesh refinement iterations are carried out, in which the position of all mesh nodes can be changed. Here, smaller target mesh element sizes are prescribed in regions of high ice velocity and strain rates. Following this global mesh refinement, an iterative 'local' mesh refinement procedure is used to refine the mesh around the grounding line. This process keeps all the nodes of the mesh fixed in space and uses a bisection algorithm to split elements in half, introducing new nodes into the mesh where refinement is required. The 'newest vertex bisection' algorithm used for this local mesh refinement guarantees that the quality of the mesh elements from the global mesh refinement is maintained. Once the required mesh resolution was achieved around the grounding line, the mesh was saved for used in model initialisation and forward experiments. Úa has the capability to adapt (refine and coarsen) the mesh throughout a transient simulation to ensure, for example, that a high resolution is maintained around the grounding line even as it migrates through the computational domain. However, this transient mesh refinement was not used in any of the model runs which are carried out in this thesis.

In addition to mesh refinement, the elements of the mesh can be deactivated (and reactivated) throughout the course of a model run. This allows for ice-shelf calving to be implemented by deactivating elements from the mesh and consequently changing the location of the model boundary along which the calving-front boundary condition (Eq. 3.9) is applied. This was the method used to perform the calving experiments in Chapters 4-6 of this thesis.

Once assembled, the non-linear system is solved through the use of the Newton-Raphson (NR) method, which has a second order rate of convergence. Further details of the numerical implementation can be found in the model documentation (Gudmundsson, 2020). To solve the time-dependent

(prognostic) system of equations, Úa uses a fully-implicit time integration, which allows for the time-step to be set independently of the spatial resolution of the finite element mesh. The time-step used is determined by an algorithm which aims to make the time-step as large as possible whilst keeping the initial estimate of the solution at the next time-step within the second-order convergence radius of the NR method (i.e. typically aiming for between 3 and 5 NR iterations per time-step). This allows for the time-step to be increased significantly when the solution is only slowly varying in time (i.e. close to a steady-state) compared with models in which the time-step is linked to the spatial resolution of the mesh.

Throughout this thesis, a minimum ice thickness is prescribed to prevent numerical issues related to regions of zero ice thickness within the model domain. The value used for the minimum ice thickness throughout this thesis is 1 m, but the consequences of using a different value when perturbing the ice-shelf thickness towards zero are tested in Chapter 4.

3.4 Model initialisation

In the governing equations, there are two unknown parameters: the rate factor, A, in the constitutive relation (Eq. 3.5); and the and the basal slipperiness coefficient, C, in the sliding law (Eq. 3.11). The other variables necessary to calculate ice velocities are determined by the geometry of the problem being addressed, and in this thesis it is geometry data from the BedMachine Antarctica v2 data set that is used (Morlighem et al., 2020).

However, it is not feasible to determine the appropriate values for A and C from direct measurements. Therefore, the approach taken in Úa is to use observations of the surface ice velocity to infer the possible values of the two parameters through inverse methods first introduced to glaciology by MacAyeal (1993). This allows for the model to be initialised into a state which approaches the observed ice velocity for a given data set describing the ice thickness and bedrock topography.

The model initialisation scheme in Úa involves the minimisation of a cost function, J, given by

$$J = I + R \tag{3.17}$$

where I is a misfit term, given by

$$I = \frac{1}{2\mathcal{A}} \int \left(\frac{u - u_{obs}}{u_{err}} \right)^2 + \left(\frac{v - v_{obs}}{v_{err}} \right)^2 d\mathcal{A}, \tag{3.18}$$

and R is a regularisation term, given by

$$\begin{aligned} R = \frac{1}{2\mathcal{A}} \int \Big[\gamma_{sA}^2 \left(\nabla \log_{10} \left(\frac{A}{\hat{A}} \right) \right)^2 + \gamma_{sC}^2 \left(\nabla \log_{10} \left(\frac{C}{\hat{C}} \right) \right)^2 + \\ \gamma_{aA}^2 \left(\log_{10} \left(\frac{A}{\hat{A}} \right) \right)^2 + \gamma_{aC}^2 \left(\log_{10} \left(\frac{C}{\hat{C}} \right) \right)^2 \Big] d\mathcal{A}. \end{aligned} \tag{3.19}$$

Here, $\mathcal{A}$ is the area of the model domain and u and v are the horizontal components of the modelled ice velocity. u_{obs} and v_{obs} are the components of the measured surface ice velocity, and the uncertainties associated with these observed velocities are given by u_{err} and v_{err} which can vary spatially. γ_{sA}, γ_{sC}, γ_{aA} and γ_{aC} are regularisation parameters that penalise deviations in the fields being optimised – in this case A and C – from their prior estimates – $\hat{A}$ and $\hat{C}$ – in terms of gradient and magnitude respectively.

This form of regularisation is known as Tikhonov regularisation, and is required to prevent over-fitting of the modelled velocity to the observed velocity, producing smoother fields for A and C than would be the case in the absence of any regularisation. The best choice for the values of the regularisation parameters cannot be determined a-priori, but the use of an L-curve method can provide some justification for the values chosen, and this approach is presented in Chapter 4.

Prior values for the fields being optimised ($\hat{A}$, $\hat{C}$) must be assigned, and the values chosen for these priors are specified in Chapters 4 and 6 in the descriptions of the model initialisation procedures for the LCIS and the Antarctic-wide set-ups used.

The misfit function within Úa (Eq. 3.18) has been developed to include observations of rates of change of ice thickness, $\partial h/\partial t$, allowing the model to fit observed thinning or thickening signals in addition to observed ice velocities. The incorporation of $\partial h/\partial t$ information into the model initialisation is explored in Section 5.2.2, but was not ultimately used in this thesis to generate the initial conditions for forward model runs.

3.5 Calculation of depth-averaged ice density

In the BedMachine Antarctica v2 data set used throughout this thesis, a firn air content field, δ, is provided – derived from the firn densification model of Ligtenberg et al. (2011) – which is defined in the supplementary material of Morlighem et al. (2020) (their Eq. S7) as

$$\delta = \frac{1}{\rho_i} \int_{firn\ layer} \left(\rho_i - \rho_f(z')\right) dz', \tag{3.20}$$

where δ is the firn air content (with the units of metres), and ρ_f is the firn density, which varies within the depth of the firn column.

To calculate a depth-averaged ice density from this firn air content field, the following equation in Úa is used

$$\rho_{av} = \rho_i \left(1 - \frac{\delta}{h}\right). \tag{3.21}$$

The impact of using a spatially variable ice density compared to a constant ice density of 917 $\mathrm{kg\,m^{-3}}$ is explored in Chapter 4.

Due to discrepancies between the ice thickness data and the firn air content data, there are regions within both the LCIS domain used in Chapters 4 and 5, and the Antarctic-wide domain in Chapter 6, where the firn air content field is of the same magnitude as – or even larger than – the ice thickness. This results in unrealistically small (and even unphysically negative) values for the depth-averaged ice density, and consequently a minimum ice density of 800 $\mathrm{kg\,m^{-3}}$ was set for all model simulations in this thesis.

Chapter 4

The instantaneous impact of calving and thinning on the Larsen C Ice Shelf

Preface

This research presented in this chapter has been published in *The Cryosphere* (Mitcham et al., 2022) with the following citation:

"**Mitcham, T.**, Gudmundsson, G. H., and Bamber, J. L.: The instantaneous impact of calving and thinning on the Larsen C Ice Shelf, The Cryosphere, 16, 883–901, https://doi.org/10.5194/tc-16-883-2022, 2022."

The author contributions were as follows: All authors were involved in conceiving the study. I (TM) conducted the modelling experiments, carried out the analysis and wrote the manuscript. GHG and JLB discussed the analysis and provided comments on the manuscript.

The majority of the text of this chapter is exactly as in the published paper, but some changes include: material from the appendices of the published paper have been integrated into the relevant sections of the main text in this chapter; and much of the 'Ice flow model' subsection of the published manuscript has been moved to the model description in Chapter 3 of this thesis.

Abstract

The Antarctic Peninsula has seen rapid and widespread changes in the extent of its ice shelves in recent decades, including the collapse of the Larsen A and B ice shelves in 1995 and 2002, respectively. In 2017 the Larsen C Ice Shelf (LCIS) lost around 10% of its area by calving one of the largest icebergs ever recorded (A68). This has raised questions about the structural integrity of the shelf and the impact of any changes in its extent on the flow of its tributary glaciers. In this work, we used an ice flow model to study the instantaneous impact of changes in the thickness and extent of the LCIS on ice dynamics, and in particular on changes in the grounding line flux (GLF). We initialised the model to a pre-A68 calving state, and first replicated the calving of the A68 iceberg. We found that there was a limited instantaneous impact on upstream flow – with speeds increasing by less than 10% across almost all of the shelf – and a 0.28% increase in GLF. This result is supported by observations of ice velocity made before and after the calving event. We then perturbed the ice-shelf geometry through a series of instantaneous, idealised calving and thinning experiments of increasing magnitude. We found that significant changes to the geometry of the ice shelf, through both calving and thinning, resulted in limited instantaneous changes in GLF. For example, to produce a doubling of GLF from calving, the new calving front needed to be moved to 5 km from the grounding line, removing almost the entire ice shelf. For thinning, over 200 m of the ice-shelf thickness had to be removed across the whole shelf to produce a doubling of GLF. Calculating the instantaneous increase in GLF (607%) after removing the entire ice shelf allowed us to quantify the total amount of buttressing provided by the LCIS. From this, we identified that the region of the ice shelf in the first 5 km downstream of the grounding line provided over 80% of the buttressing capacity of the shelf. This is due to the large resistive stresses generated in the narrow, local embayments downstream of the largest tributary glaciers.

4.1 Introduction

Around 74% of the Antarctic coastline is fringed by floating ice shelves (Bindschadler et al., 2011). These ice shelves are fed by tributary glaciers and ice streams, and lose mass predominantly through basal melting at the ice–ocean interface and calving at the ice front (Depoorter et al., 2013). When

formed in embayments, or where they locally run aground at ice rises or pinning points, ice shelves can generate resistive stresses which are transferred through the ice shelf to the grounding line (GL), where they provide a backstress to the grounded ice sheet (Thomas, 1979b). This process, known as ice-shelf buttressing, means that ice shelves can exert a mechanical control on the grounding line flux (GLF), and therefore control the rate at which the ice sheet contributes to changes in global sea level (e.g. Dupont and Alley, 2005, Gudmundsson, 2013).

The Larsen C Ice Shelf (LCIS) is situated on the eastern side of the northern Antarctic Peninsula (AP) and is the fourth-largest ice shelf in Antarctica. Over the second half of the 20th century, increasing surface air temperatures – and a subsequent increase in surface melt – have been implicated in the breakup of several ice shelves on the AP (e.g. Morris and Vaughan, 2003, Vaughan et al., 2003, Khazendar et al., 2011, Banwell et al., 2013). In 1995 the Larsen A Ice Shelf (LAIS) collapsed (Rott et al., 1996), and in 2002, the Larsen B Ice Shelf (LBIS) disintegrated in a matter of 6 weeks (Scambos et al., 2004). Domack et al. (2005) showed from a subsequent analysis of marine sediments that the LBIS had been present for at least 12,000 years.

In 2017, the LCIS calved one of the largest icebergs ever recorded – named A68 – reducing its surface area by $\sim 10\%$. The ice-shelf extent is now at its minimum since satellite observations began (Hogg and Gudmundsson, 2017). During the 2019/20 austral summer, the LCIS experienced near-record levels of surface melting (Bevan et al., 2020). All of these factors have raised questions about the future viability of the LCIS (e.g. Kulessa et al., 2014, Jansen et al., 2015, Holland et al., 2015), and what the consequences of any changes to its thickness or extent might be for the subsequent ice dynamics of the AP (e.g. Schannwell et al., 2018).

Following the collapse of the LBIS in 2002, a significant change in the flow of its tributary glaciers was observed, with some increasing in speed by close to 900% (Rignot et al., 2004). This increase in ice speeds – and consequently GLF – has been sustained to the present day (Berthier et al., 2012, Rott et al., 2018). De Rydt et al. (2015) modelled the response to this rapid loss of ice-shelf buttressing through diagnostic (or time-independent) simulations with the ice flow model Úa, which is also used in this study. They were able to reproduce the spatial variability in the response in ice velocity across the tributary glaciers, but suggested that transient experiments would be required to simulate the observed, quantitative changes. A similar approach – also using Úa – was taken

to model the response to the collapse of the LAIS (Royston and Gudmundsson, 2016). This study found that the initial increase in GLF could be reproduced with diagnostic experiments, but that modelling the transient redistribution of mass was required to reproduce changes further upstream in the tributary glaciers.

A number of studies have previously examined buttressing on the LCIS. Borstad et al. (2013) modelled the stress field in the ice shelf, calculated a local buttressing number, and modelled the impact of removing basal contact at ice rises on the dynamics of the shelf, but not the tributary glaciers. Fürst et al. (2016) mapped the 'maximum buttressing' number across the ice shelf, and from this delineated regions of 'passive ice' which could be calved without significantly increasing the ice flux across new calving fronts in the shelf. Reese et al. (2018b) computed the impact of small perturbations in ice-shelf thickness on the integrated GLF, producing a map of the 'buttressing flux response number' across the shelf. This allowed them to determine the regions in the ice shelf where a perturbation in ice thickness would produce the largest response in GLF, and they also demonstrated that small changes in ice-shelf thickness could impact the GLF hundreds of kilometres away. Gudmundsson et al. (2019) modelled the impact of an instantaneous thinning of Antarctic ice shelves on the grounded ice and GLF, with a spatial pattern and amplitude derived from observations. They highlight the fact that changes in ice-shelf buttressing have an instantaneous impact on ice velocities, after which there is a transient adjustment to the flow and a redistribution of mass. In their experiments, they were able to map, or 'fingerprint', the instantaneous ice velocity response and the reduction in buttressing due to the cumulative, observed ice-shelf thinning from 1994 to 2017. Zhang et al. (2020) explored the correlation between locally derived buttressing numbers in the ice shelf, and changes in GLF due to small perturbations in ice-shelf thickness at the same locations. They found that for a real-world ice shelf (the LCIS) there was no relationship between these two measures, and that locally derived buttressing numbers are not predictors for the impact of perturbations in ice-shelf geometry on GLF. Finally, Schannwell et al. (2018) and Sun et al. (2020) explored the transient response of the grounded ice to the complete collapse of the LCIS, and the associated removal of all ice-shelf buttressing.

Here, we build on this existing literature through a series of diagnostic perturbation experiments, including ice-shelf calving and thinning and ungrounding from ice rises. This approach allows us

to explore the buttressing capacity of the LCIS, due to the instantaneous impact that changes in buttressing have on the ice flow, but we do not examine the transient redistribution of mass in response to the perturbations. Our first objective is to model the response of the LCIS and its tributaries to the calving of the A68 iceberg and validate these results with observations. We then study the instantaneous GLF response to a series of idealised ice-shelf calving events. By quantifying the maximum GLF response, we determine the total amount of buttressing provided by the ice shelf, and examine the proportion of this total that is generated by different regions of the shelf. We simulate the loss of basal contact of the ice shelf at the Bawden and Gipps ice rises (outlined and labelled in Fig. 4.1), again examining the impact on GLF. And finally, we systematically perturb the thickness of the ice shelf by increasing amounts, again aiming to understand how much the ice-shelf geometry needs to change before a significant response in GLF is produced.

4.2 Methods

4.2.1 Ice flow model

We used the Úa ice flow model (Gudmundsson et al., 2012), which solves the vertically integrated, shallow-shelf approximation to the full Stokes equations (e.g. MacAyeal, 1989) using the finite-element method on an unstructured mesh, as described in detail in Chapter 3.

In this work, we conduct diagnostic – or time-independent – experiments, in which the equations for stress balance (Eq. 3.3) are solved together with the constitutive equation (Glen's flow law) (Eq. 3.5). The rate factor, A – which depends on ice properties including temperature, crystal fabric and damage – was optimised using inverse methods (see Sect. 4.2.3). We set the creep exponent $n = 3$ as is standard in ice flow modelling.

A non-linear Weertman type sliding law was used (Eq. 3.11). The basal slipperiness parameter, C, is also inferred using inverse methods, and $m = 3$. The results of diagnostic perturbation experiments using this ice flow model have previously been found to be largely unaffected by the value chosen for m (e.g. Hill et al., 2018, Gudmundsson et al., 2019). However, we conducted additional sensitivity tests to examine the impact of using different stress exponents (m values) in the sliding law, and found that they do not affect the conclusions of our study. The details of these

sensitivity tests are presented in Sect. 4.3.5.3.

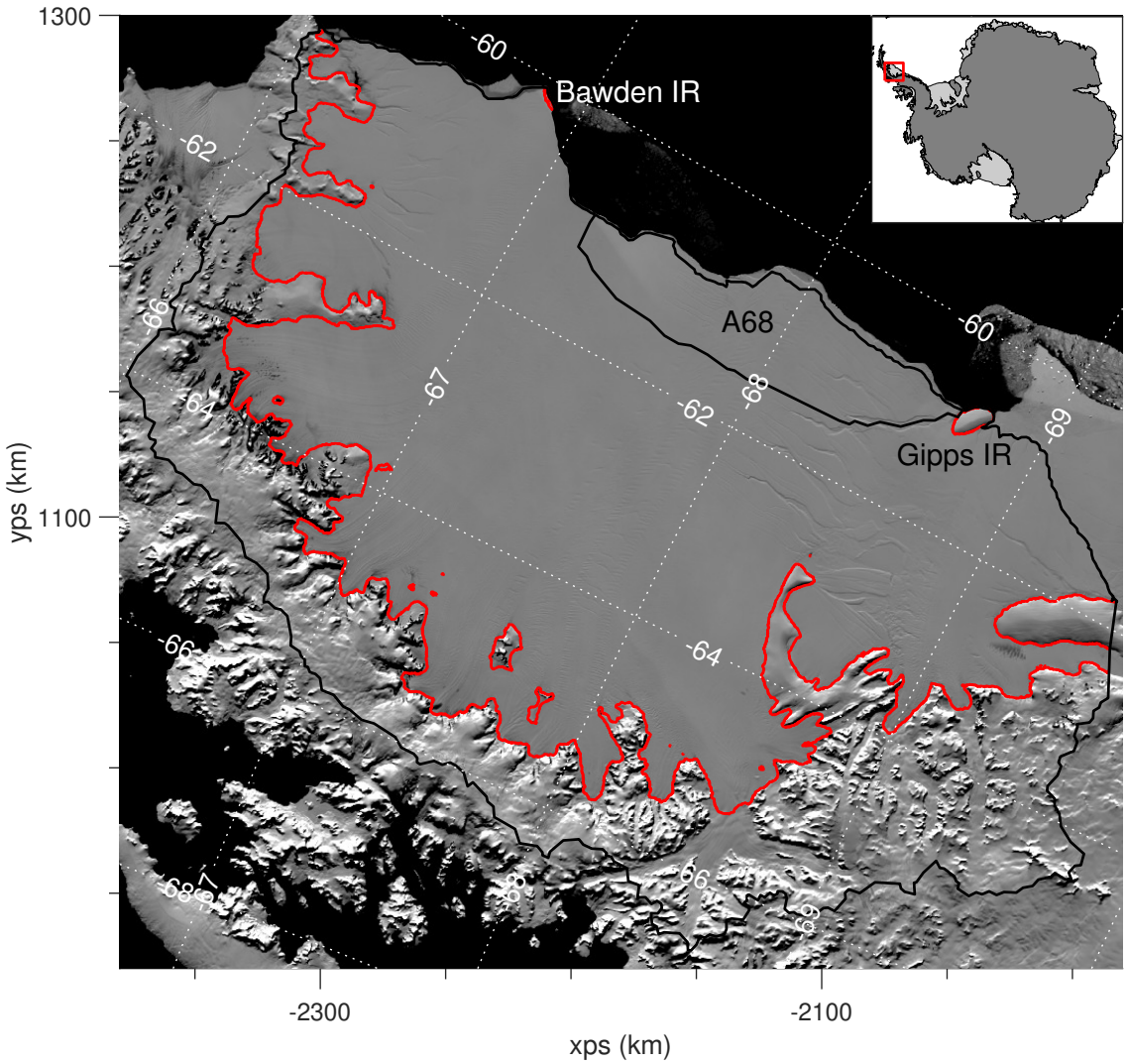

Figure 4.1: MODIS Mosaic of Antarctica (Scambos et al., 2007) image of the Larsen C Ice Shelf and its tributary glaciers, with open ocean shown in black. The boundary of the model domain is plotted in black, with the outline of the A68 iceberg which calved in July 2017 also shown. In red is the grounding line position as calculated in the model, which remains fixed throughout the experiments. The outlines of the Bawden and Gipps ice rises at the calving front of the ice shelf are also plotted in red. Lines of latitude and longitude are shown by the dotted white lines. The coordinate system used here – and in all other maps – is the WGS84 Antarctic Polar Stereographic projection (EPSG:3031), and the axis labels (also used in all other maps) refer to the x and y directions in these polar stereographic coordinates.

4.2.2 Model domain and data

The model domain, shown in Fig. 4.1, includes all of the drainage basins identified by Cook and Vaughan (2010) that drain into the LCIS. The calving front location represents a pre-July 2017

state, before the A68 iceberg calved from the shelf, and was defined as the maximum ice extent in the BedMachine Antarctica v2 data set (Morlighem et al., 2020). One artificial boundary was drawn to separate the region between the Larsen C and D Ice Shelves, and this was manually delineated by joining the ice divide to the calving front.

The finite-element mesh used in the computation was generated with the open-source Gmsh software (Geuzaine and Remacle, 2009). We chose to use linear shape functions on these elements. The target element size was set to 2 km across the floating ice shelf, with the resolution increased around the grounding line, where elements 250 m in size were used. The mesh was refined to 1 km in all tributary glaciers, and 500 m in regions of high strain rates. This ultimately produced a mesh with $\sim 154,000$ elements with a maximum, median and minimum element size of 4,000 m, 640 m and 160 m respectively. The dependence of the model results on element size was tested in a convergence analysis, and the effect was found to be negligible. The results of these convergence tests are shown in Sect. 4.3.5.1.

Along the ice divides at the boundary of the model domain, a zero-velocity boundary condition was applied. At the calving front, a stress boundary condition, arising from ocean pressure, was prescribed.

The initial ice thickness, surface elevation and bedrock topography were taken from the BedMachine Antarctica v2 data set (Morlighem et al., 2020). The surface elevation was adjusted at a few points (in areas of exposed bedrock) to ensure that at least 1 m of ice was present across the whole computational domain. A spatially variable, depth-integrated ice density was used across the model domain, the calculation of which is described in Sect. 3.5. Due to discrepancies between the ice thickness and firn air content fields, it was necessary to introduce a minimum value of 800 kgm^{-3} for the depth-integrated ice density. A map of the resulting ice density field is shown in Fig. 4.12. The impact of using a horizontally spatially variable ice density – as opposed to a constant ice density of 917 kgm^{-3} – on our results is minimal. The details and results of the sensitivity tests undertaken to determine this are outlined in Sect 4.3.5.2.

For the optimisation procedure used to initialise the model (see Sects. 3.4 and 4.2.3) we used the MEaSUREs InSAR-based Antarctic Ice Velocity v2 data set (Rignot et al., 2017; 2011, Mouginot et al., 2012). For model validation (see Sect. 4.3.1) we used ice velocity measurements generated

from Sentinel-1 synthetic aperture radar (SAR) data which were provided by ENVEO (ENVEO team, 2019). This data set consisted of monthly maps of tide-corrected ice velocities over the LCIS and its tributaries from October 2014 - September 2019.

4.2.3 Model initialisation

To generate the initial conditions for the rate factor, A, and basal slipperiness parameter, C, inverse, or control methods were used (e.g. MacAyeal, 1993), as described in detail in Chapter 3 (see Sect. 3.4). The observations of surface ice velocity – and their associated uncertainties – used in Eq. 3.18 are both here taken from the MEaSUREs InSAR-based Antarctic Ice Velocity v2 data set. The priors – ($\hat{A}$ and $\hat{C}$) in Eq. 3.18 – were chosen to be spatially uniform. The value chosen for $\hat{A} = 1.15 \times 10^{-8}$ a^{-1}kPa^{-3}, which corresponds to ice at a temperature of -10 °C as given by the equation for the rate factor in Morland and Smith (1984). The value for chosen for $\hat{C} = 1.95 \times 10^{-4}$ ma^{-1}kPa^{-3}, which was calculated from the sliding law (Eq. 3.11) assuming a basal shear stress of 80 kPa and an ice velocity of 100 ma^{-1}. We used values for the regularisation parameters in Eq. 3.18 of $\gamma_{sA/C} = 1000$ and $\gamma_{aA/C} = 1$, with the four regularisation parameter values justified using L-curve analyses (see Sect. 4.2.3.1).

The resulting ice velocity field is shown in Fig. 4.2b. There was a good fit to the observed velocities across the domain, with a spatially averaged RMS difference between the observed and modelled velocities of 11.2 ma^{-1}, and a particularly good fit across the ice shelf and at the GL. One region in which the model struggled to replicate the ice velocities is just to the north of the Gipps Ice Rise, where the nascent A68 iceberg was beginning to detach from the shelf. This gave rise to large strain rates in the shelf, which were not captured in the model, presumably due to the regularisation applied to the rate factor, A. Following the inversion, the modelled GLF across the main GL (i.e. excluding fluxes across ice rises in the shelf) was 23.2 Gta^{-1}, and this was the reference GLF to which GLF changes in perturbation experiments were compared.

4.2.3.1 L-curve analyses and A and C fields

L-curve analyses were used to determine the γ_{aA}, γ_{aC}, γ_{sA} and γ_{sC} parameters in Eq. 3.19. The values of $\gamma_{sA/C}$ were separately varied over 6 orders of magnitude, and the optimisation procedure

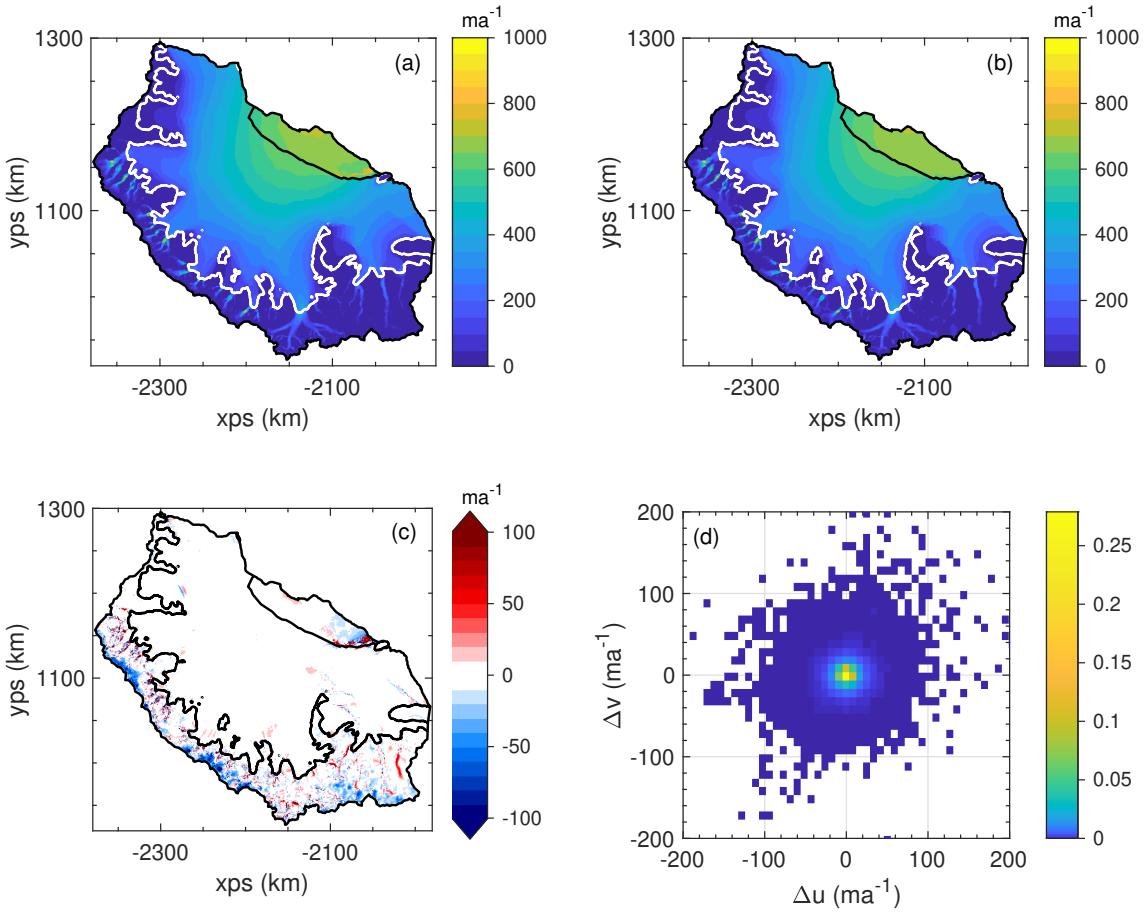

Figure 4.2: Observed ice speed **(a)** (from the MEaSUREs InSAR-based Antarctic ice velocity map) and modelled ice speed **(b)** following the initialisation procedure. Panel **(c)** shows the difference between the observed and modelled ice speed (obs - mod) and **(d)** is a normalised, bi-variate histogram of the differences between the x and y components of the observed and modelled ice velocities at each node in the computational mesh.

was carried out for each value of γ_{sA} and γ_{sC} whilst the other three parameters were held constant. This method was then repeated, separately varying γ_{aA} and γ_{aC} over 5 orders of magnitude whilst the other three parameters were held constant. The model–observation misfits for the different amounts of regularisation applied are shown in Fig. 4.3. The chosen values after the L-curve analyses were γ_{aA} and $\gamma_{aC} = 1$ and γ_{sA} and $\gamma_{sC} = 1000$. This amount of regularisation was then used to determine the A and C fields used throughout the experiments conducted in the rest of this chapter.

The fields for the rate factor, A, and basal slipperiness parameter, C, are shown in Fig. 4.4a and b, respectively. Examining the rate factor field, we can see that softer, more deformable ice is found in the shear margins of the ice shelf and between flow units emanating from the tributary

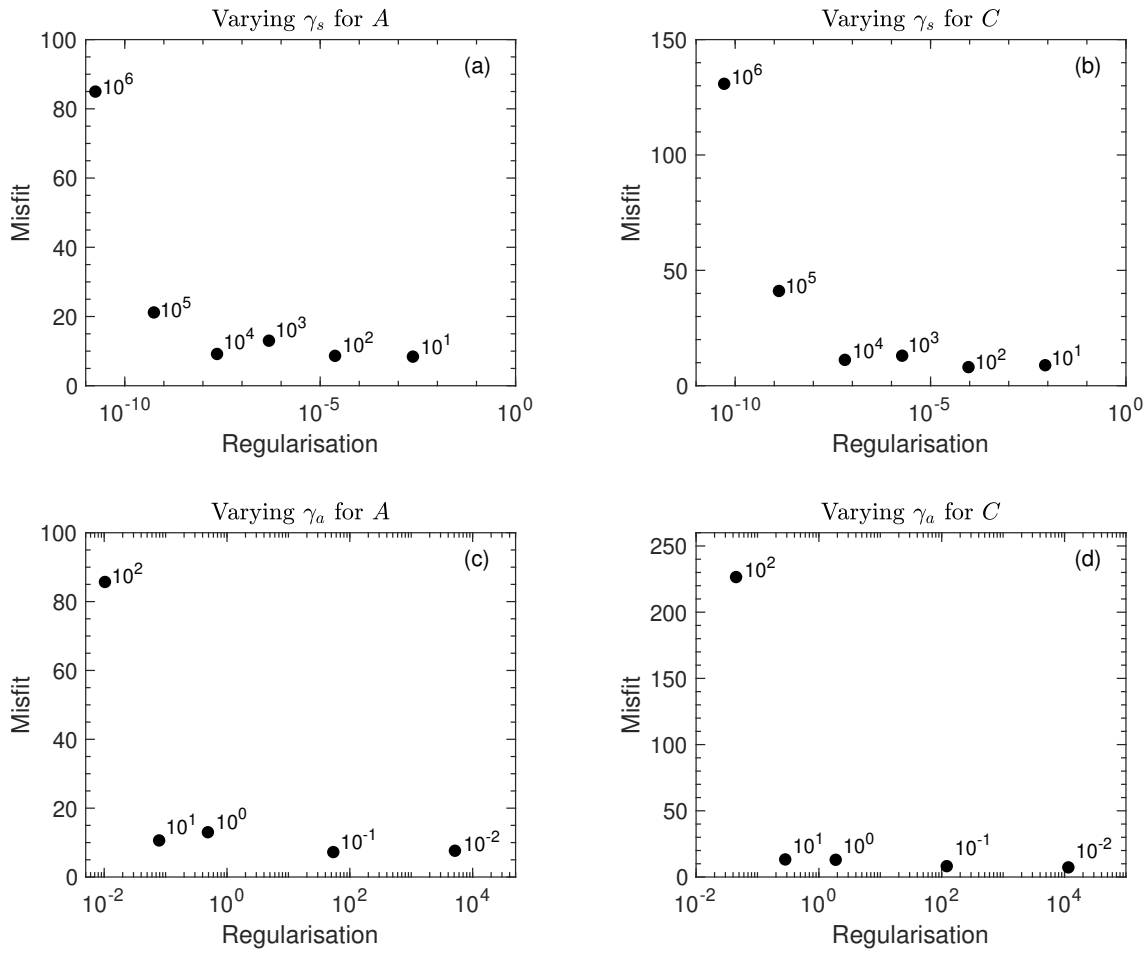

Figure 4.3: L-curves used to determine the amount of regularisation to apply in the optimisation of the A and C fields. Panel **(a)** is the misfit term (I in Eq. 5.1) plotted as a function of the regularisation applied (R (from Eq. 3.19) divided by γ_{sA}^2), whilst varying γ_{sA} (value indicated by label) with $\gamma_{sC} = 1000$ and $\gamma_{aA/C} = 1000$. Panel **(b)** is the misfit term plotted as a function of R/γ_{sC}^2 whilst varying γ_{sC}, with $\gamma_{sA} = 1$ and $\gamma_{aA/C} = 1000$. Panel **(c)** is the misfit term plotted as a function of R/γ_{aA}^2 whilst varying γ_{aA}, with $\gamma_{aC} = 1$ and $\gamma_{sA/C} = 1000$. Panel **(d)** is the misfit term plotted as a function of R/γ_{aC}^2 whilst varying γ_{aC}, with $\gamma_{aA} = 1$ and $\gamma_{sA/C} = 1000$.

glaciers. Higher values are also seen in regions where rifts are located (e.g. upstream of the Gipps Ice Rise, and at the location of the rift that eventually formed the A68 iceberg).

4.2.4 Calving experiments

From the initial conditions derived from the initialisation procedure, the geometry of the ice shelf was perturbed whilst holding all other parameters constant, generating a new stress field. This yielded an instantaneous change in the modelled ice velocity, which we compared to the initial velocity field and from which we calculated changes in GLF.

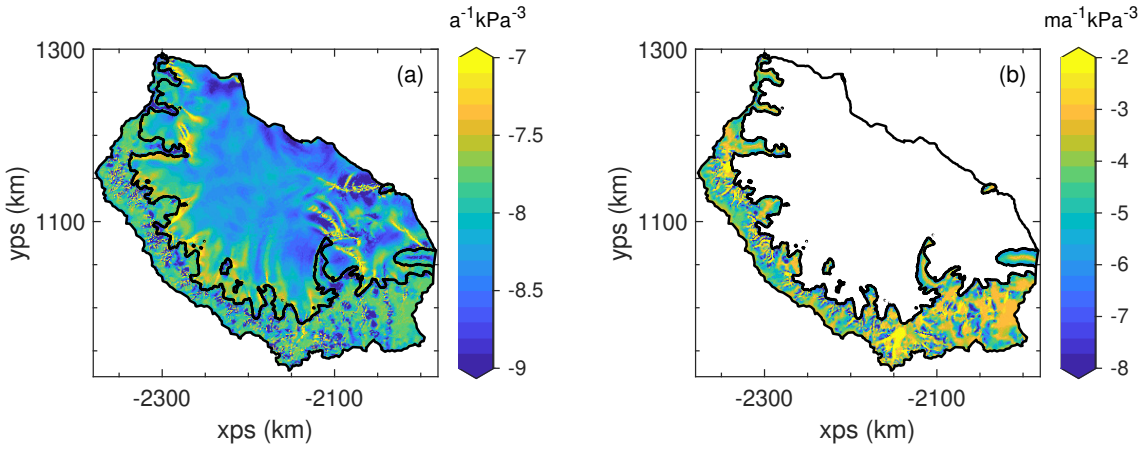

Figure 4.4: Maps of **(a)** the rate factor, A, in Glen's flow law (Eq. 3.5) and **(b)** the basal slipperiness, C, in the Weertman sliding law (Eq. 3.11) after optimisation as set out in Sect. 4.2.3. The colour bars have been saturated to allow the spatial detail in both parameters to be clearly seen.

The first experiment undertaken was to replicate the calving of the A68 iceberg, the extent of which was derived from Landsat 8 images. To perform the experiment, the mesh elements within the region that calved were removed, thereby relocating the model boundary to the new calving front. Through this procedure, the remaining elements of the mesh were left unchanged and any interpolation errors avoided.

In addition to the A68 calving event, a series of idealised calving experiments were conducted. The calving front was moved progressively nearer to the GL by removing mesh elements using a 'distance from the main grounding line' metric (mapped in Fig. 4.6c).

It is important to note that in these calving experiments (and indeed in all experiments in this study) no perturbation was applied to the nodal values of any element which crossed the main GL. This meant that there was no change in driving stresses across the GL, and that the GL location remained fixed in all experiments. This ensured that any change in GLF was due solely to changes in the buttressing provided by the ice shelf.

4.2.5 Ungrounding and thinning experiments

To simulate the ungrounding of the LCIS from the Bawden and Gipps ice rises, the bed topography was lowered so that the ice shelf became afloat without changing the ice thickness. A surface expression of the ice rise remains in the regions of the ice rises where the ice is thicker than the surrounding ice shelf, even after it begins to float. This experiment was carried out for the

ungrounding from the two ice rises individually, and then for a 'combined' ungrounding, in which both contacts were removed simultaneously.

Finally, we explored the GLF response to perturbations in ice thickness. The ice thickness at nodes belonging to elements that were fully afloat (again, to ensure no change in driving stress across the GL) was progressively reduced until the whole ice shelf had a thickness of only 1 m. The 1 m thin layer of ice across the shelf was maintained for computational reasons, and the results are insensitive to a further reduction in the minimum ice thickness. The ice thickness at ice rises within the ice shelf was not changed, and they therefore remain grounded. Locally, this thinning was done both proportionally (i.e. the ice thickness was reduced by a given fraction of the total thickness at each node) and uniformly, where thickness was reduced across the whole ice shelf by the same fixed amount. The subsequent changes in ice velocity and GLF were calculated for each step in the series of experiments.

4.3 Results

We first present the results of the A68 iceberg calving experiment before showing the changes in GLF in response to the idealised calving experiments. We then examine the ice flow response to the ungrounding of the Bawden and Gipps ice rises, before presenting the results of the ice-shelf thinning perturbations as outlined in the previous section. As previously stated, all of the modelling experiments conducted in this study are diagnostic (or time-independent) and therefore the changes in ice flow and GLF presented here are instantaneous changes.

4.3.1 A68 calving

In response to the removal of the A68 iceberg from the model domain, there was an instantaneous increase in ice velocity immediately upstream of the new calving front of up to $\sim$ 100 ma^{-1} (Fig. 4.5a). The spatial extent of this velocity response was limited, and across almost all of the ice shelf the change in velocity was smaller than 10% – even becoming negative in the region of the shelf to the north of the Gipps Ice Rise. The changes in velocity did not extend throughout the whole ice shelf, and as such there was almost no modelled increase in GLF (0.28%) due to this calving event.

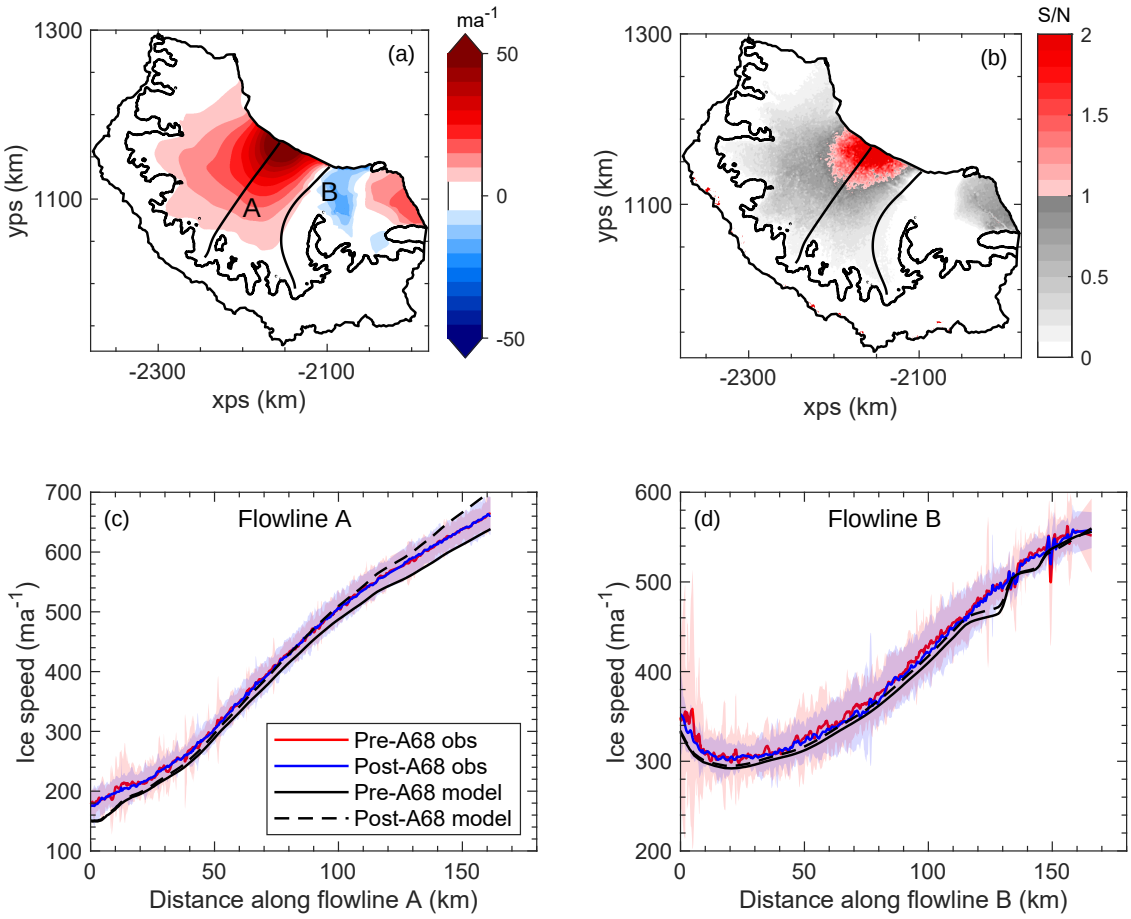

Figure 4.5: The modelled change in ice speed due to the calving of the A68 iceberg **(a)** along with the paths of the two flowlines used. Panel **(b)** is the ratio of the 'signal' (model response in panel (a)) to the 'noise' (2σ variability in the monthly observations of ice velocity). Panels **(c)** and **(d)** show the modelled ice speed before and after the calving event along two flowlines in the shelf. The mean observed speed before and after July 2017, together with shading representing the 2σ variability, is also plotted.

We compared our model results to ice velocity observations produced and provided by ENVEO from analysis of Sentinel-1 SAR data. From this monthly time series of ice velocity maps, we calculated the mean and standard deviation in ice velocity at each point in the model domain for both the October 2014 - June 2017 (pre-A68) and August 2017 - September 2019 (post-A68) periods (Fig. 4.5).

By plotting the ratio of 'signal' (the modelled response to A68 calving) to 'noise' (2σ variation in observations) in Fig. 4.5b, and examining the data along two flowlines on the shelf (Fig. 4.5 c and d), we see that the modelled response largely falls within the internal variability in the ice velocity in the shelf. We also see that the mean ice velocities before and after the A68 calving event

are nearly identical, demonstrating that during this 5-year measurement window there has been no observable change in ice velocity and no transient or sustained response to the calving of the A68 iceberg.

4.3.2 Idealised calving experiments

The impact of moving the calving front progressively closer to the GL on the GLF can be seen in Fig. 4.6a and b. It shows that a retreat of the calving front from its present-day position back into the embayment produced a limited instantaneous impact on the GLF. The calving front had to be retreated to 40 km from the GL to induce a 10% increase in GLF. For a doubling of GLF, the calving front had to be positioned 5 km from the grounding line, removing almost all of the ice shelf in the process.

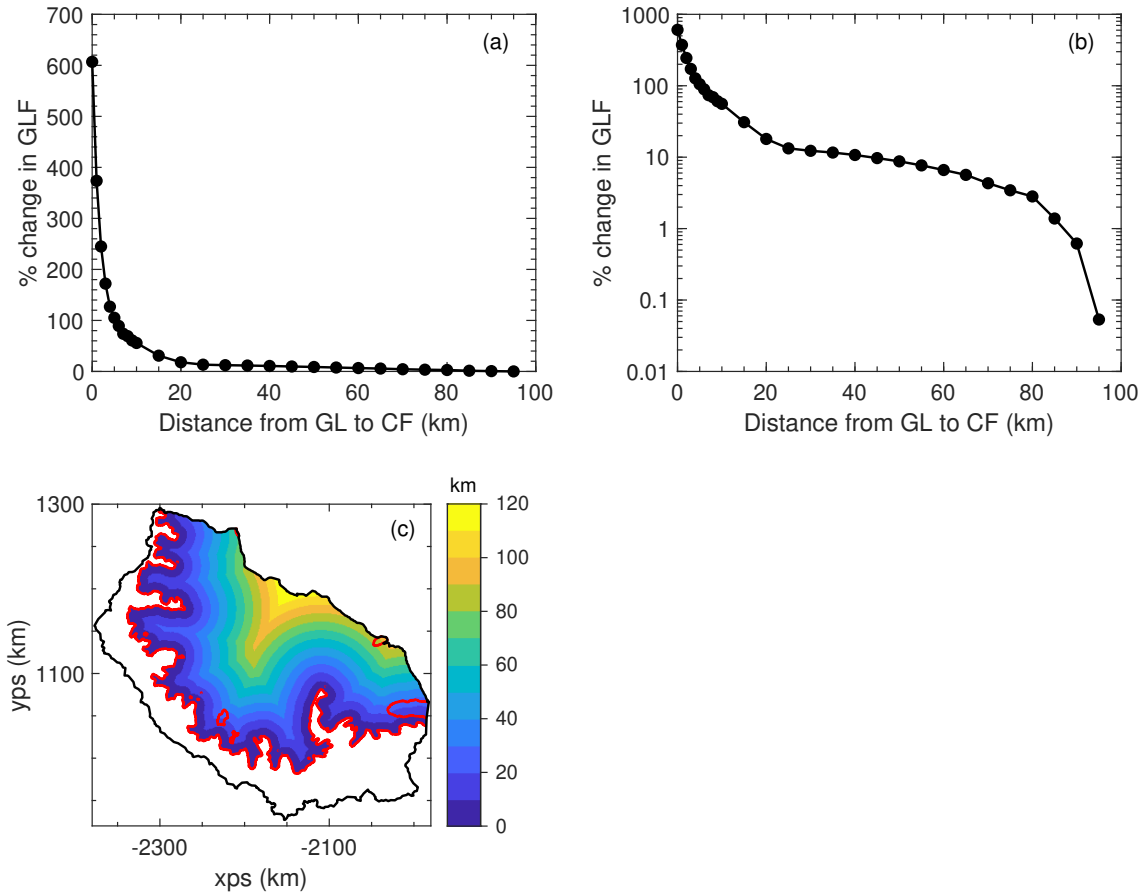

Figure 4.6: Calving experiments: **(a)** is the percentage change in grounding line flux for the each idealised calving experiment, and **(b)** shows the same data, but with a log scale on the y axis. A map of the 'distance to the main grounding line' metric, used to define the calving experiments, is shown in **(c)**, where the red line is the grounding line and the black line the boundary of the model domain.

The maximum GLF increase (607%) – from the complete removal of the ice shelf – can be thought of as representing the total buttressing provided by the LCIS in its current configuration to its grounded tributary glaciers. By comparing the instantaneous increase in GLF for each idealised calving experiment to the maximum GLF increase from complete ice-shelf removal, we are able to calculate the proportion of the total buttressing that remains after each perturbation experiment. Therefore, Fig. 4.6a and b show what proportion of the total buttressing is provided by each section of the ice shelf removed in the series of calving perturbations. From this, we see that over 95% of the total buttressing is provided by ice in the first 25 km downstream of the GL, and that over 80% is generated in the first 5 km of ice immediately downstream of the GL.

4.3.3 Ungrounding experiments

In the modelled response to the ungrounding of the LCIS from the Bawden Ice Rise there was a significant local instantaneous increase in velocity upstream of the ice rise (Fig. 4.7a) of ~ 200 ma^{-1} (and an even greater increase for the ice that was previously grounded). This represents a $\sim 50\%$ increase in ice velocity in this region. However, as with the A68 calving, this instantaneous velocity response is spatially limited and there is a just a 1% increase in GLF from this perturbation.

A similar, localised response in ice velocity is seen when the Gipps Ice Rise contact is removed (Fig. 4.7b), and a similar instantaneous increase in GLF (1.2%) is modelled. Figure 4.7c shows the ice velocity response to the simultaneous loss of contact from both ice rises, which produced an increase in velocity across the whole ice shelf. In Fig. 4.7d we show the difference between the combined ungrounding event and the sum of the two individual events. It shows that the combined ungrounding is approximately a linear superposition of the two individual events, and the corresponding change in GLF from the combined event is 2.2%. These experiments show us that the two ice rises provide a very small proportion of the total buttressing of the LCIS, but cannot tell us about the transient mass redistribution in response to the loss of basal contact at these locations.

4.3.4 Thinning experiments

The changes in GLF due to perturbations in the ice-shelf thickness are shown in Fig. 4.8 (the two different approaches to applying ice-shelf thinning are set out in Section 4.2.5). When thinning the

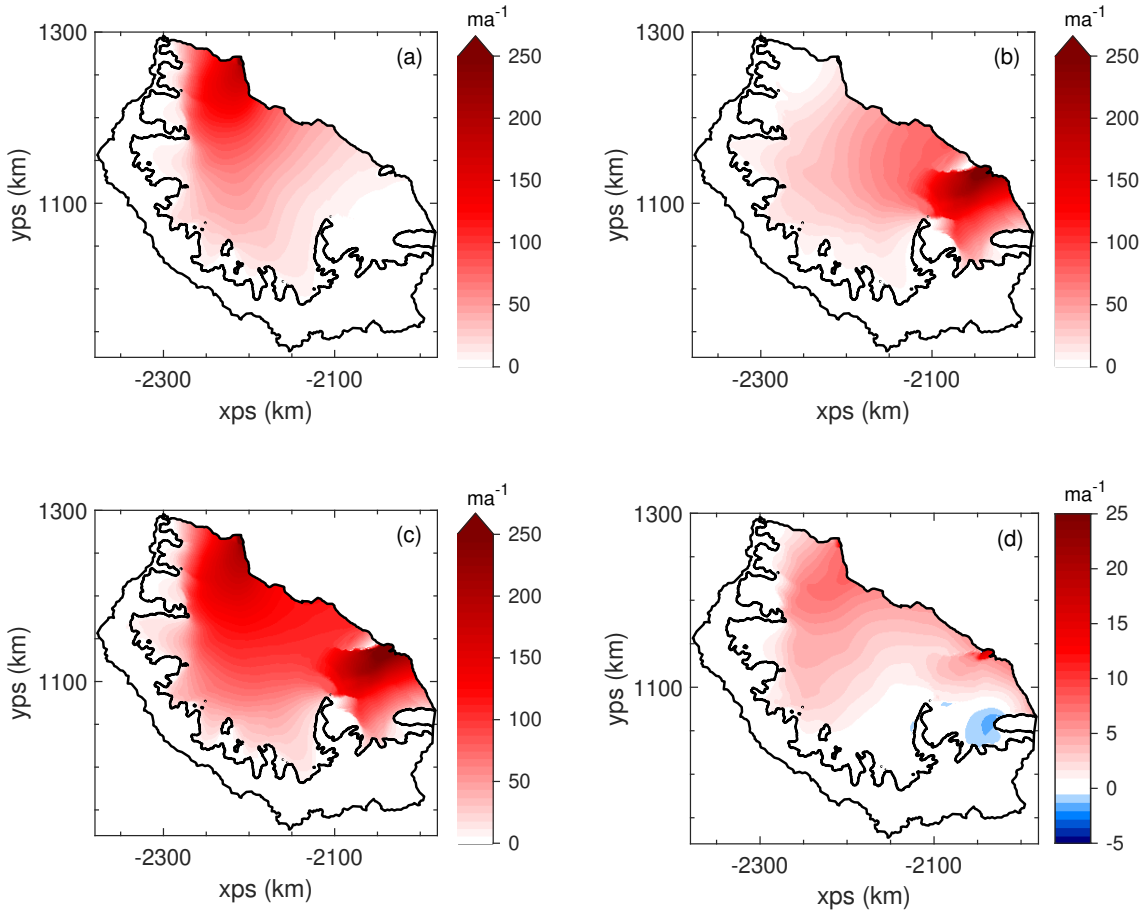

Figure 4.7: Ungrounding experiments: the change in modelled ice speed after ungrounding at the Bawden ice rise **(a)**, the Gipps Ice Rise **(b)** and at both ice rises simultaneously **(c)**. The difference between the combined ungrounding and the sum of the two individual ungrounding experiments is shown in **(d)**. Note the different scale of the colour bar in **(d)**, compared to those for panels **(a)**-**(c)**.

ice shelf in the 'uniform' sense (Fig. 4.8a) we find that $\sim$ 30 m of ice-shelf thinning is required to produce a 10% increase in GLF and that over 200 m of thinning is required to produce a doubling of GLF. 200 m of 'uniform' ice-shelf thinning removes 9,050 Gt of ice from the LCIS. The equivalent idealised calving experiment – in terms of ice mass removed – positions the calving front 15 km downstream from the GL, which only increased the GLF by around 30% (that calving experiment removed 9,350 Gt of ice from the shelf).

The initial ice thickness across the model domain is shown in Fig. 4.8d. The maximum ice thickness at a computational node in the shelf was 1,489 m. Therefore, by applying a thinning perturbation larger than this (of 1,500 m) the ice shelf was reduced to the minimum thickness of 1 m everywhere after an algorithm in the model ensured that the minimum ice thickness was present

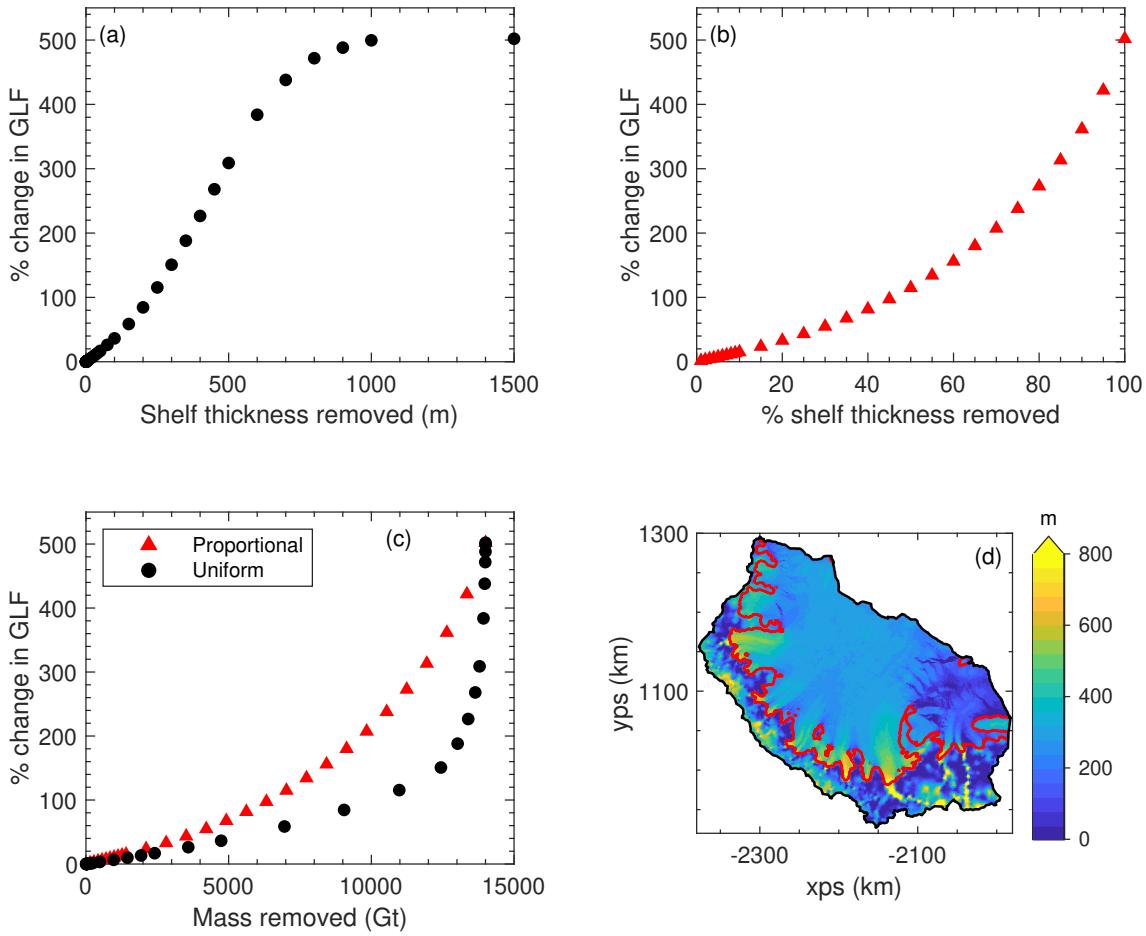

Figure 4.8: Panel **(a)** is the percentage change in grounding line flux during the 'uniform' thinning experiments, and **(b)** is the same but for the 'proportional' thinning experiments. Panel **(c)** is the response in grounding line flux for the two sets of experiments, but with the perturbations expressed in the amount of mass removed rather than the amount of thinning applied. Panel **(d)** shows a map of ice thickness across the model domain from BedMachine Antarctica v2 (Morlighem et al., 2020), with grounding lines plotted in red.

everywhere in the model domain. However, in its initial state, the median ice-shelf thickness was 290 m, 89% of the ice shelf had a thickness of less than 500 m and 99% had a thickness of less than 800 m. Therefore, the gradient of the curve in Fig. 4.8a decreases after $\sim$ 500 m of applied thinning as areas of the shelf already at the minimum thickness are not affected by further increases in perturbation amplitude.

Fig. 4.8b shows the response in GLF to the 'proportional' thinning experiments. Here, 7% of the ice-shelf thickness needed to be removed to produce a 10% increase in GLF, and 45% removed to produce a doubling of GLF.

By calculating the ice-shelf mass removed in each experiment we were able to compare the two

approaches (Fig. 4.8c). We see from the 'uniform' experiment curve, that there is a large response in GLF to a small change in mass removed towards the end of the series of perturbations, when the thickest ice is being significantly perturbed. The maximum GLF increase of 502% is identical in both the 'uniform' 1,500 m thinning and the 'proportional' 100% thinning experiments, as expected. The initial linear regimes in both sets of thinning perturbations are discussed in the following section.

4.3.4.1 Linearity of the GLF response to thinning

Fig. 4.9 focuses on the GLF response to smaller 'uniform' ice-shelf thickness perturbations. Over the first $\sim$ 100 m of applied thinning, the response in GLF is approximately linear, with a 0.36% increase in GLF for every 1 m of ice-shelf thickness removed. For the 'proportional' perturbations (Fig. 4.10) there is also an initial linear regime which extends to a 10% thinning of the shelf. In this regime there is a 1.4% increase in GLF for every 1% reduction in ice-shelf thickness.

For the 'uniform' perturbations, initially the deviation from an exact linear response is below the straight line plotted through the origin and the 0.1 m thinning point. This suggests that increasing thickness perturbations produce a relatively smaller increase in GLF when uniform thinning is applied. However, Fig 4.10 shows that when the shelf is thinned in proportion to the total ice-shelf thickness at each node, this behaviour is suppressed, and the relative response in GLF steadily increases as the proportion of the ice-shelf thickness removed increases.

The way in which the GLF response to thinning deviates below the initial linear regime is an interesting phenomenon that has yet to be explained, but has been observed in previous studies on other ice shelves (e.g. Fig. S2 in Reese et al. (2018b)). It suggests that when a uniform perturbation to ice-shelf thickness is applied across a shelf, over a certain range of perturbation size (here $\sim 1 - 50$ m), the relative increase in GLF is progressively reduced. From the lack of evidence of this behaviour in the proportional thinning experiments, we can see that this is related to the distribution of the thickness perturbation across the shelf, and the cause of this is still unknown.

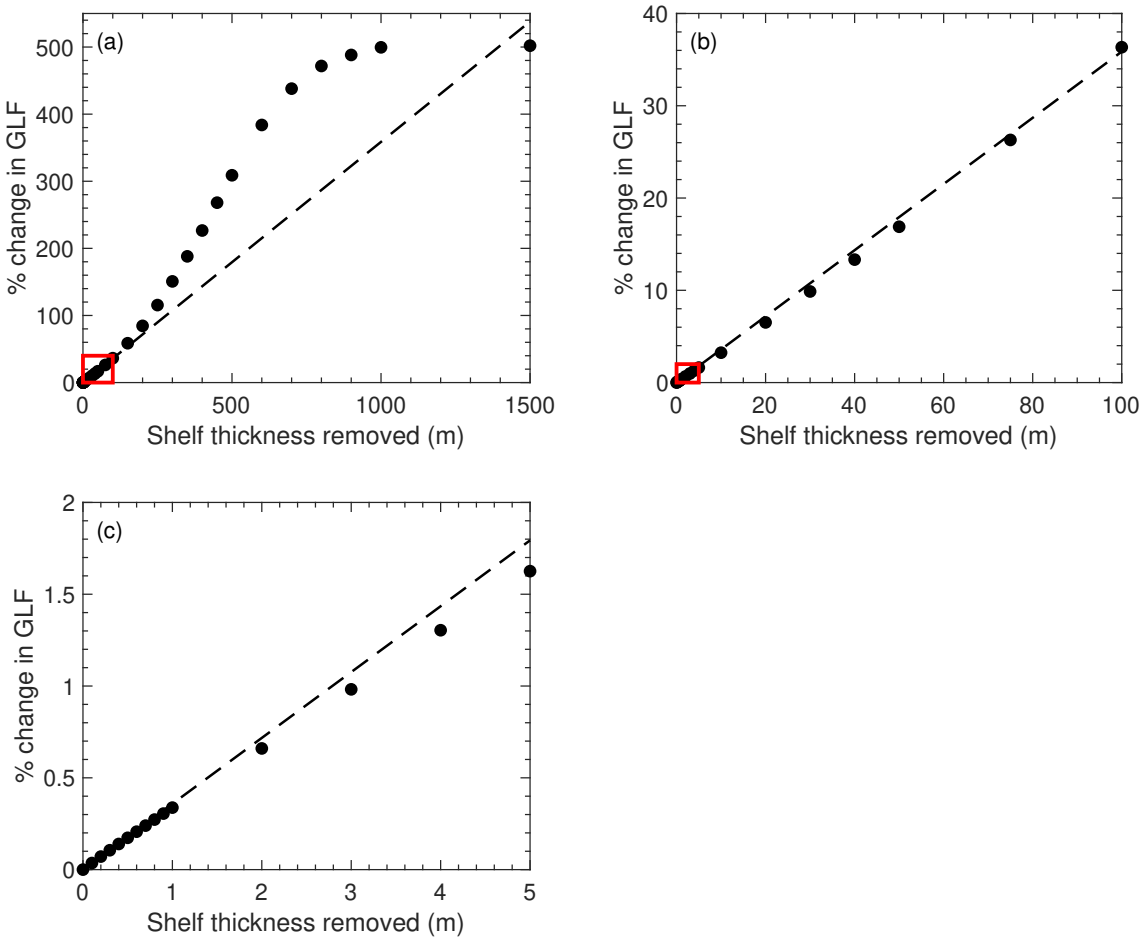

Figure 4.9: The percentage change in grounding line flux is plotted as a function of the 'uniform' thickness perturbation applied **(a)**. The dashed line is the straight line that passes through the origin and the 0.1 m 'uniform' thinning point. Panel **(b)** is the region shown in the red box in panel (a), and **(c)** is the region in the red box in (b).

4.3.5 Sensitivity testing

4.3.5.1 Mesh resolution dependence

To test the dependence of our results on mesh resolution, we repeated all of the experiments outlined in Sects. 4.2.4 and 4.2.5 with four additional computational meshes. In each case, the resolution around the GL was held constant at 250 m. This was to ensure that the calving and thinning experiments conducted with each mesh had the same physical extent – as a coarser resolution at the GL would mean that the calving experiments would not penetrate as close to the GL, and ice-shelf thinning would also not be applied as close to the GL.

The four additional meshes multiplied the original mesh resolution factors (as outlined in Sect.

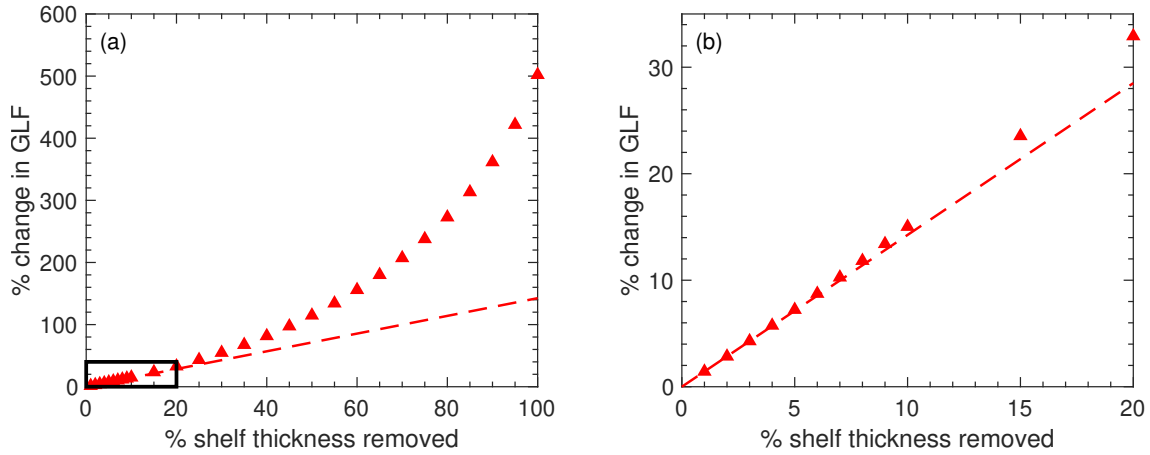

Figure 4.10: The percentage change in grounding line flux is plotted as a function of the 'proportional' thickness perturbation applied **(a)**. The dashed line is the straight line that passes through the origin and the 1% 'proportional' thinning point. Panel **(b)** is the region shown in the black box in panel (a).

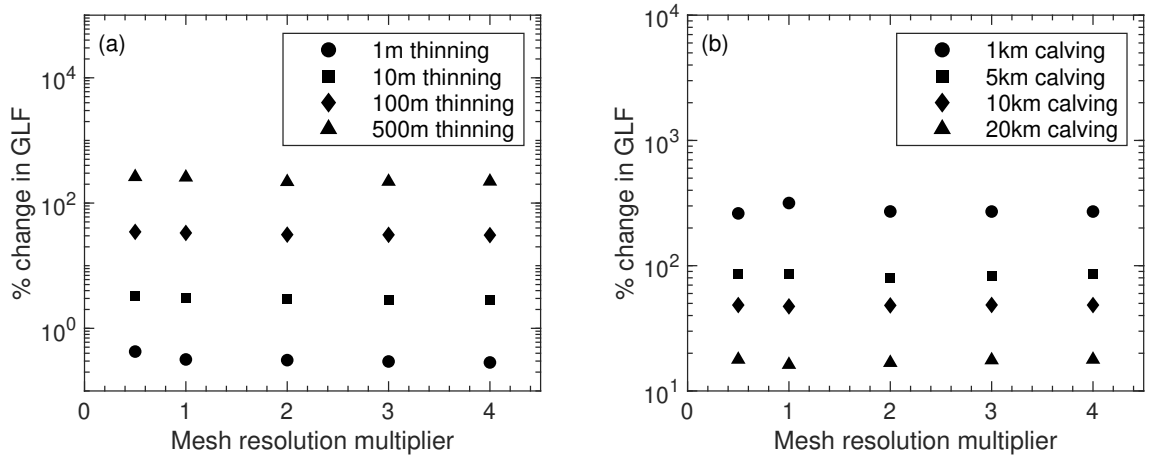

Figure 4.11: Mesh convergence analysis: Hhere, the percentage change in grounding line flux for five of the uniform thinning experiments **(a)** and five of the idealised calving experiments **(b)** is plotted for meshes in which the element sizes were half, double, triple and quadruple the size of the original mesh used for analysis in the main text.

2 based on ice velocities, strain rates and whether or not the element was afloat) by 0.5, 2, 3 and 4 respectively. The results of 10 experiments (5 calving and 5 uniform thinning) with the 5 different meshes are shown in Fig. 4.11. From this we can see that the response in GLF is consistent across the 5 different mesh resolutions for each experiment, and therefore any mesh dependence of our results is negligible.

4.3.5.2 Comparing constant- and variable-ice-density approaches

In the results presented thus far in this study, a horizontally spatially variable ice density was used, which is shown in Fig. 4.12. But many ice flow models do not account for spatial gradients in ice density and instead use a constant value, typically of 917 kgm^{-3}. Here, we test the sensitivity of our findings to this different definition of ice density by performing the A68 iceberg calving and the idealised calving experiments with a model set-up that uses a constant, depth-integrated ice density of 917 kgm^{-3} across the whole computational domain.

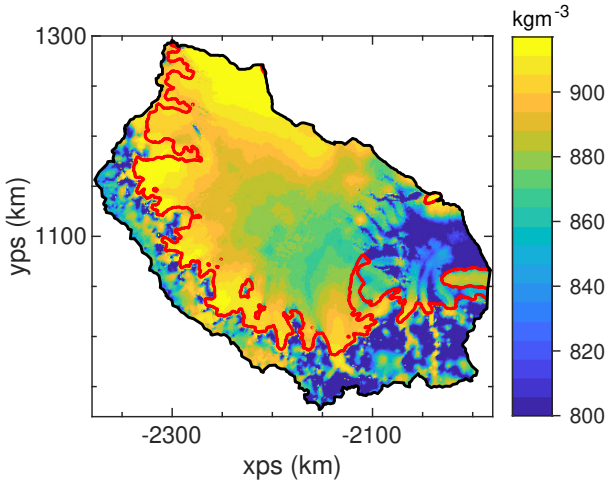

Figure 4.12: A map of the depth-integrated, spatially variable ice density (with a minimum ice density of 800 kgm^{-3}) as used in the main experiments in this study. The red line shows the grounding line and the black line the boundary of the model domain.

To set-up the model in this way, we again took the ice thickness from the BedMachine data set, but no longer applied the correction to the upper ice surface to account for the firn air content. Therefore, in the set-up with a constant ice density of 917 kgm^{-3}, the ice surface is lower than in our variable-ice-density experiments. However, the total mass of ice is the same in each case.

We then generated a new computational mesh with the same definitions of element size as outlined for the main experiments (in Section 4.2.2). We then performed a new optimisation procedure to generate A and C fields for this constant-ice-density set-up, again using the same regularisation parameter choices as for the variable-ice-density set-up. From this new initial condition with a constant ice density, we repeated the A68 iceberg calving and idealised calving front retreat experiments as set out in Sect. 4.2.4. The results of these experiments are shown in Fig. 4.13. We can see that the impact of using a constant ice density compared with a spatially variable ice

density is minimal for both small and large perturbations to the system and that our conclusions are not changed depending on which approach is taken. The largest differences in the modelled response to the A68 calving between the constant- and variable-ice-density experiments, as shown in Fig. 4.13b, are in the regions of the ice shelf that have the lowest ice density in the variable set-up (see Fig. 4.12), and therefore have the largest contrast with the density of 917 kgm^{-3} used in the constant-density set-up.

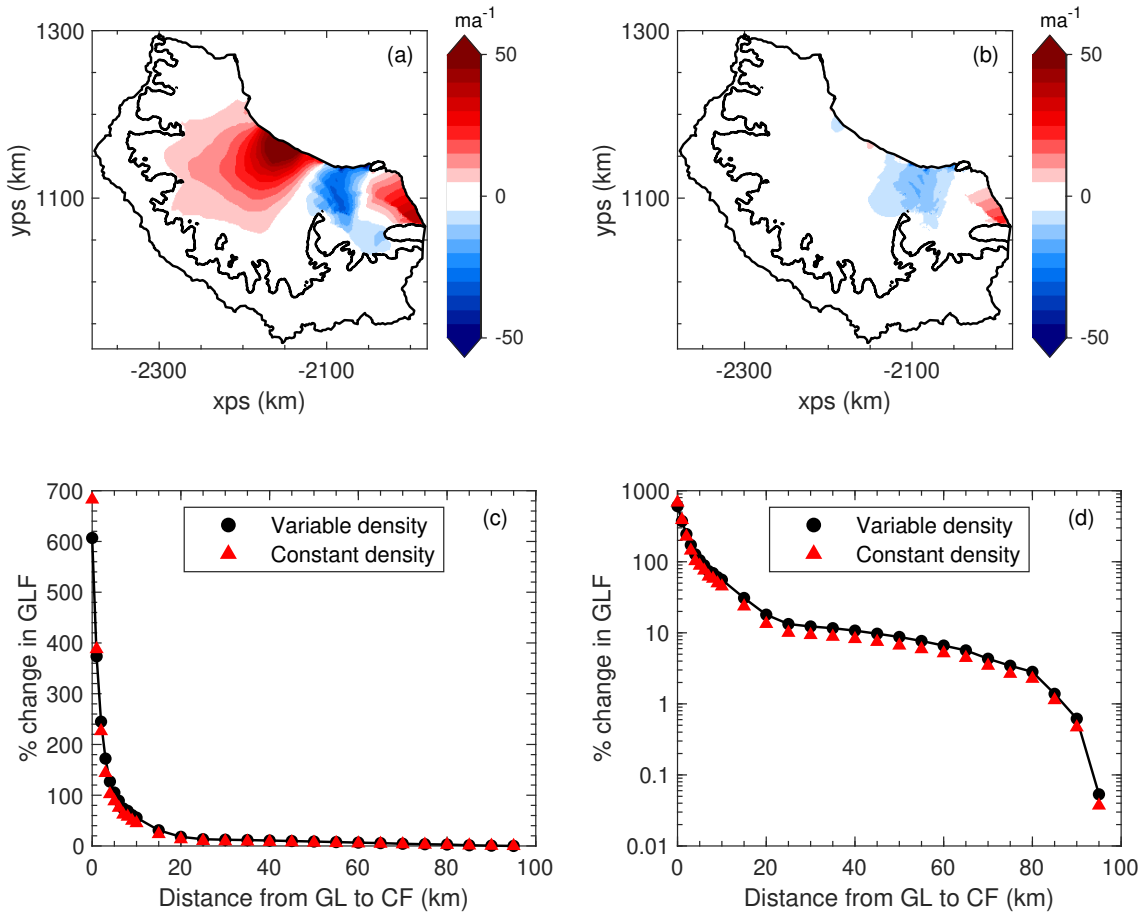

Figure 4.13: The results of calving experiments using a constant ice density of 917 kgm^{-3}. Panel **(a)** shows the modelled response to the calving of the A68 iceberg using the constant-density set-up, whilst **(b)** shows the difference between the constant-ice-density response and the variable-ice-density response to the A68 calving. Panels **(c)** and **(d)** show the instantaneous grounding line flux response to the idealised calving experiments for the variable-ice-density set-up (black; the same data as in Fig. 4.6a and b) and the constant-ice-density set-up (red).

4.3.5.3 Sensitivity to the sliding law stress exponent

The impact of different stress exponents (m values) in the Weertman sliding law (Eq. 3.11) on the response to perturbations in ice-shelf buttressing was also tested. In these experiments, we used the same computational mesh as in the main experiments, but performed new optimisation procedures to generate A and C fields that were consistent with the different versions of the sliding law being used. The range of m values tested was from $m = 1$ (a linear version of the Weertman law) to $m = 7$, a more highly non-linear version of the sliding law than the default of $m = 3$ used in our main experiments. From each of these initial conditions, we performed some of the idealised calving experiments (moving the calving front to 1, 5, 10 and 20 km downstream of the main grounding line) and calculated the instantaneous change in GLF for each of the sliding law variations. The results of these experiments are shown in Fig. 4.14.

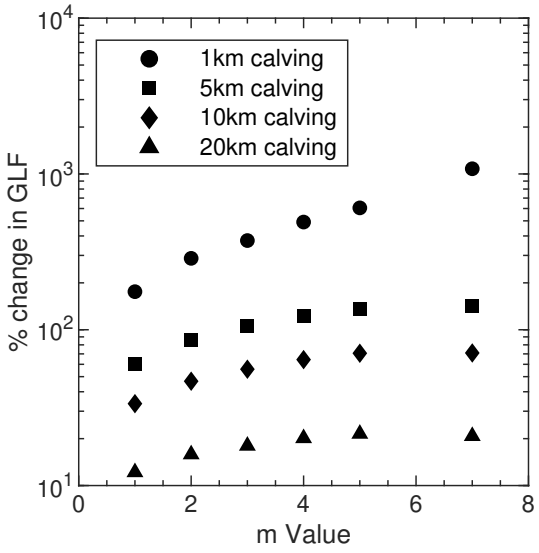

Figure 4.14: The instantaneous increase in grounding line flux for four of the idealised calving experiments, plotted as a function of the different stress exponents (m values) tested in the Weertman sliding law (Eq. 3.11). The four calving experiments are those in which the calving front was moved to 1, 5, 10 and 20km downstream of the main grounding line, as described in Sect. 4.2.4.

The pattern of instantaneous GLF increase in response to perturbations across the range of m values tested is similar to that shown in the supplementary material of Gudmundsson et al. (2019) (Fig. S9), with an increasing GLF response to perturbations as m increases. The ice flow model Úa, used here, was also used in that study. Whilst the absolute values of the GLF response to calving perturbations do vary depending on the value chosen for the stress exponent (due to the way in

which this affects the stress balance at the grounding line), the finding that the vast majority of the buttressing capacity of the LCIS is generated in the first few kilometres of ice downstream of the GL remains consistent.

4.4 Discussion

4.4.1 Calving experiments and ice-shelf buttressing

Our first objective was to model the instantaneous response of the LCIS to the calving of the A68 iceberg and compare the results to observations. The limited change in ice-shelf velocities, and lack of change in the GLF suggest that this part of the ice shelf provided almost no buttressing. This finding is in agreement with the work of Fürst et al. (2016), who classified this region as 'passive ice', and with the map of 'buttressing flux response number' that Reese et al. (2018b) produced. Borstad et al. (2017) hypothesised four potential calving events based on the trajectory in which the rift that eventually formed the A68 iceberg was growing, and modelled the response to these events. Their 'Scenario 2' is most similar to the calving event that eventually occurred, and our modelled results are in close agreement with theirs in both spatial pattern and amplitude (see Fig. 2d in Borstad et al. (2017)).

The model results show a decrease in ice velocity following the calving event in the region of the shelf just to the north of the Gipps Ice Rise. This is likely to be an artefact of the method used to perform the experiment. The rift that eventually formed the A68 iceberg had been present in the ice shelf for over a decade, and grew significantly during 2014 and 2016 (Jansen et al., 2015, Borstad et al., 2017). Therefore, the dynamic response to the detaching of the nascent A68 iceberg will have already taken place in this region, and this response is included in the ice velocity data used to initialise our model. Finally, in the model we essentially force the already-detaching iceberg to have contact with ice upstream, inducing an artificial 'pulling' effect on this upstream ice, which is removed when the iceberg is calved from the domain. Evidence of this can be seen in the larger misfit between observed and modelled ice velocities in this region in Fig. 4.2c.

When comparing our result with observations, we found that the modelled response was smaller than the internal variability in the monthly ice velocity data available. Consequently, we were

unable to validate the details in spatial pattern and amplitude of our modelled response. However, the observations do show that the mean ice velocity across the shelf before and after the calving event remained unchanged, or at least smaller than the measurement errors. This demonstrates that the calving of the A68 had little or no dynamic impact on the system, supporting our work and previous work that predicted such a response, or rather lack thereof.

The second aim of this work is to understand the instantaneous response in GLF to the migration of the calving front back towards the GL, and from that learn about the spatial distribution of the buttressing capacity of the ice shelf. Here we found that as the calving front is moved from its pre-A68 location to 25 km from the GL, there is an instantaneous increase of just 13% in GLF. It is only when regions of the shelf within 25 km of the GL are calved that ice in the narrow embayments downstream of the main tributary glaciers is removed, and this is where the increasing response in GLF begins. Calving perturbations up to this point remove more than 50% of the total ice-shelf mass, yet only induce an increase of 13% in the GLF.

Fürst et al. (2016) measured the impact of calving on the ice flux across the new marine ice front, not the GL, and therefore arrived at a different picture of buttressing on the LCIS. In their supplementary material, the impact of the same experiments on ice discharge across the GL was examined, and by that definition it was found that much more of the ice-shelf area was 'passive'. We argue that it is this second definition, the integrated impact of changes in ice-shelf geometry on stresses at the GL and consequently on instantaneous changes in GLF, that is the key measure of the buttressing capacity of ice shelves in their present configurations. This definition is in line with the original view of buttressing as the backstresses produced by an ice shelf that are felt at the grounding line (Thomas, 1979b). This is the approach used in the work of Reese et al. (2018b), Gudmundsson et al. (2019) and Zhang et al. (2020), who focus on the GLF response to ice-shelf perturbations. We find that the regions with the largest 'buttressing flux response number' (Reese et al., 2018b) correspond to the regions providing the majority of the buttressing in our calving experiments. How the system redistributes mass transiently in response to a change in ice-shelf buttressing is an important question, and changes in the geometry in the ice shelf and upstream of the grounding line may impact the longer-term response. This question is explored in Chapter 5 of the thesis. But the diagnostic (time-independent) approach used here is sufficient to reveal the

buttressing capacity of the LCIS. Changes in buttressing produce an instantaneous response in ice velocities, and consequently in the GLF, as they are determined by the current state of stress in the ice.

The previous work of Reese et al. (2018b) and Zhang et al. (2020) measured the response in GLF to small perturbations in ice-shelf geometry, but by removing the entire ice shelf and calculating the instantaneous response in GLF we are able to quantify the total amount of buttressing that the LCIS provides. This allowed us to examine what proportion of the total buttressing capacity is provided by different regions in the ice shelf. We find that over 95% of the buttressing is generated by the ice in the first 25 km downstream of the GL, and that over 80% comes from the first 5 km of ice directly downstream of the GL. The primary reason for this is that the LCIS geometry is characterised by a number of small, narrow embayments where the main tributary glaciers flow into the ice shelf. It is in these regions that the largest resistive stresses are generated, which dominate the buttressing capacity of the shelf as a whole. However, it is not the geometry of the shelf alone that controls the amount of buttressing provided, but the interaction between the length scales over which stresses are transmitted through the ice shelf and the geometry of the shelf, and this interaction is controlled by the ice rheology. Further, idealised experiments could be conducted in which the rheology of the ice shelf is varied whilst the geometry is held constant (and vice versa) to explore the interaction between the two.

Borstad et al. (2013), Fürst et al. (2016), Reese et al. (2018b) and Zhang et al. (2020) find either elevated buttressing numbers or increased sensitivity of the GLF to ice-shelf thickness perturbations in the regions of the ice shelf upstream of the Bawden and Gipps ice rises. However, we find that calving these regions from the ice shelf does not produce a significant change in the GLF. This highlights the different conceptual and methodological approach to assessing ice-shelf buttressing that we use in this study. Whilst the GLF has previously been found to be sensitive to changes in ice-shelf geometry in these regions of the LCIS, we find that they do not contribute a significant amount to the buttressing of the grounded ice when the total buttressing capacity of the shelf as a whole is considered.

4.4.2 Ice-shelf thinning and ungrounding

We also set out to examine the GLF response to ice-shelf thickness perturbations. Figure 4.8a shows that the response in GLF to thinning is approximately linear as a function of the amplitude of the thickness perturbation, as long as the amplitude is less than about 100 m (this is further explored in Sect. 4.3.4.1). For amplitudes larger than about 100 m, the response becomes progressively more non-linear, something that is also very evident when the GLF response is plotted as a function of the ice-shelf mass removed (Fig. 4.8c). Our explanation for this pattern of GLF response is that the thickest ice in the shelf, which is only reduced to the minimum ice thickness of 1 m towards the end of the series of 'uniform' experiments, is located directly downstream of the grounding line, where the largest tributary glaciers feed into the shelf. From our calving experiments, we saw that this is where the majority of the total buttressing capacity of the ice shelf is concentrated, and therefore the largest changes in GLF are seen when these regions of the shelf are thinned significantly.

The maximum increase in GLF due to the thinning experiments does not equal that of the calving experiments (502% vs 607%), as in the thinning experiments a 1 m thick layer of ice remains across the ice shelf. This means that at the new calving front the ice thickness is linearly interpolated between the unperturbed nodes in the computational mesh and the neighbouring nodes with an ice thickness of 1 m. In the calving experiments mesh elements downstream of the new calving front are removed from the computational domain. We attribute the discrepancy between the maximum GLF increases to this difference in the numerical implementation of the calving and thinning experiments, and not to any residual buttressing effect of the 1 m ice layer. The minimum ice thickness is maintained across the computational domain for numerical reasons only, and we performed sensitivity tests to determine the influence of different minimum ice thickness values. We find that increasing the minimum ice thickness to 10 m reduces the maximum GLF response from ice-shelf thinning to 475%, whilst reducing it further to 0.001 m, only increases the maximum GLF response to 505% from the 502% modelled with a 1 m minimum ice thickness.

The instantaneous response to removing the basal contacts at the Bawden and Gipps ice rises has previously been modelled with different methods to ours. Borstad et al. (2013) only modelled the floating ice shelf, and therefore simulated a loss of contact at the ice rises by manually adjusting their inferred ice-viscosity parameter (the equivalent of our rate factor, A). The spatial pattern and

amplitude of the increases in ice-shelf velocities closely match those found in our experiments, and they also found that the increase in ice-shelf velocities did not extend all the way upstream to the grounding line. Fürst et al. (2016) modelled the grounded ice as well as the shelf, and chose to set their basal friction coefficient to zero at the ice rises – removing the basal traction – rather than adjusting the ice or bed geometry. Despite these differences in approach, we found that our results are very similar in both spatial pattern and amplitude to these previous studies. In the experiment in which both ice rises were removed the instantaneous change in GLF was 2.2%. This suggests that, whilst these two ice rises may exert a significant control on the flow of the shelf upstream of the pinning points, they do not exert a strong mechanical control on the ice flux at the GL, and only contribute a small amount to the total buttressing capacity of the shelf, given that their removal only affected the stresses at the GL enough to raise the GLF by 2.2% instantaneously.

The experiments conducted here are highly idealised in nature. We only considered 'uniform' or 'proportional' thinning perturbations to the shelf, and calving front locations were determined by a 'distance to the grounding line' metric. This resulted in some unlikely calving front positions. More realistic calving experiments, using a physically based calving law or metric, could be used to model the response to more plausible ice-shelf configurations. Further to this, idealised experiments could be designed in which the contribution of ice-shelf geometry and ice-shelf thickness to the total buttressing capacity could be unpicked; and similarly, idealised experiments could be designed to compare the contribution of ice rises and lateral shear stresses to the total buttressing capacity of an ice shelf.

Finally, this work only considers the instantaneous response to perturbations in ice-shelf thickness and extent. As changes to buttressing – through changes in the stresses in the ice – are an inherently instantaneous process, this approach is appropriate and sufficient to explore the buttressing capacity of the LCIS in its present state. However, the transient mass redistribution in response to these perturbations, in which the acceleration would induce thinning and grounding line migration, requires further study and a different modelling approach. Of particular interest is whether the instantaneous GLF increases are the peak response to the perturbation, which then attenuates, or whether the GLF response is increased further by the transient evolution of the ice geometry.

4.5 Conclusions

In this study we examine the instantaneous response of the LCIS and its tributaries to both observed and idealised perturbations to the ice-shelf geometry. We found that the calving of the A68 iceberg in July 2017 produced a limited change (mostly $< 10\%$) in ice velocities in the shelf and had almost no instantaneous impact (a 0.28% increase) on the GLF. This finding is supported by observations which show no evidence of a change in velocity due to the calving event, and this furthermore confirms earlier work that suggested that the region that calved was largely 'passive ice'.

Through further, idealised calving experiments we found that a significant retreat of the calving front to 25 km downstream of the GL (removing over 50% of the ice-shelf mass) only produced a 13% instantaneous increase in GLF. Further retreat of the calving front to 5 km from the GL was needed to produce a doubling of GLF. By calculating the total buttressing provided by the LCIS – through modelling the instantaneous increase in GLF due to a complete collapse (607%) – we deduced that over 95% of the buttressing capacity of the LCIS is provided by ice within 25 km of the GL, in the narrow embayments downstream of the main tributary glaciers. We further found that over 80% of the buttressing is generated in the first 5 km of ice downstream of the GL.

We also studied perturbations of increasing size to the thickness of the ice shelf. Here, again, we found that large changes to the geometry of the ice shelf are required to produce significant changes in GLF, with 30 m of thinning across the shelf inducing a 10% increase in GLF and over 200 m of thinning required to produce a doubling of GLF. Finally, we examined the response in ice velocities to the ungrounding of the ice shelf from the Bawden and Gipps ice rises, and found that whilst there are significant local speedups of around 50%, there was a limited instantaneous increase in GLF of 2.2%. This suggests that whilst these pinning points control the local ice-shelf dynamics, they only provide a small amount of the total buttressing of the LCIS. These diagnostic experiments have given us new insight into the total amount of buttressing provided by the LCIS and where in the ice shelf this buttressing is generated. The form of the transient response to these perturbations remains an open question to be explored further, and is the focus of the following chapter in this thesis.

Chapter 5

The transient response of the Larsen C Ice Shelf to changes in buttressing

5.1 Introduction

In the previous chapter, a series of diagnostic experiments were used to perturb the Larsen C Ice Shelf (LCIS) and explore its buttressing capacity. It was determined that the vast majority of the buttressing that the ice shelf provides is generated in the first few kilometres of ice downstream of the main grounding line. The Bawden (BIR) and Gipps (GIR) ice rises – situated at the present-day calving front of the LCIS – were also found to make a negligible contribution to the total buttressing generated by the shelf. However, this diagnostic method was unable to answer questions about the temporal evolution of the ice shelf and its tributary glaciers in response to changes in ice-shelf buttressing. Of particular interest is whether the instantaneous changes in grounding line flux (GLF) found in the previous chapter are maximal, and then decay through time, or whether the transient evolution of the system leads to further increases in GLF (i.e. there is an instability present in the system). In this chapter these questions are explored, and the way in which the LCIS and its tributary glaciers respond transiently to perturbations in ice-shelf buttressing is determined.

Understanding the transient response of ice streams and tributary glaciers to changes in ice-shelf buttressing is crucial to predicting the future behaviour of the Antarctic Ice Sheet (AIS). This topic has therefore received considerable attention from theoretical and idealised approaches (e.g.

Dupont and Alley, 2005, Goldberg et al., 2009, Gudmundsson, 2013), real-world modelling studies (e.g. Favier et al., 2014, Cornford et al., 2015, Schannwell et al., 2018, Martin et al., 2019, Hill et al., 2021) and ice sheet model intercomparison projects (e.g. Pattyn et al., 2013, Cornford et al., 2020, Seroussi et al., 2020, Sun et al., 2020).

Dupont and Alley (2005) modelled the sensitivity of an idealised ice stream to an instantaneous reduction in the buttressing provided by its ice shelf, and found that the largest response occurred at the beginning of their model runs, which then reduced in time as a new steady state was approached. For a glacier with the length, width, thickness and velocity scales of Pine Island Glacier, this translated to a time scale of 41 years for the new state to be reached. As discussed in Sect. 2.3.1, a small perturbation to the state of an ice shelf (i.e. calving front position, ice-shelf thickness, or loss of contact at a pinning point) can cause runaway changes in the GLF, grounding line position and the ice volume above flotation (VAF) when a retrograde bedrock slope is present, due to the marine ice sheet instability (MISI) (e.g. Schoof, 2007). However, in the presence of an ice shelf which provides buttressing, grounding lines situated on retrograde slopes can be stabilised and the onset of MISI cannot be determined by the local bed slope alone (Gudmundsson, 2013). Further to this, Pegler (2018a) and Haseloff and Sergienko (2018) demonstrated the central role that an ice-shelf – providing even a small amount of buttressing – can play in controlling the flux across, and the position of the grounding line of a marine ice sheet. The Antarctic BUttressing Model Intercomparison Project (ABUMIP) (Sun et al., 2020) explored the transient evolution of the whole AIS to the immediate and sustained collapse of all ice shelves. In this way, they were able to explore the impact of removing all ice-shelf buttressing forces from the ice sheet, and found that this leads to multi-metre increases in global mean sea level over the 500 year model run time used in their experiments.

Returning to the LCIS, there has been a focus in recent work on the role of the BIR and GIR in the dynamics of the LCIS and its tributaries. Borstad et al. (2013) examined the stress state in the ice, calculated a local buttressing number in the shelf, and inferred that the BIR plays a strong controlling role in the dynamics of the northern part of the ice shelf. They suggested that the acceleration in ice-shelf velocities induced by the loss of contact in the ice rise could destabilise the shelf and cause a retreat of the calving front. Holland et al. (2015) also considered the loss of

contact at the BIR as a possible source of instability for the LCIS. From their analysis, they gave a conservative estimate of 130 years of melting at the current rate before the ice shelf would lose complete contact at the BIR. Kulessa et al. (2014) introduced the concept of the stress-flow angle – the angle between the first principal stress direction in an ice shelf and the ice velocity vector – to analyse the structural integrity of the LCIS. The validity of this metric for assessing ice-shelf structural integrity is explored further in Chapter 7, but their work suggested that the loss of a stabilising ice rise at the front of the LCIS may lead to a change in the distribution of stress-flow angles in the shelf and therefore a change its structural integrity.

Ice rises have been shown, in certain settings, to have a significant influence on the transient dynamics of an ice shelf-tributary glacier system. Favier and Pattyn (2015) demonstrated in an idealised modelling scenario that the presence of ice rises, or pinning points, can control the rate at which grounding lines migrate in response to ice-shelf perturbations, but noted that they do not control the steady state position of those grounding lines, which is controlled by factors such as the local bedrock topography and the ice-shelf buttressing as a whole. In a realistic setting with the potential for MISI – in Dronning Maud Land, Antarctica – Favier et al. (2016) also showed that the presence of a pinning point can significantly delay the onset of MISI due to the role it plays in controlling ice-shelf velocities and thinning rates.

Only one study has specifically examined the transient mass redistribution of the LCIS in response to ice-shelf perturbations using a model incorporating the necessary membrane stresses in the momentum equations to replicate the effects of ice-shelf buttressing (Schannwell et al., 2018). The transient response of the ice shelf and its tributary glaciers to both ice-shelf calving and complete ice-shelf collapse was explored. Following the complete collapse of the LCIS they found that the resulting mass loss was between 0.5 and 1.5 mm SLE after 100 years, and between 0.6 and 4.2 mm SLE after 300 years. The 7-fold variation in the mass loss they found was due to: using three different models, each with a different approximation to the full Stokes equations and a different numerical implementation; using both Weertman and Coulomb-limited basal sliding laws with a range of stress exponents; and using two different bedrock topography and ice thickness data sets.

Here, the findings from the previous chapter – and from previous studies – are built on by exploring the relationship between changes in ice-shelf buttressing and the subsequent, transient

evolution of the LCIS and its tributaries. First, the changes required to the model set-up and initialisation to perform transient perturbation experiments are outlined. Then, some of the key perturbation experiments from the previous chapter — the calving of the A68 iceberg, the loss of basal contact at the BIR and GIR and the systematic retreat of the calving front towards the grounding line — are repeated and the system is allowed to evolve for 100 years following each perturbation. In each case the changes in ice speed, thickness, VAF and GLF are quantified, allowing for the comparison between the transient and instantaneous response to the perturbations. This provides an insight into the relationship between the separate, but linked processes of ice-shelf buttressing and transient mass redistribution for the LCIS and its tributary glaciers.

5.2 Methods

5.2.1 Model set-up

To model the transient evolution of the shallow-shelf approximation to ice-flow in Úa, the momentum equation (Eq. 3.3) is solved together with the vertically-integrated form of mass conservation (Eq. 3.16), with the necessary boundary conditions, constitutive equation and basal sliding law as outlined in Chapters 3 and 4.

As detailed in Sect. 3.3, Úa uses a fully implicit method to solve the time-dependent system, so the time-step can be chosen independently of the mesh resolution. The value used was varied throughout the model runs, based on an automatic time-stepping algorithm that aimed to have as large a time-step as possible whilst remaining in the second-order convergence radius of the Newton-Raphson solver.

The boundary of the model domain is the same as that used in the previous chapter and plotted in Fig. 4.1. The BedMachine Antarctica v2 (Morlighem et al., 2020) ice thickness, bedrock elevation, ice surface elevation, and firn air content fields are again used to define the initial geometry of the LCIS. These are used to calculate the spatially variable, depth-averaged ice density which is also the same as that used in the previous chapter (and plotted in Fig. 4.12). The treatment of the lateral boundaries of the computational domain in transient simulations is detailed in Section 3.2.3.

One difference made to the model geometry in this chapter is in the bathymetry beneath the ice

shelf. The data used in the BedMachine product for the bathymetry below the LCIS is inherited from a long chain of earlier data sets. Firstly, the bathymetry data is the same as that used in Bedmap2 (Fretwell et al., 2013). In turn, Bedmap2 used a bathymetry product generated by Timmermann et al. (2010), who used data from ALBMAP (Le Brocq et al., 2010) and adjusted it where required to ensure a 10 m water column beneath the ice shelf. For the LCIS, the ALBMAP bathymetry appears to be the same as that in the original BEDMAP product (Lythe and Vaughan, 2001). Timmermann et al. (2010) ensured that the bathymetry conformed to the observed grounding line location, but stated that the "bathymetry in the Larsen C Ice Shelf cavity in our data set is hardly more than an educated guess".

As a result of this process, downstream of the grounding line, the ocean water column depth in the BedMachine data compilation can be less than ten metres in some places. Consequently, any transient thickening in the excess of ten meters can cause grounding and an advance of the grounding line. To prevent this grounding, the bathymetry beneath the ice shelf was manually lowered by 500 m at all model nodes that were strictly downstream of the grounding line (i.e. not belonging to elements that crossed the grounding line). A further justification for this approach is that, in the experiments conducted here, a reduction in ice-shelf buttressing is induced, which is associated with thinning and a retreat of the grounding line rather than advance. Hence, this approach of excavating the bathymetry, whilst not physically motivated, is suitable for the purposes of the experiments in this chapter, and has been used in both the generation of bathymetry data sets and previous modelling studies.

One final difference to the model set-up is in the finite element mesh used. The mesh resolution is similar to that in the previous chapter – with higher resolution in regions of high velocity and strain rates – but the highest resolution at the grounding line is 500 m rather than 250 m. After some initial testing, and from the results of previous work (Schannwell et al., 2018, Sun et al., 2020), it became clear that even under the most extreme perturbation to the ice shelf (a complete collapse), the maximum grounding line retreat was limited to 10-15 km upstream of the initial grounding line. Therefore, it was found that the most computationally efficient way to run the transient simulations was not to use the adaptive mesh refinement capabilities of Úa, but to instead ensure that the initial mesh had the highest resolution (500 m) in the 15 km region upstream of the initial grounding line

– regions through which the grounding line might migrate in the course of a 100 year simulation. This resulted in a finite element mesh with 208,027 elements with a maximum, mean, median and minimum size of 4,214, 741, 480 and 207 m respectively.

5.2.2 Model initialisation

In the previous chapter, observed surface ice velocities were used to optimise both the rate factor and the basal slipperiness parameters through inverse methods (see Sect 4.2.3).

However, there is often a mismatch between the equations used to model ice flow and the observations of surface ice velocity, ice thickness and bedrock topography. These inconsistencies between the equations and the data sets can lead to 'transient' effects at the beginning of a prognostic ice sheet model run. Typically this leads to nonphysically large rates of change in ice thickness (dh/dt) and ice velocity ($d\boldsymbol{u}/dt$) during the first few years of a simulation. One solution to this problem that is often taken in ice sheet modelling studies – a 'relaxation' approach – is to run the model for a set period of time (on the order of years to decades of model time) and allow these transient effects to dampen out before beginning any perturbation experiments. However, by relaxing the ice sheet in this way, the ice surface, thickness and velocity fields can be significantly different from the initial, 'observed' fields defined at the start of the relaxation run. This 'model drift' away from the initial state, in which the location of the grounding line can also move, would have created problems for comparing the results of this chapter against those of Chapter 4, and therefore I decided not to use this approach here.

In initialising the model for the transient experiments in this chapter, I attempted to minimise the impact of these short wavelength, large amplitude signals firstly by including 'observations' of the rate of change of ice thickness into the information used in the optimisation procedure. This feature was recently implemented in Úa and has been used in recently published studies (e.g. De Rydt et al., 2021, Rosier et al., 2021). In addition to fitting modelled ice velocities to observations, modelled rates of ice thickness change (dh/dt) – as calculated from mass conservation (Eq. 3.16) – are also fitted to available observations of dh/dt. Only the ice velocities are allowed to vary in this model initialisation procedure, and the ice thickness field is fixed to the values in the data set used. The

misfit term in the cost function (Eq. 3.18) is therefore updated, and given by

$$I = \frac{1}{2\mathcal{A}} \int \left(\frac{\boldsymbol{u} - \boldsymbol{u_{obs}}}{\boldsymbol{u_{err}}} \right)^2 d\mathcal{A} + \frac{1}{2\mathcal{A}} \int \left(\frac{\dot{h} - \dot{h}_{obs}}{\dot{h}_{err}} \right)^2 d\mathcal{A}, \tag{5.1}$$

where $\dot{h}$ is the modelled rate of change of ice thickness, and $\dot{h}_{obs}$ and $\dot{h}_{err}$ are, respectively, the 'observed' rate of change of ice thickness, and the uncertainty associated with that observation.

In the testing of this capability, to penalise large values of dh/dt, actual observations of dh/dt are not used, but rather the dh/dt 'observations' are set to zero everywhere in the domain to drive the optimisation towards producing a steady initial condition. The associated dh/dt uncertainty variable is then used as weighting factor, to determine whether the observations of ice velocity or dh/dt are given more importance in solving the optimisation problem.

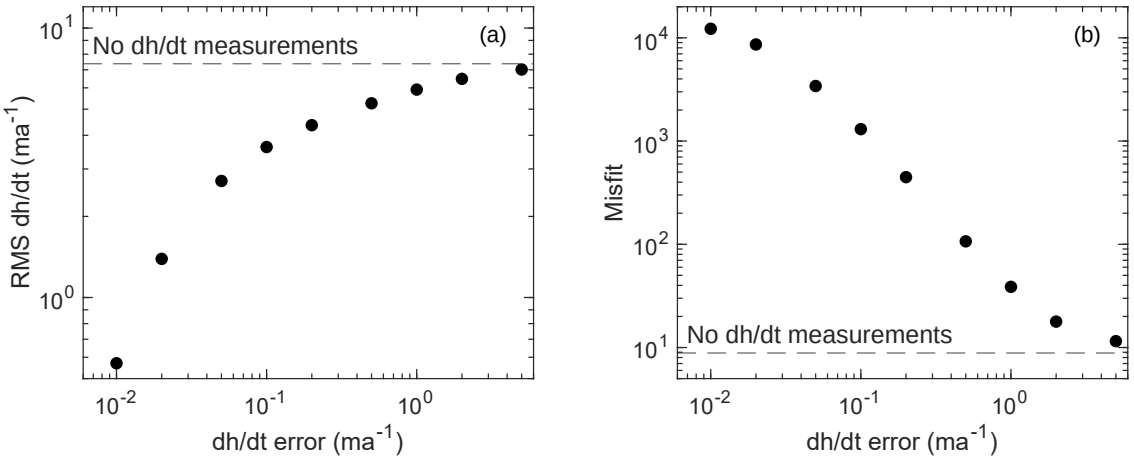

Figure 5.1: **(a)** is the area normalised RMS dh/dt following model initialisation with different weightings given to the dh/dt observations (the smaller the dh/dt error value, the higher the weighting). The dh/dt observations themselves were set to zero across the whole model domain. **(b)** is the value of the misfit term, I (Eq. 5.1) in the cost function at the end of the model initialisation, again as a function of the error value set for the dh/dt observations. The horizontal dashed lines show the RMS dh/dt and misfit function values following initialisation without dh/dt observations. These are the values that were eventually used in the following perturbation experiments.

As shown in Fig. 5.1, attempting to drive down the rates of change in ice thickness means compromising on the fit to observed ice velocities, and hence increasing the overall value of the misfit term (Eq. 5.1). Due to this trade off between fitting velocities or reducing dh/dt, it was decided that this compromise was not required for the set of experiments conducted in this work, and therefore I reverted to using observations of ice velocity alone in the optimisation procedure. This is the same approach that was used in the previous chapter. To generate a steady reference

run with which perturbations could be compared, a 'synthetic mass balance' approach was used instead, and is detailed in the following section.

5.2.3 Synthetic mass balance

In this chapter, the primary scientific question to be answered is how the LCIS and its tributary glaciers respond transiently to a perturbation in the ice-shelf buttressing, not to make projections of the future mass balance of the LCIS and its tributary glaciers under specific climate scenarios.

In order to asses the impact of a perturbation on the system, quantities need to be compared to those in a reference simulation, or a control run. To ensure a steady control run in which key properties such as the grounding line location and VAF do not drift far from the initial state, a 'synthetic mass balance' field is used. It is equal to the ice flux divergence ($\nabla_{xy} \cdot \boldsymbol{q}$) in Eq. 3.16 – with a set to zero – and is calculated after the model has been initialised. The map of the 'synthetic mass balance' field is shown in Fig. 5.2, and when integrated over the model domain is equivalent to a mass balance of $+22.86$ Gt a^{-1} over the grounded regions and -6.08 Gt a^{-1} over the floating ice shelf. The banding apparent in the ice shelf upstream of the GIR – with successive regions of positive and negative mass balance in the flow direction – opposes the advection of the crevasses in this region, and is an artefact of the approach taken here. Applying this field in place of a in Eq. 3.16 minimises the drift of the system from its initial state, although it does result in accumulation and ablation which is nonphysical – with values much larger than those expected from a realistic surface mass balance or basal melt-rate field, and with shorter wavelength variability. As stated earlier, this is required to compensate for the discrepancies between the data sets and equations used for modelling ice flow. This was the approach used in Schannwell et al. (2018) and a similar method has been used in earlier modelling studies (e.g. Cornford et al., 2015, Favier et al., 2016). The synthetic mass balance is applied throughout the control run and all perturbation experiments.

5.2.4 Ice-shelf perturbations

In addition to a control run, a set of experiments are conducted in which a perturbation is made at $t = 0$, after which the model is run for 100 years. The experiments include the replication of the A68 calving experiment, the loss of basal contact at the BIR, the simultaneous loss of basal

contact at both the BIR and GIR, and the systematic retreat of the calving front through idealised calving experiments. In each case, the perturbation is applied with exactly the same methodology as detailed in the previous chapter. In the case of the calving experiments, once the calving front position has been perturbed, the new calving front location remains fixed throughout the 100 year simulation, and does not evolve with the changing position of the grounding line. The GLF values presented throughout the results in this chapter are always calculated on the moving grounding line.

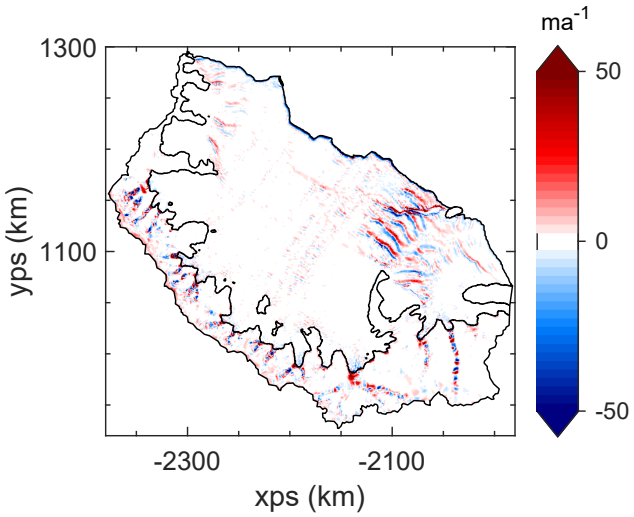

Figure 5.2: A map of the synthetic mass balance field, applied throughout all control and perturbation experiments – in place of a realistic surface mass balance and ice-shelf basal melting field – to obtain a control run that remained close to the initial state.

5.3 Results

In this section, the results of the control run over the 100 year model run are first presented. The results from the removal of the basal contact at the BIR and GIR are then shown, before examining the transient response to the calving of the A68 iceberg. Finally, the transient response to the series of idealised calving experiments is presented. In each case, the change in the GLF, changes in ice shelf and tributary glacier velocities and thickness, grounding line migration, and the changes in VAF (measured as an equivalent change in global mean sea level) are shown. It is important to note that for the perturbation experiments, all quantities are calculated and plotted relative to the control run in each year of the model run.

5.3.1 Control run

Examining the evolution of the control run, shown in Fig. 5.3, the VAF in the model domain remains very close to its initial value, with some small model drift initially promoting ice thickening, followed by thinning in the grounded region. After 100 years, the change in VAF is 0.009 mm SLE, which is a change of just 0.07% on the initial VAF of 12.69 mm SLE. The change in grounding line position is also negligible (there are two grounding lines plotted in Fig. 5.3, at $t = 0$ and $t = 100$ years, but they largely lie on top of one another). This result was manufactured by using the synthetic mass balance approach, which acts to keep the ice geometry close to its initial state.

An interesting feature of the control run is the rapid drop of ~ 3 % in the GLF in the first few years of the simulation. To see this more clearly, the change in VAF and GLF in the first two years of the control run are plotted in Fig. 5.4, with model output taken every 0.02 years (approximately one week). The largest drop in GLF occurs in the first model time-step, which suggests that the cause is a mismatch between the ice thickness and surface velocity data used in the initialisation procedure in key tributary glaciers. Figure 5.3d shows that after the first year, ice velocities at the grounding line have already slowed by 10-20 ma^{-1} in some regions. The drop in GLF remains constant at a value ~ 3 % lower than the initial condition for the remaining run time.

The ice velocities on the ice shelf also adjust at the beginning of the control run. Here, we see that the ice velocity towards the calving front and close to the GIR increases, which again suggests discrepancies between data sets used in the model initialisation process. In this case, as discussed in Sect. 4.2.3, the problem arises from the impact that the detaching of the nascent A68 iceberg had on the surface velocity data set used in the model initialisation. To try and fit the ice thickness data to the enhanced surface velocity in the region beginning to calve, the ice was made anomalously 'soft', with an enhanced rate factor, such that the ice velocity increased in this region during the transient run.

After 100 years, there has been an increase in ice velocity to the north of the ice shelf, upstream of the BIR, of around 10 ma^{-1} (Fig. 5.3f). This is due to a slight reduction in the area of basal contact with the BIR during the control run, even after all attempts to minimise model drift have been made. The map of changes in ice thickness show a modest thinning of the ice shelf towards the calving front, where the ice velocity increase was largest, and also shows the patterning associated

with the advection of crevasses upstream of the GIR.

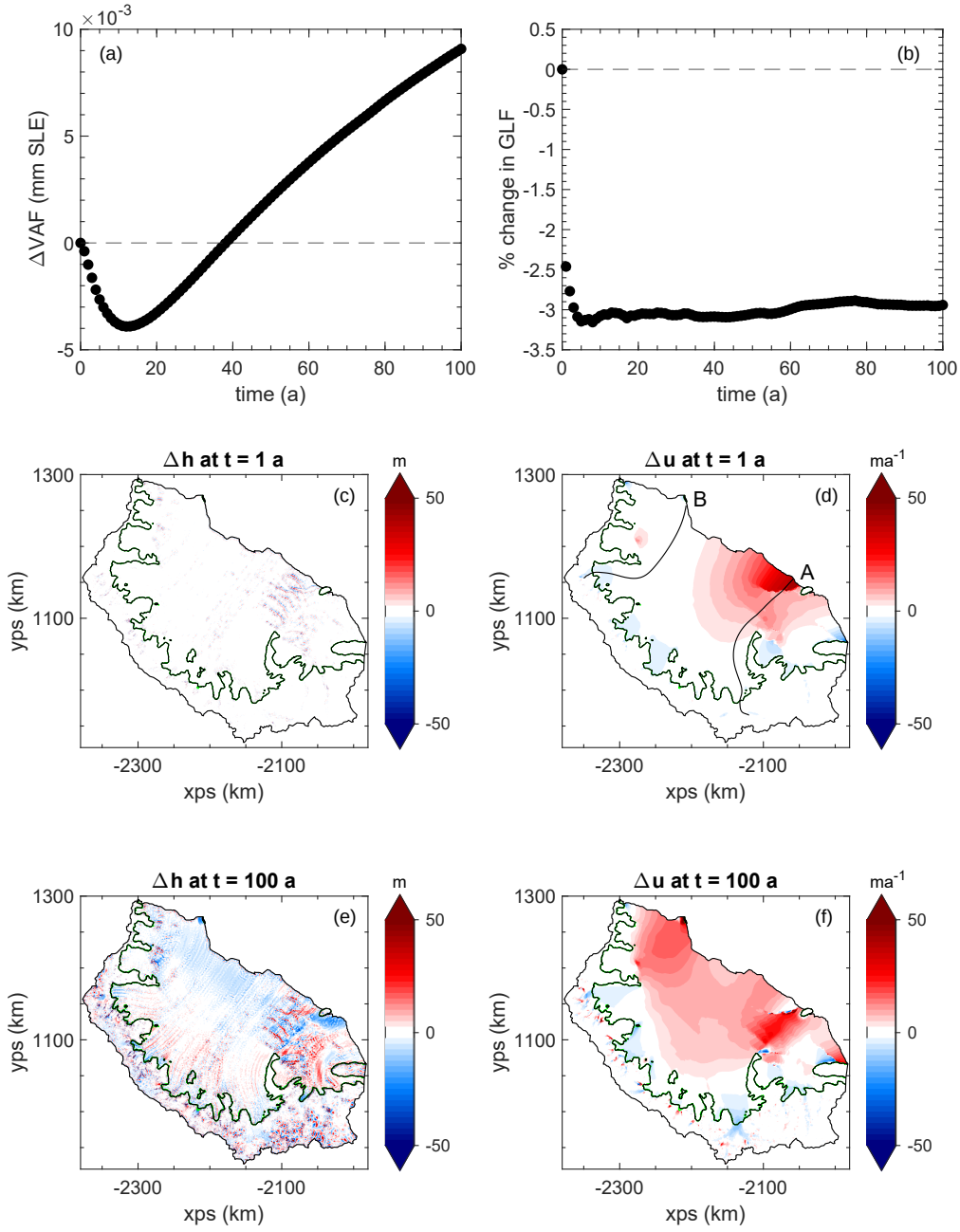

Figure 5.3: Details of the changes in key parameters during the control run. **(a)** shows the change in ice volume above flotation (VAF) expressed as a contribution to global mean seal level rise (positive values indicates ice loss). Note that the units are mm SLE x 10^{-3}. **(b)** is the percentage change in grounding line flux (GLF) during the run. **(c)** and **(d)** show the cumulative changes in ice thickness and ice speed after one year, respectively. The flowlines labelled A and B in **(d)** are used for profile plots in Fig. 5.10. Panels **(e)** and **(f)** show the cumulative changes in these quantities after the full 100 year experiment run time. In panels **(c)-(f)** the black line shows the initial grounding line position and the green line the grounding line position at the stated model time. The green grounding line is not visible due to a lack of change in grounding line position compared to the initial state.

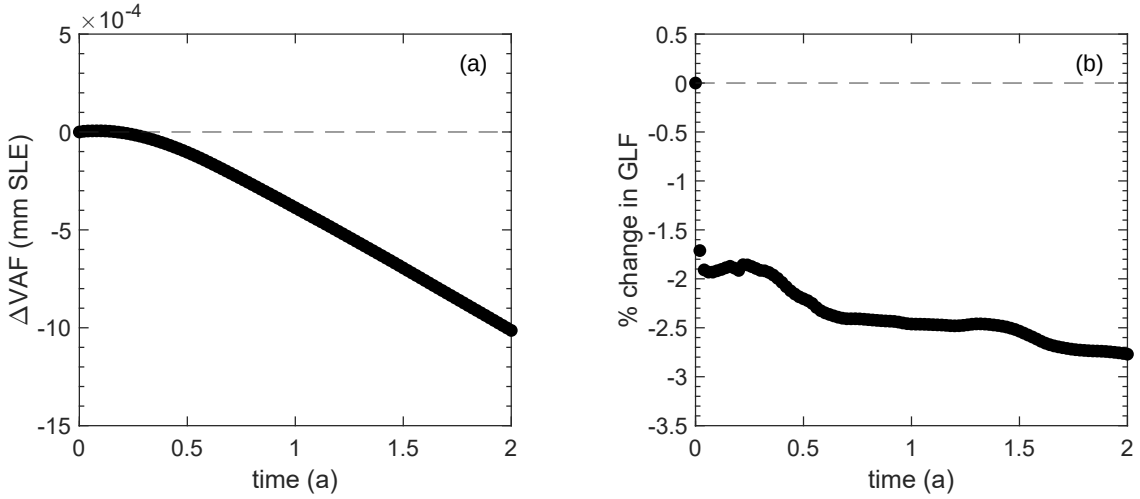

Figure 5.4: The change in VAF **(a)** and the percentage change in GLF **(b)** during the first two years of the control run.

In the following presentation of the results of the perturbation experiments, all of the quantities discussed – VAF, GLF and changes in ice thickness and velocity – are calculated relative to the control run. This removes the impact of the model drift observed in the control run, such that any remaining changes in the system are due to the perturbation applied to the ice shelf.

5.3.2 Ice-rise ungrounding

The first set of perturbations explored were those removing the basal contact at the BIR, and then at the BIR and GIR simultaneously, by lowering the bathymetry at the ice rises by 500 m.

Figure 5.5 shows the transient evolution of the system following the removal of the basal contact at the BIR. The change in ice velocity after one year (Fig. 5.5d) is almost identical to that found in the instantaneous experiments presented in the previous chapter, and in the first year there is almost no change in the ice thickness of the shelf (Fig. 5.5c). Looking to the cumulative changes after 100 years (Fig. 5.5e and f), we see that an increase in ice speed has been maintained in the shelf, although the amplitude of that increase is reduced to below 100 ma^{-1} across most of the shelf. This reduction in speed during the run is due to the thinning of the ice shelf caused by the initial acceleration which produces a reduction in the driving stress in the shelf. The ice-shelf thinning itself is concentrated in the region just upstream of the BIR and exceeds 50 m over the 100 year run time in a few localised points.

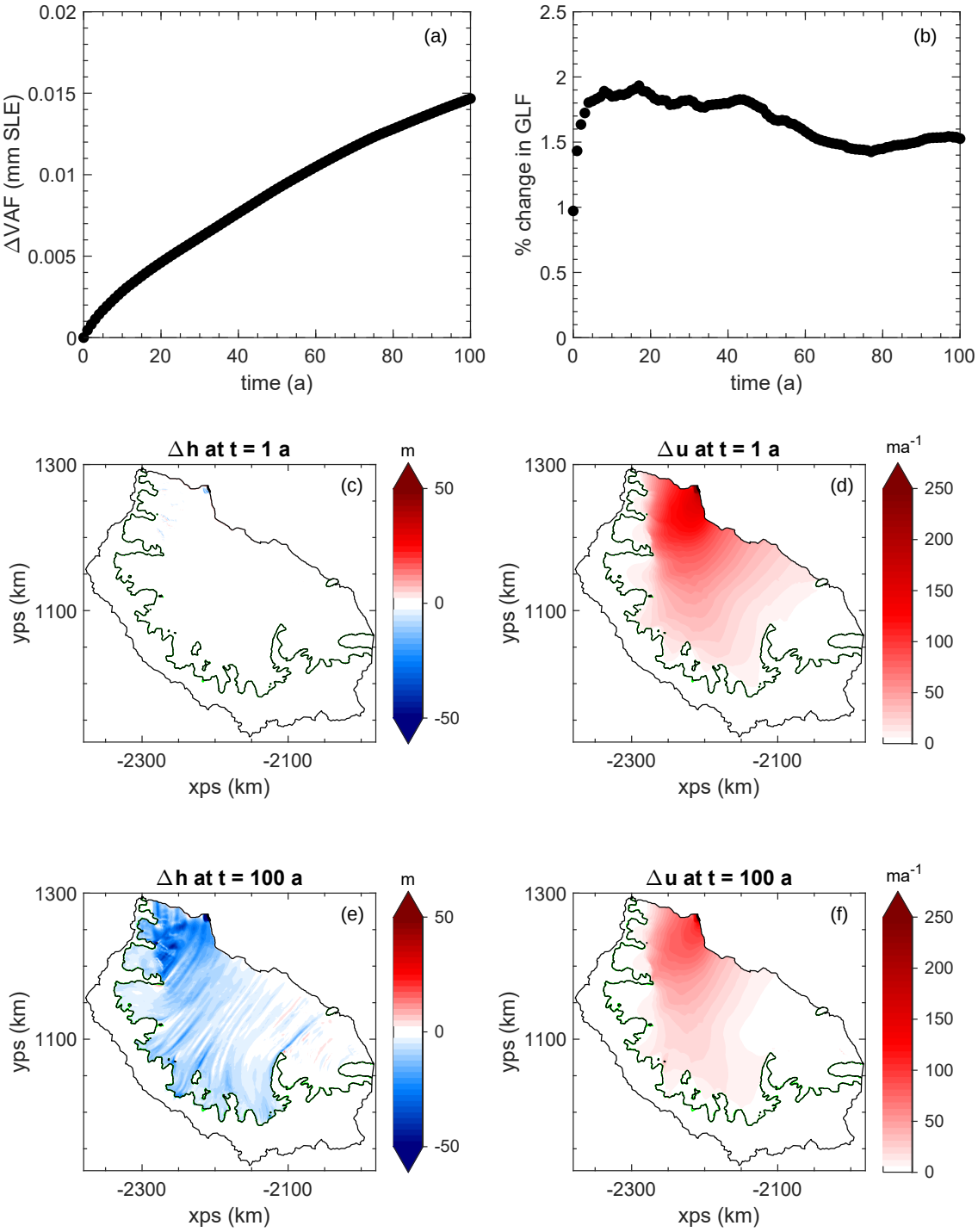

Figure 5.5: The response of the LCIS system to the loss of contact at the Bawden Ice Rise. **(a)** and **(b)** show the changes in VAF and GLF, respectively. **(c)** and **(d)** show the changes in ice thickness and ice speed after one year with respect to changes in the control run. **(e)** and **(f)** show the cumulative changes in these quantities after 100 years. Black lines show the initial grounding line and green the grounding line at the stated model time.

However, almost all of the changes in ice velocity and thickness are limited to the ice-shelf itself, with almost no acceleration or thinning of the ice upstream of the grounding line. This is reflected in the very small changes in VAF induced by the loss of basal contact at the BIR (around 0.015 mm SLE after 100 years, or a 0.12% change on the initial VAF above and beyond that of the control run). The instantaneous change in the GLF of 1% is almost identical to that modelled in the previous chapter as expected (although not exactly the same due to the different mesh used in these experiments and the new model initialisation that was performed). Figure 5.5b shows that the perturbation in GLF grows slightly larger in the first few years of the model run. However, it reaches a maximum value of a 1.9% increase, before falling towards a new steady state, 1.5% higher than the control run GLF.

The impact of losing basal contact at both the BIR and GIR simultaneously is shown in Fig. 5.6. As before, the change in ice velocity (Fig. 5.6d) after one year matches the response found in the instantaneous experiments in the previous chapter, with a significant acceleration of the ice shelf upstream of the ice rises. Again we see that this increase in ice-shelf speeds is sustained throughout the 100 year run time (Fig. 5.6f), but that the amplitude of that change is reduced, particularly across the central regions of the ice shelf. The larger ice-shelf acceleration caused by the loss of both ice rises translates into more extensive ice-shelf thinning, with greater ice loss across the whole ice shelf. For the loss of both ice rises, we find that the initial response in GLF is maximal, and that there is a reduction in GLF throughout the model run, with the system heading towards a new steady state with a GLF elevated by 1.7% compared to the control run value. Finally, the change in VAF of 0.03 mm SLE is double that of the change in VAF due to the loss of the BIR alone. But, again this is a small fraction of the initial VAF, and we find that the loss of basal contact at these ice rises alone has no significant impact on the grounded ice dynamics of the LCIS tributary glaciers.

5.3.3 A68 calving

The first transient, calving perturbation conducted was the replication of the calving of the A68 iceberg, the results of which are shown in Fig. 5.7. Once again, the changes in ice speed after one year are almost identical to those found in the instantaneous experiment conducted in the previous

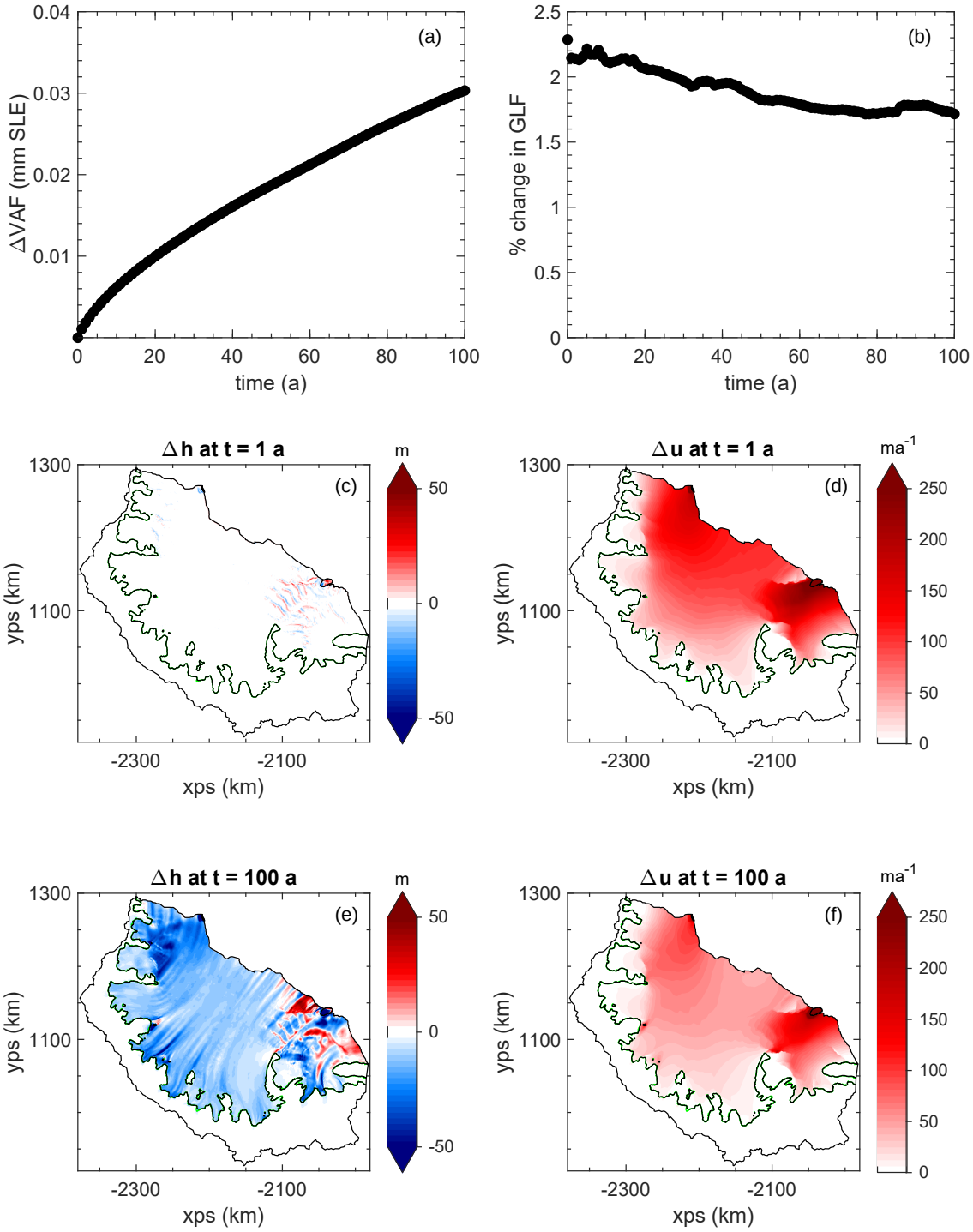

Figure 5.6: The response of the LCIS system to the loss of contact at both the Bawden Ice Rise and Gipps Ice Rise simultaneously. **(a)** and **(b)** show the changes in VAF and GLF respectively. **(c)** and **(d)** are the changes in ice thickness and ice speed after one year. **(e)** and **(f)** show the change in ice thickness and ice velocity after 100 years. Black lines show the initial grounding line and green the grounding line at the stated model time.

chapter, with almost no ice-shelf thinning occurring on this short timescale (Fig. 5.7c). Looking at the changes after 100 years (Fig. 5.7e and f) we can firstly see that the speedup in the centre of the ice shelf has reduced in amplitude, in response to the thinning of the shelf and the reduction in driving stresses, but that there has been a further slowdown in ice speed upstream of the GIR, and this slowdown causes an increase in ice thickness in this region. Upstream of the BIR, the model produces a small slowdown, on the order of 10 ma^{-1}, when compared to the control run. This is due to the fact that in the control run, there is a change in the grounded area at the BIR, which causes an acceleration in the ice flow. This change in BIR grounding line position does not occur to the same extent following the calving of the A68, and therefore when compared against the control run, the ice speed here appears to be reduced. This is a consequence of having a control run that exhibits some model drift, even after efforts have been made to reduce its impact through the use of the synthetic mass balance.

The impact on the GLF again increases slightly from its instantaneous increase of 0.28%, reaching a maximum value of 1.7% before settling to a new steady state around 1.3% higher than the control run. This shows, together with the maps of thickness and speed change (Fig. 5.7e and f), that there is almost no impact on the grounded ice from the loss of the A68 iceberg, and that after 100 years the change in VAF is just 0.0024 mm SLE, an order of magnitude smaller than the changes in VAF due to the loss of contact at the BIR and GIR, which themselves were small.

5.3.4 Idealised ice-shelf calving

The final set of perturbation experiments conducted here are the transient versions of the idealised calving experiments performed in the previous chapter. The results from the full 100 year simulations are shown in Fig. 5.8, a focussed view on the first five years of the runs is presented in Fig. 5.9 and a profile plot of ice thickness changes along two flowlines is shown in Fig. 5.10. The maps in Fig. 5.8c-f show the changes in ice thickness and speed following the complete collapse of the ice shelf, the largest perturbation applied. It is important to note here again that once the calving perturbation is applied, the position of the calving front remains fixed throughout the model run, and is not advected with the flow.

Firstly, examining Fig 5.8b, it can be seen that the instantaneous increase in GLF in response

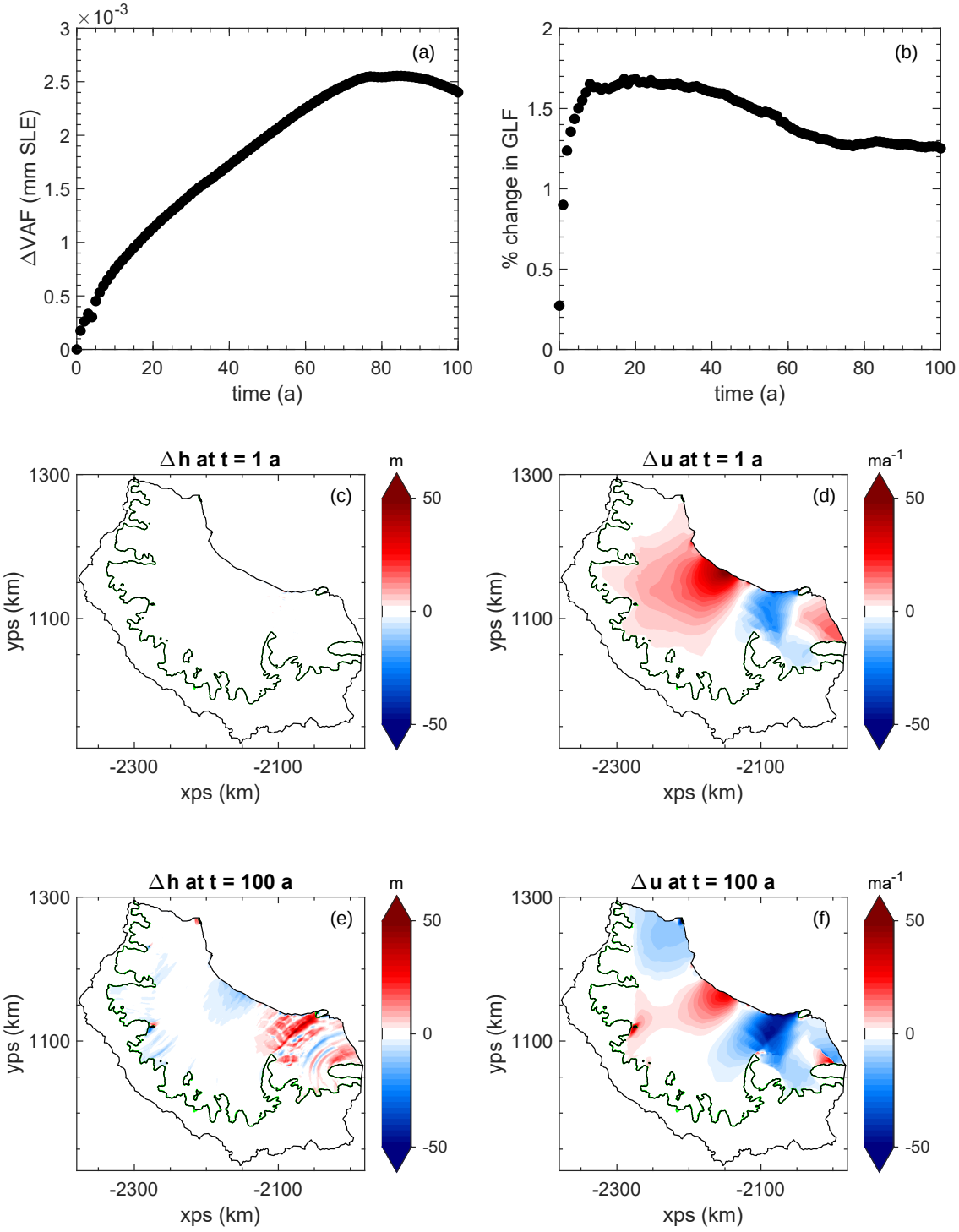

Figure 5.7: The transient response of the LCIS system to the calving of the A68 iceberg. **(a)** and **(b)** show the changes in VAF (note that the units are mm SLE x 10^{-3}) and GLF respectively. **(c)** and **(d)** are the changes in ice thickness and ice speed after one year. **(e)** and **(f)** show the change in ice thickness and ice velocity after 100 years. Black lines show the initial grounding line and green the grounding line at the stated model time.

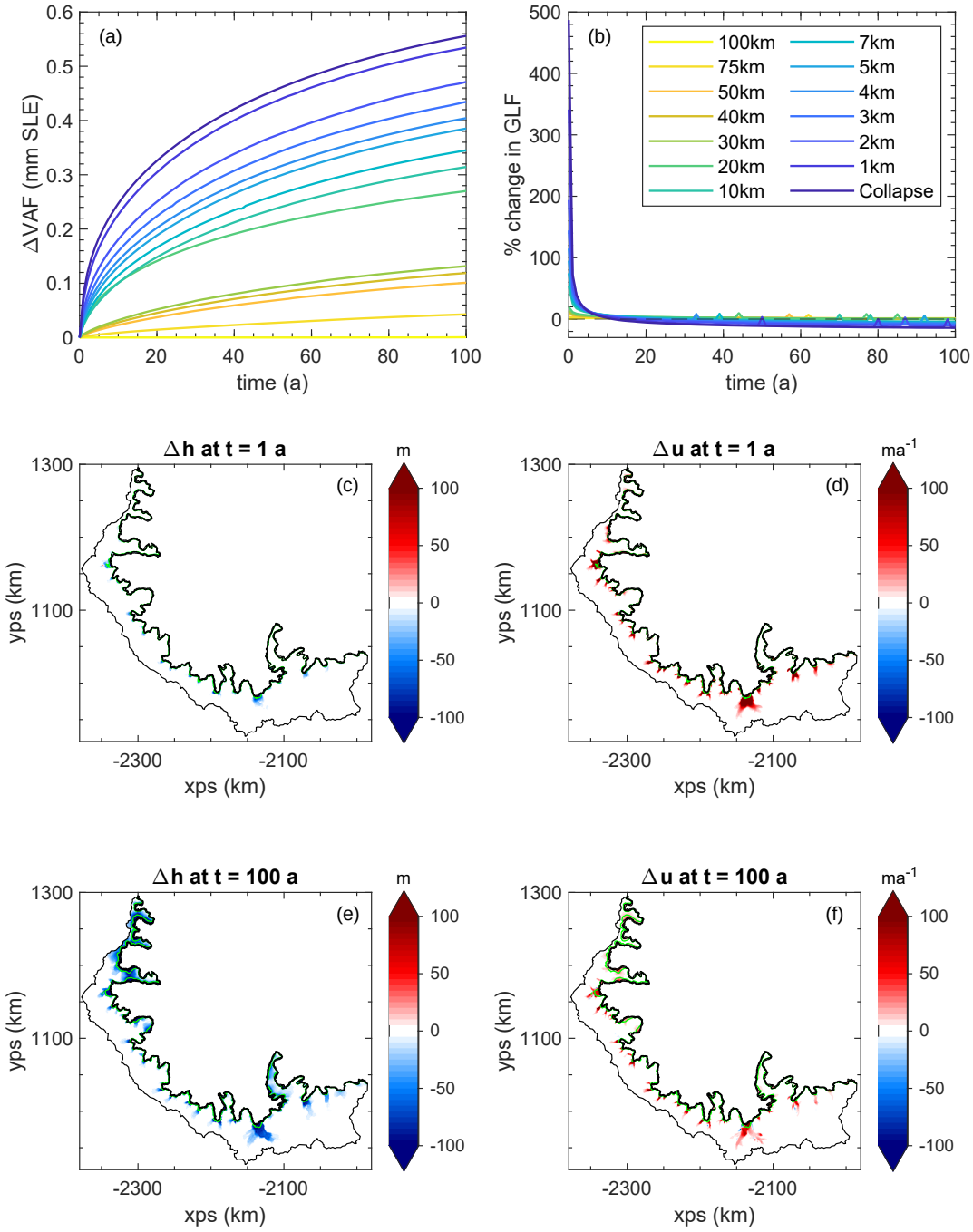

Figure 5.8: The transient response of the LCIS system to the idealised calving experiments. **(a)** and **(b)** show the changes in VAF and GLF respectively for the 14 perturbed calving front positions that were studied. The line colours in **(a)** and **(b)** refer to the location of the calving front as measured by the 'distance from the grounding line metric' in each experiment. **(c)** and **(d)** are the changes in ice thickness and ice speed after one year following the complete ice shelf collapse experiment. **(e)** and **(f)** show the change in ice thickness and ice velocity after 100 years in the same, complete shelf collapse experiment. Black lines show the initial grounding line and green the grounding line at the stated model time.

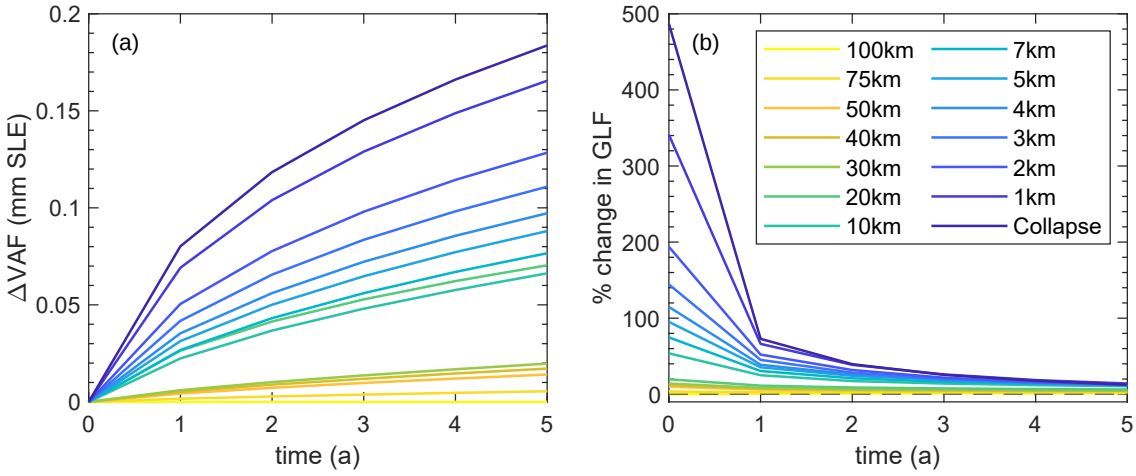

Figure 5.9: Focus on the evolution of **(a)** the VAF and **(b)** the GLF in the first five years following the idealised calving front perturbations. Again, the line colours refer to the distance of the calving front from the grounding line following the perturbation.

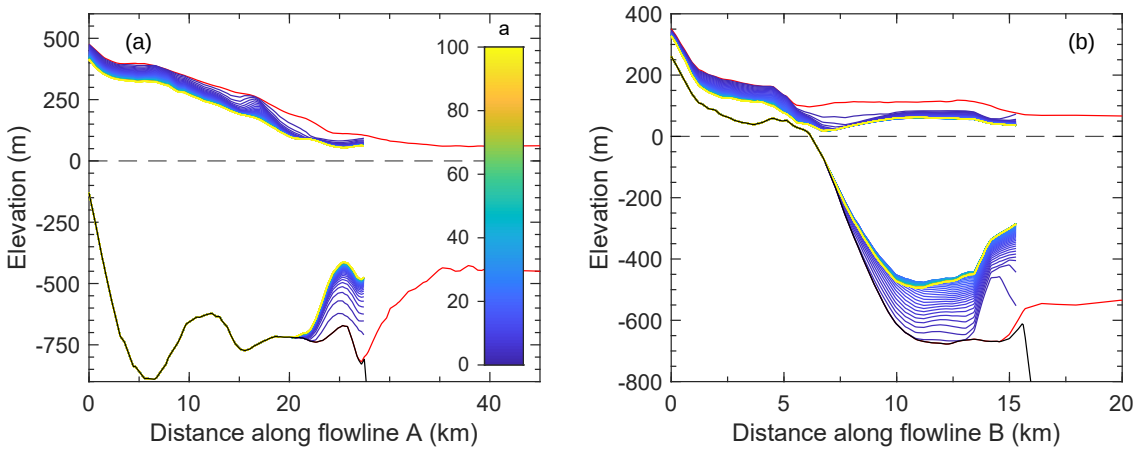

Figure 5.10: Profile plots of changes in ice thickness along flowlines A and B (the paths of which are plotted in Fig. 5.3d) in response to the complete collapse of the LCIS. In red is the initial ice surface and ice base, in black is the bedrock topography, and the coloured curves running from blue to yellow show the ice surface and ice base in each year of the model run.

to the perturbation falls rapidly back towards the initial GLF, and indeed for many of the larger ice-shelf perturbations, the GLF actually falls below that of the control run. Figure. 5.9b shows that nearly all of this reduction in the instantaneous increase in GLF occurs in the first 5 years, with the largest reduction coming in the first year immediately after the perturbation.

The change in ice velocity in the first year after the complete collapse of the ice shelf (Fig. 5.8d) is greater than 100 ma^{-1} in a region extending as far as 10 km upstream of the grounding line in some tributary glaciers. This acceleration is accompanied by a rapid thinning in these tributary

glaciers of up to 100 m, as shown in Fig. 5.8c and the elevation profiles in Fig. 5.10. This thinning is accompanied by a retreat in the grounding line of up to 5 km in some tributary glaciers within the first year following the complete collapse of the ice shelf. After 100 years, the thinning signal has travelled tens of kilometres upstream of the grounding line, and there is grounding line retreat of more than 10 km in some tributary glaciers. Examining the elevation profiles in Fig. 5.10, it can be seen that the majority of the changes in ice thickness occur in the first 10 years after the perturbation (the dark blue profiles), and that the rate of change in ice thickness falls rapidly as a new steady state is approached.

Turning to Fig. 5.8a, we see that as the calving front is moved closer to the grounding line – and more of the ice shelf is removed in the perturbation – the resulting VAF change after 100 years increases monotonically. This is also shown in Fig. 5.11a, in which the final VAF change after 100 years is plotted as a function of the distance of the calving front from the initial grounding line following the perturbation. However, there is also a clear step change in the loss of VAF between the perturbation that moves the calving front 30 km downstream of the grounding line (a final change in VAF of 0.13 mm SLE) and the calving front location 20 km downstream of the grounding line (a change in VAF of 0.27 mm SLE). It is also clear from Fig. 5.9a that this step change in VAF response is established within the first year of the model run.

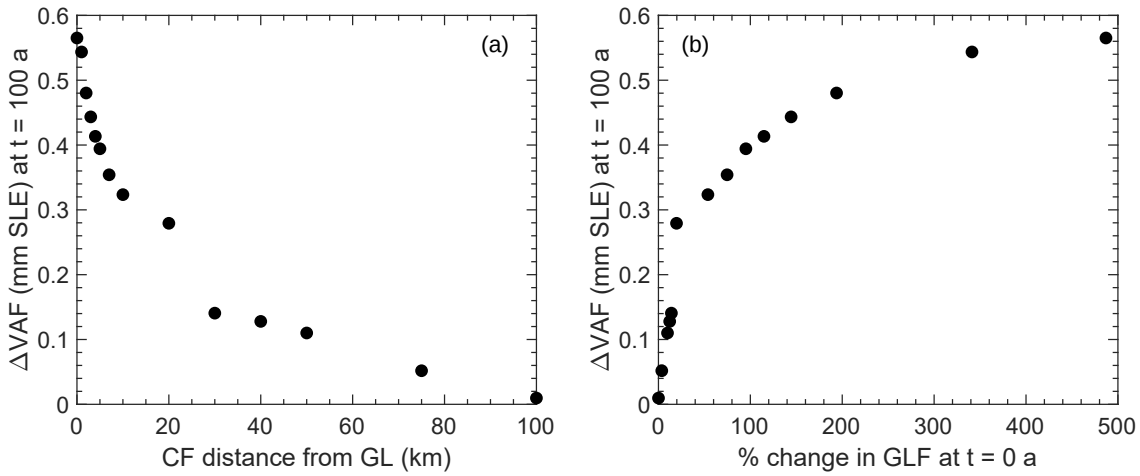

Figure 5.11: The change in ice volume above flotation (VAF) 100 years after the calving front perturbation is applied as a function of **(a)** the distance of the new calving front from the initial grounding line, and (b) as a function of the instantaneous change in grounding line flux (GLF) following the calving front perturbation – a measure of the amount of buttressing lost as a result of the perturbation.

Figure 5.8a also shows that for the largest calving perturbations, the final change in VAF is very sensitive to the exact location of the calving front. Placing the calving front 1 km downstream of the grounding line leads to a change in VAF of 0.54 mm SLE after 100 years, but positioning the calving front 2 km downstream of the grounding line leads to a change in VAF of only 0.47 mm SLE – a 13% reduction in mass loss after 100 years for a calving front position that differs by only 1 km.

Figure 5.11a shows that, just as for the distribution of buttressing in the previous chapter, the transient mass loss of the LCIS following calving perturbations is particularly sensitive to changes just downstream of the grounding line, as evidenced by the increasing gradient of the curve for smaller calving front distances from the grounding line. Indeed, the curve very closely resembles that in Fig. 4.6a of the previous chapter, which was used to assess where within the ice shelf the majority of the buttressing is generated. However, another way to look at the relationship between changes in ice-shelf buttressing and the transient evolution of the system is shown in Fig. 5.11b. Here, the change in VAF 100 years after the perturbation is plotted as a function of the instantaneous change in GLF from the same perturbation, the measure used to quantify the amount of buttressing removed in the perturbation. This curve shows that, for the LCIS, the change in VAF is most *sensitive* to small changes in ice-shelf buttressing (i.e. the gradient of this curve is steepest for small instantaneous GLF changes). As the amount of buttressing removed is increased (larger instantaneous GLF change values) the change in VAF starts to 'saturate' (i.e. the gradient of the curve tends towards zero). For example, by removing $\sim 10\%$ of the total buttressing capacity of the LCIS (positioning the calving front 10 km downstream of the grounding line), the mass loss of the system after 100 years is reduced by 57% of the maximum mass loss (from complete ice shelf collapse and 100% buttressing loss).

5.4 Discussion

5.4.1 Ice-rise ungrounding

As discussed in Sect. 2.4.3 and 5.1 there has been a significant focus on the impact that the ice rises of the LCIS have on the flow of the ice shelf and its tributary glaciers, the buttressing they provide, and the impact that any loss of contact may have on the structural integrity of the ice shelf. In the

previous chapter, it was found that both the BIR and GIR provide negligible amounts of buttressing to the grounded tributaries, as measured by the impact of their loss on the instantaneous change in GLF.

In this chapter, for the first time, the transient evolution of the LCIS and its tributaries has been examined in response to the loss of contact at the BIR and at the BIR and GIR simultaneously. The findings in the previous chapter left open the possibility that, whilst the buttressing provided by these two pinning points may not be significant, the resulting transient mass redistribution in response to their loss may be. The results presented here in Sect. 5.3.2 support the conclusion that neither the BIR or GIR play a significant, direct role in the transient dynamics of the grounding line of the LCIS. Whilst the acceleration in the ice shelf speeds is maintained after the loss of both ice rises, the amplitude of this change decreases through time, and we find that the GLF settles towards a new steady state, elevated on that of the control run by between 1 and 2%.

This work adds to the existing literature that explores the way in which ice rises can control the flow of ice shelves and their tributaries by presenting a case in which the dynamics of the tributary glaciers remains largely unaffected by the loss of contact at an ice rise. Favier et al. (2016) – studying the Dronning Maud Land coast of East Antarctica – also simulated the loss of basal contact at an ice rise, allowing their system to evolve for 1,000 years after the perturbation. Their results suggest that, despite the loss of basal contact not inducing a significant change in GLF after the perturbation (and hence demonstrating that the ice rise is not providing much buttressing to the tributary glaciers) the loss of basal contact can affect the longer-term dynamics of the system. This is due to the fact that the region they modelled contains tributaries on retrograde bedrock slopes, allowing for MISI to be initiated. They find that the loss of contact at the ice rise, and the associated acceleration of the ice shelf and thinning, causes the onset of rapid grounding line retreat to be advanced by 200 years when compared to simulations with the ice rise present. For the LCIS, the bedrock topography of the tributary glaciers is almost entirely prograde, and there is no potential for runaway grounding line retreat or mass loss. This demonstrates an important reason that ice-shelf buttressing and transient mass redistribution should be considered as separate, but linked processes. In both the LCIS and Dronning Maud Land cases, the ice rises do not provide significant buttressing to the grounded ice, but the role of the ice rises in the subsequent transient

evolution differs significantly. The factor that determines the importance of the ice rise for transient changes in the ice dynamics is the bedrock topography beneath the tributary glaciers upstream of the grounding line, rather than the buttressing provided by the ice rise itself.

The only remaining mechanism by which the loss of basal contact at the BIR or GIR could influence the dynamics of the system – which is not explored here – is that the increase in ice shelf speeds could affect the formation of fractures or the rate of growth of rifts, potentially leading to a retreat of the calving front or ice-shelf breakup. This is not a process that could be explored in these simulations, as a model in which the processes of viscous ice flow and ice fracture are coupled would be required. However, it is possible to state that the loss of contact at the BIR would not have a significant, direct impact on the dynamics of the tributary glaciers of the LCIS.

5.4.2 Idealised calving experiments

Another key finding of this chapter is the relationship between changes in VAF after 100 years and the systematic retreat of the calving front (and associated reduction in ice-shelf buttressing). In addition to finding that the mass loss is an increasing function of the calving perturbation, we see that there is a step change in the VAF response which occurs between calving front positions located 20 and 30 kilometres downstream of the initial grounding line (Fig. 5.8a). This is due to the fact that when the calving front is positioned 20 km downstream of the grounding line, regions of the ice shelf in the narrow embayments downstream of the main tributaries are removed, and the findings from the previous chapter showed that this is where the majority of the buttressing capacity of the LCIS is generated. Another important aspect of the results shown in Fig. 5.8a and Fig. 5.9a, is the difference in mass loss from calving fronts positioned just 1 km apart. This further demonstrates the sensitivity of the force balance at the grounding line to the geometry of the ice-shelf just downstream of the grounding line. It also shows, more generally, that when simulating large perturbations to an ice shelf – for example through calving or hydrofracture – that remove ice close to the grounding line, the exact location of the new calving front is an important detail which can have a significant impact on the resulting evolution of the system. It is therefore crucial to model the calving front, as well as the grounding line, with sufficient model resolution to ensure accurate results.

The method employed in these calving perturbations was to adjust the calving front position and then hold it fixed in place throughout the model run. This ensured that the perturbation applied in these transient experiments was the same as that in the previous chapter, so that the impact that a specified loss of ice-shelf buttressing has on the transient evolution of the system could be analysed. However, by holding the calving front location fixed, a new region of ice shelf is formed just downstream of the grounding line as it retreats. As shown previously, even the presence of a region of floating ice a few kilometres in length downstream of the grounding line can significantly alter the stress balance across the grounding line. The generation of these new regions of ice shelf acts to counter the initial perturbation in ice-shelf buttressing, by generating additional resistive stresses at the grounding line when compared to the state immediately after the perturbation. This may be one of the reasons that, for the largest perturbations which saw significant grounding line retreat, the GLF was reduced so rapidly, and that the VAF loss after 100 years also began to saturate towards 0.6 mm SLE of mass loss upon an increasing loss of buttressing (Fig. 5.11b).

In the discussion of their transient modelling study of the LCIS, Schannwell et al. (2018) state that "the LCIS does not provide strong buttressing forces" to its tributary glaciers. They draw this conclusion based on the limited changes in VAF due to the complete ice-shelf collapse (0.6-4.2 mm SLE after 300 years) when considered on an Antarctic-wide scale. I argue that this is not the correct interpretation of their findings. The actual buttressing that the LCIS provides is significant, as evidenced by the instantaneous changes in GLF presented in the previous chapter, and when compared with other ice shelves around the Antarctic Ice Sheet in the following chapter. It is not the case, therefore, that the LCIS does not provide strong buttressing forces to its tributary glaciers. It is rather that the transient mass loss in response to the loss of buttressing is limited. The constraints on this are predominantly the prograde bedrock topography on which the tributary glaciers are situated, and the small area over which marine based glaciers can retreat, that limits the total mass loss from the LCIS basin. Again, this is why it is important to consider the ideas of ice-shelf buttressing and the transient mass redistribution in response to the loss of that buttressing as separate, but linked, processes. It does not directly follow that if the transient mass loss is limited that the ice-shelf buttressing was small, and equally that a small amount of ice-shelf buttressing does not mean that the transient response to the loss of that buttressing will itself be small.

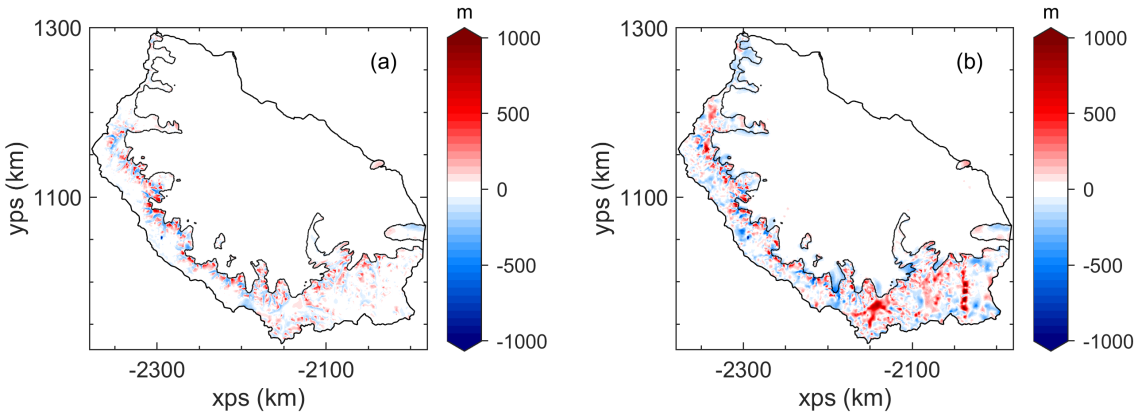

Figure 5.12: Maps showing the differences between the Bedmap2 (Fretwell et al., 2013) and BedMachine (Morlighem et al., 2020) ice and bed geometry data (BedMachine minus Bedmap2). **(a)** is the elevation difference in the ice surface and **(b)** is the difference in the bedrock elevation. In both cases red colours indicate that the BedMachine surface or bed is at a higher elevation than the Bedmap2 surface or bed.

An important detail to note in these results is the value of mass loss after 100 years from the complete collapse of the LCIS, which in this modelling study is 0.58 mm SLE. This is approximately half of the value that was found in Schannwell et al. (2018) after 100 years, in which three different ice flow models were used to explore the response to the same, complete collapse of the ice shelf. One key difference in the simulations presented here is that the BedMachine Antarctica v2 data set (Morlighem et al., 2020) was used, whereas Schannwell et al. (2018) used the Bedmap2 data set (Fretwell et al., 2013), as did all of the models in the ABUMIP experiments (other then the f.ETISh model which used BedMachine (Sun et al., 2020)). The ABUMIP experiments found that the Larsen C basin – which is larger in that study than the basin used here, and includes the former Larsen A and B Ice Shelf basins – actually gained mass over the course of the 500 year simulations, even when all ice shelves are removed. This result is largely driven by the surface accumulation field used in the ABUMIP experiments.

The differences between the BedMachine and Bedmap2 bedrock topography and ice thicknesses are large. As shown in Fig. 5.12b, in some of the key regions of tributary glacier flow, the bedrock topography is over 1,000 m deeper in the Bedmap2 data than in BedMachine. Since their ice surfaces are similar in these regions, that means that there is an additional kilometre of ice thickness in the tributary glaciers in Bedmap2 in regions that experience grounding line retreat (see e.g. Fig. 5 and Fig.8 in Schannwell et al. (2018)). The deeper bedrock provides a larger area of marine based

topography (i.e. situated below sea level) over which the tributary glaciers can retreat, and this factor is the largest cause of the difference between the results presented here and those found in Schannwell et al. (2018) and the reason we that find a smaller VAF loss after 100 years than in their study. Additionally, there is clearly scope to extend the work in this chapter by testing the sensitivity of the results to different sliding laws and to different parameter combinations within those sliding laws.

5.5 Conclusions

The results from the previous chapter showed that the vast majority of the buttressing capacity of the LCIS is generated in the regions of the ice shelf just downstream of the main grounding line. However, that work left open the question of how the LCIS system might respond transiently to the series of perturbation experiments explored. Those questions have, for the first time, been answered in this chapter.

Firstly, the perturbations in which the basal contact was removed at the BIR, and then the BIR and GIR simultaneously, were repeated and the ice flow model was allowed to evolve for 100 years. In both of these experiments, the change in GLF settled towards a new steady state between 1 and 2% higher than in the control run. The changes in ice-shelf speed that were modelled instantaneously in the previous chapter were found to be sustained throughout the 100 year model run, although the amplitude of these increases reduced through time. This effect was focussed in the regions just upstream of the ice rises, and resulted in ice-shelf thinning on the order of tens of metres over the 100 year run time. As evidenced by the limited changes in GLF and VAF, there was no significant impact on the grounded ice dynamics as a result of the loss of contact at these ice rises. This shows that, in addition to the finding from the previous chapter that these ice rises generate a negligible amount of the buttressing of the LCIS, they also have a very limited, direct impact on the grounding line dynamics through transient mass redistribution in response to their loss. This is controlled by the prograde bedrock topography of the tributaries, in contrast to studies conducted elsewhere in Antarctica with the potential for MISI where ice rises have been shown to play a far larger role in the grounding line dynamics. The only potential impact that the loss of contact at the BIR and GIR could have that was not considered in these modelling experiments is that the acceleration in

the ice shelf could lead to changes in the structural integrity of the shelf, although an assessment using a model incorporating fracture mechanics would be necessary to determine this.

Following this, the calving of the A68 iceberg was replicated and the transient evolution of the system modelled for 100 years. Again, it was found that the the impact on the grounding line dynamics, and changes in VAF throughout the 100 year model run were negligible. This reinforces the conclusions from the previous chapter, and of previous work, that the region of ice removed in the A68 calving event was passive ice.

Finally, the idealised calving perturbations from the previous chapter were repeated in a series of transient experiments. It was found that the change in VAF after 100 years is an increasing function of the size of the calving perturbation. However, there is also a step change in the response in VAF between the calving front being positioned 30 km and 20 km downstream of the grounding line, due to ice in the narrow embayments just downstream of the main tributaries being removed, which is where the majority of the buttressing of the LCIS is generated. Additionally, it was shown that the mass loss is particularly sensitive to the exact location of the calving front when it is located close to the grounding line. Placing the calving front 1 km downstream of the grounding line, compared to 2 km, resulted in a difference of 13% in the total mass loss after 100 years.

The change in VAF was also found to be an increasing function of the amount of buttressing removed from the ice shelf (Fig 5.11b) – as measured by the instantaneous change in flux after the calving perturbation – but this relationship is nonlinear. The gradient of this curve is greatest for small changes in buttressing, and the change in VAF after 100 years saturates as an increasing proportion of the total ice-shelf buttressing is lost. This is because the prograde bedrock topography only allows for limited grounding line retreat and thinning before a new equilibrium state is approached. Again, this demonstrates the need to consider the transient mass redistribution of an ice shelf-tributary system separately to the buttressing provided by the ice shelf. In this case, whilst the buttressing that the LCIS provides is significant, the resulting impact from the loss of that buttressing is limited. The mass loss – 0.58 mm SLE after 100 years – in response to the complete collapse of the LCIS is approximately half that found in the one previous study that modelled the impact of the collapse of the LCIS specifically. This is predominantly due to the differences in bedrock topography between the Bedmap2 data set used previously, and the BedMachine data used

here, which vary by over 1,000 m in ice thickness in key regions of the LCIS tributaries.

Chapter 6

The buttressing capacity of Antarctic ice shelves

6.1 Introduction

In Chapter 4, the buttressing capacity of the the Larsen C Ice Shelf (LCIS) was explored by systematically moving the calving front position closer to the grounding line and modelling the instantaneous changes in grounding line flux (GLF). It was found that the LCIS provides strong buttressing forces to its grounded tributary glaciers, and that most of this buttressing is generated in the first few kilometres of ice downstream of the grounding line. Then, in Chapter 5, the consequences of changes in ice-shelf buttressing on the transient mass redistribution of the LCIS and its tributary glaciers was examined. In this chapter, an Antarctic-wide modelling set-up is used to assess the total buttressing capacity of eight more of the major Antarctic ice shelves for the first time, and the regions in which the majority of the total buttressing is generated within the ice shelves are determined.

Recent theoretical studies have emphasised the central role that ice shelves have in controlling the grounding line dynamics of marine ice sheets. Pegler (2018b) showed that, in the presence of even small amounts of ice-shelf buttressing, the geometry of an ice shelf can completely control the ice thickness at the grounding line and its location. This is in contrast to the situation in which an ice sheet is fringed by an unconfined ice shelf, in which the absence of buttressing means that

the ice shelf plays no role in the grounding line dynamics (Schoof, 2007). Haseloff and Sergienko (2018) derived an analytical solution for the flux across the grounding line of an idealised marine ice sheet under different levels of ice-shelf buttressing. They showed that in the presence of strong buttressing, the GLF ceases to be a function of the ice sheet's basal stress conditions, but is instead controlled by the ice-shelf width and length.

Numerical work has also demonstrated the significant, observable impact that recent changes in ice-shelf thickness and extent (and the associated changes in ice-shelf buttressing) have had on the acceleration of tributary glaciers, dynamic thinning, and mass loss around the AIS, particularly in the Amundsen Sea sector (e.g. Minchew et al., 2018, Gudmundsson et al., 2019, De Rydt et al., 2021, Joughin et al., 2021). There have been suggestions that the loss of ice-shelf buttressing in this region may have already triggered the marine ice sheet instability at Pine Island and Thwaites glaciers (e.g. Favier et al., 2014, Joughin et al., 2014, Rignot et al., 2014), and that rapid ice loss may occur in the coming decades, although recent observations have suggested that the speed of grounding line retreat and mass loss may be slower than some models have predicted (Bamber and Dawson, 2020). The location at which perturbations in ice-shelf thickness are applied has also been shown to be important for the evolution of grounding line dynamics and transient mass changes, and is directly linked to the regions of the ice shelf that generate the most buttressing (e.g. Goldberg et al., 2009, Gagliardini et al., 2010, Goldberg et al., 2019).

As outlined in Chapter 2 and discussed in Chapter 4, it is possible to model the impact of changes in ice-shelf geometry and buttressing using diagnostic model experiments, as stress perturbations are transmitted instantaneously across an ice shelf to the grounding line, and this approach has been used in the key studies on which this chapter builds.

In the existing literature there are two, somewhat contrasting, maps of ice-shelf buttressing for the whole AIS (Fürst et al., 2016, Reese et al., 2018b). Fürst et al. (2016) calculated a local 'maximum buttressing number' across all Antarctic ice shelves, and then performed a series of calving experiments along isolines of this local buttressing number. They then defined regions of passive ice as areas of the ice shelves that could be calved without inducing an increase in flux *across the new calving front in the shelf* of more than 10%. Reese et al. (2018b) took a different approach to the question of Antarctic ice-shelf buttressing, and examined the sensitivity of the GLF

to small perturbations in ice-shelf thickness applied to 20 x 20 km grid cells across the continent's ice shelves. By focussing on the impact of perturbations in the ice-shelf at the grounding line, rather than changes in flux within the ice shelves themselves, they found that GLF was most sensitive to perturbations in the ice-shelf applied close to grounding lines and in shear margins.

Zhang et al. (2020) studied both locally defined buttressing numbers and GLF sensitivity for an idealised ice shelf and a real-world ice shelf (the LCIS), and found that there was almost no correlation between the two measures of buttressing. They also found that GLF was most sensitive to ice-shelf perturbations applied close to the grounding line. Goldberg et al. (2019) examined the sensitivity of transient mass loss to ice-shelf melting, and also found that grounded ice dynamics are most sensitive to perturbations in regions close to the grounding line and in shear margins, directly linked to regions in which ice-shelf buttressing is generated.

Here, I build on this work examining ice-shelf buttressing around Antarctica by extending the methods employed in Chapter 4 to the rest of the AIS. Again, it is important to note that diagnostic, time-independent experiments are used to determine the impact of calving perturbations on the buttressing provided by these ice shelves, and questions relating to how the ice sheet would redistribute mass transiently in response to these changes in ice-shelf buttressing are not examined here. Instead of focussing on GLF sensitivity, as in Reese et al. (2018b), the total buttressing capacity of eight other ice shelves around the AIS (in addition to the LCIS) is calculated, and the regions in which the majority of that total buttressing is generated are determined. The ice shelves chosen for analysis span a range of scales and geometric settings, including the largest ice shelves of the continent (the Filchner-Ronne and Ross Ice Shelves) and smaller ice shelves that are known to be crucial for determining the future behaviour of the ice sheet (including Pine Island, Thwaites and Totten Glacier Ice Shelves).

In the rest of this chapter, the changes to the model set-up required to simulate the whole AIS are set out, as is the approach taken to defining calving front perturbations applicable to ice shelves of vastly different scales around the AIS. The response in GLF to calving perturbations for the selected ice shelves is then presented and the similarities and differences in their responses are compared. Finally, the results are discussed in the context of the existing ice-shelf buttressing literature, and the implications for AIS dynamics are outlined.

6.2 Methods

6.2.1 Model set-up

The Úa ice flow model is again used in its diagnostic mode – solving the same set of equations outlined in Sect. 3.2.1 – but now with a model set-up that encompasses the whole AIS.

To specify the boundary of the model domain, the longest zero ice-thickness contour of the BedMachine v2 data set (Morlighem et al., 2020) was extracted, which corresponds to the boundary of the ice sheet, and was used to generate a set of boundary coordinates by re-sampling this contour at intervals of 3 km. Re-sampling the boundary contour was required because each point on the boundary is translated into a node in the computational mesh, and therefore having a smaller distance between boundary nodes results in a mesh with a large number of elements in regions that don't necessarily require a high resolution in these experiments.

As there were no artificial boundaries introduced into this domain (unlike in the LCIS case where an ice divide was used as one edge of the model domain) the natural, ocean pressure boundary condition was applied along the entire model boundary (see Sect. 3.2.3 for details on the natural boundary conditions within Úa). Within the model domain, the ice thickness, ice surface topography and bedrock topography are all derived from the BedMachine v2 data set, and – just as in the LCIS case – a spatially-variable ice density was calculated and used, based on the firn air content field in that data set (see Sect. 3.5 for details).

The finite-element mesh used for the whole ice sheet was refined locally based on ice velocities, strain rates and the distance from the grounding line. Due to the substantial increase in the area being modelled in comparison to the LCIS case, the corresponding size of the mesh elements used is larger, with a target element size of 1,000 m applied to the regions around the grounding line, and a 2,000 m target element size in the fastest flowing regions of the domain and areas of highest strain rates. This resulted in a finite element mesh with 784,682 elements, with a maximum, mean, median and minimum size of 84,505, 3,001, 1,843 and 126 m, respectively.

6.2.2 Model initialisation

To initialise the model, the data assimilation capabilities of Úa were used, as described in Sect. 3.4 and utilised in the two preceding chapters. The observed ice velocities were again taken from the MEaSUREs InSAR-based Antarctic Ice Velocity v2 data set (Rignot et al., 2017; 2011, Mouginot et al., 2012), and the errors associated with the measurements, and used in Eq. 3.18, were also taken from that data set.

The regularisation parameters were the same as those used in Chapters 4 and 5 ($\gamma_{sA/C} = 1000$ and $\gamma_{aA/C} = 1$). The prior estimate for the rate factor was also the same as in the previous chapters, chosen to be spatially uniform with a value of $\hat{A} = 1.15 \times 10^{-8}$ a^{-1}kPa^{-3}, corresponding to an ice temperature of -10 °C. However, in this Antarctic-wide set-up, the prior estimate for the basal slipperiness parameter, $\hat{C}$, was chosen to be spatially variable in order to reduce the number of inverse iterations required to reach an acceptable initial condition. It was calculated using the inverted form of the basal sliding law, given by

$$\hat{C} = \frac{||\boldsymbol{u}_b||}{\boldsymbol{\tau}^m}, \tag{6.1}$$

assuming a basal shear stress of $\boldsymbol{\tau} = 80$ kPa, and using a basal ice velocity, $\boldsymbol{u}_b$, equal to that in the observational data set used in the initialisation.

The stress exponents in both Glen's flow law (n) and the Weertman-type sliding law (m), were set to 3 for these experiments, as in previous chapters.

Using the errors directly from the velocity data set led to a systematic and significant under-estimation of the ice velocities in all of the ice streams of the Siple Coast flowing into the eastern Ross Ice Shelf. To improve this, the uncertainties were manually reduced by a factor of 10 for all ice flowing faster than 50 ma^{-1} within this region of the ice sheet. This gave the velocity observations in the fast flowing regions of the Siple Coast a higher weighting in the cost function, meaning that they were targeted more rapidly by the gradient-based optimisation algorithm.

The resulting initial conditions are presented in Figure 6.1. As can be seen from the bi-variate histogram, there is a significantly larger spread of model-data misfit following the initialisation when compared with the LCIS case (see Fig. 4.2), but the histogram is still sharply peaked around zero, as can also be seen from the map of model-observation misfit in Fig. 6.1c. The reduction in

uncertainties over the Siple Coast ice streams to improve the fit to observations means that the MacAyeal and Bindschadler Ice Streams are now well represented in the model. However, this did not resolve the problems of a large model-data misfit over the ice plain upstream of the grounding lines of the Whillans and Mercer Ice Streams, where the surface slopes, and hence driving stresses, are small. In this region, the ice is almost stagnant in the model, which has consequences for the accurate representation of the response of the grounded ice in this region to any perturbations in the ice shelf. Another approach that could be tried in the model initialisation procedure would be to use the calculated driving stresses from the ice stream geometry in Eq. 6.1, rather than a constant value of 80 kPa, but there was not time to test this method for inclusion in this thesis.

Despite this, the model captures the present day ice velocities in almost all of the key ice shelves and tributary glaciers of the ice sheet studied in this chapter, and the observed and modelled ice velocities have an overall rms difference of 22.4 ma^{-1}.

6.2.3 Prescribing calving front positions

In Chapter 4, a distance from the main grounding line metric was used to define calving front perturbations for the LCIS. However, in these Antarctic-wide experiments, a calving front location metric was needed that could be applied equally to ice shelves of vastly different sizes, from Thwaites Glacier Ice Shelf with an area of 3,371 km^2, to the Ross Ice Shelf with an area of 478,460 km^2.

Therefore, a 'proportional' distance from the main grounding line metric was used to define calving front positions, which from here on is termed the 'GL-CF distance' (grounding line to calving front distance). First, the straight line (or 'as the crow flies') distance from every finite element mesh node in each ice shelf to the closest point on its main grounding line (excluding ice rises, ice rumples and islands) was calculated. The distance of each node from the grounding line was then scaled by the maximum distance to the grounding line for each ice shelf, giving each ice shelf node a GL-CF distance metric between 0% and 100%, with 100% corresponding to the node that is furthest from any of the main grounding lines of the shelf. The resulting maps of the GL-CF distance are presented in Figures 3-11 for each ice shelf analysed.

Calving front locations for the series of perturbation experiments were then defined along isolines of this GL-CF distance metric. The method for perturbing the calving front location using mesh

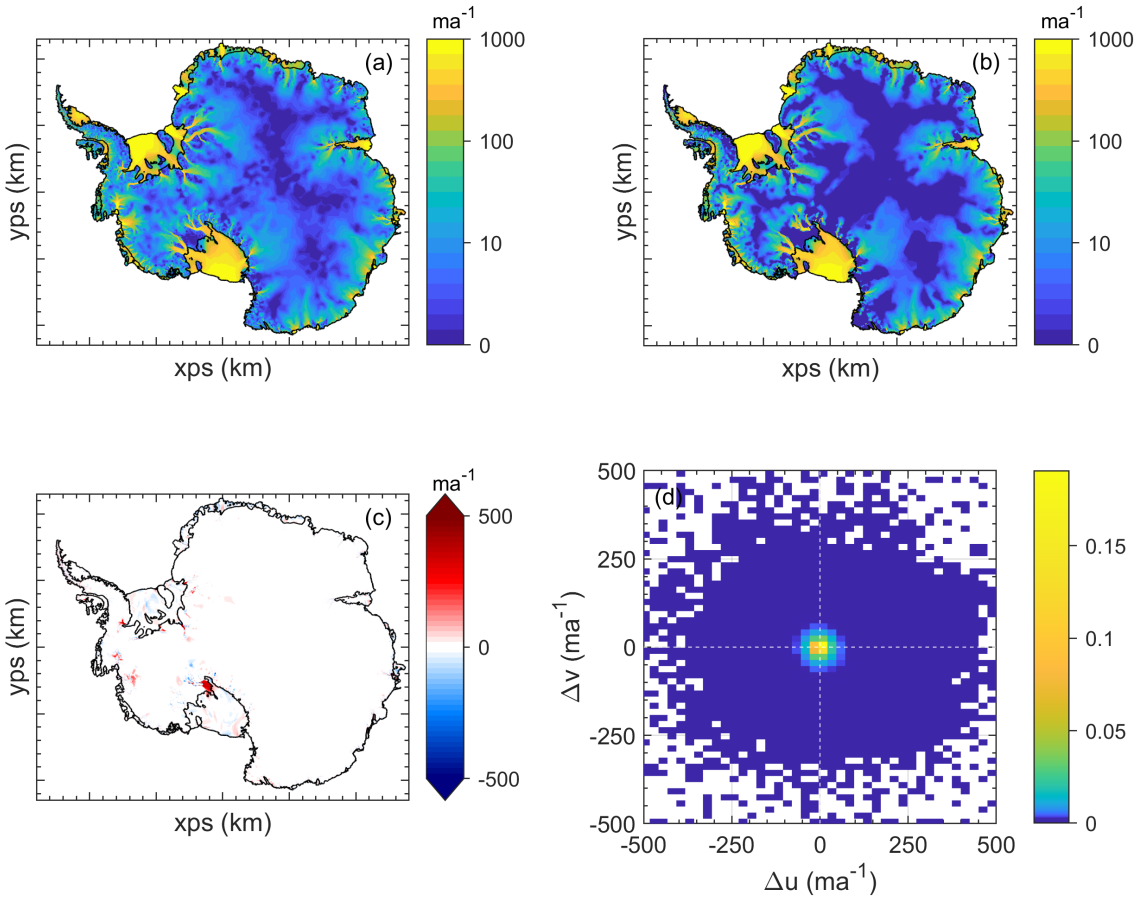

Figure 6.1: Panel **(a)** is the observed ice speed and panel **(b)** shows the modelled ice speed after the model initialisation. The difference between the two fields (observed - modelled) is shown in panel **(c)**, and in panel **(d)** those differences are shown on a normalised histogram, with the velocity differences separated into their x and y components. Note the region of high misfit in **(c)**, over the Whillans and Mercer Ice Streams.

element deactivation is the same as in Chapter 4. For example, to move the calving front to 50% of the maximum GL-CF distance, all ice shelf elements which contain a node that is greater than or equal to 50% of the maximum GL-CF distance from the grounding line are identified and deactivated from the finite element mesh, and the diagnostic equations are solved with this new calving front position. As in the LCIS case outlined in Sect. 4.2, any node that is a part of an element which crosses the grounding line was left unperturbed, even in the 'complete collapse' experiments, so as not to change the driving stress across the grounding line, and to ensure that any change in GLF can be attributed directly to a change in ice-shelf buttressing.

When the ice shelves are calved according to this metric, the calving perturbations do not remove equal areas of the ice shelf. Therefore, to make the results presented below more meaningful, and

to aid comparison with previous studies, the percentage of the ice shelf area removed is calculated for each calving perturbation, and the GLF response is plotted as a function of the area removed in Figures 3-11. The relationships between the GL-CF distance used to define the calving front locations, and the ice shelf areas removed in each calving perturbation are shown in Figure 6.2.

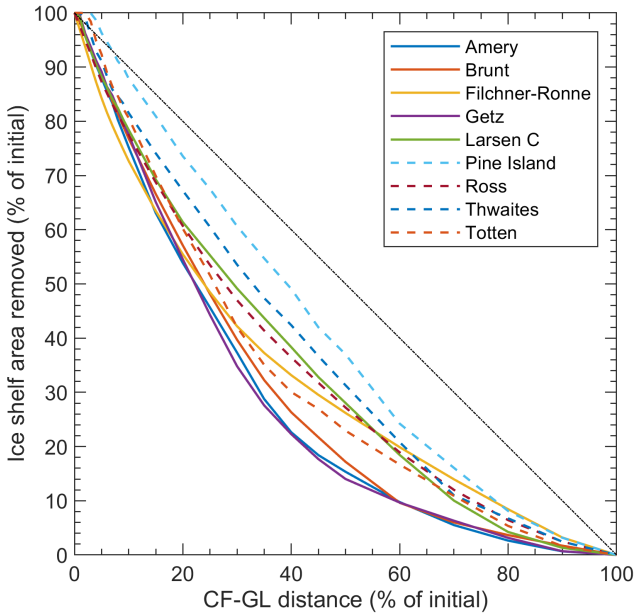

Figure 6.2: Relationship between the GL-CF distance metric used to define the calving front positions in the perturbation experiments, and the ice shelf area removed in those calving experiments for each ice shelf analysed here.

6.2.4 Passive ice definition

Fürst et al. (2016) defined regions of passive ice as areas of an ice shelf that could be calved without inducing an increase in flux across the new calving front of more than 10%. In this thesis the definition of ice-shelf buttressing has been emphasised as the resistance that an ice-shelf as a whole generates and transmits to ice *at the grounding line*, and this has motivated the overall approach throughout this research. Therefore, passive ice shelf areas here are defined as regions of the ice shelf that can be calved without inducing a 10% increase in the GLF of that ice shelf. The choice of 10% is arbitrary, but aids comparison with the regions of passive ice that were inferred by Fürst et al. (2016).

In the results that follow, the exact definition of passive ice areas is very likely to be dependent on the method chosen for defining calving front positions, and in that sense is not necessarily a

fundamental metric of the ice shelf. An extension to the work presented in this chapter would be to test the robustness of the results to the use of different definitions of the systematic retreat of a calving front.

6.3 Results

Here, the response of the GLF to perturbations in the calving front position for nine of the largest ice shelves around the AIS, which vary significantly in scale and geometric setting, are presented in order to gain insight into the variation in total ice-shelf buttressing between and within the ice shelves of the AIS. I first present a summary table of the key results, which can then be referred to throughout the discussion of the individual results of the major ice shelves analysed.

6.3.1 Summary of results

In Table 6.1, the results showing the impact of the series of calving perturbations on the GLF of the nine Antarctic ice shelves studied are summarised. The key metrics that have been identified – including the total buttressing capacity, the proportion of the shelf that generates 80% of the total buttressing, and the area of the shelf considered passive ice – are presented for each ice shelf.

Table 6.1: Summary of the grounding line flux (GLF) response to calving front perturbations for the nine Antarctic ice shelves analysed. The calculation of the maximum GL-CF distance is described in the main text. The total buttressing is calculated as the change in GLF in response to complete removal of the shelf. 80% of the total buttressing capacity is calculated as the ice-shelf area remaining when 80% of the maximum GLF response has been reached through calving. The definition of passive ice used here is defined in the main text.

Ice shelf	**Initial ice shelf area (km^2)**	**Maximum GL-CF distance (km)**	**Total buttressing (max GLF % increase)**	**80% of total buttressing (% of shelf area)**	**Passive shelf area (%)**
Filchner-Ronne	425,400	383	3,090	15	26
Ross	478,500	380	802	15	27
Amery	60,630	119	2,140	25-37	22
Larsen C	56,220	121	315	12	61
Brunt/Riiser-Larsen	78,420	198	201	14	48
Getz	32,690	111	185	82	9
Totten	6,398	40	1,320	49-58	30
Pine Island	6,059	54	96	83	24
Thwaites	3,371	53	49	15	85

6.3.2 Larsen C, Filchner-Ronne and Ross Ice Shelves

Figure 6.3 shows the instantaneous change in GLF in response to ice-shelf calving events of increasing magnitude for the LCIS. In this chapter, the LCIS is perturbed as part of an Antarctic-wide set-up with a different mesh resolution, a new model initialisation, and a different metric for calculating the location of calving fronts for perturbation experiments. One clear difference between the results here and those presented in Chapter 4 (see Fig. 4.6), is that the total buttressing capacity, as measured by the instantaneous change in GLF in response to the complete removal of the shelf, has been reduced by $\sim$ 50%, from 607% to 315%. The causes of this fall in the maximum GLF response are explored further in Sect 6.3.6, but are related both to the lower mesh resolution around the grounding line used in this chapter, and to the differences in the initial stress state in the ice following model initialisation in the detailed LCIS set-up and the Antarctic-wide set-up.

Despite this difference in the value calculated for the total buttressing capacity of the LCIS, the characteristic pattern for the response in GLF to calving events of increasing magnitude remains unchanged. Over 80% of the total buttressing capacity of the LCIS is found to be generated in the first 12% of ice shelf area downstream of the grounding line. To aid comparison with the values calculated for the distribution of buttressing in Chapter 4, it should be noted that the maximum GL-CF distance for the LCIS is 121 km. Converting the GL-CF distance based calving front positions into kilometres downstream of the grounding line, it is found that with this new model set-up, 95% of the total buttressing capacity of the LCIS is generated in the first 18 km of ice shelf downstream of the grounding line, and over 80% from the first 6 km downstream of the main grounding line (equivalent to the 12% of total ice shelf area quoted above). These values are similar to those found in the detailed modelling of the LCIS in Chapter 4, which were 25 km and 5 km downstream of the main grounding line for 95% and 80% of the total buttressing capacity, respectively. Again, the differences are explored further in Sect. 6.3.6

The consistency of the results for the distribution of buttressing generation within the shelf provide confidence that an Antarctic-wide approach can be taken to determine the buttressing capacity of the major ice shelves. However, it is likely that the values found for the total buttressing capacity of each ice shelf would be larger when calculated as part of local modelling study with a higher mesh resolution across the ice shelf and at the grounding line.

By determining the point at which a 10% increase in GLF is achieved through ice-shelf calving, it is found that 61% of the ice shelf area of the LCIS consists of passive ice. This corresponds to positioning the calving front at 20% of the maximum GL-CF distance downstream of the grounding line. Using this definition for passive ice on the results from the experiments conducted on the LCIS in Chapter 4, it is found that 40% of the LCIS could be considered passive ice. Again, the reasons for this discrepancy are explored further in Sect 6.3.6.

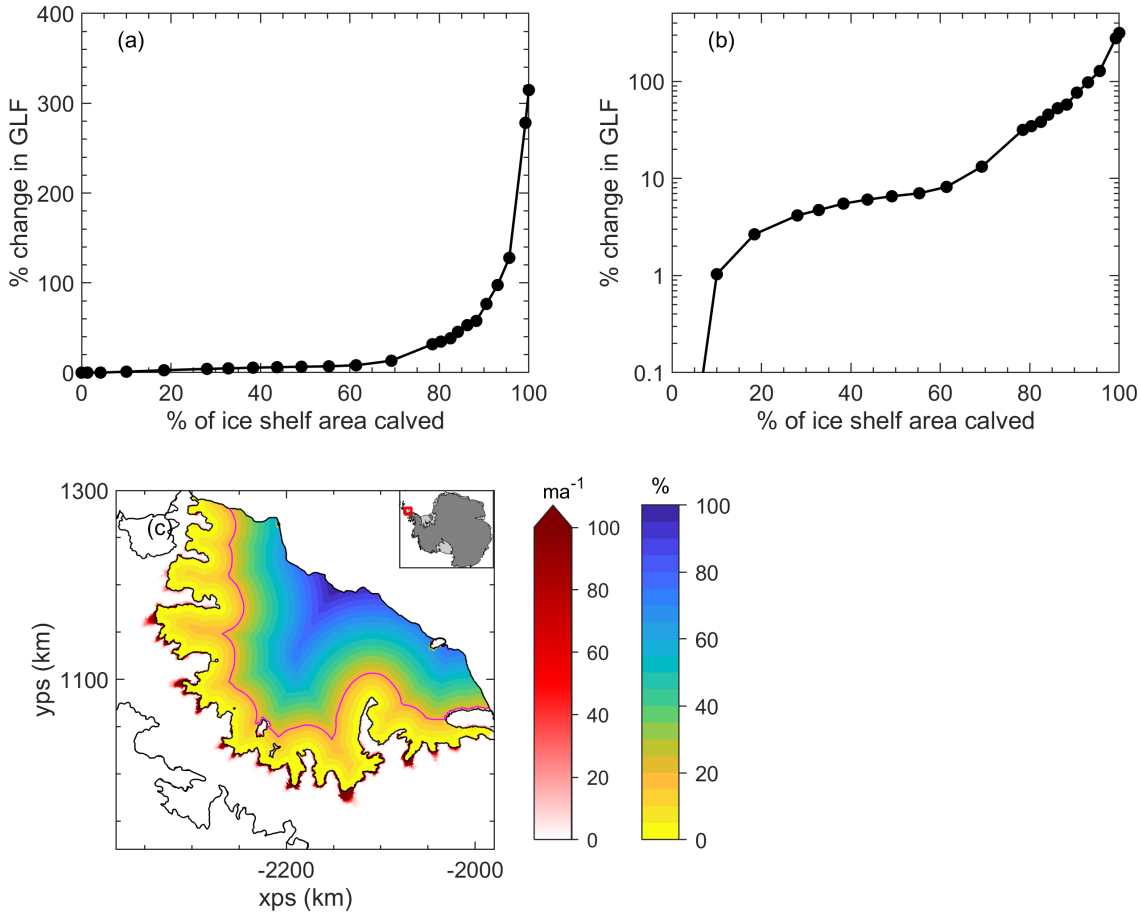

Figure 6.3: Instantaneous change in grounding line flux (GLF) for the Larsen C Ice Shelf, when perturbed as part of the Antarctic-wide model set-up. Panel **(a)** is the response in GLF as a function of the % of the initial ice shelf area removed in the calving experiment. **(b)** is the same information plotted on a logarithmic y-axis scale for detail. **(c)** shows the distance of each ice-shelf model node from the main grounding line as a % of the maximum the GL-CF distance. The contours of this field were used to define the calving front positions in the series of calving experiments. In red is the instantaneous increase in ice velocity over the grounded ice for the complete collapse experiment (i.e. removing 100% of the ice-shelf area). The magenta contour line in the ice shelf corresponds the calving front position that results in a 10% increase in GLF, with ice downstream of this point classified as 'passive ice' by this approach.

The response of the Filchner-Ronne Ice Shelf (FRIS) to calving perturbations is presented in

Figure 6.4. The total buttressing capacity of the FRIS is an order of magnitude larger than for the LCIS, with an instantaneous GLF increase of 3,090% in response to the complete removal of the ice shelf. This is the largest value of any ice shelf analysed here, demonstrating that the FRIS provides the most buttressing to its grounded tributary glaciers, as calculated by this metric. For the FRIS, over 80% of the total buttressing capacity is generated in the first 15% of the ice shelf area downstream of the grounding line, corresponding to regions of the ice shelf that encompass the long and narrow embayments that are formed just downstream of the principal ice streams that flow into the shelf.

To produce a 10% increase in the GLF the calving front had to be placed 45% of the maximum GL-CF distance downstream of the grounding line. This means that 26% of the ice shelf area of the FRIS can be considered passive ice.

The results for the largest ice shelf in Antarctica by area, the Ross Ice Shelf, are shown in Figure 6.5. The same pattern in the instantaneous response of the GLF to increased ice-shelf calving is observed for the Ross Ice Shelf as for the LCIS and the FRIS. The total buttressing capacity of the shelf is between that of the LCIS and FRIS, with a maximum instantaneous increase in GLF of 802%. Over 80% of the total buttressing capacity of the Ross Ice Shelf is generated in the first 15% of the ice shelf area downstream of the grounding line, the same as for the FRIS and very similar to the LCIS.

27% of the Ross Ice Shelf area can be considered passive, with a 10% increase in GLF only being induced when the calving front is positioned at 50% of the maximum GL-CF distance downstream of the grounding line.

An important caveat on the results presented for the Ross Ice Shelf is that the impact of calving perturbations on the GLF response of the Whillans and Mercer Ice Streams is likely to be underestimated as the modelled velocities are significantly smaller than the observed velocities here. This would change the value calculated for the total buttressing capacity of the Ross Ice Shelf, but the pattern of how this total buttressing is distributed throughout the shelf is not expected to be significantly affected.

The LCIS, FRIS and Ross Ice Shelf have been presented together due to the similarities in their GLF response curves, and the fact the over 80% of the total buttressing capacity of these

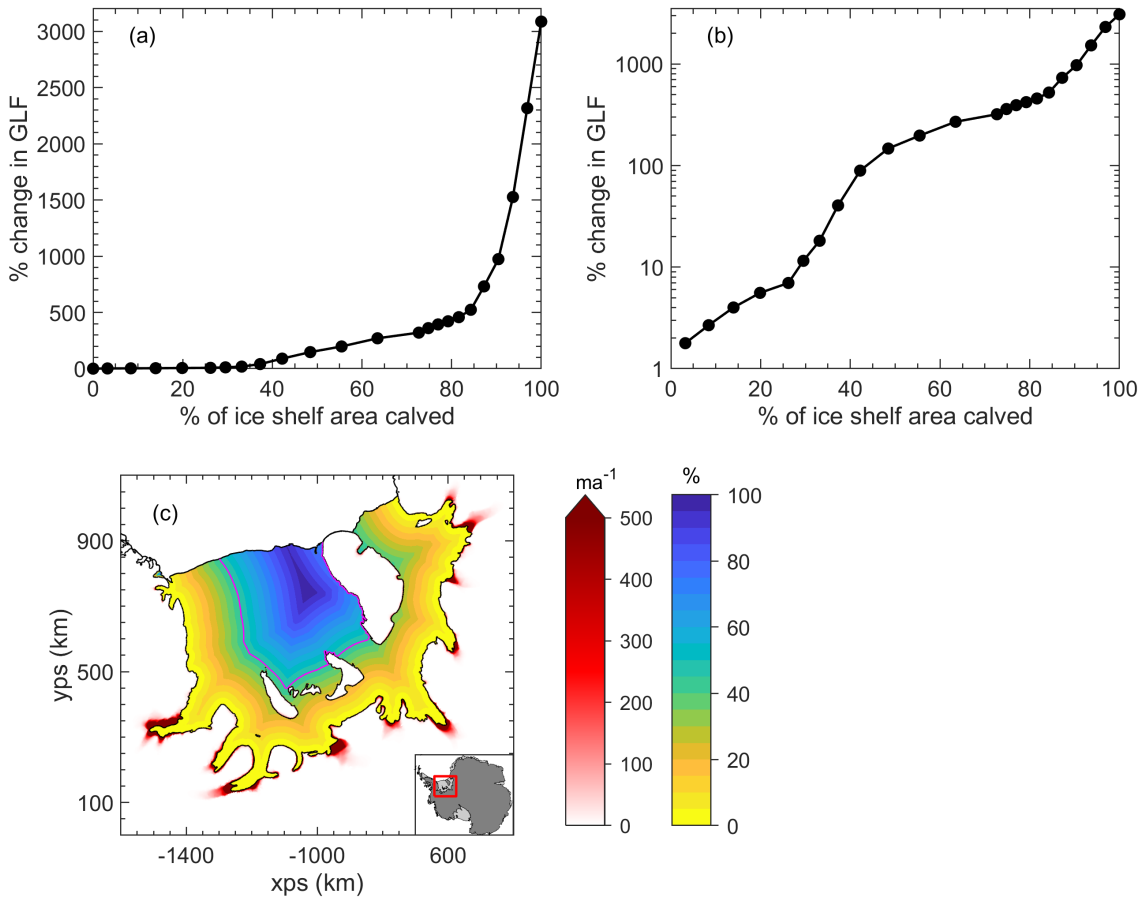

Figure 6.4: Instantaneous change in grounding line flux (GLF) for the Filchner-Ronne Ice Shelf. Panel **(a)** is the response in GLF as a function of the % of the initial ice shelf area removed in the calving experiment. **(b)** is the same information plotted on a logarithmic y-axis scale for detail. **(c)** shows the distance of each ice-shelf model node from the main grounding line as a % of the maximum the GL-CF distance. The contours of this field were used to define the calving front positions in the series of calving experiments. In red is the instantaneous increase in ice velocity over the grounded ice for the complete collapse experiment (i.e. removing 100% of the ice-shelf area). The magenta contour line in the ice shelf corresponds the calving front position that results in a 10% increase in GLF, with ice downstream of this point classified as 'passive ice' by this approach.

shelves is generated by the ice shelf area between 12% and 15% downstream of the grounding line. Their geometric settings are similar, in that each shelf is formed in an over-arching embayment, with smaller, narrower embayments just downstream of the grounding lines of the main tributary glaciers, where the majority of the shelves' buttressing is generated.

6.3.3 Amery and Totten Ice Shelves

In Figure 6.6, the GLF response of the Amery Ice Shelf to calving is presented. There is a significant amount of buttressing provided by the Amery Ice Shelf, with a maximum increase in GLF of 2,140%

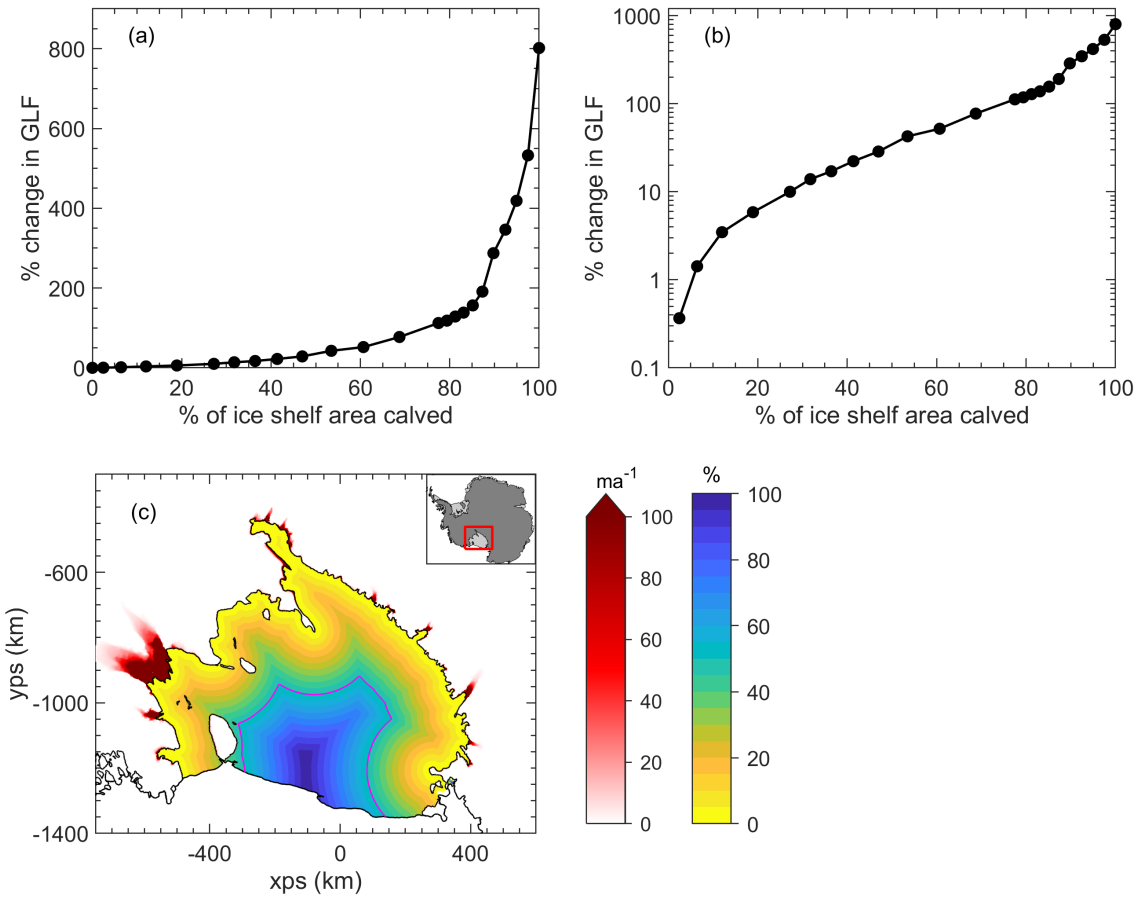

Figure 6.5: Instantaneous change in grounding line flux (GLF) for the Ross Ice Shelf. Panel **(a)** is the response in GLF as a function of the % of the initial ice shelf area removed in the calving experiment. **(b)** is the same information plotted on a logarithmic y-axis scale for detail. **(c)** shows the distance of each ice-shelf model node from the main grounding line as a % of the maximum the GL-CF distance. The contours of this field were used to define the calving front positions in the series of calving experiments. In red is the instantaneous increase in ice velocity over the grounded ice for the complete collapse experiment (i.e. removing 100% of the ice-shelf area). The magenta contour line in the ice shelf corresponds the calving front position that results in a 10% increase in GLF, with ice downstream of this point classified as 'passive ice' by this approach.

in response to the complete removal of the ice shelf. However, in contrast to the more gradual increase in the GLF response in the previous three ice shelves examined, the GLF curve has a step change once 65% of the ice shelf area has been calved. Again, this is directly linked to the geometry of the embayment, with the step change occurring when ice in the narrowest part of the embayment, just downstream of the grounding line of Lambert Glacier, is calved. Over 80% of the total buttressing capacity of the ice shelf comes from the first 25-37% of the ice shelf area downstream of the grounding line. The exact value is difficult to determine as it lies somewhere within the step-change response between calving fronts positioned 15% and 10% of the maximum

GL-CF distance downstream of the grounding line.

For a 10% GLF increase to be generated, the calving front had to be positioned between 35 and 40% of the maximum GL-CF distance downstream of the grounding line. Taking the more conservative estimate, with the calving front positioned 40% of the maximum GL-CF distance downstream of the grounding line (which induced a 4.5% increase in GLF), this corresponds to 22% of the Amery Ice Shelf being considered passive.

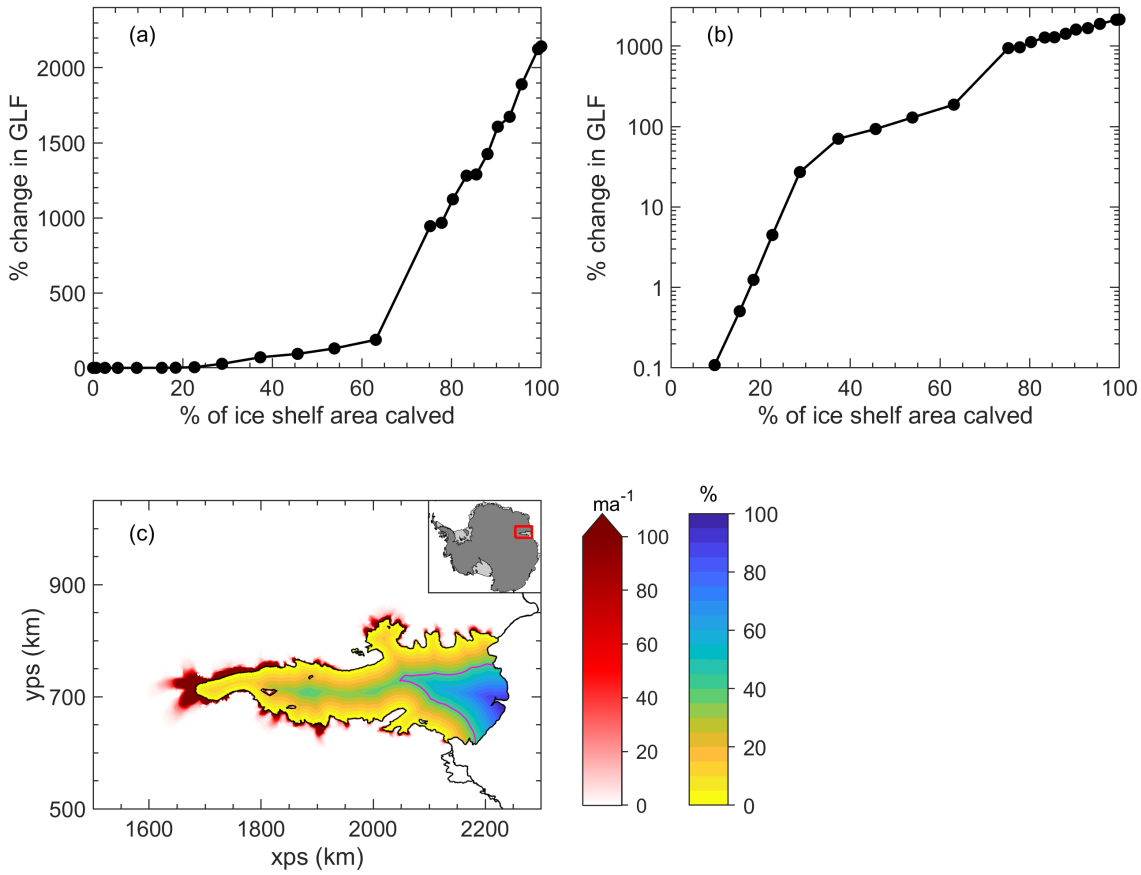

Figure 6.6: Instantaneous change in grounding line flux (GLF) for the Amery Ice Shelf. **(a)** is the response in GLF as a function of the % of the initial ice shelf area removed in the calving experiment. **(b)** is the same information plotted on a logarithmic y-axis scale for detail. **(c)** shows the distance of each ice-shelf model node from the main grounding line as a % of the maximum the GL-CF distance. The contours of this field were used to define the calving front positions in the series of calving experiments. In red is the instantaneous increase in ice velocity over the grounded ice for the complete collapse experiment (i.e. removing 100% of the ice-shelf area). The magenta contour line in the ice shelf corresponds the calving front position that results in a 10% increase in GLF, with ice downstream of this point classified as 'passive ice' by this approach.

The Totten Ice Shelf, presented in Figure 6.7, has a similar geometry to the Amery, with one long, narrow embayment downstream of the primary ice stream in the drainage basin, in this case

Totten Glacier. The total buttressing provided by Totten Ice Shelf is again significant, with an instantaneous increase in GLF of 1,320% in response to the complete removal of the ice shelf. Just as for the Amery Ice Shelf, we see that there is also a step change in the GLF response when regions of the ice shelf in the narrow, fjord-like embayment begins to be calved. Over 80% of the total buttressing capacity of the shelf comes from the first 49-58% of the ice shelf area downstream of the grounding line. Again, the exact amount of the shelf area that provides this buttressing is hard to determine due to the significant increase in GLF response between the calving fronts positioned at 30% and 25% of the maximum GL-CF distance.

In order to increase the GLF by 10%, the calving front had to be moved to between 40% and 35% of the maximum GL-CF distance downstream of the grounding line. This means that, taking the more conservative estimate again, 30% of the Totten Ice Shelf area can be considered passive.

In this section the results for the Amery and Totten Ice Shelves have been presented together, due to the similarities in their geometric settings and their GLF response curves. Despite the order of magnitude difference in their surface areas, they both consist of one primary, narrow embayment downstream of one major ice stream. The regions of passive ice shelf area for the Amery and Totten ice shelves are 22% and 30%, respectively, which maps directly to the areas of the ice shelves that lie downstream of the narrow embayment.

6.3.4 Brunt/Riiser-Larsen and Getz Ice Shelves

The response of the Brunt and Riiser-Larsen Ice Shelves – here analysed together as one ice shelf – to calving perturbations is shown in Figure 6.8. The total buttressing capacity of the ice shelf is an order of magnitude smaller than for the Amery Ice Shelf, despite its similar surface area. The instantaneous increase in GLF is 201% upon the removal of the whole shelf. The Brunt/Riiser-Larsen Ice Shelf is open and unbounded at its lateral margins, with three smaller, narrow embayments just downstream of the main tributary glaciers. It is here that the majority of the buttressing from this ice shelf system is generated. Over 80% of the total buttressing capacity is generated in the first 14% of the ice shelf area downstream of main grounding line.

A calving front positioned at 20% of the maximum GL-CF distance downstream of the grounding line produces a 10% increase in GLF. This corresponds to 48% of the Brunt/Riiser-Larsen Ice Shelf

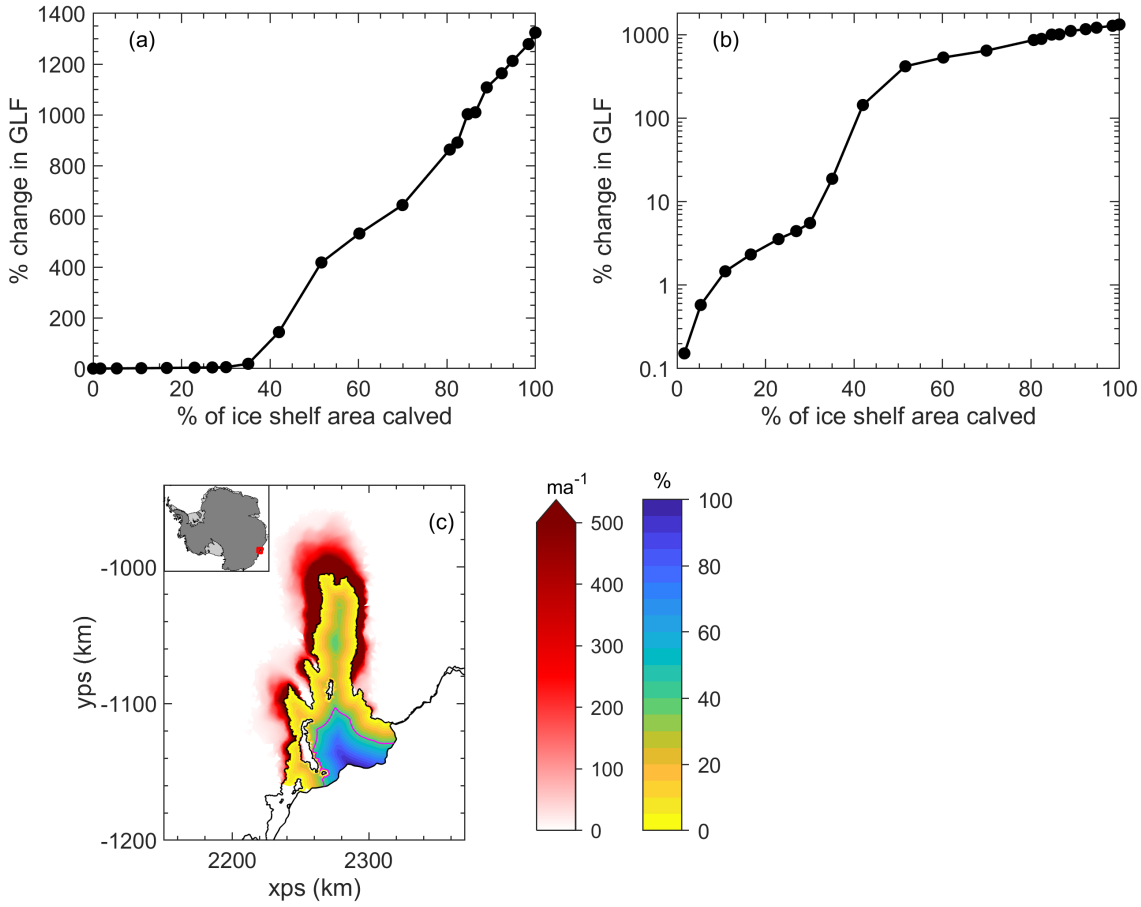

Figure 6.7: Instantaneous change in grounding line flux (GLF) for the Totten Ice Shelf. Panel **(a)** is the response in GLF as a function of the % of the initial ice shelf area removed in the calving experiment. **(b)** is the same information plotted on a logarithmic y-axis scale for detail. **(c)** shows the distance of each ice-shelf model node from the main grounding line as a % of the maximum the GL-CF distance. The contours of this field were used to define the calving front positions in the series of calving experiments. In red is the instantaneous increase in ice velocity over the grounded ice for the complete collapse experiment (i.e. removing 100% of the ice-shelf area). The magenta contour line in the ice shelf corresponds the calving front position that results in a 10% increase in GLF, with ice downstream of this point classified as 'passive ice' by this approach.

being classed as passive ice.

The Getz Ice Shelf, like the Brunt/Riiser-Larsen Ice Shelf, is not formed in a confined embayment. Figure 6.9 shows that that the total buttressing provided by the Getz Ice Shelf is comparable to that provided by the Brunt/Riiser-Larsen, with an instantaneous increase in GLF of 185% in response to the complete removal of the shelf. Interestingly, for this ice shelf we see that a larger proportion of the total buttressing is generated by the regions of the ice shelf further from the grounding line. 80% of the total buttressing capacity is generated by 82% of the ice shelf area

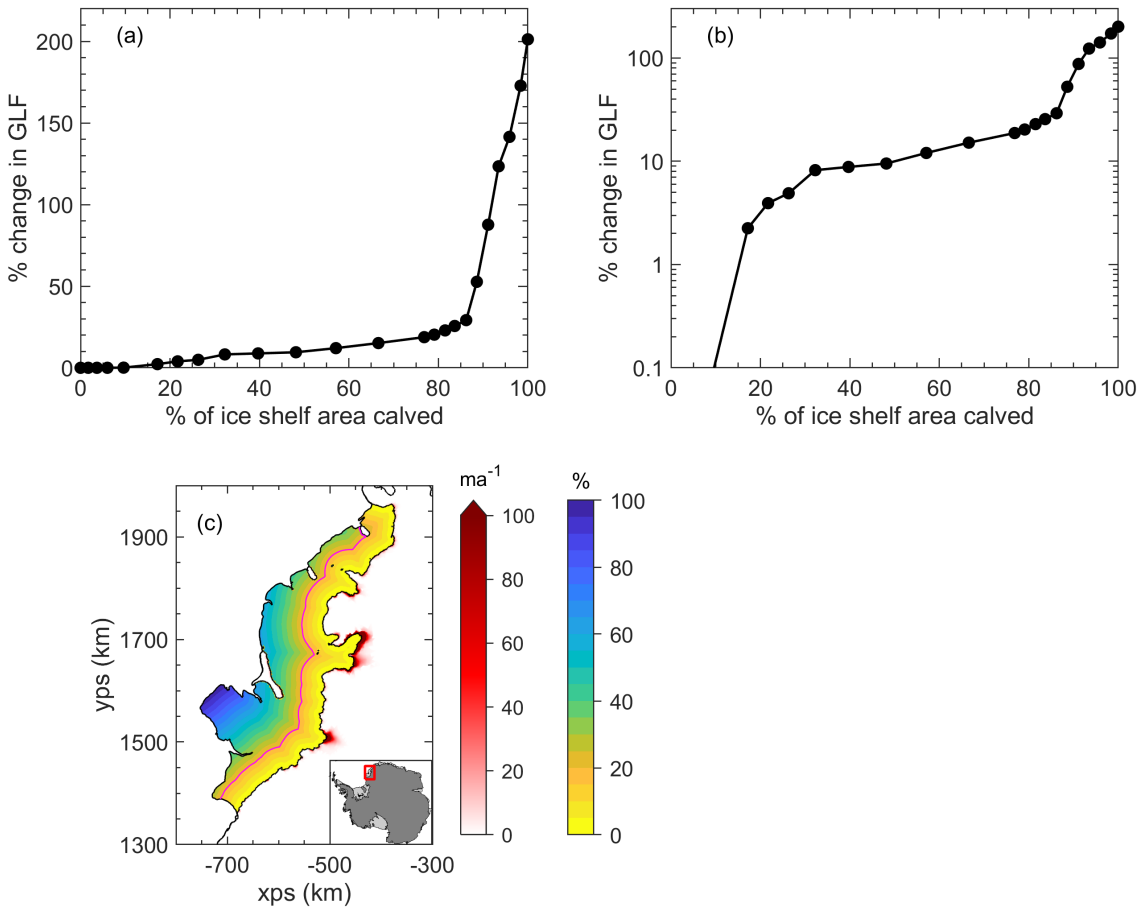

Figure 6.8: Instantaneous change in grounding line flux (GLF) for the Brunt/Riiser-Larsen Ice Shelf. Panel **(a)** is the response in GLF as a function of the % of the initial ice shelf area removed in the calving experiment. **(b)** is the same information plotted on a logarithmic y-axis scale for detail. **(c)** shows the distance of each ice-shelf model node from the main grounding line as a % of the maximum the GL-CF distance. The contours of this field were used to define the calving front positions in the series of calving experiments. In red is the instantaneous increase in ice velocity over the grounded ice for the complete collapse experiment (i.e. removing 100% of the ice-shelf area). The magenta contour line in the ice shelf corresponds the calving front position that results in a 10% increase in GLF, with ice downstream of this point classified as 'passive ice' by this approach.

downstream of the main grounding line, nearly 6 times more than the Brunt/Riiser-Larsen. This feature can also be seen by the shallower gradient in the GLF curves in Figure 6.9a and b. Examining the geometric setting of the Getz Ice Shelf, shown in Fig. 6.9c, we see that this buttressing pattern is linked to the large ice rises that stabilise the Getz Ice Shelf in its current formation.

To induce a 10% increase in GLF, the calving front has to be positioned at 60% of the maximum GL-CF distance downstream of the grounding line. This in turn means that just 9% of the Getz Ice Shelf area can be considered passive by this definition, the smallest of any of the ice shelves

analysed here.

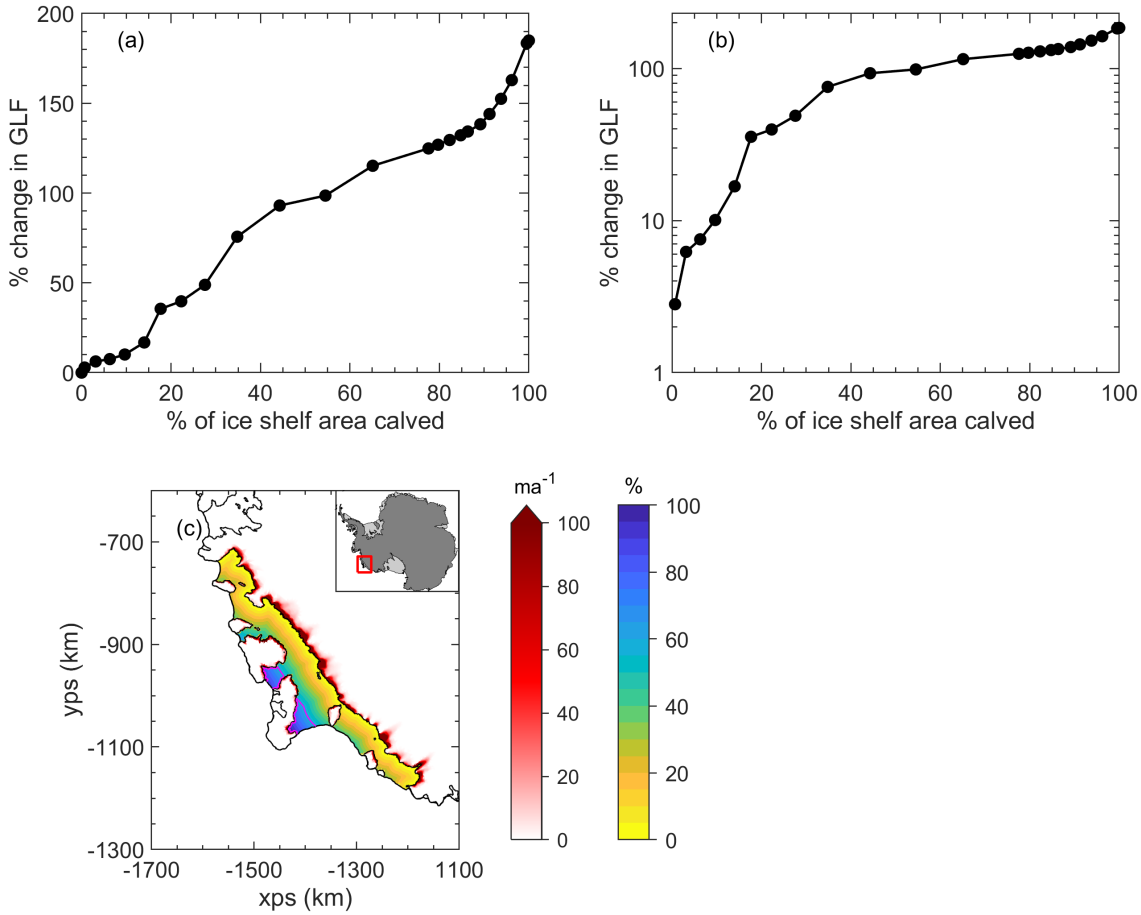

Figure 6.9: Instantaneous change in grounding line flux (GLF) for the Getz Ice Shelf. Panel **(a)** is the response in GLF as a function of the % of the initial ice shelf area removed in the calving experiment. **(b)** is the same information plotted on a logarithmic y-axis scale for detail. **(c)** shows the distance of each ice-shelf model node from the main grounding line as a % of the maximum the GL-CF distance. The contours of this field were used to define the calving front positions in the series of calving experiments. In red is the instantaneous increase in ice velocity over the grounded ice for the complete collapse experiment (i.e. removing 100% of the ice-shelf area). The magenta contour line in the ice shelf corresponds the calving front position that results in a 10% increase in GLF, with ice downstream of this point classified as 'passive ice' by this approach.

6.3.5 Pine Island Glacier and Thwaites Glacier Ice Shelves

Finally, the results for the two smallest ice shelves considered in this analysis, Pine Island Glacier Ice Shelf (PIGIS) and Thwaites Glacier Ice Shelf (TGIS) are presented. They were chosen for analysis due to their importance for the dynamics of the West Antarctic Ice Sheet.

Figure 6.10a, shows that the total buttressing provided by PIGIS is limited when compared to other ice shelves around the Antarctic Ice Sheet, with a 96% increase in GLF in response to the complete loss of the ice shelf. The buttressing provided by the ice shelf is also much more evenly distributed throughout the shelf, as was the case for the Getz Ice Shelf. For PIGIS, 80% of the total buttressing capacity is generated in the first 83% of the ice shelf area downstream of the grounding line. To induce a 10% increase in the GLF, the calving front had to be positioned at 50% of the maximum GL-CF distance, which gives a passive ice shelf area of 24% for PIGIS.

However, the limitations of taking an Antarctic-wide approach to study the buttressing of smaller ice shelves is evident when examining PIGIS. The maximum GLF response saturates towards the end of the series of perturbations, with the same GLF increase calculated for a calving front positioned at 3% of the maximum GL-CF distance downstream of the grounding as for the complete collapse of the shelf. There are in fact three data points on top of on another at the 100% of ice shelf area calved value in Figure 6.10a and b. This is due to the fact that the maximum GL-CF distance is just 54 km, such that a 1% change in the calving front position corresponds to a difference of 500m, smaller than the mesh resolution around the grounding line in this set-up. The same behaviour is observed for the other small ice shelves in this study, Totten and Thwaites.

The results for the GLF response to calving for TGIS are shown in Figure 6.11. TGIS is almost entirely unconfined, and regions of the shelf have weakened over the past decade, with some areas now being formed of icebergs held together by sea ice, rather than structural shelf ice (Miles et al., 2020). Consequently, it provides the smallest amount of buttressing to its grounding line of any ice shelf studied here, with a maximum GLF increase of 49% in response to the complete removal of the shelf. A 10% increase in GLF is generated by calving ice up to 8% of the maximum GL-CF distance, which means that 85% of TGIS can be considered passive, the largest proportion of any of the ice shelves analysed here.

6.3.6 Mesh resolution sensitivity testing

To test the sensitivity of the values found for the total buttressing capacity of these Antarctic ice shelves, the calving experiments were repeated with a mesh that had a target resolution of 500 m

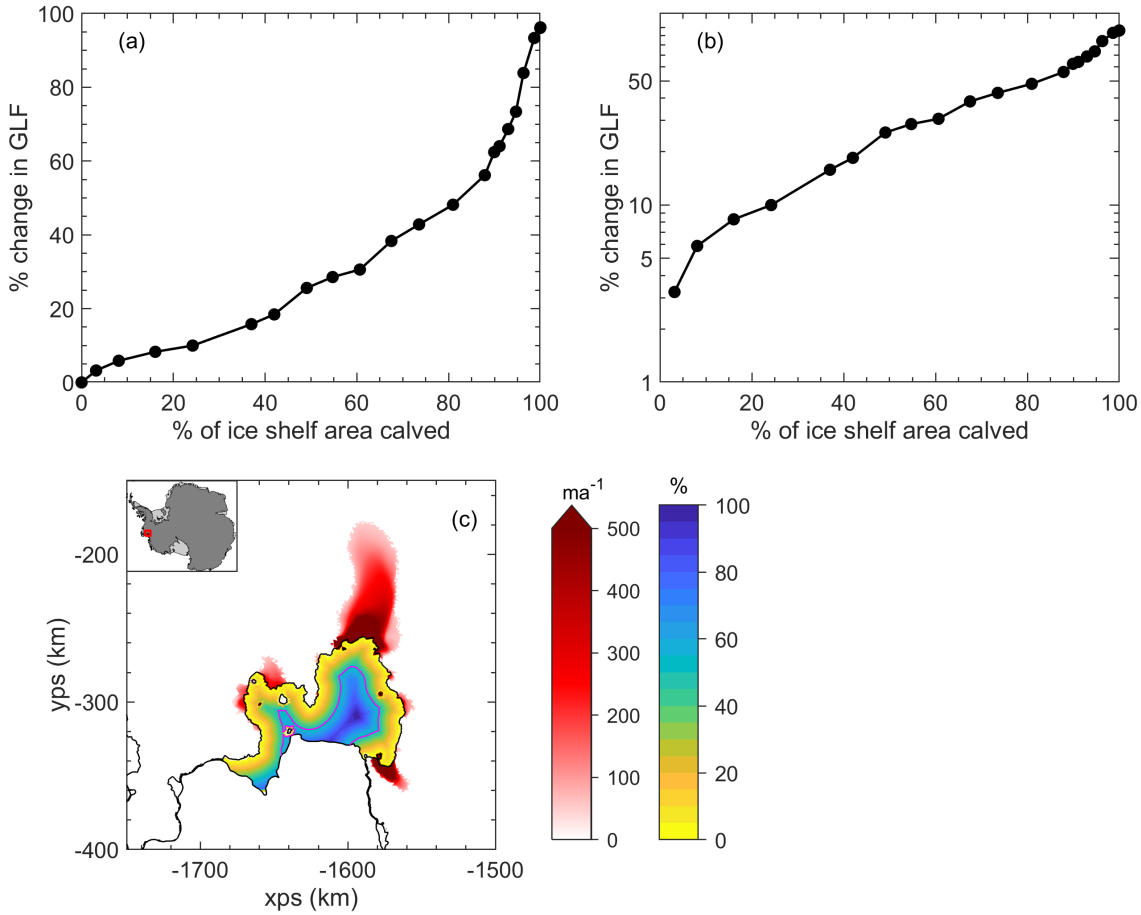

Figure 6.10: Instantaneous change in grounding line flux (GLF) for the Pine Island Glacier Ice Shelf. Panel **(a)** is the response in GLF as a function of the % of the initial ice shelf area removed in the calving experiment. **(b)** is the same information plotted on a logarithmic y-axis scale for detail. **(c)** shows the distance of each ice-shelf model node from the main grounding line as a % of the maximum the GL-CF distance. The contours of this field were used to define the calving front positions in the series of calving experiments. In red is the instantaneous increase in ice velocity over the grounded ice for the complete collapse experiment (i.e. removing 100% of the ice-shelf area). The magenta contour line in the ice shelf corresponds the calving front position that results in a 10% increase in GLF, with ice downstream of this point classified as 'passive ice' by this approach.

around the grounding line. This new finite element mesh had 1,960,000 elements and due to time constraints this meant that a new model initialisation procedure was not performed on this mesh. Instead, the fields for the rate factor, A, and the basal slipperiness, C, – as optimised from the initialisation on the coarser mesh – were linearly interpolated onto the new mesh.

Whilst a new initialisation would have been preferable – as errors can be introduced when interpolating, particularly where the grounding line position is moved as a result of using a higher resolution – this sensitivity test still provides insight into the effect of mesh resolution on the

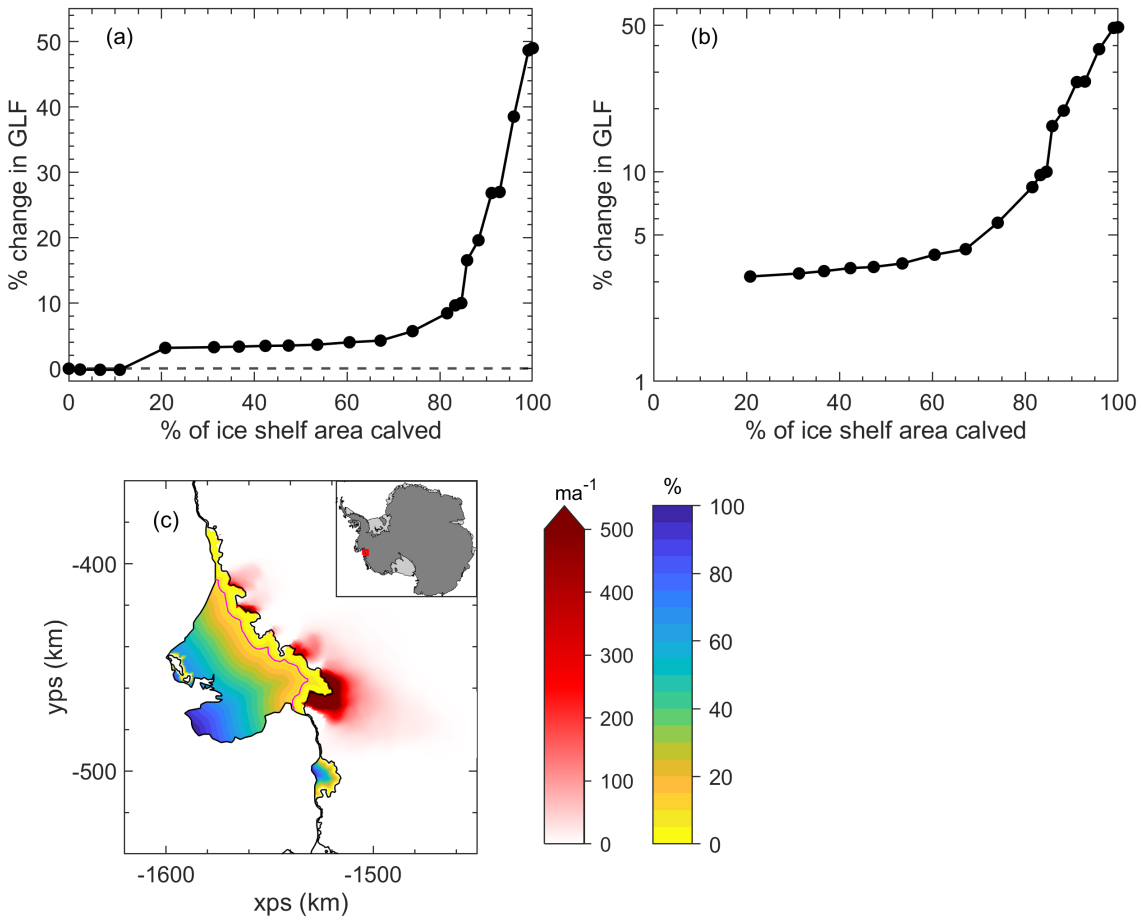

Figure 6.11: Instantaneous change in grounding line flux (GLF) for the Thwaites Glacier Ice Shelf. Panel **(a)** is the response in GLF as a function of the % of the initial ice shelf area removed in the calving experiment. **(b)** is the same information plotted on a logarithmic y-axis scale for detail. **(c)** shows the distance of each ice-shelf model node from the main grounding line as a % of the maximum the GL-CF distance. The contours of this field were used to define the calving front positions in the series of calving experiments. In red is the instantaneous increase in ice velocity over the grounded ice for the complete collapse experiment (i.e. removing 100% of the ice-shelf area). The magenta contour line in the ice shelf corresponds the calving front position that results in a 10% increase in GLF, with ice downstream of this point classified as 'passive ice' by this approach.

calculated buttressing capacity of the ice shelves. The results of this sensitivity test are presented in Table 6.2.

It is clear that the necessity of using a mesh of finite resolution around the grounding line means that the total buttressing capacity of each of the ice shelves is underestimated. By increasing the resolution around the grounding line, the maximum GLF response is increased for every ice shelf analysed, and consequently a greater proportion of the total buttressing would be found to be generated just downstream of the grounding line. However, the form of the curves in Figs. 3-11 is

Table 6.2: Sensitivity testing of the GLF dependence on the mesh resolution use around the grounding line.

Ice shelf	Total buttressing (max GLF % increase)	
	1 km GL resolution	500 m GL resolution
Filchner-Ronne	3,090	3,130
Ross	802	959
Amery	2,140	2,220
Larsen C	315	361
Brunt/Riiser-Larsen	201	227
Getz	185	339
Totten	1,320	1,430
Pine Island	96	119
Thwaites	49	76

unlikely to be changed significantly. Additionally, this higher mesh resolution at the grounding line is not likely to affect the quantification of the amount of passive ice present in each ice shelf, as this is determined by the calving front position when the GLF increases by 10% and this is typically significantly downstream of the grounding line.

The larger proportional increase in the total buttressing capacity of the Getz Ice Shelf is caused by the higher mesh resolution allowing for ice in a small embayment downstream of a large tributary glacier to be calved. With element sizes of 1,000 m, the ice in this region of the shelf was not removed, as all mesh nodes in this part of the shelf belonged to elements which crossed the grounding line. This, again, demonstrates the extent to which the generation of ice-shelf buttressing can be concentrated in narrow embayments close to the grounding line.

6.3.6.1 Maximum GLF response for the LCIS

Comparing the difference between the total buttressing calculated for the LCIS with the two different mesh resolutions, we see that the increase in resolution has not significantly increased the maximum GLF. Although the 500 m mesh resolution around the grounding line is closer to that of the mesh used in Chapter 4 (with a grounding line resolution of 250 m), and has the same nominal resolution around the grounding line as the mesh used in Chapter 5, the instantaneous change in GLF is still reduced in comparison to the results from both previous chapters following the complete collapse

of the ice shelf.

Instead, the primary cause for the difference in GLF increase is attributed to the difference in the initial stress state in the ice, prior to the perturbation. Figure 6.12 shows the fields for the rate factor, A, and basal slipperiness parameter, C, over the LCIS domain following the Antarctic-wide model initialisation. The equivalent fields following the LCIS-specific model initialisation can be seen in Figure 4.4. Figure 6.13 then shows the difference in the modelled ice speed following the initialisation performed in Chapter 4 and the initialisation performed in this chapter. The significant differences in ice speed mean that the stress balance in the ice shelf and across the grounding line will also be different. For example, the lower spatial resolution in the Antarctic-wide initialisation means that the shear margins are less well resolved (compare Fig. 6.12a with Fig. 4.4a), which may limit the magnitude of the lateral shear stresses generated and alter the modelled buttressing capacity. Similarly, differences in the basal slipperiness parameter close to the grounding line will change the extent to which basal drag and ice-shelf buttressing balance the driving stress, resulting in a different response to perturbations in the ice-shelf geometry. In the Antarctic-wide set-up, the LCIS is found to be providing less total buttressing to its grounded tributary glaciers than when the stress state was inferred in the more highly resolved model initialisation performed in Chapter 4. This suggests that further work, with more localised, high resolution studies of individual ice shelves may be required to more accurately determine the total buttressing capacity of Antarctica's ice shelves.

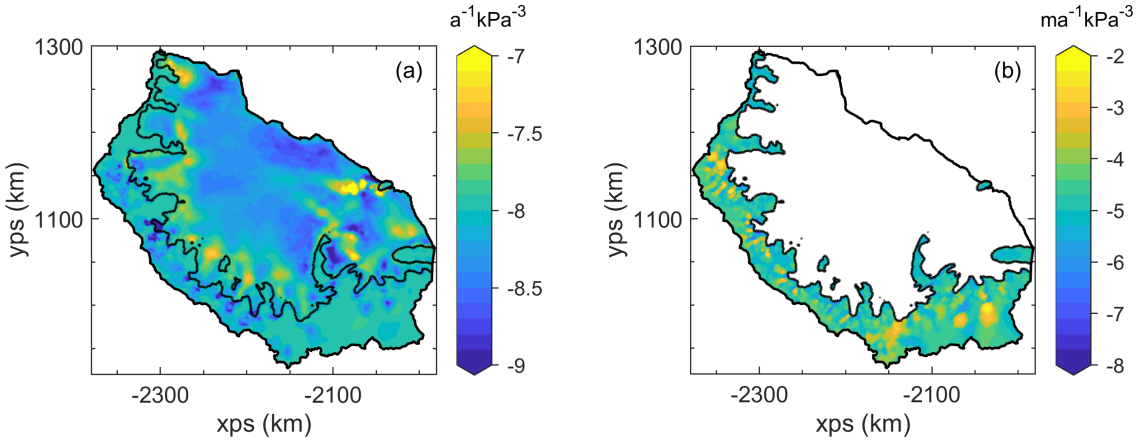

Figure 6.12: Maps of **(a)** the rate factor, A, in Glen's flow law (Eq. 3.5) and **(b)** the basal slipperiness, C, in the Weertman sliding law (Eq. 3.11) over the LCIS after model initialisation over the whole Antarctic domain. The colour bars have been saturated to allow the spatial detail in both parameters to be clearly seen.

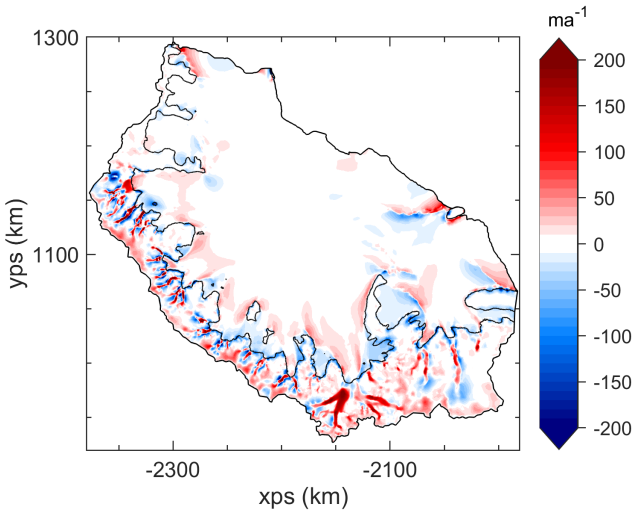

Figure 6.13: A map of the difference in the ice velocity over the LCIS and its tributary glaciers between the 'LCIS specific' initialisation performed in Chapter 4 and the Antarctic-wide model initialisation performed in this chapter. The field plotted is the 'LCIS specific initialisation' ice speed minus the 'Antarctic-wide initialisation' ice speed.

6.4 Discussion

In this chapter, for the first time, the total buttressing capacity of a selection of the major ice shelves of the AIS has been calculated. Previous work that has examined ice-shelf buttressing on an Antarctic scale has either: focussed on the sensitivity of the GLF to small perturbations in the ice shelf thickness (Reese et al., 2018b) or observed thinning patterns (Gudmundsson et al., 2019); calculated local buttressing numbers in the ice shelves and explored the sensitivity of fluxes across new ice-shelf calving fronts to calving events (Fürst et al., 2016); or explored the transient evolution of the ice sheet to the complete loss of ice-shelf buttressing (e.g. Martin et al., 2019, Sun et al., 2020).

The total buttressing capacity of Antarctic ice shelves is found to vary by two orders of magnitude, from the FRIS – with a maximum increase in GLF of 3,086% upon the complete removal of the shelf – to the TGIS, where the instantaneous increase in GLF is 49% when the entire ice shelf is removed. This difference in the total buttressing capacity of the shelf cannot be determined by sensitivity studies, nor can it be determined from theoretical arguments, but it requires the calculation of the stress state at the grounding line in the presence of (and in the absence of) the

ice shelves, as performed here. These changes in stress states at the grounding line in response to calving perturbations have been expressed as instantaneous changes in GLF, in line with previous studies exploring ice-shelf buttressing. By computing the relative changes in GLF in response to calving, it has allowed the buttressing capacity of ice shelves which vary in size by two orders of magnitude to be compared.

6.4.1 Ice-shelf buttressing and geometry

A commonality amongst the ice shelves of different scales and geometries studied here is the concentration of the buttressing capacity in the narrow embayments just downstream of the main tributary glaciers. This was diagnosed for the LCIS in Chapter 4, and the same pattern of GLF response has here been found for the FRIS and Ross Ice Shelf. Even for the Brunt/Riiser-Larsen Ice Shelf, which is a largely unconfined ice shelf, the buttressing that it does provide is almost entirely generated within the three small embayments just downstream of the main tributary glaciers. For these ice shelves, when the geometry is characterised by narrow embayments close to the main grounding line, over 80% of the total buttressing comes from the first 12-15% of the ice shelf area downstream of the grounding line.

For the ice shelves formed in one primary, narrow embayment – the Amery and Totten Ice Shelves – the passive ice areas, 22% and 30% respectively, correspond to regions of the ice shelf that are downstream of the embayments, where the ice shelf becomes unconfined and begins to laterally spread. Whilst there is the potential for these unconfined regions to provide resistance to the grounding line through hoop stresses, these are typically insignificant in Antarctic settings (Wearing et al., 2020).

The fact that the majority of ice-shelf buttressing can be generated from relatively small regions of confined ice shelf is linked to the theoretical analysis of Haseloff and Sergienko (2018), who showed that the amount of buttressing generated by an ice shelf depends strongly on the ice shelf width and length, i.e. its aspect ratio. In the narrow embayments close to the grounding line, the effective width-to-length ratio of the shelf is significantly reduced compared to regions in the larger over-arching embayment, and much larger resistive shear stresses can be generated, leading to higher levels of buttressing.

The finding that buttressing is heavily concentrated downstream of tributary glaciers is entirely in agreement with the results of Reese et al. (2018b) (see their Fig. 1). It is not surprising that such a close agreement should be seen, as the method employed here also considers the impact of ice-shelf perturbations on the instantaneous change in GLF. However, with the approach taken in this chapter the *total* buttressing capacity of each shelf can be quantified, rather than just the sensitivity of the GLF to small thickness perturbations. It also allows for the distribution of that total buttressing between different regions of the ice shelves to be determined. In that sense, the findings of this chapter should be seen as complementary to those of Reese et al. (2018b).

Because the total buttressing capacity of many Antarctic ice shelves is so heavily concentrated close to the grounding line, the response in GLF is particularly sensitive to the exact location of the calving front position when it is close to the grounding line. It is therefore imperative that ice sheet models that examine the impact of significant calving events, or ice-shelf collapse, ensure that the calving front position is accurately determined. In Chapter 5, it was shown for the LCIS that not only is the instantaneous change in GLF sensitive to the exact calving front position, but that there were also significant differences in the transient mass loss between experiments in which the calving front positions differed by just 1 km.

Another consideration that follows from the concentration of buttressing capacity close to the grounding line is in the potential impact of ice-shelf hydrofracture and ice-shelf collapse on grounded ice dynamics. Lai et al. (2020) mapped regions of Antarctica's ice shelves that would potentially be vulnerable to hydrofracture (based on the stress state in the ice) in a hypothetical scenario in which surface melting was widespread across all Antarctic ice shelves. By comparing this vulnerability map with the map of passive shelf ice produced by Fürst et al. (2016), they determined that around 60% of Antarctica's ice shelves were both vulnerable to hydrofracture and provided buttressing. However, in addition to the fact that much more of Antarctica's ice shelves could be considered passive by the definition used in this chapter, it is also the case that the regions of the ice shelves found to be least vulnerable to hydrofracture were precisely those regions in the narrow embayments just downstream of the grounding line (see Lai et al. (2020) Extended Data Figure. 8b), which have been shown here to generate the majority of the buttressing capacity of major Antarctic ice shelves. Therefore, even in the hypothetical future scenario in which all of Antarctica's ice shelves were inundated with

surface meltwater, and widespread hydrofracture driven ice-shelf collapse was possible, key regions of the ice shelves – in which the majority of their buttressing capacity is generated – could remain intact and continue to provide resistance to their tributary glaciers and ice streams.

6.4.2 Ice rises and passive ice areas

By defining passive ice shelf ice as that which can be calved without inducing a greater than 10% increase in GLF, the proportion of passive ice is found to be larger than that calculated by Fürst et al. (2016) for every ice shelf studied here. Taking the FRIS as an example, the proportion of passive ice increases from 6.8% to 26% under this change of definition. The 'maximum buttressing' numbers calculated along the western edge of Berkner Island are large (see Fürst et al. (2016) Fig. 1), and Reese et al. (2018b) also find their buttressing flux response number to be elevated in this region (see their Fig. 1) and highlight it as a key area of 'tele-buttressing' (see their Fig. 3a). However, in this chapter, it is found that ice in this region can be calved from the shelf without inducing an increase in GLF of more than 10%, demonstrating that it contributes a limited amount towards the total buttressing capacity of the FRIS.

The role of ice rises in the buttressing of ice at the grounding line has also been illuminated by these experiments. For the Getz Ice Shelf, which is supported by a number of ice rises, the total buttressing of the ice shelf is more evenly distributed throughout the shelf, with 80% of the total buttressing actually being generated by more than 80% of the total ice shelf area. Other ice shelves which contain ice rises, such as the Brunt/Riiser-Larsen and LCIS, do not see an equivalent, even distribution of ice-shelf buttressing. Matsuoka et al. (2015) state that "the net effect of an ice rise on the flow of grounded ice depends on the ice rise's location within an ice shelf". Here, we find that the geometry of the ice shelf upstream of the ice rise, and close to the grounding line, is key to determining the importance of an ice rise for ice-shelf buttressing. In a shelf with narrow embayments at the grounding line – like the LCIS or FRIS – the ice rises at the calving front are less likely to generate significant proportions of the total buttressing capacity of the shelf. This highlights one of the key benefits of the approach taken in this chapter to quantify the total buttressing capacity of ice shelves. Studies that examine the sensitivity of the GLF to ice-shelf perturbations, or calculate local buttressing numbers, tend to find increased values around ice rises

(e.g. upstream of the Gipps Ice Rise on the LCIS (Borstad et al., 2013)) even when they do not provide a significant proportion of the total buttressing capacity of the ice shelf.

6.4.3 Pine Island Glacier and Thwaites Glacier Ice Shelves

For both PIGIS and TGIS, the total amount of buttressing generated is relatively small compared with other Antarctic ice shelves, with instantaneous increases in GLF of 96% and 49% respectively upon complete removal of the shelves. De Rydt et al. (2021) demonstrated that the buttressing capacity of PIGIS was reduced between 1996 and 2016 – with an equal amount being lost due to calving front retreat as to basal melting – leading to the observed increase in discharge and its current mass imbalance (Rignot et al., 2019). Likewise TGIS has seen its buttressing capacity reduced due both to ocean forced increases in basal melting (Seroussi et al., 2017) and the fracturing of the Thwaites Glacier Ice Tongue into mélange and the weakening of its shear margin (Miles et al., 2020). This loss of ice-shelf buttressing from TGIS over recent decades may have already triggered the irreversible retreat of Thwaites Glacier through the marine ice sheet instability (Joughin et al., 2014).

A feature of the buttressing provided by PIGIS found in this analysis is that a smaller proportion of its total buttressing capacity is concentrated at the grounding line compared with what one could expect from an ice shelf in its geometric setting in a confined embayment. The shear margins within PIGIS are actually located towards the centre of the ice shelf, directly downstream of where Pine Island Glacier enters the shelf (e.g. Alley et al., 2019, Lhermitte et al., 2020). This is different to the other ice shelves studied, in which the shear margins – where the largest lateral shear stress gradients are generated – are located closer to the the grounding line. For PIGIS the shear margin extends all the way to the calving front through the centre of the embayment, leading to the more equal distribution of buttressing capacity throughout the shelf area. This finding is in agreement with a recent study that attributed an increase in the GLF of Pine Island Glacier to calving front retreat on PIGIS in the period from 2017-2020 (Joughin et al., 2021), and again emphasises that it is the relationship between the geometry of an ice shelf and its rheology that can determine an ice shelf's buttressing capacity.

6.4.4 Concluding remarks

With the method employed in this chapter, the exact location in which buttressing is generated within a 'band' of ice shelf that is calved in a perturbation experiment cannot be determined. To illuminate this, it is the approach of Reese et al. (2018b) which gives insight. As their map of buttressing flux response numbers show, ice shelf regions directly downstream of tributary glaciers and ice streams are where the GLF is most sensitive to ice-shelf perturbations. Regions which are downstream of stagnant ice, whilst close to the grounding line, do not generate significant buttressing forces (see Reese et al. (2018b) Fig. 1b and c), something which the calving method used in this chapter cannot differentiate.

It is important to note once more that the process of ice-shelf buttressing is separate, but intimately linked, to that of the transient mass redistribution in response to a change in ice-shelf buttressing. Here, only the instantaneous response to ice-shelf calving, and hence changes in buttressing, is examined. The two preceding chapters have shown that, whilst the LCIS provides a significant buttressing force to its grounded tributary glaciers, the transient mass loss in response to the loss of the shelf is limited. On the other hand, numerical studies have found that changes in ice-shelf buttressing observed at PIGIS, through calving and melting, have had a significant impact on the grounded ice dynamics (e.g. Favier et al., 2014, De Rydt et al., 2021, Joughin et al., 2021). This is despite the finding here that the total buttressing capacity of PIGIS is limited when compared with other Antarctic ice shelves. A significant buttressing capacity does not imply that the transient mass redistribution in response to the loss of that buttressing will be large, whilst a lack of buttressing does also not mean that its reduction will necessarily lead to negligible changes in the transient response of the grounded tributary glaciers. The transient response of a glacier to a loss of buttressing is largely determined by the bedrock topography upstream of the grounding line (e.g. Seroussi et al., 2017, Nias et al., 2018).

6.5 Conclusions

In this chapter, an Antarctic-wide ice flow model set-up has been used to explore the buttressing capacity of nine major ice shelves around the AIS. To do this, a series of calving experiments were

performed, based on a 'proportional distance from the main grounding line' metric, such that they could be equally applied to ice shelves that vary by two orders of magnitude in area. Following each calving front perturbation, the instantaneous change in GLF was calculated. This approach allowed the total buttressing capacity of these ice shelves to be calculated for the first time. It was found that the total buttressing capacity varies by two orders of magnitude around the continent, with the FRIS having the largest buttressing capacity – as measured by a 3,086% increase in GLF upon the removal of the entire ice shelf – and the TGIS having the smallest, with a GLF increase of 49% upon the complete removal of the shelf.

As was found for the LCIS in Chapter 4, the majority of the ice-shelf buttressing for most ice shelves studied here is generated close to the grounding line, in narrow embayments just downstream of the main tributary glaciers. Whilst previous work has demonstrated that GLF is most sensitive to perturbations in ice-shelf thickness in the embayments downstream of the grounding line, the method employed here allows for the quantification of the proportion of the total buttressing that arises from these areas. For the FRIS, Ross Ice Shelf, LCIS and Brunt/Riiser-Larsen Ice Shelf – that all have a number of narrow embayments at their grounding lines – over 80% of the total buttressing capacity of the shelves is generated by between 12% and 15% of the ice shelf area downstream of the grounding line. It is the regions that generate the majority of the buttressing capacity that are also likely to be the most resistant to ice-shelf hydrofracture due to the more compressive stress regime in the ice (Lai et al., 2020).

Two shelves that exhibit different buttressing patterns are the Getz Ice Shelf and PIGIS. For the Getz Ice Shelf, the lack of any narrow embayments close to its grounding line means that the stabilising ice rises that are present at the ice-shelf calving front make a significant contribution to the buttressing of the grounding line, with 80% of the total buttressing capacity being generated by more than 80% of the total ice shelf area. This is in contrast to the LCIS, in which the ice rises were found to provide very limited amounts of buttressing to the grounding line. For PIGIS, the ice-shelf buttressing is also less concentrated at the grounding line, due to the fact that the shear margins within the shelf are located centrally within the embayment, downstream of where Pine Island Glacier enters the shelf, and extend all the way to the calving front. Therefore, by the methods used in this chapter it is found that 80% of the total buttressing capacity of PIGIS is also

generated by more than 80% of the total ice shelf area downstream of the grounding line.

By defining passive ice as that which can be calved without inducing a 10% increase in GLF, much more of Antarctica's ice shelves are determined to be passive than in previous work (Fürst et al., 2016). The areas in which buttressing is found to be most concentrated align with the map of buttressing flux response number produced by Reese et al. (2018b). The findings of this chapter can be seen as complimentary to that work, as not only is the GLF most sensitive to perturbations in the ice shelf applied in narrow embayments close to the grounding line, but this is where the vast majority of the total buttressing capacity of these ice shelves is generated.

Chapter 7

On the validity of the stress-flow angle metric for ice-shelf stability

Preface

A version of this chapter – shortened to comply with the requirements of the journal – has been accepted for publication in the *Journal of Glaciology* with the following citation:

"**Mitcham, T.**, Gudmundsson, G. H. (in press): On the validity of the stress-flow angle metric for ice-shelf stability, Journal of Glaciology."

The author contributions were as follows: I (TM) initiated the investigation of the stress-flow angle, carried out the analysis and wrote the manuscript. GHG advised on the analysis and provided comments on the manuscript.

7.1 Introduction

In their paper examining the impact of marine ice on the structural integrity of the Larsen C Ice Shelf (LCIS), Kulessa et al. (2014) argue that the angle between the ice velocity vector and the direction of the first principal stress at any point in an ice shelf – the *stress-flow angle* – can be used as a "first-order criterion on which to judge an ice-shelf's stability". While we have not been able to find an exact mathematical definition of the stress-flow angle in Kulessa et al. (2014), or in any of the papers subsequently using this metric, it appears reasonable to conclude from their description

that it can be calculated as

$$\cos\theta = \frac{\boldsymbol{u} \cdot \boldsymbol{P}_1}{\|\boldsymbol{u}\|\|\boldsymbol{P}_1\|} \tag{7.1}$$

where θ is the stress-flow angle, $\boldsymbol{u}$ is the ice velocity vector, and $\boldsymbol{P}_1$ is the first principal stress vector.

Here, we demonstrate that Eq. 7.1 is not *frame-indifferent*, outline why this creates problems for determining the calving front dynamics or stability of an ice shelf with this metric, and emphasise that the principle of frame-indifference must hold for any metric or relation which seeks to give insight into the dynamics of an ice shelf.

Before proceeding further with our short overview of this topic, we like to clarify our use of the terms *(in)stability* and *structural integrity*. We use the term *calving instability* to refer to the process of self-sustained ice-shelf collapse through calving-front retreat, and we use the term *structural integrity* to describe the ability of an ice shelf to withstand internal and external forces without failing due to fracture. Hence, in our terminology, an isolated calving event could be ascribed to a lack of structural integrity, whilst a calving instability only occurs when an initial calving event creates the conditions for further calving events, resulting in a run-away process of calving-front retreat.

The introduction of the stress-flow angle by Kulessa et al. (2014) is motivated by observations that rifts on ice shelves tend to form perpendicular to the direction of ice flow. By also assuming that rifts tend to open up when orientated perpendicular to the direction of maximum tensile stress (the first principal stress direction), it follows that when the angle between the ice velocity vector, $\boldsymbol{u}$, and the first principal stress vector, $\boldsymbol{P}_1$ – the stress-flow angle – approaches zero, rift growth would be promoted. They suggest that a calving front situated in a region of low stress-flow angles could result in an unstable frontal retreat. Conversely, a stress-flow angle close to 90 degrees (when the maximum tensile stress is aligned along the rifts) would act to suppress rift growth. They used the stress-flow angle to analyse the conditions leading to the collapse of the Larsen B Ice Shelf (LBIS) in 2002, and found that stress-flow angles at the calving front of the LBIS were near-zero following the 1995 calving event, and argued that this led to its eventual large-scale demise in early 2002. For the LCIS, again using the stress-flow angle as a "first-order criterion", they concluded that the calving events between 1995 and 2002 on the LBIS "might serve as a plausible blue-print

for Larsen C's future".

Jansen et al. (2015) used the stress-flow angle approach to analyse the LCIS, in particular by examining the growing rift that would eventually result in the calving of the A68 iceberg in 2017 (Hogg and Gudmundsson, 2017). Their work suggested that the propagation of the rift – and the subsequent calving of a large, tabular iceberg – could lead the new ice shelf calving front to be in an unstable configuration. In their study of the Wilkins Ice Shelf, Rankl et al. (2017) explored a number of metrics for categorising ice-shelf stability, including the stress-flow angle, and concluded that it did not provide any additional information beyond that already contained in the principal stresses and strain rates. Borstad et al. (2017) also calculated the stress-flow angles for the LCIS and assessed its use as a stability criterion. They suggested that – because this metric does not consider the magnitude of the stresses – its use is limited in understating how rifts would propagate through the ice shelf. They also stated that it cannot account for regions of high stress-flow angle in which the second principal stress (by definition perpendicular to the first principal stress direction) is also tensile, meaning that rift growth would still be promoted.

7.2 Theory

7.2.1 Frame-indifference

One of the foundations of classical mechanics is that the laws of physics should be the same in different inertial reference frames – i.e. they must have the same form under a Galilean transformation. No measurements or experiments should privilege one inertial reference frame over another. In continuum mechanics this is encompassed in the principle of *frame-indifference* (e.g. Jog, 2015; pp. 204), which is typically introduced as a somewhat stricter condition, also requiring invariance with respect to time-dependent frame rotation and velocity, and including the Galilean transformation as a special case. However, any relation which is not objective under a Galilean transformation, is also not frame-indifferent.

To illustrate this principle we consider two observers in different inertial reference frames, labelled S (with coordinates x, y and t) and S' (x', y' and t'). The frame S' is moving at a constant velocity v_x relative to S in the positive x direction, and v_y relative to S in the positive y

direction. Their origins coincide at $t = t' = 0$.

The coordinates in the two reference frames are related to one another through the following Galilean transformation

$$\begin{aligned} x' &= x - v_x t, \\ y' &= y - v_y t, \\ t' &= t. \end{aligned} \tag{7.2}$$

Differentiating these with respect to t (or t') gives the corresponding transformation for velocities between the two frames

$$\begin{aligned} u'_x &= u_x - v_x, \\ u'_y &= u_y - v_y. \end{aligned} \tag{7.3}$$

where u'_x and u'_y are the ice velocity components in the x and y directions as measured in S', and u_x and u_y are the same components of ice velocity, but measured in S. From this, we can see that velocity vectors are not invariant under a Galilean transformation.

7.2.2 Ice flow

The governing equations of ice flow – derived from the laws of the conservation of mass and momentum – are frame-indifferent by construction. The only other way in which the frame-indifference of the governing equations could be broken is through the constitutive relation, which in ice flow modelling is typically Glen's flow law (Eq. 7.5) (Glen, 1955). Therefore, one of the criteria for an admissible constitutive relation is that it must be frame-indifferent. Glen's flow law is no exception, as it relates the stress and strain-rate tensors and their invariants, which most textbooks on continuum mechanics will demonstrate are all frame-indifferent. It follows that the closed set of governing equations for ice flow are therefore frame-indifferent, and as a consequence the analysis of the subsequent dynamics will be independent of the choice of reference frame.

We now apply the Galilean transformation to the relevant quantities used for calculating the stress-flow angle to demonstrate its lack of frame-indifference.

Here, the ice velocity is defined as $\boldsymbol{u} = (u_x, u_y)^T$, and the corresponding components of the strain rate tensor in the ice are given by

$$\dot{\epsilon}_{ij} = \frac{1}{2}\left[\frac{\partial u_i}{\partial x_j} + \frac{\partial u_j}{\partial x_i}\right]. \tag{7.4}$$

Glen's flow law is given by

$$\dot{\epsilon}_{ij} = A\,\tau^{(n-1)}\tau_{ij} \tag{7.5}$$

where $\dot{\epsilon}_{ij}$ are the components of the strain rate tensor, τ_{ij} are the components of the deviatoric stress tensor, τ is the second invariant of the deviatoric stress tensor, given by

$$\tau = \sqrt{\tau_{ij}\tau_{ij}/2} \tag{7.6}$$

and the rate factor, A is a constant which depends on the material properties of the ice. Typically the creep exponent $n = 3$. From these equations, we see that the components of the deviatoric stress tensor only depend on the spatial gradients in ice velocity (the strain rates), and not their absolute values. For an isotropic flow law, as used here, the first principal stress direction is the same whether calculated using deviatoric or Cauchy stresses, and therefore the stress-flow angle is identical in either case.

7.2.3 Transforming equations for stress-flow angle

For completeness we show here how the strain rates are independent of the relative velocity vector, $\boldsymbol{v}$, between two inertial frames.

Taking the spatial derivatives of the ice velocity in the S' reference frame returns the strain rates, from which, using the constitutive relation (Eq. 7.5), the stress field in the ice can be calculated. Differentiating Eqs. (7.3) with respect to x' gives the following transformation for the strain rates

$$\frac{\partial u'_x}{\partial x'} = \frac{\partial u_x}{\partial x'} - \frac{\partial v_x}{\partial x'},$$
$$\frac{\partial u'_y}{\partial x'} = \frac{\partial u_y}{\partial x'} - \frac{\partial v_y}{\partial x'}. \tag{7.7}$$

The second terms on the right hand side of both equations are zero as v_x and v_y are constants. The result is the same for the derivatives with respect to y'. We therefore see that the spatial gradients of the velocity field are the same in both inertial reference frames. The fact that the strain rates are unchanged by a change in frame means that the components of the stress tensor are also left unchanged by the transformation (from Eq. 7.5). Finally, to calculate the stress-flow angle we use Eq. (7.1), with the velocity and first principal stress vectors defined in their respective reference frames.

As previously stated, the first principal stress vector is invariant under the transformation between frames, but the velocity vector is not (Eqs. 7.3). Therefore, θ will also be changed under the Galilean transformation, violating the principle of frame-indifference. Because the stress-flow angle is a metric that is calculated point-wise across an ice shelf to determine, locally, the structural integrity and calving-front stability, this lack of frame-indifference raises problems for its use as a physical description of these processes. We now highlight this with an example on the LCIS.

7.3 Larsen C Ice Shelf case study

Here, we use the Úa ice flow model (Gudmundsson, 2020) to calculate the stress-flow angles on the LCIS in two inertial reference frames. The first principal stress vector, $\boldsymbol{P}_1$, is obtained by finding the eigenvector of the deviatoric stress tensor, $\boldsymbol{\tau}$, with the largest corresponding eigenvalue. This is the direction in which the normal, tensile stress in the ice is maximised.

The model set-up and the data assimilation to initialise the model and to calculate the ice velocities is as described in Chapter 4. To summarise, we use the ice thickness, bedrock and surface elevation data from BedMachine Antarctica v2 (Morlighem et al., 2020). We also use the firn air content field from this data set to calculate a horizontally spatially variable ice density. The (horizontally) spatially variable rate factor, A (in Eq. 7.5) was determined through inverse methods,

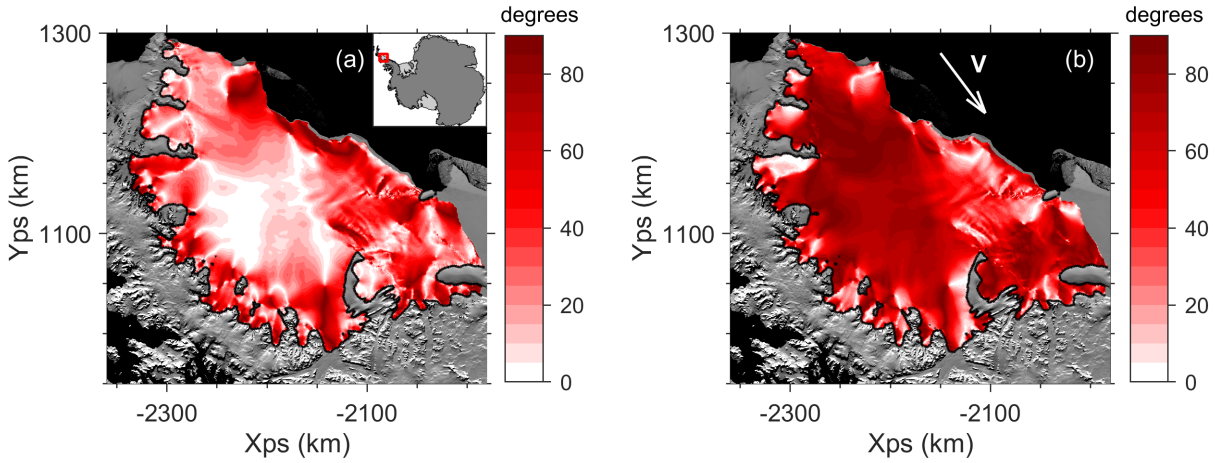

Figure 7.1: The stress-flow angle, calculated for the LCIS in two different inertial reference frames overlain on a MODIS Mosaic of Antarctica image (Scambos et al., 2007), with the grounding line plotted in black. **(a)** corresponds to a frame (S) at rest with respect to the bedrock below the ice shelf, and **(b)** a frame (S') moving with at a constant velocity $\boldsymbol{V}$ of 3 km a^{-1} in the positive x direction and -4 km a^{-1} in the positive y direction with respect to S, in a polar stereographic coordinate system. This relative velocity is shown by the labelled arrow in panel **(b)**. The large differences in stress-flow angle between the two frames, particularly in the centre of the shelf, show that the two observers would reach different conclusions about the structural integrity of the shelf, violating the principle of frame-indifference.

by minimising a cost function consisting of a misfit term and a regularisation term. The misfit term included modelled ice velocities and observations taken from the MEaSUREs InSAR-based Antarctic Ice Velocity v2 data set (Rignot et al., 2017; 2011, Mouginot et al., 2012).

With the modelled stresses and ice velocities, we first calculate the stress-flow angle in a frame at rest with respect to the bedrock below the ice shelf – frame S – using Eq. (7.1). We then calculate the stress-flow angle again in a different frame, S', moving with a constant velocity of 3 km a^{-1} in the positive x direction and -4 km a^{-1} in the positive y direction with respect to S. To make this transformation from S to S', we simply use Eqs. (7.3) to update the ice velocities calculated in the model. The resulting fields for the stress-flow angle in S and S' are shown in Fig. 7.1.

From the two maps, we see that the observers in S and S' will measure very different values of the stress-flow angle. Therefore, they will also draw different conclusions about the structural integrity of the ice shelf and the stability of its calving front position from this metric. The future behaviour of the ice shelf would then confirm or privilege one observer's measurement over the other's, violating the principle of frame-indifference.

7.4 Concluding remarks

We have shown that the stress-flow angle metric introduced by Kulessa et al. (2014), and subsequently used to asses the stability and structural integrity of ice shelves, is not frame-indifferent due to its direct dependence on the material ice-shelf velocity. For a grounded ice sheet or glacier, the ice velocity can naturally be defined relative to the solid earth with which its lower boundary is in physical contact. This relative velocity difference between the ice and the solid earth is invariant under a Galilean transformation, and can therefore be used in physically meaningful dynamic relations, such as a basal sliding law. Importantly, the equations governing the dynamics of the ice sheet are frame-indifferent by construction, and are therefore also equally valid in a frame that is not at rest with respect to the solid earth. This is not the case for the stress-flow angle metric, as has been demonstrated here.

Whilst the ice-shelf velocity can also be defined relative to the solid earth, the relative velocity between a local point on a floating ice shelf and the bedrock below it – with which it is not in contact – cannot plausibly be of any physical importance to the local calving dynamics that the stress-flow angle seeks to describe. If the stress-flow angle metric were to be updated to explicitly refer to the velocity relative to a lateral boundary velocity, this would raise further questions about what those boundary velocities should be, and the metric would no longer be local. This is not how the stress-flow angle has been presented in the existing literature.

We suggest that the principle of frame-indifference could be respected by constructing laws and metrics for ice-shelf structural integrity and calving-front stability that use the stress, strain, strain rates, etc. or any of the invariants of those tensor quantities, rather than the material ice velocity directly.

Chapter 8

Conclusions

As set out in Chapter 1, there were three key research aims for this thesis. The first was to quantify, for the first time, the total buttressing capacity of the Larsen C Ice Shelf (LCIS) and to determine where within the ice shelf that buttressing is generated. The second was to characterise the relationship between changes in ice-shelf buttressing on the LCIS and the transient mass redistribution in response to that change, and also to conduct the first transient simulations of the loss of basal contact at the Bawden (BIR) and Gipps (GIR) ice rises. The final research aim was to calculate the total buttressing capacity of other ice shelves around the AIS, and by doing so better understand how buttressing varies around the ice sheet as well as what drives that variation.

To achieve these research aims, the ice flow model Úa was utilised in both a diagnostic (time-independent) and prognostic (time-dependent) mode to assess the impact that perturbations in ice-shelf geometries have on the stress state at, and ice flux across, the grounding line.

The reason that the focus of much of this thesis has been on the Larsen C Ice Shelf (LCIS) is due to the recent retreat and collapse of its more northerly, neighbouring ice shelves and the subsequent questions that have been raised about its future viability (e.g. Holland et al., 2015, Jansen et al., 2015). Existing studies have proposed possible mechanisms by which the LCIS could become destabilised, including through a loss of basal contact at the BIR, or following a significant calving event that could lead to a runaway calving instability. The recent calving of the A68 iceberg also provided an opportunity to test the capabilities of the Úa ice flow model to reproduce the observed response in ice velocities.

The buttressing provided by the ice shelves of the AIS has previously been systematically assessed primarily in two existing studies: Fürst et al. (2016) and Reese et al. (2018b). These works produced somewhat contrasting interpretations of the buttressing provided by Antarctic ice shelves, largely due to the differences in their focus between the impact of ice-shelf perturbations on the grounding line flux (GLF) or on changes in the flow of the ice shelf itself. The work in this thesis has directly responded to both of these studies, but has taken a different methodological approach. Here, the total buttressing capacity of a selection Antarctic ice shelves has been quantified for the first time, allowing for an assessment of the proportion of that total buttressing that is generated in different regions of the ice shelves.

The remainder of this chapter reiterates the key research findings from each of the results chapters, and how they addressed the three primary research aims. It then highlights the limitations of the work conducted in this thesis, before suggesting avenues for further research.

8.1 Key findings in Chapter 4

Chapter 4 sought to tackle the first research aim: to quantify the total buttressing capacity of the LCIS and determine where within the ice shelf that buttressing is generated. To answer these questions, the instantaneous response of the LCIS and its tributaries to both observed and idealised perturbations to the ice-shelf geometry were examined.

The first key finding came from the replication of the calving of the A68 iceberg within the model, which produced a limited change in ice-shelf velocities and had a negligible impact on the GLF (a 0.28% increase). It was attempted to use this result to test the capabilities of the ice flow model to reproduce the observed behaviour of the ice shelf in response to the perturbation, but it was found that the 'signal' caused by the calving of the A68 iceberg was almost everywhere smaller than the 'noise' in the data set available. However, both the modelling and observational evidence presented confirms the work of Fürst et al. (2016), Borstad et al. (2017) and Reese et al. (2018b) which suggested that the region that calved was mostly 'passive ice'.

The second key finding of the chapter was that the increase in GLF due to a complete collapse of the LCIS was found to be 607%. This quantified the total buttressing capacity of the ice shelf for the first time, achieving the first primary research aim. Through idealised calving experiments it was

found that over 95% of the total buttressing capacity of the LCIS is provided by ice within 25 km of the grounding line, and that over 80% of the total buttressing capacity of the shelf is generated in the first 5 km of ice downstream of the grounding line. By comparing the changes in GLF from the calving and thinning experiments, we can see that the majority of the buttressing comes from lateral drag as opposed to ice rises close to the grounding line. Regions of the LCIS upstream of the BIR and GIR – that in previous work has been found to have larger, locally derived buttressing numbers or increased GLF sensitivity to perturbations (Borstad et al., 2013, Fürst et al., 2016, Reese et al., 2018b, Zhang et al., 2020) – are not found to contribute significantly to the buttressing capacity of the ice shelf as a whole.

The final key finding came from the experiments examining the response to the ungrounding of the ice shelf from the BIR and GIR. Whilst there were local accelerations of around 50% in the speed of the ice shelf, the instantaneous increase in GLF was just 2.2% upon the loss of contact at both ice rises simultaneously. This suggests that whilst these ice rises do control the local ice-shelf dynamics, they only contribute a small amount to the total buttressing capacity of the LCIS.

The diagnostic experiments conducted in this chapter have provided new insights into the total amount of buttressing provided by the LCIS and where within the ice shelf the majority of that buttressing is generated, satisfying the first research aim of this thesis.

8.2 Key findings in Chapter 5

In Chapter 5 the work form the previous chapter was extended to look at the transient mass redistribution of the LCIS and its tributary glaciers in response to perturbations in the ice shelf from calving events and from the loss of basal contact at the BIR and GIR.

Despite the significant interest in the role that the BIR and GIR play in the dynamics of the LCIS (e.g. Borstad et al., 2012, Jansen et al., 2015, Holland et al., 2015, Borstad et al., 2017), transient simulations of the impact of the loss of basal contact at one or both ice rises have not previously been published. The first key finding of this chapter was that in response to the loss of basal contact at the BIR alone, and at the BIR and GIR simultaneously, the change in GLF approached a new steady state between 1 and 2% higher than in the control run. There was an increase in ice-shelf speeds upstream of the ice rises which resulted in ice-shelf thinning on the order

of tens of metres over the 100 year model runs. However, as the limited changes in GLF and volume above flotation (VAF) show, there was no significant impact on the grounded ice dynamics as a result of the loss of contact at these ice rises. Therefore, in addition to our finding from the previous chapter that these ice rises generate a negligible amount of the total buttressing of the LCIS, it is found that their loss also has a very limited, direct impact on the grounded tributary glaciers.

The second key finding of this chapter was the characterisation of the change in VAF after 100 years as a function of both the size of the calving perturbation and the loss of ice-shelf buttressing. The change in VAF was found to be an increasing function of the size of the calving perturbation, however, there was also a step change in the response in VAF between the calving front being positioned 30 km and 20 km downstream of the grounding line. When the calving front is placed 20 km downstream of the grounding line, ice in the narrow embayments downstream of the main tributary glaciers begins to be removed, which is where the majority of the buttressing of the LCIS was found to be generated in Chapter 4. Additionally, it was shown that the transient mass loss is particularly sensitive to the exact location of the calving front as it approaches the grounding line. For example, placing the calving front 1 km downstream of the grounding line, compared to 2 km, resulted in a difference of 13% in the total mass loss after 100 years.

The change in VAF after 100 years was also found to be an increasing, but nonlinear, function of the amount of buttressing removed from the LCIS. The change in VAF 'saturates' as an increasing proportion of the total ice-shelf buttressing is lost. This behaviour is controlled by the prograde bedrock topography of the LCIS tributaries, which only allows for limited thinning and grounding line retreat before a new steady state is approached. This finding demonstrates the need to consider the transient mass redistribution of an ice shelf-tributary system in response to a loss of buttressing as a separate, but linked process to that of the buttressing capacity of the ice shelf itself.

By characterising the transient response of the LCIS to the loss of basal contact at the BIR and GIR, and by exploring the link between changes in ice-shelf buttressing and the subsequent transient mass redistribution, the second research aim of this thesis has been satisfied.

8.3 Key findings in Chapter 6

Having explored the buttressing capacity and transient ice dynamics of the LCIS under a series of ice-shelf perturbations, the diagnostic ice flow modelling approach of Chapter 4 was applied to the whole AIS in Chapter 6. This approach allowed the third and final primary research aim – characterising the total buttressing capacity of other ice shelves around Antarctica and exploring the variation of that buttressing – to be tackled.

From a series of idealised calving experiments with an Antarctic-wide ice flow model set-up, the total buttressing capacity of eight major Antarctic ice shelves (in addition to the LCIS) was quantified for the first time. The first key finding was that that the total buttressing capacity of the ice shelves analysed varies by two orders of magnitude. The Filchner-Ronne Ice Shelf (FRIS) had the largest calculated buttressing capacity – as measured by a 3,086% increase in GLF upon the removal of the entire ice shelf – and Thwaites Glacier Ice Shelf (TGIS) had the smallest, with a GLF increase of 49% upon the complete removal of the shelf.

Where ice shelves contain narrow embayments just downstream of their main tributary glaciers, it was found that – as for the LCIS in Chapter 4 – this is where the vast majority of the buttressing capacity of those shelves is generated. For the FRIS, Ross Ice Shelf, LCIS and Brunt/Riiser-Larsen Ice Shelf – that all have a number of narrow embayments at their grounding lines – over 80% of the total buttressing capacity of the shelves is generated by between 12% and 15% of the ice shelf area downstream of the grounding line.

A second key finding of this chapter is that the contribution of ice rises to the total buttressing capacity of the ice shelves in which they are situated is controlled by the geometry of the ice shelf close to the grounding line. For example, the lack of any narrow embayments close to the grounding line of the Getz Ice Shelf means that its ice rises make a much larger contribution to the total buttressing capacity of the ice shelf. This is in contrast to the LCIS, where the Bawden and Gipps ice rises were found to provide a negligible proportion of the total buttressing due to the presence of narrow embayments within the ice shelf close to the grounding line, where the vast majority of the buttressing is generated.

The final key finding of this chapter is that – by defining passive ice as that which can be calved without inducing a 10% increase in GLF – much more of Antarctica's ice shelves could be

considered to be 'passive ice' than previously determined (Fürst et al., 2016). Across all of the ice shelves analysed, the areas in which the majority of the total buttressing is found to be generated matches up with the regions of largest buttressing flux response number found in Reese et al. (2018b). As such, the findings presented in Chapter 6 can be seen as complimentary to the map of GLF sensitivity to ice-shelf thickness perturbations produced in that work (ibid.).

By quantifying the total buttressing capacity of other Antarctic ice shelves for the first time, and by exploring both the commonalities and the variation in that buttressing around the ice sheet, the third primary research aim of this thesis has been satisfied.

8.4 Key findings in Chapter 7

The idea for the analysis presented in Chapter 7 arose whilst assessing the literature related to the LCIS and its future viability. The work was not conducted in response to one of the original research aims, but was included in the thesis as it contributes to the discussion in the literature about how the structural integrity of the LCIS can be assessed.

Kulessa et al. (2014) proposed a metric – the stress-flow angle – that they suggested could be used as a "first-order criterion on which to judge an ice shelf's stability". Examining this metric in further detail, it was shown that it is not *frame-indifferent*, i.e. observers in two different inertial reference frames would disagree on the value of the stress-flow angle and thus on the stability of an ice shelf's calving front position. This raises problems with its use as a metric for describing the structural integrity of an ice shelf.

This lack of frame-indifference is due to the direct dependence of the stress-flow angle on the material ice-shelf velocity. In this chapter, we suggested that for any ice-shelf metric used for assessing structural integrity or calving-front stability to be frame-indifferent, it should depend on the stress, strain, strain rates, or any of the invariants of those tensor quantities, rather than the material ice velocity directly.

8.5 Limitations and suggestions for future work

In addition to the discussion of the limitations of the research conducted in this thesis within Chapters 4-7, here a more general discussion of the limitations is presented together with suggestions for how they could be overcome or lead to further research.

Throughout this thesis, the Úa ice flow model has been used to perform both diagnostic and transient experiments. As outlined in Chapter 3, Úa uses the shallow-shelf approximation (SSA) to the full Stokes equations for viscous ice flow. This approximation, in a two-horizontal dimensional, 'plan-view' model retains the necessary terms in the momentum balance to explicitly model the impact of ice-shelf buttressing on the grounded ice sheet. However, it would be illuminating to conduct a selection of the experiments in this thesis with other ice sheet models which incorporate higher-order terms in the momentum balance equation, or even with a full Stokes model. This would allow for an assessment of the impact that including these additional terms has on the calculated buttressing capacity of the LCIS as well as on the transient evolution in response to the loss of that buttressing.

Further to this, experiments to test the sensitivity of the results of Chapters 4-6 on the formulation of the basal boundary condition (i.e. the 'sliding law') could be performed. In this thesis, only a Weertman sliding law was implemented, with a sensitivity test presented in Chapter 4 that investigated the impact of using different stress exponents. Further modelling experiments could be conducted to determine the impact that different sliding laws have on the stress balance across the grounding line, and consequently on the quantification of the buttressing capacity of the LCIS. Different sliding laws would also impact the way in which the tributary glaciers respond to a loss of ice-shelf buttressing, and this dependence could be explored further.

With additional time, a full uncertainty quantification analysis could have been performed for the transient experiments on the LCIS in Chapter 5, along the lines of that performed in Hill et al. (2021). This would allow for a full assessment of the sensitivity of the model results – in particular the change in volume above flotation after 100 years – to different parameter choices made within the model. The results in Chapter 5 for the transient evolution of the LCIS in response to calving perturbations could then be presented with their associated uncertainties due to model choices, rather than simply as point-estimates as they currently are.

Considering further the limitations of the ice flow model used throughout this thesis, it was stated in Chapter 5 that the an additional impact that the loss of basal contact at the BIR and GIR could have on the transient dynamics of the LCIS would be on the structural integrity of the ice shelf. Repeating these experiments with a model which incorporated a damage mechanics component (e.g. Borstad et al., 2012; 2016, Sun et al., 2017, Lhermitte et al., 2020), or the explicit modelling of rift propagation, would be a significant advance on the work presented here. It would allow for a more complete assessment of the effect that the loss of contact at the ice rises would have on the dynamics of the shelf.

Turning to the work in Chapter 6, more work could be done to explore the impact of the finite-element mesh resolution on the values calculated for the total buttressing capacity of the ice shelves analysed. As the sensitivity test presented in Sect. 6.3.6 showed, increasing the grounding line resolution will effect the value calculated for the total buttressing by allowing more of the ice shelf to be calved. Of particular interest would be to see whether the values for the total buttressing capacity converge, or whether the finer resolution continues to reveal additional, small embayments close to the grounding line, such that the total buttressing capacity calculated with this method continues to grow.

Another limitation of the experiments performed in Chapter 6 is the unrealistic nature of the calving fronts derived using the 'distance from the grounding line' metric. Further experiments could be performed in which the metric used to calculate the location of calving fronts is formulated differently. For example, the calving fronts could be: defined based on a 'distance from the initial calving front' metric; calculated as a proportion of the total distance along a set of flowlines across the ice shelf; or generated in the same way that the ice-shelf 'boxes' are calculated in the PICO ice-shelf cavity model (Reese et al., 2018c). Each one is likely to have its own unique quirks, and no systematic, idealised way of generating synthetic calving fronts will reproduce the calving fronts that would likely occur in nature. Fürst et al. (2016) used calving fronts defined along isolines of a locally calculated 'maximum buttressing number', which also seems to result in unrealistic calving front positions. The key feature of interest would be how robust the findings of this chapter are to different definitions of the calving front perturbations.

One of the key research aims of this thesis was to explore the transient response of the LCIS to

a reduction of ice-shelf buttressing. For the LCIS it was found that, despite significant buttressing forces provided by the ice shelf, the subsequent transient response of the grounded tributary glaciers was limited, due to the predominantly prograde bedrock topography beneath them. It would, therefore, be interesting to systematically explore the transient response of other ice shelf-tributary systems to the same experimental approach taken in Chapter 5 of this thesis. In regions where there is the potential for MISI, it may be that the correlation between the loss of buttressing in the calving event and the subsequent change in VAF breaks down, due to the triggering of the instability by a relatively small perturbation to the ice-shelf geometry. In particular, the systematic calving of Pine Island Glacier Ice Shelf or Thwaites Glacier Ice Shelf and the subsequent transient evolution of the system could give a fascinating insight into how the calving front position may control the future behaviour of these two crucial glaciers for determining the ice sheet's contribution to global sea level rise.

Another way in which the findings of this thesis could be extended would be to conduct a systematic study of the proportion of the total buttressing provided by all Antarctic ice rises. This could be done using the methods employed in Chapter 4 to assess the proportion of the total buttressing provided by the BIR and GIR. Following this, transient experiments could be conducted to assess the impact that the loss of contact at an ice rise has on the transient evolution of the ice shelf-tributary system, analogous to the experiments performed in Chapter 5. In this way a map of all Antarctic ice rises could be developed which determined how much buttressing was provided by each ice rise, and also which ice rises are important for the transient ice dynamics of the ice sheet.

Finally, in Chapter 7 the lack of frame-indifference of the stress-flow angle metric was demonstrated, and the reasons that it is therefore not a valid metric of ice shelf structural integrity or calving-front stability were outlined. However, in this commentary no superior measure of these ice-shelf properties was proposed. Whilst it was suggested that any metric should use stresses or strain rates – or the invariants of those tensor quantities – further work could be done to devise a new metric that might provide a valid description of the structural integrity and calving-front stability of an ice shelf. Additionally, it is hoped that the work in Chapter 7 will be taken forward by the community to ensure that any new, proposed calving laws or ice-shelf metrics abide by the principle of frame-indifference.

8.6 Concluding remarks

This thesis has contributed to knowledge by utilising an ice flow model to quantify the buttressing capacity of Antarctic ice shelves and to explore the transient response of the LCIS to a systematic reduction in buttressing.

The total buttressing capacity of the LCIS was calculated for the first time, and by doing so, it was found that the vast majority of the buttressing capacity of the LCIS is generated in the first few kilometres of the ice shelf downstream of the grounding line. It has also been shown that the ice rises at the front of the LCIS provide a negligible amount of the total buttressing of the ice shelf. Through conducting the first transient experiments examining the loss of basal contact at the BIR and GIR, it was determined that they also have a very limited, direct impact on the transient evolution of the grounding line and tributary glaciers of the LCIS.

The analysis of the buttressing capacity of the LCIS was then extended to other ice shelves around the AIS. It was found that the buttressing capacity of the major ice shelves of the ice sheet selected for analysis varies by two orders of magnitude. The ice shelf geometry – particularly the presence of narrow embayments close the grounding line – strongly controls the total buttressing capacity of these ice shelves, and also determines the distribution of the generation of that buttressing capacity.

The work in this thesis has advanced our understanding of the buttressing provided by Antarctic ice shelves, and also highlighted how the transient response to a loss of ice-shelf buttressing should be considered as a separate, but linked processes to that of the ice-shelf buttressing itself. To extend the work, the methods employed in this thesis could be applied to more localised studies around the AIS, to further determine the link between ice-shelf buttressing and transient mass redistribution, and to better understand the the consequences of future changes in the extent of Antarctica's ice shelves.

References

Adusumilli, S., Fricker, H. A., Medley, B., Padman, L., and Siegfried, M. R. (2020). Interannual variations in meltwater input to the Southern Ocean from Antarctic ice shelves. *Nature Geoscience*, 13:616–620.

Adusumilli, S., Fricker, H. A., Siegfried, M. R., Padman, L., Paolo, F. S., and Ligtenberg, S. R. M. (2018). Variable Basal Melt Rates of Antarctic Peninsula Ice Shelves, 1994-2016. *Geophysical Research Letters*, 45(9):4086–4095.

Alley, K. E., Scambos, T. A., Alley, R. B., and Holschuh, N. (2019). Troughs developed in ice-stream shear margins precondition ice shelves for ocean-driven breakup. *Science Advances*, 5(10):1–8.

Bamber, J. L. and Dawson, G. J. (2020). Complex evolving patterns of mass loss from Antarctica's largest glacier. *Nature Geoscience*, 13(2):127–131.

Bamber, J. L., Oppenheimer, M., Kopp, R. E., Aspinall, W. P., and Cooke, R. M. (2019). Ice sheet contributions to future sea-level rise from structured expert judgment. *Proceedings of the National Academy of Sciences*, 166(23):11195–11200.

Bamber, J. L., Riva, R. E. M., Vermeersen, B. L. A., and Le Brocq, A. M. (2009). Reassessment of the Potential Sea-Level Rise from a Collapse of the West Antarctic Ice Sheet. *Science*, 324(May):901–904.

Bamber, J. L., Vaughan, D. G., and Joughin, I. (2000). Widespread complex flow in the interior of the antarctic ice sheet. *Science*, 287(5456):1248–1250.

Bamber, J. L., Westaway, R. M., Marzeion, B., and Wouters, B. (2018). The land ice contribution to sea level during the satellite era.

Banwell, A. F., Datta, R. T., Dell, R. L., Moussavi, M., Brucker, L., Picard, G., Shuman, C. A., and Stevens, L. A. (2020). 32-year record-high surface melt in 2019/2020 on the northern George VI Ice Shelf, Antarctic Peninsula. *The Cryosphere*, 15:909–925.

Banwell, A. F., MacAyeal, D. R., and Sergienko, O. V. (2013). Breakup of the Larsen B Ice Shelf triggered by chain reaction drainage of supraglacial lakes. *Geophysical Research Letters*, 40(22):5872–5876.

Bassis, J. N., Berg, B., Crawford, A. J., and Benn, D. I. (2021). Transition to marine ice cliff instability controlled by ice thickness gradients and velocity. *Science*, 372(6548):1342–1344.

Bassis, J. N. and Walker, C. C. (2012). Upper and lower limits on the stability of calving glaciers from the yield strength envelope of ice. *Proceedings of the Royal Society A: Mathematical, Physical and Engineering Sciences*, 468(2140):913–931.

Bell, R. E. and Seroussi, H. (2020). History, mass loss, structure, and dynamic behavior of the Antarctic Ice Sheet. *Science*, 367(6484):1321–1325.

Benn, D. I. and Evans, D. J. A. (2014). *Glaciers & Glaciation*. Routledge, Oxford, 2nd edition.

Berthier, E., Scambos, T. A., and Shuman, C. A. (2012). Mass loss of Larsen B tributary glaciers (Antarctic Peninsula) unabated since 2002. *Geophysical Research Letters*, 39(13):1–6.

Bevan, S. L., Luckman, A. J., Hendon, H., and Wang, G. (2020). The 2020 Larsen C Ice Shelf surface melt is a 40-year record high. *The Cryosphere*, 14:3551–3564.

Bindschadler, R. A., Choi, H., Wichlacz, A., Bingham, R. G., Bohlander, J. A., Brunt, K. M., Corr, H. F. J., Drews, R., Fricker, H. A., Hall, M., Hindmarsh, R. C. A., Kohler, J., Padman, L., Rack, W., Rotschky, G., Urbini, S., Vornberger, P., and Young, N. W. (2011). Getting around Antarctica: New high-resolution mappings of the grounded and freely-floating boundaries of the Antarctic ice sheet created for the International Polar Year. *The Cryosphere*, 5(3):569–588.

Borstad, C. P., Khazendar, A., Larour, E. Y., Morlighem, M., Rignot, E., Schodlok, M. P., and Seroussi, H. (2012). A damage mechanics assessment of the Larsen B ice shelf prior to collapse: Toward a physically-based calving law. *Geophysical Research Letters*, 39(17):1–5.

Borstad, C. P., Khazendar, A., Scheuchl, B., Morlighem, M., Larour, E. Y., and Rignot, E. (2016). A constitutive framework for predicting weakening and reduced buttressing of ice shelves based on observations of the progressive deterioration of the remnant Larsen B ice shelf. *Geophysical Research Letters*, 43:2027–2035.

Borstad, C. P., McGrath, D., and Pope, A. (2017). Fracture propagation and stability of ice shelves governed by ice shelf heterogeneity. *Geophysical Research Letters*, 44(9):4186–4194.

Borstad, C. P., Rignot, E., Mouginot, J., and Schodlok, M. P. (2013). Creep deformation and buttressing capacity of damaged ice shelves: Theory and application to Larsen C ice shelf. *The Cryosphere*, 7(6):1931–1947.

Brondex, J., Gagliardini, O., Gillet-Chaulet, F., and Durand, G. (2017). Sensitivity of grounding line dynamics to the choice of the friction law. *Journal of Glaciology*, 63(241):854–866.

Brunt, K. M., Fricker, H. A., Padman, L., Scambos, T. A., and O'Neel, S. (2010). Mapping the grounding zone of the Ross Ice Shelf, Antarctica, using ICESat laser altimetry. *Annals of Glaciology*, 51(55):71–79.

Clerc, F., Minchew, B. M., and Behn, M. D. (2019). Marine Ice Cliff Instability Mitigated by Slow Removal of Ice Shelves. *Geophysical Research Letters*, 46(21):12108–12116.

Cook, A. J. and Vaughan, D. G. (2010). Overview of areal changes of the ice shelves on the Antarctic Peninsula over the past 50 years. *The Cryosphere*, 4(1):77–98.

Cook, C. P., Van De Flierdt, T., Williams, T., Hemming, S. R., Iwai, M., Kobayashi, M., Jimenez-Espejo, F. J., Escutia, C., González, J. J., Khim, B. K., McKay, R. M., Passchier, S., Bohaty, S. M., Riesselman, C. R., Tauxe, L., Sugisaki, S., Galindo, A. L., Patterson, M. O., Sangiorgi, F., Pierce, E. L., Brinkhuis, H., Klaus, A., Fehr, A., Bendle, J. A., Bijl, P. K., Carr, S. A., Dunbar, R. B., Flores, J. A., Hayden, T. G., Katsuki, K., Kong, G. S., Nakai, M., Olney, M. P., Pekar,

S. F., Pross, J., Röhl, U., Sakai, T., Shrivastava, P. K., Stickley, C. E., Tuo, S., Welsh, K., and Yamane, M. (2013). Dynamic behaviour of the East Antarctic ice sheet during Pliocene warmth. *Nature Geoscience*, 6(9).

Cornford, S. L., Martin, D. F., Graves, D. T., Ranken, D. F., Le Brocq, A. M., Gladstone, R. M., Payne, A. J., Ng, E. G., and Lipscomb, W. H. (2013). Adaptive mesh, finite volume modeling of marine ice sheets. *Journal of Computational Physics*, 232(1):529–549.

Cornford, S. L., Martin, D. F., Payne, A. J., Ng, E. G., Le Brocq, A. M., Gladstone, R. M., Edwards, T. L., Shannon, S. R., Agosta, C., van den Broeke, M. R., Hellmer, H. H., Krinner, G., Ligtenberg, S. R. M., Timmermann, R., and Vaughan, D. G. (2015). Century-scale simulations of the response of the West Antarctic Ice Sheet to a warming climate. *The Cryosphere*, 9(4):1579–1600.

Cornford, S. L., Seroussi, H., Asay-Davis, X. S., Gudmundsson, G. H., Arthern, R. J., Borstad, C. P., Christmann, J., Dias dos Santos, T., Feldmann, J., Goldberg, D. N., Hoffman, M. J., Humbert, A., Kleiner, T., Leguy, G. R., Lipscomb, W. H., Merino, N., Durand, G., Morlighem, M., Pollard, D., Rückamp, M., Williams, C. R., and Yu, H. (2020). Results of the third Marine Ice Sheet Model Intercomparison Project (MISMIP+). *The Cryosphere*, 14:2283–2301.

Cuffey, K. M. and Paterson, W. S. B. (2010). *The Physics of Glaciers*. Butterworth-Heinemann, Oxford, 4th edition.

De Rydt, J., Gudmundsson, G. H., Rott, H., and Bamber, J. L. (2015). Modeling the instantaneous response of glaciers after the collapse of the Larsen B Ice Shelf. *Geophysical Research Letters*, 42(13):5355–5363.

De Rydt, J., Reese, R., Paolo, F. S., and Gudmundsson, G. H. (2021). Drivers of Pine Island Glacier speed-up between 1996 and 2016. *The Cryosphere*, 15(1):113–132.

DeConto, R. M. and Pollard, D. (2016). Contribution of Antarctica to past and future sea-level rise. *Nature*, 531(7596):591–597.

Depoorter, M. A., Bamber, J. L., Griggs, J. A., Lenaerts, J. T. M., Ligtenberg, S. R. M., van den Broeke, M. R., and Moholdt, G. (2013). Calving fluxes and basal melt rates of Antarctic ice shelves. *Nature*, 502(7469):89–92.

De Rydt, J. and Gudmundsson, G. H. (2016). Coupled ice shelf-ocean modeling and complex grounding line retreat from a seabed ridge. *Journal of Geophysical Research F: Earth Surface*, 121(5):865–880.

Doake, C. S. M., Corr, H. F. J., Rott, H., Skvarca, P., and Young, N. W. (1998). Breakup and conditions for stability of the nothern Larsen Ice Shelf, Antarctica. *Nature*, 391:778–780.

Domack, E., Duran, D., Leventer, A., Ishman, S., Doane, S., McCallum, S., Amblas, D., Ring, J., Gilbert, R., and Prentice, M. (2005). Stability of the Larsen B ice shelf on the Antarctic Peninsula during the Holocene epoch. *Nature*, 436(7051):681–685.

Dupont, T. K. and Alley, R. B. (2005). Assessment of the importance of ice-shelf buttressing to ice-sheet flow. *Geophysical Research Letters*, 32(4):1–4.

Durand, G., Gagliardini, O., Zwinger, T., Le Meur, E., and Hindmarsh, R. C. A. (2009). Full Stokes modeling of marine ice sheets: Influence of the grid size. *Annals of Glaciology*, 50(52):109–114.

Dutrieux, P., De Rydt, J., Jenkins, A., Holland, P. R., Ha, H. K., Lee, S.-H., Steig, E. J., Ding, Q., Abrahamsen, E. P., and Schroder, M. (2014). Strong Sensitivity of Pine Island Ice-Shelf Melting to Climatic Variability. *Science*, 343:174–178.

Dutrieux, P., Vaughan, D. G., Corr, H. F. J., Jenkins, A., Holland, P. R., Joughin, I., and Fleming, A. H. (2013). Pine Island glacier ice shelf melt distributed at kilometre scales. *The Cryosphere*, 7(5):1543–1555.

Edwards, T. L., Brandon, M., Durand, G., Edwards, N. R., Golledge, N. R., Holden, P. B., Nias, I. J., Payne, A. J., Ritz, C., and Wernecke, A. (2019). Revisiting Antarctic ice loss due to marine ice cliff instability. *Nature*, 566:58–64.

Edwards, T. L., Nowicki, S. M. J., Marzeion, B., Hock, R., Goelzer, H., Seroussi, H., Jourdain, N. C., Slater, D., Turner, F. E., Smith, C. J., McKenna, C. M., Simon, E. G., Abe Ouchi, A., Gregory, J. M., Larour, E. Y., Lipscomb, W. H., Payne, A. J., Shepherd, A., Agosta, C., Alexander, P., Albrecht, T., Anderson, B., Asay-Davis, X. S., Aschwanden, A., Barthel, A., Bliss, A., Calov, R., Chambers, C., Champollion, N., Choi, Y., Cullather, R., Cuzzone, J., Dumas, C., Felikson, D., Fettweis, X., Fujita, K., Galton-Fenzi, B. K., Gladstone, R. M., Golledge, N. R., Greve, R., Hattermann, T., Hoffman, M. J., Humbert, A., Huss, M., Huybrechts, P., Immerzeel, W., Kleiner, T., Kraaijenbrink, P., Le clec'h, S., Lee, V., Leguy, G. R., Little, C. M., Lowry, D., Malles, J.-H., Martin, D. F., Maussion, F., Morlighem, M., O'Neill, J. F., Nias, I. J., Pattyn, F., Pelle, T., Price, S. F., Quiquet, A., Radić, V., Reese, R., Rounce, D. R., Rückamp, M., Sakai, A., Shafer, C., Schlegel, N.-J., Shannon, S. R., Smith, R., Straneo, F., Sun, S., Tarasov, L., Trusel, L. D., Van Breedam, J., van de Wal, R. S. W., van den Broeke, M. R., Winkelmann, R., Zekollari, H., Zhao, C., Zhang, T., and Zwinger, T. (2021). Projected land ice contributions to twenty-first-century sea level rise. *Nature*, 593:74–82.

ENVEO team (2019). Antarctic Ice Sheet monthly velocity maps from Copernicus Sentinel-1, 2014-2019, ESA Antarctic Ice Sheet CCI [v1.1] [data set], http://cryoportal.enveo.at (last acces: 29/05/2020).

Favier, L., Durand, G., Cornford, S. L., Gudmundsson, G. H., Gagliardini, O., Gillet-Chaulet, F., Zwinger, T., Payne, A. J., and Le Brocq, A. M. (2014). Retreat of Pine Island Glacier controlled by marine ice-sheet instability. *Nature Climate Change*, 4(2):117–121.

Favier, L., Jourdain, N. C., Jenkins, A., Merino, N., Durand, G., Gagliardini, O., Gillet-Chaulet, F., and Mathiot, P. (2019). Assessment of sub-shelf melting parameterisations using the ocean-ice-sheet coupled model NEMO(v3.6)-Elmer/Ice(v8.3). *Geoscientific Model Development*, 12:2255–2283.

Favier, L. and Pattyn, F. (2015). Antarctic ice rise formation, evolution, and stability. *Geophysical Research Letters*, 42(11):4456–4463.

Favier, L., Pattyn, F., Berger, S., and Drews, R. (2016). Dynamic influence of pinning points on marine ice-sheet stability: a numerical study in Dronning Maud Land, East Antarctica. *The Cryosphere*, 10:2623–2635.

Fretwell, P. T., Pritchard, H. D., Vaughan, D. G., Bamber, J. L., Barrand, N. E., Bell, R. E., Bianchi, C., Bingham, R. G., Blankenship, D. D., Casassa, G., Catania, G., Callens, D., Conway, H., Cook, A. J., Corr, H. F. J., Damaske, D., Damm, V., Ferraccioli, F., Forsberg, R., Fujita, S.,

Gim, Y., Gogineni, P., Griggs, J. A., Hindmarsh, R. C. A., Holmlund, P., Holt, J. W., Jacobel, R. W., Jenkins, A., Jokat, W., Jordan, T. A., King, E. C., Kohler, J., Krabill, W. B., Riger-Kusk, M., Langley, K. A., Leitchenkov, G., Leuschen, C., Luyendyk, B. P., Matsuoka, K., Mouginot, J., Nitsche, F. O., Nogi, Y., Nost, O. A., Popov, S. V., Rignot, E., Rippin, D. M., Rivera, A., Roberts, J., Ross, N., Siegert, M. J., Smith, A. M., Steinhage, D., Studinger, M., Sun, B., Tinto, B. K., Welch, B. C., Wilson, D., Young, D. A., Xiangbin, C., and Zirizzotti, A. (2013). Bedmap2: Improved ice bed, surface and thickness datasets for Antarctica. *The Cryosphere*, 7(1):375–393.

Fürst, J. J., Durand, G., Gillet-Chaulet, F., Tavard, L., Rankl, M., Braun, M., and Gagliardini, O. (2016). The safety band of Antarctic ice shelves. *Nature Climate Change*, 6(5):479–482.

Gagliardini, O., Durand, G., Zwinger, T., Hindmarsh, R. C. A., and Le Meur, E. (2010). Coupling of ice-shelf melting and buttressing is a key process in ice-sheets dynamics. *Geophysical Research Letters*, 37(14):1–5.

Garbe, J., Albrecht, T., Levermann, A., Donges, J. F., and Winkelmann, R. (2020). The Hysteresis of the Antarctic Ice Sheet. *Nature*, 585:538–544.

Gardner, A. S., Moholdt, G., Scambos, T. A., Fahnestock, M. A., Ligtenberg, S. R. M., van den Broeke, M. R., and Nilsson, J. (2018). Increased West Antarctic and unchanged East Antarctic ice discharge over the last 7 years. *The Cryosphere*, 12(2):521–547.

Geuzaine, C. and Remacle, J. F. (2009). Gmsh: a three-dimensional finite element mesh generator with built-in pre- and post-processing facilities. *International Journal for Numerical Methods in Engineering*, 79(11):1309–1331.

Glasser, N. F., Kulessa, B., Luckman, A. J., Jansen, D., King, E. C., Sammonds, P. R., Scambos, T. A., and Jezek, K. C. (2009). Surface structure and stability of the Larsen C ice shelf, Antarctic Peninsula. *Journal of Glaciology*, 55(191):400–410.

Glen, J. W. (1955). The creep of polycrystalline ice. *Proceedings of the Royal Society A: Mathematical, Physical and Engineering Sciences*, 228(1175):519–538.

Goldberg, D. N., Gourmelen, N., Kimura, S., Millan, R., and Snow, K. (2019). How Accurately Should We Model Ice Shelf Melt Rates? *Geophysical Research Letters*, 46(1):189–199.

Goldberg, D. N., Holland, D. M., and Schoof, C. G. (2009). Grounding line movement and ice shelf buttressing in marine ice sheets. *Journal of Geophysical Research: Earth Surface*, 114(4):1–23.

Gudmundsson, G. H. (2013). Ice-shelf buttressing and the stability of marine ice sheets. *The Cryosphere*, 7(2):647–655.

Gudmundsson, G. H. (2020). Úa Source Code: Version v2019b, Zenodo [code].

Gudmundsson, G. H., Krug, J., Durand, G., Favier, L., and Gagliardini, O. (2012). The stability of grounding lines on retrograde slopes. *The Cryosphere*, 6(6):1497–1505.

Gudmundsson, G. H., Paolo, F. S., Adusumilli, S., and Fricker, H. A. (2019). Instantaneous Antarctic ice sheet mass loss driven by thinning ice shelves. *Geophysical Research Letters*, 46(23):13903–13909.

Hanna, E., Pattyn, F., Navarro, F., Favier, V., Goelzer, H., van den Broeke, M. R., Vizcaino, M., Whitehouse, P. L., Ritz, C., Bulthuis, K., and Smith, B. E. (2020). Mass balance of the ice sheets and glaciers – Progress since AR5 and challenges. *Earth-Science Reviews*, 201:1–17.

Haseloff, M. and Sergienko, O. V. (2018). The effect of buttressing on grounding line dynamics. *Journal of Glaciology*, 64(245):1–15.

Helm, V., Humbert, A., and Miller, H. (2014). Elevation and elevation change of Greenland and Antarctica derived from CryoSat-2. *The Cryosphere*, 8(4):1539–1559.

Hill, E. A., Gudmundsson, G. H., Carr, J. R., and Stokes, C. R. (2018). Velocity response of Petermann Glacier, northwest Greenland to past and future calving events. *The Cryosphere*, 12:3907–3921.

Hill, E. A., Rosier, S. H. R., Gudmundsson, G. H., and Collins, M. (2021). Quantifying the potential future contribution to global mean sea level from the Filchner–Ronne basin, Antarctica. *The Cryosphere*, 15(10):4675–4702.

Hindmarsh, R. C. A. and Le Meur, E. (2001). Dynamical processes involved in the retreat of marine ice sheets. *Journal of Glaciology*, 47(157):271–282.

Hogg, A. E. and Gudmundsson, G. H. (2017). Commentary: Impacts of the Larsen-C Ice Shelf calving event. *Nature Climate Change*, 7(8):540–542.

Holland, P. R., Bracegirdle, T. J., Dutrieux, P., Jenkins, A., and Steig, E. J. (2019). West Antarctic ice loss influenced by internal climate variability and anthropogenic forcing. *Nature Geoscience*, 12(9):718–724.

Holland, P. R., Brisbourne, A. M., Corr, H. F. J., McGrath, D., Purdon, K., Paden, J., Fricker, H. A., Paolo, F. S., and Fleming, A. H. (2015). Oceanic and atmospheric forcing of Larsen C Ice-Shelf thinning. *The Cryosphere*, 9(3):1005–1024.

Holland, P. R., Corr, H. F. J., Vaughan, D. G., Jenkins, A., and Skvarca, P. (2009). Marine ice in Larsen Ice Shelf. *Geophysical Research Letters*, 36(11):1–6.

Hulbe, C. L., Scambos, T. A., Youngberg, T., and Lamb, A. K. (2008). Patterns of glacier response to disintegration of the Larsen B ice shelf, Antarctic Peninsula. *Global and Planetary Change*, 63(1):1–8.

Jansen, D., Kulessa, B., Sammonds, P. R., Luckman, A. J., King, E. C., and Glasser, N. F. (2010). Present stability of the Larsen C ice shelf, Antarctic Peninsula. *Journal of Glaciology*, 56(198):593–600.

Jansen, D., Luckman, A. J., Cook, A. J., Bevan, S. L., Kulessa, B., Hubbard, B., and Holland, P. R. (2015). Brief Communication: Newly developing rift in Larsen C Ice Shelf presents significant risk to stability. *The Cryosphere*, 9(3):1223–1227.

Jenkins, A., Shoosmith, D. R., Dutrieux, P., Jacobs, S., Kim, T. W., Lee, S.-H., Ha, H. K., and Stammerjohn, S. E. (2018). West Antarctic Ice Sheet retreat in the Amundsen Sea driven by decadal oceanic variability. *Nature Geoscience*, 11:733–738.

Jog, C. S. (2015). *Continuum Mechanics*. Cambridge University Press, Delhi, India, 3rd edition.

Joughin, I. and Alley, R. B. (2011). Stability of the West Antarctic ice sheet in a warming world. *Nature Geoscience*, 4(8):506–513.

Joughin, I., Shapero, D., Smith, B., Dutrieux, P., and Barham, M. (2021). Ice-shelf retreat drives recent Pine Island Glacier speedup. *Science Advances*, 7:1–6.

Joughin, I., Smith, B. E., and Medley, B. (2014). Marine Ice Sheet Collapse Potentially Under Way for the Thwaites Glacier Basin, West Antarctica. *Science*, 344(6185):735–738.

Khazendar, A., Borstad, C. P., Scheuchl, B., Rignot, E., and Seroussi, H. (2015). The evolving instability of the remnant Larsen B Ice Shelf and its tributary glaciers. *Earth and Planetary Science Letters*, 419:199–210.

Khazendar, A., Rignot, E., and Larour, E. Y. (2007). Larsen B Ice Shelf rheology preceding its disintegration inferred by a control method. *Geophysical Research Letters*, 34(19):1–6.

Khazendar, A., Rignot, E., and Larour, E. Y. (2011). Acceleration and spatial rheology of Larsen C Ice Shelf, Antarctic Peninsula. *Geophysical Research Letters*, 38(9):1–5.

Konrad, H., Shepherd, A., Gilbert, L., Hogg, A. E., McMillan, M., Muir, A., and Slater, T. (2018). Net retreat of Antarctic glacier grounding lines. *Nature Geoscience*, 11(4):258–262.

Kulessa, B., Jansen, D., Luckman, A. J., King, E. C., and Sammonds, P. R. (2014). Marine ice regulates the future stability of a large Antarctic ice shelf. *Nature Communications*, 5(3707):1–7.

Lai, C.-Y., Kingslake, J., Wearing, M. G., Chen, P.-H. C., Gentine, P., Li, H., Spergel, J. J., and van Wessem, J. M. (2020). Vulnerability of Antarctica's ice shelves to meltwater-driven fracture. *Nature*, 584:574–578.

Lazeroms, W. M. J., Jenkins, A., Gudmundsson, G. H., and Van De Wal, R. S. W. (2018). Modelling present-day basal melt rates for Antarctic ice shelves using a parametrization of buoyant meltwater plumes. *The Cryosphere*, 12(1):49–70.

Le Brocq, A. M., Payne, A. J., and Vieli, A. (2010). An improved Antarctic dataset for high resolution numerical ice sheet models (ALBMAP v1). *Earth System Science Data*, 2(2):247–260.

Levermann, A., Winkelmann, R., Albrecht, T., Goelzer, H., Golledge, N. R., Greve, R., Huybrechts, P., Jordan, J., Leguy, G. R., Martin, D. F., Morlighem, M., Pattyn, F., Pollard, D., Quiquet, A., Rodehacke, C. B., Seroussi, H., Sutter, J., Zhang, T., Van Breedam, J., Calov, R., DeConto, R. M., Dumas, C., Garbe, J., Gudmundsson, G. H., Hoffman, M. J., Humbert, A., Kleiner, T., Lipscomb, W. H., Meinshausen, M., Ng, E. G., Nowicki, S. M. J., Perego, M., Price, S. F., Saito, F., Schlegel, N.-J., Sun, S., and van de Wal, R. S. W. (2020). Projecting Antarctica's contribution to future sea level rise from basal ice shelf melt using linear response functions of 16 ice sheet models (LARMIP-2). *Earth System Dynamics*, 11(1):35–76.

Lhermitte, S., Sun, S., Shuman, C. A., Wouters, B., Pattyn, F., Wuite, J., Berthier, E., and Nagler, T. (2020). Damage accelerates ice shelf instability and mass loss in Amundsen Sea Embayment. *Proceedings of the National Academy of Sciences*, 117(40):24735–24741.

Ligtenberg, S. R., van de Berg, W. J., van den Broeke, M. R., Rae, J. G., and van Meijgaard, E. (2013). Future surface mass balance of the Antarctic ice sheet and its influence on sea level change, simulated by a regional atmospheric climate model. *Climate Dynamics*, 41(3-4):867–884.

Ligtenberg, S. R. M., Helsen, M. M., and van den Broeke, M. R. (2011). An improved semi-empirical model for the densification of Antarctic firn. *The Cryosphere*, 5(4):809–819.

Lythe, M. B. and Vaughan, D. G. (2001). BEDMAP: A new ice thickness and subglacial topographic model of Antarctica. *Journal of Geophysical Research: Solid Earth*, 106(B6):11335–11351.

MacAyeal, D. R. (1989). Large-Scale Ice Flow Over a Viscous Basal Sediment: Theory and Application to Ice Stream B, Antarctica. *Journal of Geophysical Research*, 94:4071–4087.

MacAyeal, D. R. (1993). A tutorial on the use of control methods in ice-sheet modelling. *Journal of Glaciology*, 39(131):91–98.

Martin, D. F., Cornford, S. L., and Payne, A. J. (2019). Millennial-Scale Vulnerability of the Antarctic Ice Sheet to Regional Ice Shelf Collapse. *Geophysical Research Letters*, 46(3):1467–1475.

Martín-Español, A., Bamber, J. L., and Zammit-Mangion, A. (2017). Constraining the mass balance of East Antarctica. *Geophysical Research Letters*, 44(9):4168–4175.

Massom, R. A., Scambos, T. A., Bennetts, L. G., Reid, P., Squire, V. A., and Stammerjohn, S. E. (2018). Antarctic ice shelf disintegration triggered by sea ice loss and ocean swell. *Nature*, 558(7710):383–389.

Matsuoka, K., Hindmarsh, R. C. A., Moholdt, G., Bentley, M. J., Pritchard, H. D., Brown, J., Conway, H., Drews, R., Durand, G., Goldberg, D. N., Hattermann, T., Kingslake, J., Lenaerts, J. T. M., Martín, C., Mulvaney, R., Nicholls, K. W., Pattyn, F., Ross, N., Scambos, T. A., and Whitehouse, P. L. (2015). Antarctic ice rises and rumples: Their properties and significance for ice-sheet dynamics and evolution. *Earth-Science Reviews*, 150:724–745.

McGrath, D., Steffen, K., Holland, P. R., Scambos, T. A., Rajaram, H., Abdalati, W., and Rignot, E. (2014). The structure and effect of suture zones in the Larsen C Ice Shelf, Antarctica. *Journal of Geophysical Research: Earth Surface*, 119(3):588–602.

McMillan, M., Shepherd, A., Sundal, A. V., Briggs, K. H., Muir, A., Ridout, A., Hogg, A. E., and Wingham, D. J. (2014). Increased ice losses from Antarctica detected by CryoSat-2. *Geophysical Research Letters*, 41(11):3899–3905.

Mercer, J. H. (1978). West Antarctic ice sheet and CO2 greenhouse effect: a threat of disaster. *Nature*, 271:321–325.

Miles, B. W., Stokes, C. R., Jenkins, A., Jordan, J. R., Jamieson, S. S., and Gudmundsson, G. H. (2020). Intermittent structural weakening and acceleration of the Thwaites Glacier Tongue between 2000 and 2018. *Journal of Glaciology*, 66(257):485–495.

Minchew, B. M., Gudmundsson, G. H., Gardner, A. S., Paolo, F. S., and Fricker, H. A. (2018). Modeling the dynamic response of outlet glaciers to observed ice-shelf thinning in the Bellingshausen Sea Sector, West Antarctica. *Journal of Glaciology*, 64(244):333–342.

Minchew, B. M. and Joughin, I. (2020). Toward a universal glacier slip law. *Science*, 368(6486):29–30.

Mitcham, T., Gudmundsson, G. H., and Bamber, J. L. (2022). The instantaneous impact of calving and thinning on the Larsen C Ice Shelf. *The Cryosphere*, 16(3):883–901.

Morland, L. W. and Smith, G. D. (1984). Influence of non-uniform temperature distribution on the steady motion of ice sheets. *Journal of Fluid Mechanics*, 140:113–133.

Morlighem, M., Rignot, E., Binder, T., Blankenship, D. D., Drews, R., Eagles, G., Eisen, O., Ferraccioli, F., Forsberg, R., Fretwell, P. T., Goel, V., Greenbaum, J. S., Gudmundsson, G. H., Guo, J., Helm, V., Hofstede, C., Howat, I. M., Humbert, A., Jokat, W., Karlsson, N. B., Lee, W. S., Matsuoka, K., Millan, R., Mouginot, J., Paden, J., Pattyn, F., Roberts, J., Rosier, S., Ruppel, A., Seroussi, H., Smith, E. C., Steinhage, D., Sun, B., Broeke, M. R. v. d., Ommen, T. D. v., van Wessem, J. M., and Young, D. A. (2020). Deep glacial troughs and stabilizing ridges unveiled beneath the margins of the Antarctic ice sheet. *Nature Geoscience*, 13:132–137.

Morris, E. M. and Vaughan, D. G. (2003). Spatial and temporal variation of surface temperature on the Antarctic Peninsula and the limit of viability of ice shelves. *Antarctic Research Series*, 79:61–68.

Mouginot, J., Scheuchl, B., and Rignot, E. (2012). Mapping of ice motion in antarctica using synthetic-aperture radar data. *Remote Sensing*, 4(9):2753–2767.

Naughten, K. A., De Rydt, J., Rosier, S., Jenkins, A., Holland, P. R., and Ridley, J. K. (2021). Two-timescale response of a large Antarctic ice shelf to climate change. *Nature Communications*, 12(1991):1–10.

Nias, I. J., Cornford, S. L., and Payne, A. J. (2018). New Mass-Conserving Bedrock Topography for Pine Island Glacier Impacts Simulated Decadal Rates of Mass Loss. *Geophysical Research Letters*, 45(7):3173–3181.

Nicholls, K. W., Makinson, K., and Venables, E. J. (2012). Ocean circulation beneath Larsen C Ice Shelf, Antarctica from in situ observations. *Geophysical Research Letters*, 39(19):1–6.

Nowicki, S., Goelzer, H., Seroussi, H., Payne, A. J., Lipscomb, W. H., Abe-Ouchi, A., Agosta, C., Alexander, P., Asay-Davis, X. S., Barthel, A., Bracegirdle, T. J., Cullather, R., Felikson, D., Fettweis, X., Gregory, J. M., Hattermann, T., Jourdain, N. C., Kuipers Munneke, P., Larour, E., Little, C. M., Morlighem, M., Nias, I., Shepherd, A., Simon, E., Slater, D., Smith, R. S., Straneo, F., Trusel, L. D., Van Den Broeke, M. R., and Van De Wal, R. (2020). Experimental protocol for sea level projections from ISMIP6 stand-alone ice sheet models. *The Cryosphere*, 14(7):2331–2368.

Oppenheimer, M., Glavovic, B., Hinkel, J., van de Wal, R., Magnan, A., Abd-Elgawad, A., Cai, R., Cifuentes-Jara, M., DeConto, R., Ghosh, T., Hay, J., Isla, F., Marzeion, B., Meyssignac, B., and Sebesvari, Z. (2019). Sea Level Rise and Implications for Low-Lying Islands, Coasts and Communities. In *IPCC Special Report on the Ocean and Cryosphere in a Changing Climate*.

Paolo, F. S., Fricker, H. A., and Padman, L. (2015). Volume loss from Antarctic ice shelves is accelerating. *Science*, 348(6232):327–331.

Paolo, F. S., Padman, L., Fricker, H. A., Adusumilli, S., Howard, S., and Siegfried, M. R. (2018). Response of Pacific-sector Antarctic ice shelves to the El Niño/Southern Oscillation. *Nature Geoscience*, 11(2):121–126.

Pattyn, F. (2017). Sea-level response to melting of Antarctic ice shelves on multi-centennial timescales with the fast Elementary Thermomechanical Ice Sheet model (f.ETISh v1.0). *The Cryosphere*, 11(4):1851–1878.

Pattyn, F. (2018). The paradigm shift in Antarctic ice sheet modelling. *Nature Communications*, 9(2728):1–3.

Pattyn, F., Favier, L., Sun, S., and Durand, G. (2017). Progress in Numerical Modeling of Antarctic Ice-Sheet Dynamics. *Current Climate Change Reports*, 3:174–184.

Pattyn, F. and Morlighem, M. (2020). The uncertain future of the Antarctic Ice Sheet. *Science*, 367(6484):1331–1335.

Pattyn, F., Perichon, L., Durand, G., Favier, L., Gagliardini, O., Hindmarsh, R. C. A., Zwinger, T., Albrecht, T., Cornford, S. L., Docquier, D., Fürst, J. J., Goldberg, D. N., Gudmundsson, G. H., Humbert, A., Hütten, M., Huybrechts, P., Jouvet, G., Kleiner, T., Larour, E. Y., Martin, D. F., Morlighem, M., Payne, A. J., Pollard, D., Rückamp, M., Rybak, O., Seroussi, H., Thoma, M., and Wilkens, N. (2013). Grounding-line migration in plan-view marine ice-sheet models: Results of the ice2sea MISMIP3d intercomparison. *Journal of Glaciology*, 59(215):410–422.

Pattyn, F., Schoof, C. G., Perichon, L., Hindmarsh, R. C. A., Bueler, E., De Fleurian, B., Durand, G., Gagliardini, O., Gladstone, R. M., Goldberg, D. N., Gudmundsson, G. H., Huybrechts, P., Lee, V., Nick, F. M., Payne, A. J., Pollard, D., Rybak, O., Saito, F., and Vieli, A. (2012). Results of the marine ice sheet model intercomparison project, MISMIP. *The Cryosphere*, 6(3):573–588.

Payne, A. J., Nowicki, S., Abe-Ouchi, A., Agosta, C., Alexander, P., Albrecht, T., Asay-Davis, X., Aschwanden, A., Barthel, A., Bracegirdle, T. J., Calov, R., Chambers, C., Choi, Y., Cullather, R., Cuzzone, J., Dumas, C., Edwards, T. L., Felikson, D., Fettweis, X., Galton-Fenzi, B. K., Goelzer, H., Gladstone, R., Golledge, N. R., Gregory, J. M., Greve, R., Hattermann, T., Hoffman, M. J., Humbert, A., Huybrechts, P., Jourdain, N. C., Kleiner, T., Munneke, P. K., Larour, E., Le clec'h, S., Lee, V., Leguy, G., Lipscomb, W. H., Little, C. M., Lowry, D. P., Morlighem, M., Nias, I., Pattyn, F., Pelle, T., Price, S. F., Quiquet, A., Reese, R., Rückamp, M., Schlegel, N. J., Seroussi, H., Shepherd, A., Simon, E., Slater, D., Smith, R. S., Straneo, F., Sun, S., Tarasov, L., Trusel, L. D., Van Breedam, J., van de Wal, R., van den Broeke, M., Winkelmann, R., Zhao, C., Zhang, T., and Zwinger, T. (2021). Future Sea Level Change Under Coupled Model Intercomparison Project Phase 5 and Phase 6 Scenarios From the Greenland and Antarctic Ice Sheets. *Geophysical Research Letters*, 48(16).

Pegler, S. S. (2018a). Marine ice sheet dynamics: The impacts of ice-shelf buttressing. *Journal of Fluid Mechanics*, 857:605–647.

Pegler, S. S. (2018b). Suppression of marine ice sheet instability. *Journal of Fluid Mechanics*, 857:648–680.

Pegler, S. S. and Worster, M. G. (2012). Dynamics of a viscous layer flowing radially over an inviscid ocean. *Journal of Fluid Mechanics*, 696:152–174.

Pollard, D. and DeConto, R. M. (2012). Description of a hybrid ice sheet-shelf model, and application to Antarctica. *Geoscientific Model Development*, 5(5):1273–1295.

Pollard, D., DeConto, R. M., and Alley, R. B. (2015). Potential Antarctic Ice Sheet retreat driven by hydrofracturing and ice cliff failure. *Earth and Planetary Science Letters*, 412:112–121.

Pritchard, H. D., Ligtenberg, S. R. M., Fricker, H. A., Vaughan, D. G., van den Broeke, M. R., and Padman, L. (2012). Antarctic ice-sheet loss driven by basal melting of ice shelves. *Nature*, 484(7395):502–505.

Rankl, M., Fürst, J. J., Humbert, A., and Braun, M. (2017). Dynamic changes on the Wilkins Ice Shelf during the 2006-2009 retreat derived from satellite observations. *The Cryosphere*, 11(3):1199–1211.

Reese, R., Albrecht, T., Mengel, M., Asay-Davis, X. S., and Winkelmann, R. (2018a). Antarctic sub-shelf melt rates via PICO. *The Cryosphere*, 12(6):1969–1985.

Reese, R., Gudmundsson, G. H., Levermann, A., and Winkelmann, R. (2018b). The far reach of ice-shelf thinning in Antarctica. *Nature Climate Change*, 8(1):53–57.

Reese, R., Winkelmann, R., and Gudmundsson, G. H. (2018c). Grounding-line flux formula applied as a flux condition in numerical simulations fails for buttressed Antarctic ice streams. *The Cryosphere*, 12:3229–3242.

Rignot, E., Casassa, G., Gogineni, P., Krabill, W. B., Rivera, A., and Thomas, R. (2004). Accelerated ice discharge from the Antarctic Peninsula following the collapse of Larsen B ice shelf. *Geophysical Research Letters*, 31(18):2–5.

Rignot, E., Jacobs, S., Mouginot, J., and Scheuchl, B. (2013). Ice Shelf Melting Around Antarctica. *Science*, 341:266–270.

Rignot, E., Mouginot, J., Morlighem, M., Seroussi, H., and Scheuchl, B. (2014). Widespread, rapid grounding line retreat of Pine Island, Thwaites, Smith, and Kohler glaciers, West Antarctica, from 1992 to 2011. *Geophysical Research Letters*, 41(10):3502–3509.

Rignot, E., Mouginot, J., and Scheuchl, B. (2011). Ice flow of the Antarctic ice sheet. *Science*, 333:1427–1430.

Rignot, E., Mouginot, J., and Scheuchl, B. (2017). MEaSUREs InSAR-Based Antarctica Ice Velocity Map, Version 2. *Boulder, Colorado USA. NASA National Snow and Ice Data Center Distributed Active Archive Center.*

Rignot, E., Mouginot, J., Scheuchl, B., van den Broeke, M. R., van Wessem, J. M., and Morlighem, M. (2019). Four decades of Antarctic Ice Sheet mass balance from 1979-2017. *Proceedings of the National Academy of Sciences*, 116(4):1095–1103.

Ritz, C., Edwards, T. L., Durand, G., Payne, A. J., Peyaud, V., and Hindmarsh, R. C. A. (2015). Potential sea-level rise from Antarctic ice-sheet instability constrained by observations. *Nature*, 528(7580):115–118.

Robel, A. A. and Banwell, A. F. (2019). A Speed Limit on Ice Shelf Collapse Through Hydrofracture. *Geophysical Research Letters*, 46(21):12092–12100.

Rosier, S. H. R., Reese, R., Donges, J. F., De Rydt, J., Gudmundsson, G. H., and Winkelmann, R. (2021). The tipping points and early warning indicators for Pine Island Glacier, West Antarctica. *The Cryosphere*, 15(3):1501–1516.

Rott, H., Abdel Jaber, W., Wuite, J., Scheiblauer, S., Floricioiu, D., van Wessem, J. M., Nagler, T., Miranda, N., and van den Broeke, M. R. (2018). Changing pattern of ice flow and mass balance for glaciers discharging into the Larsen A and B embayments, Antarctic Peninsula, 2011 to 2016. *The Cryosphere*, 12(4):1273–1291.

Rott, H., Skvarca, P., and Nagler, T. (1996). Rapid Collapse of Northern Larsen Ice Shelf, Antarctica. *Science*, 271(5250):788–792.

Royston, S. and Gudmundsson, G. H. (2016). Changes in ice-shelf buttressing following the collapse of Larsen A Ice Shelf, Antarctica, and the resulting impact on tributaries. *Journal of Glaciology*, 62(235):905–911.

Scambos, T. A., Berthier, E., Haran, T. M., Shuman, C. A., Cook, A. J., Ligtenberg, S. R. M., and Bohlander, J. A. (2014). Detailed ice loss pattern in the northern Antarctic Peninsula: Widespread decline driven by ice front retreats. *The Cryosphere*, 8(6):2135–2145.

Scambos, T. A., Bohlander, J. A., Shuman, C. A., and Skvarca, P. (2004). Glacier acceleration and thinning after ice shelf collapse in the Larsen B embayment, Antarctica. *Geophysical Research Letters*, 31(18):2001–2004.

Scambos, T. A., Haran, T. M., Fahnestock, M. A., Painter, T. H., and Bohlander, J. A. (2007). MODIS-based Mosaic of Antarctica (MOA) data sets: Continent-wide surface morphology and snow grain size. *Remote Sensing of Environment*, 111(2):242–257.

Scambos, T. A., Hulbe, C. L., Fahnestock, M. A., and Bohlander, J. A. (2000). The Link between Climate Warming and Ice Shelf Breakups in the Antarctic Peninsula. *Journal of Glaciology*, 46(154):516–530.

Schannwell, C., Cornford, S. L., Pollard, D., and Barrand, N. E. (2018). Dynamic response of Antarctic Peninsula Ice Sheet to collapse of Larsen C and George VI ice shelves. *The Cryosphere*, 12:2307–2326.

Schoof, C. G. (2007). Ice sheet grounding line dynamics: Steady states, stability, and hysteresis. *Journal of Geophysical Research: Earth Surface*, 112(3):1–19.

Schoof, C. G. and Hewitt, I. (2013). Ice-Sheet Dynamics. *Annual Review of Fluid Mechanics*, 45(1):217–239.

Schoof, C. G. and Hindmarsh, R. C. A. (2010). Thin-film flows with wall slip: An asymptotic analysis of higher order glacier flow models. *Quarterly Journal of Mechanics and Applied Mathematics*, 63(1):73–114.

Sergienko, O. V. and Wingham, D. J. (2022). Bed topography and marine ice-sheet stability. *Journal of Glaciology*, 68(267):124–138.

Seroussi, H., Nakayama, Y., Larour, E., Menemenlis, D., Morlighem, M., Rignot, E., and Khazendar, A. (2017). Continued retreat of Thwaites Glacier, West Antarctica, controlled by bed topography and ocean circulation. *Geophysical Research Letters*, 44(12):6191–6199.

Seroussi, H., Nowicki, S. M. J., Payne, A. J., Goelzer, H., Lipscomb, W. H., Abe Ouchi, A., Agosta, C., Albrecht, T., Asay-Davis, X. S., Barthel, A., Calov, R., Cullather, R., Dumas, C., Gladstone,

R. M., Golledge, N. R., Gregory, J. M., Greve, R., Hattermann, T., Hoffman, M. J., Humbert, A., Huybrechts, P., Jourdain, N. C., Kleiner, T., Larour, E. Y., Leguy, G. R., Lowry, D., Little, C. M., Morlighem, M., Pattyn, F., Pelle, T., Price, S. F., Quiquet, A., Reese, R., Schlegel, N.-J., Shepherd, A., Simon, E. G., Smith, R., Straneo, F., Sun, S., Trusel, L. D., Van Breedam, J., van de Wal, R. S. W., Winkelmann, R., Zhao, C., Zhang, T., and Zwinger, T. (2020). ISMIP6 Antarctica: a multi-model ensemble of the Antarctic ice sheet evolution over the 21st century. *The Cryosphere*, 14:3033–3070.

Shepherd, A., Ivins, E. R., Geruo, A., Barletta, V. R., Bentley, M. J., Bettadpur, S., Briggs, K. H., Bromwich, D. H., Forsberg, R., Galin, N., Horwath, M., Jacobs, S., Joughin, I., King, M. A., Lenaerts, J. T. M., Li, J., Ligtenberg, S. R. M., Luckman, A. J., Luthcke, S. B., McMillan, M., Meister, R., Milne, G., Mouginot, J., Muir, A., Nicolas, J. P., Paden, J., Payne, A. J., Pritchard, H. D., Rignot, E., Rott, H., Sørensen, L. S., Scambos, T. A., Scheuchl, B., Schrama, E. J. O., Smith, B. E., Sundal, A. V., van Angelen, J. H., van de Berg, W. J., Van Den Broeke, M. R., Vaughan, D. G., Velicogna, I., Wahr, J., Whitehouse, P. L., Wingham, D. J., Yi, D., Young, D. A., and Zwally, H. J. (2012). A reconciled estimate of ice-sheet mass balance. *Science*, 338:1183–1189.

Shepherd, A., Ivins, E. R., Rignot, E., Smith, B. E., van den Broeke, M. R., Velicogna, I., Whitehouse, P. L., Briggs, K. H., Joughin, I., Krinner, G., Nowicki, S. M. J., Payne, A. J., Scambos, T. A., Schlegel, N.-J., Geruo, A., Agosta, C., Ahlstrøm, A., Babonis, G., Barletta, V. R., Blazquez, A., Bonin, J., Csatho, B. M., Cullather, R., Felikson, D., Fettweis, X., Forsberg, R., Gallée, H., Gardner, A. S., Gilbert, L., Groh, A., Gunter, B., Hanna, E., Harig, C., Helm, V., Horvath, A., Horwath, M., Khan, S. A., Kjeldsen, K. K., Konrad, H., Langen, P., Lecavalier, B., Loomis, B., Luthcke, S. B., McMillan, M., Melini, D., Mernild, S., Mohajerani, Y., Moore, P., Mouginot, J., Moyano, G., Muir, A., Nagler, T., Nield, G., Nilsson, J., Noel, B., Otosaka, I., Pattle, M. E., Peltier, W. R., Pie, N., Rietbroek, R., Rott, H., Sandberg-Sørensen, L., Sasgen, I., Save, H., Scheuchl, B., Schrama, E. J. O., Schröder, L., Seo, K.-W., Simonsen, S. B., Slater, T., Spada, G., Sutterley, T. C., Talpe, M., Tarasov, L., van de Berg, W. J., van der Wal, W., van Wessem, J. M., Vishwakarma, B. D., Wiese, D., and Wouters, B. (2018). Mass balance of the Antarctic Ice Sheet from 1992 to 2017. *Nature*, 558(7709):219–222.

Shepherd, A., Wingham, D. J., Payne, A. J., and Skvarca, P. (2003). Larsen Ice Shelf Has Progressively Thinned. *Science*, 302(5646):856–859.

Shuman, C. A., Berthier, E., and Scambos, T. A. (2011). 2001-2009 elevation and mass losses in the Larsen A and B embayments, Antarctic Peninsula. *Journal of Glaciology*, 57(204):737–754.

Smith, B. E., Fricker, H. A., Gardner, A. S., Medley, B., Nilsson, J., Paolo, F. S., Holschuh, N., Adusumilli, S., Brunt, K. M., Csatho, B. M., Harbeck, K., Markus, T., Neumann, T. A., Siegfried, M. R., and Zwally, H. J. (2020). Pervasive ice sheet mass loss reflects competing ocean and atmosphere processes. *Science*, 368(6496):1239–1242.

Sun, S., Cornford, S. L., Moore, J. C., Gladstone, R., and Zhao, L. (2017). Ice shelf fracture parameterization in an ice sheet model. *The Cryosphere*, 11(6):2543–2554.

Sun, S., Pattyn, F., Simon, E. G., Albrecht, T., Cornford, S. L., Calov, R., Dumas, C., Gillet-Chaulet, F., Goelzer, H., Golledge, N. R., Greve, R., Hoffman, M. J., Humbert, A., Kazmierczak, E., Kleiner, T., Leguy, G. R., Lipscomb, W. H., Martin, D. F., Morlighem, M., Nowicki, S. M. J., Pollard, D., Price, S. F., Quiquet, A., Seroussi, H., Schlemm, T., Sutter, J., van de Wal, R. S. W.,

Winkelmann, R., and Zhang, T. (2020). Antarctic ice sheet response to sudden and sustained ice-shelf collapse (ABUMIP). *Journal of Glaciology*, 66(260):891–904.

Thomas, R. H. (1979a). Ice shelves: a review. *Journal of Glaciology*, 24(90):273–285.

Thomas, R. H. (1979b). The dynamics of marine ice sheets. *Journal of Geophysical Research: Solid Earth*, 24(90):167–178.

Timmermann, R., Le Brocq, A., Deen, T., Domack, E., Dutrieux, P., Galton-Fenzi, B., Hellmer, H., Humbert, A., Jansen, D., Jenkins, A., Lambrecht, A., Makinson, K., Niederjasper, F., Nitsche, F., Nøst, O. A., Smedsrud, L. H., and Smith, W. H. (2010). A consistent data set of Antarctic ice sheet topography, cavity geometry, and global bathymetry. *Earth System Science Data*, 2(2):261–273.

Tsai, V. C., Stewart, A. L., and Thompson, A. F. (2015). Marine ice-sheet profiles and stability under Coulomb basal conditions. *Journal of Glaciology*, 61(226):205–215.

Turner, J., Lu, H., White, I., King, J. C., Phillips, T., Hosking, J. S., Bracegirdle, T. J., Marshall, G. J., Mulvaney, R., and Deb, P. (2016). Absence of 21st century warming on Antarctic Peninsula consistent with natural variability. *Nature*, 535(7612):411–415.

van den Broeke, M. R. (2005). Strong surface melting preceded collapse of Antarctic Peninsula ice shelf. *Geophysical Research Letters*, 32(12):1–4.

van Wessem, J. M., Ligtenberg, S. R. M., Reijmer, C. H., van de Berg, W. J., van den Broeke, M. R., Barrand, N. E., Thomas, E. R., Turner, J., Wuite, J., Scambos, T. A., and van Meijgaard, E. (2016). The modelled surface mass balance of the Antarctic Peninsula at 5.5 km horizontal resolution. *The Cryosphere*, 10(1):271–285.

van Wessem, J. M., van de Berg, W. J., Noel, B., van Meijgaard, E., Birnbaum, G., Jakobs, C. L., Krüger, K., Lenaerts, J. T. M., Lhermitte, S., Ligtenberg, S. R. M., Medley, B., Reijmer, C. H., van Tricht, K., Trusel, L. D., van Ulft, L. H., Wouters, B., Wuite, J., and van den Broeke, M. R. (2018). Modelling the climate and surface mass balance of polar ice sheets using RACMO2, part 2: Antarctica (1979-2016). *The Cryosphere*, 12:1479–1498.

Vaughan, D. G. and Doake, C. S. M. (1996). Recent atmospheric warming and retreat of ice shelves on the Antarctic Peninsula. *Nature*, 379:328–331.

Vaughan, D. G., Marshall, G. J., Connolley, W. M., Parkinson, C., Mulvaney, R., Hodgson, D. A., King, J. C., Pudsey, C. J., and Turner, J. (2003). Recent rapid regional climate warming on the Antarctic Peninsula. *Climatic Change*, 60:243–274.

Vieli, A. and Payne, A. J. (2005). Assessing the ability of numerical ice sheet models to simulate grounding line migration. *Journal of Geophysical Research: Earth Surface*, 110(1):1–18.

Vieli, A., Payne, A. J., Shepherd, A., and Du, Z. (2007). Causes of pre-collapse changes of the Larsen B ice shelf: Numerical modelling and assimilation of satellite observations. *Earth and Planetary Science Letters*, 259(3-4):297–306.

Wearing, M. G., Kingslake, J., and Worster, M. G. (2020). Can unconfined ice shelves provide buttressing via hoop stresses? *Journal of Glaciology*, 66(257):349–361.

Weertman, J. (1957). On the sliding of glacires. *Journal of Glaciology*, 3(21):33–38.

Weertman, J. (1974). Stability of the Junction of an Ice Sheet and an Ice Shelf. *Journal of Glaciology*, 13(67):3–11.

Wingham, D. J., Francis, C. R., Baker, S. G., Bouzinac, C., Brockley, D., Cullen, R., de Chateau-Thierry, P., Laxon, S. W., Mallow, U., Mavrocordatos, C., Phalippou, L., Ratier, G., Rey, L., Rostan, F., Viau, P., and Wallis, D. W. (2006). CryoSat: A mission to determine the fluctuations in Earth's land and marine ice fields. *Advances in Space Research*, 37(4):841–871.

Wuite, J., Rott, H., Hetzenecker, M., Floricioiu, D., De Rydt, J., Gudmundsson, G. H., Nagler, T., and Kern, M. (2015). Evolution of surface velocities and ice discharge of Larsen B outlet glaciers from 1995 to 2013. *The Cryosphere*, 9(3):957–969.

Yu, H., Rignot, E., Seroussi, H., and Morlighem, M. (2018). Retreat of Thwaites Glacier, West Antarctica, over the next 100 years using various ice flow models, ice shelf melt scenarios and basal friction laws. *The Cryosphere*, 12:3861–3876.

Zhang, T., Price, S. F., Hoffman, M. J., Perego, M., and Asay-Davis, X. S. (2020). Diagnosing the sensitivity of grounding-line flux to changes in sub-ice-shelf melting. *The Cryosphere*, 14:3407–3424.

Zoet, L. K. and Iverson, N. R. (2020). A slip law for glaciers on deformable beds. *Science*, 368(6486):76–78.